

ENERGY RECOVERY LINEAR ACCELERATOR
LATTICE DESIGN
&
COHERENT SYNCHROTRON RADIATION

A Dissertation

Presented to the Faculty of the Graduate School
of Cornell University

in Partial Fulfillment of the Requirements for the Degree of
Doctor of Philosophy

by

Christopher Earl Mayes

May 2009

© 2009 Christopher Earl Mayes

ALL RIGHTS RESERVED

ENERGY RECOVERY LINEAR ACCELERATOR LATTICE DESIGN

&

COHERENT SYNCHROTRON RADIATION

Christopher Earl Mayes, Ph.D.

Cornell University 2009

Energy Recovery Linear Accelerators (ERLs) are potential drivers for novel fourth-generation synchrotron light sources. An ERL combines the high quality beams of a linear accelerator with the high currents possible in a storage ring. The excessive power needs of a lone linac are avoided by circulating accelerated particles back through the linac to recover their energy. This dissertation is focused on the lattice design of a high energy ERL synchrotron light source at Cornell University. In order to illustrate general ERL requirements, a simpler design is also presented. The mathematics needed to describe such a machine are particular to accelerator physics, and so a separate chapter is devoted to developing all of the relevant concepts.

The short bunch lengths and high bunch charges possible in an ERL can give rise to Coherent Synchrotron Radiation (CSR) which can potentially limit the operation of the accelerator. CSR is a collective phenomenon where the energy radiated at wavelengths longer than the bunch length is enhanced by the number of charges in the bunch. The final chapter develops an exact model for CSR from an infinitely thin bunch. It reveals many interesting effects, including CSR at low energies, through multiple bends in a lattice, and in bunch compression. The model is also used to obtain the limits of validity of previously known approximations. Finally, CSR is examined for the ERL designs presented.

BIOGRAPHICAL SKETCH

Christopher Earl Mayes was born on July 2, 1980 in Boone, North Carolina. In June of 1998 graduated from Lyman Hall High School in Wallingford, Connecticut. At the College of William & Mary in Williamsburg, Virginia he majored in mathematics and physics, and graduated with highest honors in May of 2002. The following August he arrived in Ithaca, New York to pursue a Ph.D. in physics at Cornell University.

For Granny, Nanny, and PawPaw

ACKNOWLEDGEMENTS

I would like to thank Sol Gruner and Saul Teukolsky for supervising my graduate school career, and especially my advisor Georg Hoffstaetter for his expertise, guidance, and friendship. I would also like to thank David Sagan for his invaluable code *Bmad* , and James Crittenden for his aid with the lattice design. This work was funded through grant PHY 0131508 from the National Science Foundation.

TABLE OF CONTENTS

Biographical Sketch	iii
Dedication	iv
Acknowledgements	v
Table of Contents	vi
List of Tables	viii
List of Figures	ix
1 Introduction	1
1.1 Synchrotron Radiation	1
1.2 Modern Synchrotron Light Sources	5
1.3 Energy Recovery Linear Accelerators	8
1.4 Coherent Synchrotron Radiation	11
2 Accelerator Lattice Design	16
2.1 Beam Optics Fundamentals	16
2.1.1 Accelerator Coordinate System	17
2.1.2 Equations of Motion	19
2.1.3 Accelerator Magnets	23
2.1.4 Accelerating Cavities	27
2.1.5 Linear Optics	29
2.1.6 Nonlinear Optics	46
2.2 Radiative Emittance Growth	53
2.3 Accelerator Simulation	55
2.3.1 Bmad & Tao	56
2.3.2 Optimization Example	58
3 Minimal ERL	63
3.1 Introduction & Layout	63
3.2 Optics	67
3.2.1 Linacs	70
3.2.2 Turnaround Arc	76
3.2.3 Return Arc	82
3.3 Particle Tracking	88
3.4 Time of Flight in ERL Arcs	96
3.5 Bunch Compression	101
4 Cornell ERL	108
4.1 Site	108
4.2 Layout	112
4.3 Optics	115
4.3.1 LA & LB – Linac A and B	120
4.3.2 TA & TB – Turnaround A and B	126

4.3.3	SA – South Arc	133
4.3.4	CE – CESR	142
4.3.5	NA – North Arc	155
4.4	Particle Tracking	165
4.5	Bunch Compression	174
5	Coherent Synchrotron Radiation	179
5.1	Exact 1D model for CSR	179
5.2	Single Bending Magnet	183
5.2.1	Steady State	185
5.2.2	Shielding by Parallel Plates	191
5.2.3	Retarded Bunch Visualization	196
5.3	Multiple Bends and Drifts	199
5.4	CSR in a Drift Between Bends	204
5.5	Bunch Compression	207
5.6	Coherent Power Spectrum	210
5.7	CSR in the MERL	216
5.8	CSR in the CERL	221
5.9	Conclusion	225
A	Equations of motion	227
B	Linear Transfer Matrices	231
C	CSR Formulas for Multiple Bends and Drifts	233

LIST OF TABLES

1.1	Light Source Comparison	10
2.1	Selected Multipole Field Strengths	26
3.1	MERL & CERL Parameters	64

LIST OF FIGURES

1.1	GE Synchrotron Photograph	3
1.2	Undulator versus Dipole Brilliance	6
1.3	ERL Conceptual Layout	9
1.4	The coherent power spectrum	12
1.5	Steady-State CSR-wakes	13
1.6	The shielded coherent power spectrum	14
2.1	Accelerator Coordinate System	18
2.2	Quadrupole and Sextupole Fields	27
2.3	Quadrupole Transverse Phase Space	32
2.4	Phase Space Ellipse	37
2.5	Longitudinal phase space through a linac	45
2.6	Example Optimization	60
2.7	Horizontal Particle Trajectories	61
2.8	Horizontal Phase Space Slices	62
3.1	MERL Layout	66
3.2	MERL Optics	68
3.3	MERL Emittance Growth and Energy	69
3.4	MERL Linac Optics Scheme	71
3.5	MERL linac quadrupole k_1 strengths	73
3.6	Optics for LB	74
3.7	Optics for LA	75
3.8	Layout for the MERL Turnaround Arc	76
3.9	Layout for the beginning of the MERL Turnaround Arc	77
3.10	Optics for the MERL TA Cell A and B	79
3.11	Optics for the MERL TA	80
3.12	MERL TA Emittance Growth and Time of Flight	81
3.13	Layout for the beginning of the MERL Return Arc	84
3.14	Optics for the MERL Return Arc Cells A and B	85
3.15	Optics for the MERL Return Arc	86
3.16	MERL Return Arc Radiative Emittance Growth and Time of Flight	87
3.17	Initial particles for MERL simulations	90
3.18	Particles at the beginning and end of the RA, Mode A	91
3.19	Particles at the end of the MERL	92
3.20	Bunch widths and normalized emittances through the RA	93
3.21	MERL normalized emittances and energy spread from particle tracking	94
3.22	MERL bunch widths and bunch length from particle tracking	95
3.23	Maximum energy deviations at the dump for combinations of r_{56} terms, on-crest	98
3.24	Maximum energy deviations at the dump for combinations of t_{566} terms, on-crest	99

3.25	Maximum energy deviations at the dump for combinations of r_{56} and t_{566} terms, off-crest	100
3.26	Minimum bunch lengths versus ϕ_{rf} using first and second order compression	102
3.27	Longitudinal phase space before and after compression	103
3.28	Contours of bunch lengths	104
3.29	MERL Mode C Dispersion and Time of Flight	105
3.30	MERL Mode C Bunch Width and Length	106
3.31	Longitudinal phase space slices in the MERL short pulse undulators	107
4.1	Cornell Topographic Map	110
4.2	CERL Layout	111
4.3	CERL on the Campus Map	114
4.4	CERL Emittance Growth and Energy	118
4.5	CERL Optics	119
4.6	Standard CERL Cryomodule	120
4.7	CERL linac quadrupole k_1 strengths	123
4.8	Optics for LA	124
4.9	Optics for LB	125
4.10	Layout for TA & TB	126
4.11	Layout showing the beginning of TA and TB	128
4.12	Optics for TA Cell B	129
4.13	Optics for TA Cell A and TB Cell A	130
4.14	TA Optics	131
4.15	TA emittance growth and time of flight	132
4.16	Layout showing the South and North Arcs	133
4.17	Layout for the beginning of the SA section	134
4.18	Layout for the end of the SA	136
4.19	Optics for SA Cell A	137
4.20	Optics for the first SA Cell B	138
4.21	Optics for SA Cell E	139
4.22	SA Optics	140
4.23	SA Emittance Growth and Time of Flight	141
4.24	Layout for CE	142
4.25	CE Optics	143
4.26	CE Emittance Growth and Time of Flight	144
4.27	Layout for low emittance CE upgrade	146
4.28	Optics for the CE Upgrade Cell P	148
4.29	Emittance growth and Time of Flight for CE Upgrade Cell P	149
4.30	Optics for CE Upgrade Cell B	150
4.31	Optics for CE Upgrade Cell A	151
4.32	Optics for CE Upgrade Cell F	152
4.33	CE Optics	153

4.34	CE Upgrade Emittance Growth and Time of Flight	154
4.35	Layout for the NA	155
4.36	Layout showing the NA Cell D	156
4.37	Optics for NA Cell B	158
4.38	Optics for NA Cell C	159
4.39	Optics for NA Cell A	160
4.40	Optics for NA Cell D	161
4.41	Emittance growth and Time of Flight for NA Cell D	162
4.42	NA Optics	163
4.43	NA Emittance Growth and Time of Flight	164
4.44	Initial particles for CERL simulations	165
4.45	Particles at the beginning and end of the SA, Mode A	167
4.46	Particles at the beginning and end of the NA, Mode A	168
4.47	Particles at the end of the CERL	169
4.48	Mode A bunch widths and normalized emittances through the SA	170
4.49	Mode A bunch widths and normalized emittances through the NA	171
4.50	CERL Mode A normalized emittances and energy spread from particle tracking	172
4.51	CERL Mode A bunch widths and bunch length from particle tracking	173
4.52	CERL SA-CE-NA Mode C Dispersion and Time of Flight	175
4.53	CERL SA-CE-NA Mode C Bunch Length and u_{5666}	176
4.54	CERL SA-CE-NA Mode C Bunch Length and u_{5666} with up- graded CE	177
4.55	Longitudinal phase space slices in the CERL short pulse undula- tors	178
5.1	Single bend geometry	183
5.2	Steady-state retarded angle α versus $\kappa \Delta$	186
5.3	Steady-state CSR-wake for various energies	187
5.4	Steady-state CSR-wake from forward particles	188
5.5	Comparison of energy losses using a simple CSR-wake formula .	189
5.6	Comparison of energy losses using a more accurate CSR-wake formula	190
5.7	Shielded CSR-wake showing image charge contributions	192
5.8	Average energy loss and energy spread versus the shielding pa- rameter b_s	195
5.9	The retarded distributions seen by various test particles	197
5.10	The retarded distributions seen by various test particles, includ- ing image charges	198
5.11	Geometry for two bends	199
5.12	Average energy loss and energy spread through a bend	201
5.13	The retarded distributions seen by various test particles in a two bend geometry, including image charges	202

5.14	CSR-wakes in the drift region after a bend	205
5.15	Average energy loss and energy spread in the drift region after a bend	206
5.16	Average energy loss and energy spread through a bend compressing a bunch	209
5.17	The coherent power spectrum for various coherence parameters a_c	211
5.18	Behavior of different approximations to the coherence function $T_c(a_c)$	213
5.19	The relative error for the average energy loss from the exact CSR-wakes compared with the analytic losses calculated from the power spectrum	214
5.20	The dividing like beyond which coherent power dominates the total power	215
5.21	b_s in the MERL bends	216
5.22	Ratio of incoherent to coherent steady-state radiation power in the MERL bends	217
5.23	Bunch lengths through the MERL RA using $Bmad$ for particle tracking and CSR	219
5.24	Longitudinal phase space slices in the MERL RA with CSR . . .	220
5.25	b_s in the CERL bends	221
5.26	Ratio of incoherent to coherent steady-state radiation power in the CERL bends	222
5.27	Bunch lengths through the CERL SA-CE-NA sections using $Bmad$ for particle tracking and CSR	223
5.28	Longitudinal phase space slices in the CERL NA with CSR	224

CHAPTER 1
INTRODUCTION

1.1 Synchrotron Radiation

The electromagnetic radiation of an accelerated charged particle has been of fundamental importance to physics for more than a century now. The power radiated by a nonrelativistic charge was first calculated by Larmor (1897), and his result is known today as the Larmor formula. The relativistically correct version was first derived in Liénard (1898) using potentials for Maxwell's equations, and this power radiated is

$$P = \frac{2}{3} \frac{r_c m}{c^3} \gamma^4 \left[c^2 \mathbf{a}^2 + \gamma^2 (\mathbf{v} \cdot \mathbf{a})^2 \right], \quad (1.1)$$

in which \mathbf{v} is the velocity vector and \mathbf{a} is the acceleration vector of the particle. Additionally m is the mass of the particle, r_c is the classical (electromagnetic) radius of the particle, γ is the Lorentz factor, and c is the speed of light. For purely transverse acceleration, this reduces to

$$P = \frac{2}{3} \frac{r_c m c^3 \beta^4 \gamma^4}{R^2} \quad (1.2)$$

where R is the instantaneous radius of curvature and βc is the magnitude of the velocity.

Further developments came from Schott in his Adams Prize¹ essay of 1909, on the subject of "The Radiation from Electric Systems or Ions in Accelerated Motion and the Mechanical Reactions on their Motion which Arise from It"

¹Prior winners of the Adams Prize included J. C. Maxwell in 1857, J. J. Thompson in 1882, J. H. Poynting in 1893, and J. Larmor in 1899.

(Schott, 1912, is the published version). Written in a time before the establishment of relativity and quantum mechanics, this work contains interesting discussions regarding various extended models of the electron, superluminal particle motion, and the influence of the æther. However, like Larmor and Liénard, he generally only assumes that Maxwell's equations are correct, and in examining the motion of an electron moving in a circle of radius R he finds the spatial distribution of the radiated fields and, in particular, he finds that the electromagnetic power radiated in the n^{th} harmonic of the revolution frequency is

$$P_n = n \frac{2\beta c r_c m c^2}{R^2} \left[\beta^2 J'_{2n}(2n\beta) - n(1 - \beta^2) \int_0^\beta dx J_{2n}(2nx) \right], \quad (1.3)$$

in which J_n is the n^{th} Bessel function of the first kind. It was hoped that the origin of atomic spectral lines would be explained by such radiation, but this approach ultimately failed.

Untouched for some thirty years, the subject was picked up by Iwanenko & Pomeranchuk (1944), who noted that these radiative losses by electrons would limit the maximum energy attainable in a betatron accelerator. Their remarks prompted Blewett in 1945 to search for such losses in the 100 MeV betatron at the General Electric Research Laboratory in Schenectady, New York. He found (published in Blewett, 1946) that radiative losses accounted for a shrinkage in the orbit of the electrons in the machine, but in looking at the microwave part of the spectrum he observed no radiation.

Meanwhile the problem had been introduced to Schwinger in late 1944, and in 1945 he performed more detailed calculations on these losses. In a then unpublished report (Schwinger, 1945) he recovers Schott's results, including Eq. (1.3). He observes that this expression, for small n , shows none of the dependence on γ that Eq. (1.2) would imply, and concludes that a great many

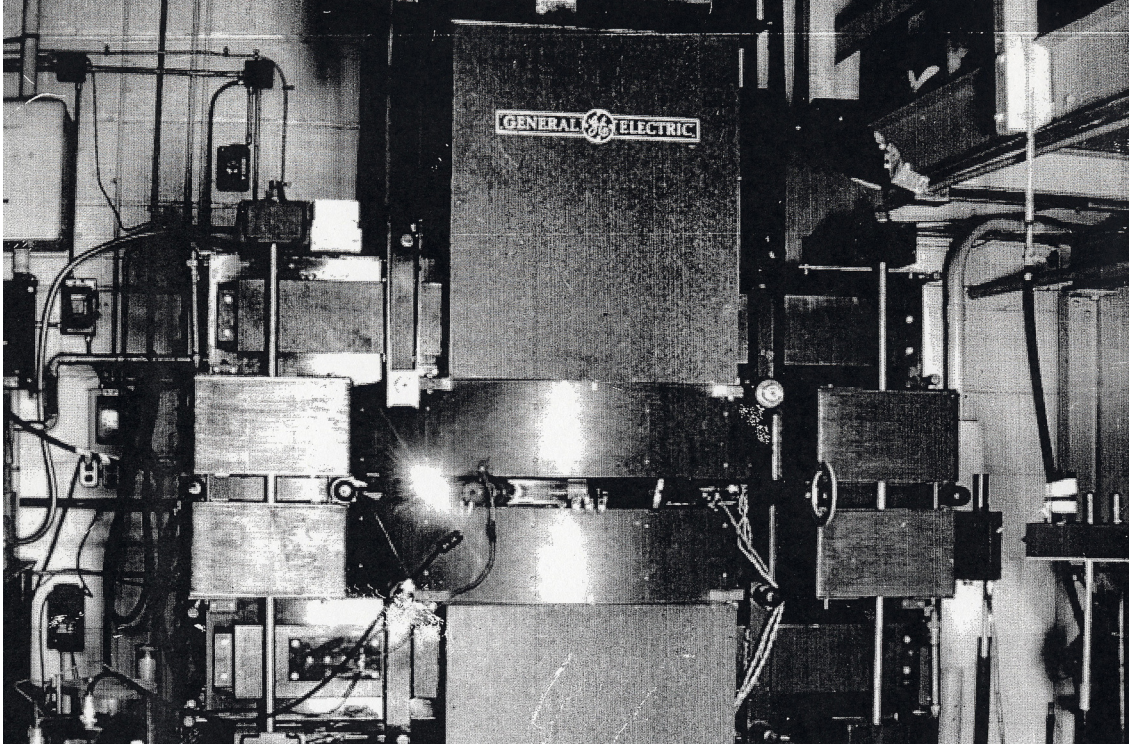


Figure 1.1: The General Electric 70 MeV synchrotron in 1947, built and operated in Schenectady, New York.

harmonics must contribute to the total radiated power. Using approximations for Bessel functions, such as

$$J_\nu(\nu\beta) \approx \frac{\sqrt{1-\beta^2}}{\pi\sqrt{3}} K_{1/3}\left(\frac{\nu}{3}(1-\beta^2)^{3/2}\right), \quad (1.4)$$

valid for $\nu \gg 1$, he finds

$$P_n = \frac{\sqrt{3}\beta r_c m c^2}{2\pi R^2} \left(\frac{2n}{3}\right)^{1/3} \xi^{2/3} \int_\xi^\infty dx K_{5/3}(x) \quad (1.5)$$

with $\xi \equiv \frac{2n}{3\gamma^3}$, which is peaked around $n \sim \gamma^3$. Equation (1.5) is the form perhaps best known by modern physicists (see for example, Jackson, 1999). His findings were circulated privately and presented at the American Physical Society meeting in New York in September the next year (Schwinger, 1946).

In 1947 a team at General Electric led by Pollock constructed the world's

second synchrotron, operating at 70 MeV. Unlike the 100 MeV betatron, the beam chamber was transparent, and in this machine the soon to be called “synchrotron radiation” was first observed. In a letter to Pollock, fellow team member Langmuir writes:

I have very definite and clear remembrances about the discovery of synchrotron radiation. I don't remember the date (presumably 24 April 1947) but in the afternoon one of the technicians reported to me that there seemed to be sparking in the synchrotron tube. He observed this by looking in a large (about 6 ft high by 3 ft wide) mirror that permitted us to observe the machine without getting too much radiation. You were at the controls of the machine. Upon seeing the light, I asked you to ruin the timing, which you did and the light went away. It returned when you returned the injection pulse to the proper time. I immediately said that must be Schwinger radiation. The whole incident took about thirty seconds.

In the following two years the laboratory was visited by many from the academic community in order to see this light, including six Nobel prize winners. Other notable visitors included the actor Ronald Reagan (who was not particularly impressed) and the physicist and Russian spy Klaus Fuchs (convicted in 1950 for disclosing atomic secrets) (Pollock, 1982).

While synchrotron radiation was readily used as an accelerator diagnostic, there was some question as to whether the classical calculations were valid (Parzen, 1951). Experiments using the 300 MeV synchrotron at Cornell University confirmed that they were, with the first accurate measurements of the energy loss by Corson (1953) and the first accurate measurements of the radiation spectrum by Tombouliau & Hartman (1956).

The subsequent use of synchrotron radiation from accelerators is typically divided into generations of facilities (much of this history can be found in Robinson, 2001). The first generation is characterized by the “parasitic” use of radiation from accelerators primarily designed for particle physics experiments. The first of these was the Synchrotron Ultraviolet Radiation Facility, which used the 180 MeV synchrotron at the National Bureau of Standards in the United States (Madden & Codling, 1963). Facilities in Europe and Asia soon followed. This generation includes the Cornell High Energy Synchrotron Source (CHESS) at the Cornell Electron Storage Ring. Accelerators built for the exclusive production of synchrotron radiation marked the beginning of a second generation of light sources. The first of these was the Synchrotron Radiation Source in the United Kingdom, a 2 GeV electron storage ring which began conducting experiments in 1981.

1.2 Modern Synchrotron Light Sources

Today synchrotron radiation has proven to be an invaluable tool for expanding the frontiers of physics, chemistry, materials sciences, biology, and medicine (Bilderback *et al.*, 2005). There are approximately 70 major particle accelerators spread around the globe that exist for the production of synchrotron radiation.

The most advanced of these are of the third generation of accelerators, and are primarily marked by the use of undulators to produce radiation. These devices (also called wigglers for large deflections) are built out of periodic arrangements of magnets that bend particles through a roughly sinusoidal path (see

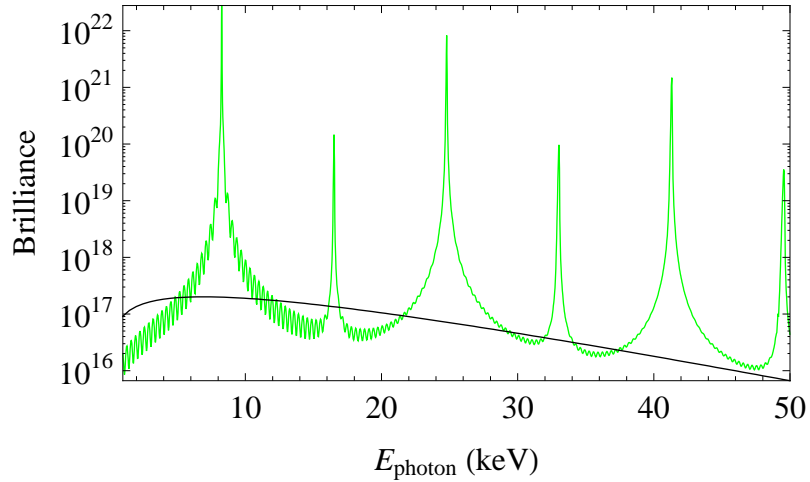


Figure 1.2: Undulator (green) versus Dipole (black) Brilliance

Motz, 1951, for early calculations). The radiation at particular wavelengths can constructively interfere, resulting in enhancements in the spectrum.

One important quantity of merit for these facilities is the brilliance \mathcal{B} , which is usually defined as the average photon flux per unit volume of transverse phase space, and is proportional to

$$\mathcal{B} \propto \frac{I_{\text{av}}}{\epsilon_x \epsilon_y}, \quad (1.6)$$

in which I_{av} is the average beam current. The quantities ϵ_x and ϵ_y are the horizontal and vertical emittances, which are the areas occupied in the horizontal and vertical phase spaces of the beam, and are properly defined in Chapter 2. Particles are usually bunched with an R.M.S. length σ , so the peak brilliance $\hat{\mathcal{B}}$ is

$$\hat{\mathcal{B}} \propto \frac{I_{\text{av}}}{\epsilon_x \epsilon_y \sigma}. \quad (1.7)$$

Figure 1.2 shows how an undulator can further enhance the brilliance over a dipole magnet. The harmonics can clearly be seen, with the brilliance amplified by five orders of magnitude over the dipole.

These photon energies, of course, are only possible if the particles have sufficient energy. Currently there are three high energy (> 4 GeV) dedicated third generation light sources: the Advanced Photon Source (APS) in Illinois, the European Synchrotron Radiation Facility (ESRF) in Grenoble, France, and the SPring-8 facility in Hyogo, Japan. They are all configured as storage rings, in which particles circulate billions of times through the machine before they are discarded, producing radiation in every pass. Because of this circulation, storage rings can operate with relatively high average currents (~ 100 mA), as the particle energy lost per turn is a small fraction of the total energy. This energy is restored by accelerating cavities in each pass.

Unfortunately, the quantum nature of synchrotron radiation increases the emittance in dipole magnets, which is eventually balanced by a damping of the emittance by the accelerating cavities, resulting in an equilibrium emittance. Roughly speaking, this equilibrium emittance is determined by the arrangement of elements in the ring, and is decoupled from the initially injected emittance. The bunch length is determined by the ring in a similar manner. Furthermore, the three facilities listed above are operating near their theoretical limits.

These problems can be circumvented if the bends are eliminated, resulting in a linac. The emittance in a linac actually decreases with energy, because the transverse momentum becomes smaller relative to the longitudinal momentum with acceleration. The bunch length is essentially unchanged from injection, and can even be compressed by a short section of bends.

Unfortunately for a linac, the average current is limited by the available electrical power. Simply from conservation of energy, the power needed to operate

an electron linac scales as

$$P_{\text{linac}} = 1 \text{ MW} \left(\frac{I_{\text{av}}}{\text{mA}} \right) \left(\frac{\Delta\mathcal{E}}{\text{GeV}} \right) \quad (1.8)$$

for a total linac energy gradient $\Delta\mathcal{E}$. Thus, 100 mA at 5 GeV would require 500 MW of power, which is comparable to the output of a modern nuclear power plant.

Nevertheless, linac light sources are being pursued, in the form of self amplified spontaneous emission free electron lasers, or SASE FELs. Such devices work by sending very short bunches through a very long undulator. They rely on an instability that further partitions the bunches into “micro-bunches”, which then emit photons in phase resulting in a much amplified X-ray brilliance. One prominent SASE FEL is the Linac Coherent Light Source at the Stanford Linear Accelerator, which is currently in construction (Arthur *et al.*, 2002).

Another option is to combine the benefits of a linac with the benefits of a ring, and such an arrangement is an Energy Recovery Linac.

1.3 Energy Recovery Linear Accelerators

An Energy Recovery Linac (ERL) is a potential driver for a novel fourth-generation synchrotron light source. The concept originated many years ago with Tigner (1965), in which a machine for accelerating, colliding, and decelerating beams is described. An ERL light source would combine the low emittances and short bunch lengths possible from a linac with the high currents possible in a ring, thus maximizing important quantities such as the peak brilliance in Eq. (1.7). Additionally, the operating characteristics and X-ray beamline config-

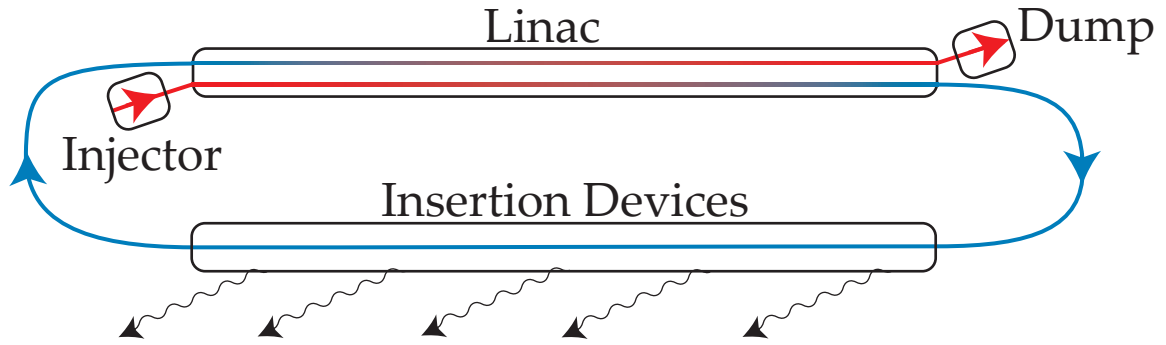


Figure 1.3: Conceptual Layout for an ERL.

urations of such a machine would be sufficiently familiar to users of the current storage rings that experiments could be easily transferred to take advantage of the higher quality synchrotron light (Gruner and Bilderback, 2003).

The simplest conceptual design for an ERL light source is shown in Fig. 1.3. Particle bunches with low emittance are accelerated to a low energy in an injector, and then sent to a linac where they are further accelerated to a high energy. These high energy particles can be sent through a series of insertion devices (undulators and wigglers) that extract synchrotron light. They are then reintroduced to the beginning of the linac, with the timing adjusted so that particles are decelerated through the linac, thus returning their energy to the fields in the structure. At the end of the linac they have a low energy, and can be sent to a dump.

Currently there are small functioning ERLs at the Thomas National Accelerator Jefferson Facility (Neil *et al.*, 2000), the Japan Atomic Energy Research Institute (Sawamura *et al.*, 2003), and the Siberian Synchrotron Radiation Center (Antokhin *et al.*, 2004). Several laboratories are pursuing ERL options for large scale purposes, including an ERL extension to the APS facility (Borland *et al.*, 2005). A listing of these projects can be found in Smith *et al.* (2005).

Table 1.1: The maximum particle energy, average current, horizontal emittance, and bunch length for the proposed Cornell ERL along with existing light source facilities.

Name	Energy (GeV)	Current (mA)	Emittance (pm)	Bunch Length (ps)
ESRF	6	200	4000	20
APS	7	100	2514	20
SPring 8	8	100	3000	13
CERL mode A	5	100	31	2
mode B	5	25	8	2
mode C	5	1	511	0.1

The focus of this dissertation is the layout and design of the beam optics for an ERL light source at Cornell University. The original study for such a machine can be found in Gruner & Tigner, eds. (2001), and an early layout is described in Hoffstaetter *et al.* (2003). All designs have incorporated the existing CESR ring, thus taking advantage of much of the existing infrastructure and expertise at Cornell. Beam properties for three operating modes of the Cornell ERL (CERL) are given in Tab. 1.1, along with parameters from the APS, ESRF, and SPring8 light sources. While this project is currently in the design phase, the injector has already been constructed (Liepe *et al.*, 2008).

In order to design an ERL, one must be familiar with a fair amount of background material, and therefore Chapter 2 is devoted to establishing a mathematical basis for describing particle motion in an accelerator. Some effort has been spent to keep it relatively self-contained, and it concludes with an overview of the simulation and optimization of an accelerator on computer.

The Cornell design contains many features that are particular to that project, so in order to illustrate general ERL requirements a simpler design, called the Minimal ERL (MERL), is presented in Chapter 3. The MERL uses the operating

modes listed in Tab. 1.1. It is built out of sections that are highly symmetric and periodic, which greatly shortens the the time needed to modify and optimize the design. Chapter 4 then presents the CERL design. Many of the sections parallel ones in Chapter 3. Much of this material will be put into the conceptual design report for the official project proposal. Note that this CERL design has been regularly used in other studies, for example the influence of ion distributions on electron dynamics (Hoffstaetter & Spethman, 2008) and intra-beam scattering in ERLs (Hoffstaetter *et al.*, 2008).

1.4 Coherent Synchrotron Radiation

In 1949 Schwinger published his derivation of the synchrotron radiation spectrum in the Physical Review. His 1945 report, however, is in many ways a superior document. Most notably, this report has calculations and discussions about the radiation due to multiple accelerating charges, a topic that is becoming relevant for modern particle accelerators (see Murphy, 2004, for a comprehensive overview). In particular, the radiation due to the short bunch lengths and high bunch charges possible in an ERL can potentially be a limiting factor for the operation of such a machine.

Coherent Synchrotron Radiation (CSR), in the far-field, can be thought of as an enhancement of the synchrotron radiation spectrum due to localized accelerating charges. When N particles are longitudinally bunched with R.M.S. size σ , the radiation due to the individual particles at wavelengths $\lambda \gtrsim \sigma/c$ are approximately in phase, which enhances the power spectrum per particle by a factor of N at these long wavelengths. Such an enhancement can be seen in Fig. 1.4.

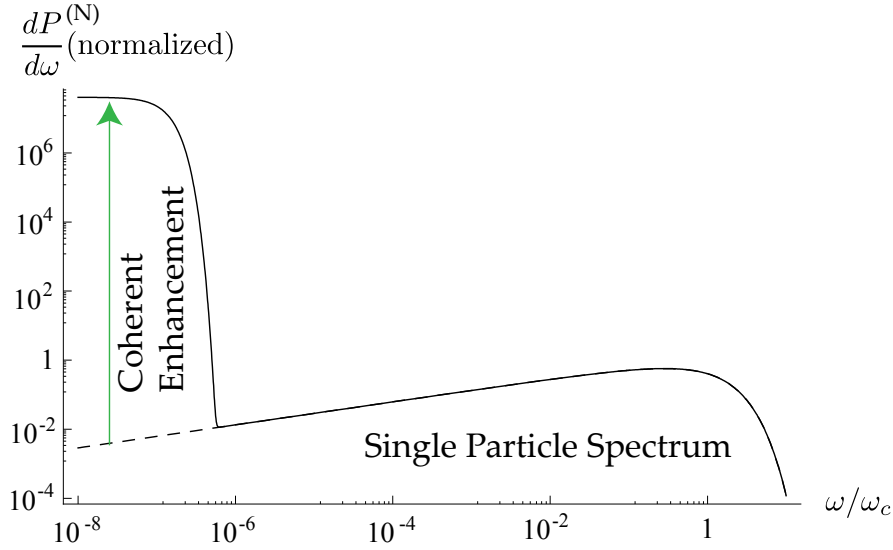


Figure 1.4: The power spectrum of $N = 6 \times 10^9$ charges (corresponding to 1 nC of electrons) traveling at 5 GeV in a magnet with $R = 100$ m. These charges have a longitudinal Gaussian profile with R.M.S. size $\sigma = 0.6$ mm. The green arrow indicates the enhancement by a factor of N for frequencies below c/σ . The vertical axis is normalized by $N \cdot P^{(1)}/\omega_c$, where $P^{(1)}$ is the total power radiated by a single charge, and ω_c is the critical frequency.

Most of the power in the single particle spectrum occurs around the critical frequency $\omega_c = \frac{3}{2}\gamma^3 c/R$, where R is the bending radius of path of the particles, and there is relatively little power in the low frequencies. However, if a sufficient number of particles are present, the power in these low frequencies can dominate the total power. This coherent contribution to the total power becomes appreciable when

$$\frac{\sigma}{R} \lesssim \frac{N^{3/4}}{\gamma^3}. \quad (1.9)$$

This is particularly relevant for the CERL Mode C parameters shown in Tab. 1.1. In this mode, a magnet with $R = 100$ m radiates a total coherent power that is approximately 180 times the total incoherent power.

The energy radiated is energy that is lost by individual particles. This is important in particle accelerators, and especially in ERL accelerators, because

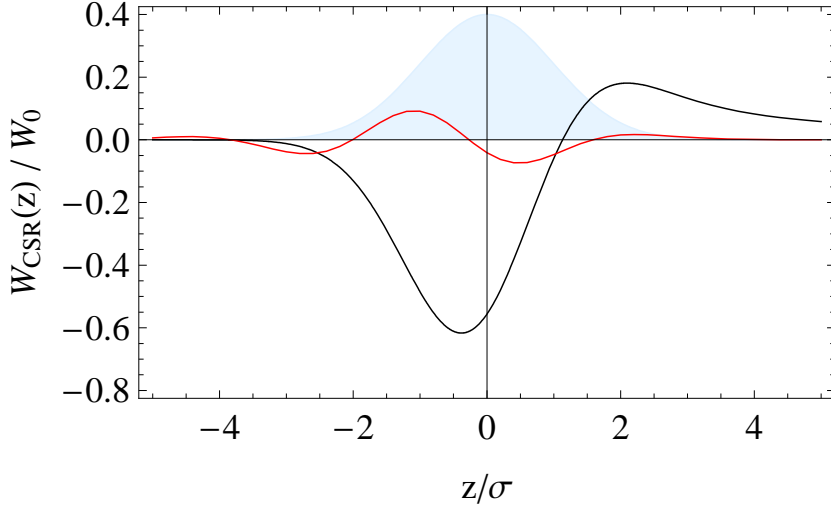


Figure 1.5: The steady-state CSR-wake for a Gaussian bunch density. The black curve is the second term in Eq. (1.10), which corresponds to CSR in free space. The red curve includes the effect of a conducting beam chamber, which can greatly reduce the effect. The scaling factor W_0 is defined in Eq. (5.40).

the longitudinal positions and energies must be carefully controlled. For this reason the “recoil” effect of CSR on the source particles is of particular interest, and we will refer to this as the CSR-wake.

CSR is difficult to model using discrete particles exactly because the problem scales with the number of particles N as N^2 . This can be simplified by using a 1-dimensional model which projects the transverse particle density onto the longitudinal dimension. Formulas for the CSR field from this line charge can then be used to calculate forces on each particle and then propagate the full bunch distribution. While this makes the calculation tractable, the electromagnetic fields on the world-sheet of this charged line are singular. Pioneering efforts described in Derbenev *et al.* (1995) and Murphy *et al.* (1995) circumvent this problem by examining the non-singular terms only.

In more detail, Saldin *et al.* (1997) regularize the longitudinal force between

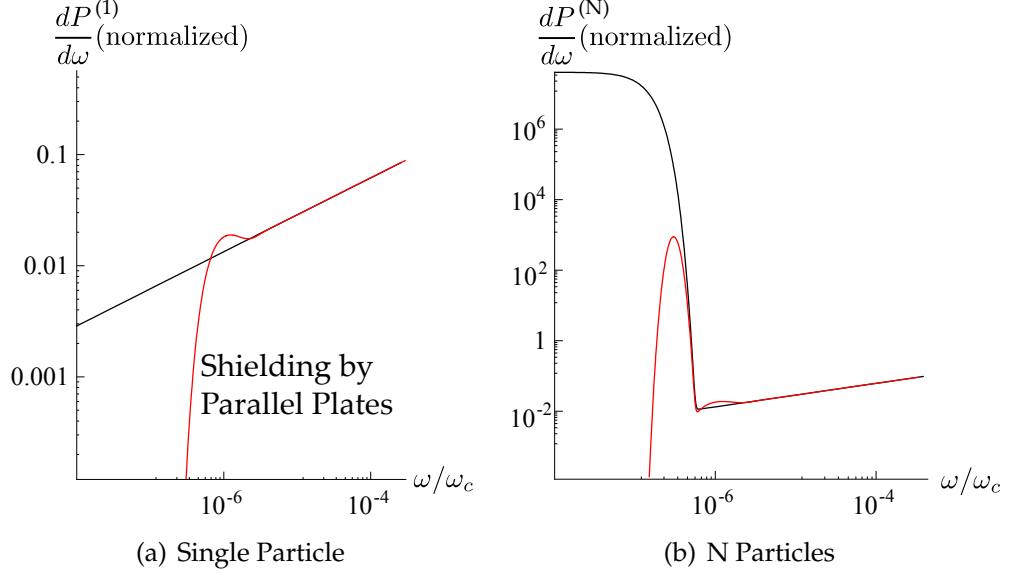


Figure 1.6: The power spectrum for particles traveling between conducting parallel plates. The single particle spectrum is shown in Fig. 1.6(a), while the N particle spectrum is shown in Fig. 1.6(b). The parameters used are the same as in Fig. 1.4, with the plates separated by a distance of 2.54 cm.

two charges traveling on the arc of a circle by subtracting off the Coulomb force, calculated as if the charges traveled on a straight line, from the force calculated using Liénard-Wiechert fields. The result is an always finite CSR force. In the ultra-relativistic limit, their formula for the CSR-wake due to a bunch entering from a straight path into a bend is

$$W_{\text{CSR}}(z) = -\frac{2 N r_c m c^2}{3^{1/3} R^{2/3}} \left\{ \frac{\lambda(z - z_L) - \lambda(z - 4z_L)}{z_L^{1/3}} + \int_{z-z_L}^z \frac{1}{(z - z')^{1/3}} \frac{d\lambda}{dz'} dz' \right\} \quad (1.10)$$

$$z_L \equiv \frac{R \phi^3}{24} ,$$

where $\lambda(z)$ is the normalized longitudinal bunch density centered at $z = 0$, and ϕ is the angle traveled into the magnet by the bunch center.

The first term in Eq. (1.10) is the transient effect when a bunch enters a magnet. When z_L exceeds several times the bunch length, it becomes irrelevant, and the CSR-wake assumes a “steady-state” form given by the second term. The

characteristic shape of such a curve is shown for a Gaussian $\lambda(z)$ in Fig. 1.5. There, one sees that the bulk of the bunch loses energy, while the head of the bunch ($z \approx 2\sigma$) actually gains some energy. This is due to fields propagating forward from the tail of the bunch, and catching up the the head of the bunch.

Fortunately for particle accelerators, this intense coherent power is typically suppressed, because particles often travel through conducting beam-pipes with relatively small transverse size. This CSR “shielding” effect was first pointed out by Schwinger (1945), who shows that the synchrotron radiation spectrum gets modified at low frequencies. Such a spectrum is shown in Fig. 1.6(a) for a Gaussian bunch. The resulting CSR-wake is correspondingly modified, as shown by the red curve in Fig 1.5.

Calculations using the power spectrum are only valid for steady-state situations, and CSR-wake formulas such as Eq. (1.10) are often only valid of ultra-relativistic particles. It is important to understand the range of applicability of these formulas, so an exact 1-D model for CSR is presented in Chapter 5. The bulk of this material is published in Mayes & Hoffstaetter (2009). Finally, this dissertation concludes with a discussions and estimates of the CSR effect in the MERL and CERL designs.

CHAPTER 2

ACCELERATOR LATTICE DESIGN

2.1 Beam Optics Fundamentals

The physical principles by which a beam of particles is transported and focused along an accelerator are referred to as the **beam optics**. This chapter serves as an outline of the basic mathematical concepts for optics design in an accelerator, and defines some terms particular to the subject, many of which were first collected in Courant & Snyder (1958). It draws heavily from classical mechanics and electrodynamics, about which one is referred to the standard references of Goldstein (1965), Jackson (1999), and Landau and Lifschitz Vols. I & II (2001, 2002). For more complete expositions on beam optics, the reader is referred an introduction by Wille (2000) and two volumes by Wiedemann (1999).

Central to optics design is the accelerator **lattice**, which is the sequential list of elements that the beam passes through. Possible elements in a lattice include accelerating cavities, dipole magnets, quadrupole magnets, sextupole magnets, and undulators, along with their appropriate dimensions and field strengths. Straight sections without electromagnetic fields are called **drifts**. The lattice thus serves as our theoretical model of the accelerator, with which the machine can be simulated on a computer.

2.1.1 Accelerator Coordinate System

In a particle accelerator, one is mainly concerned with the dynamics of a particle **bunch**, which consists of many localized charged particles traveling relativistically through the machine. In general, the equation of motion for any one particle would look quite complicated if written in a fixed Cartesian coordinate system, so particle coordinates will always be written in terms of a **reference orbit**, a path along the accelerator. The reference orbit is often taken as the path that an ideal particle would take, such as the arc of a circle in a dipole magnet, or a straight line in a drift or a quadrupole magnet, but it is sometimes defined as a path that no particle would take, such as a straight line through an undulator. For the purposes of this section, it will be sufficient to only consider reference orbits in the horizontal plane. Such is the case for the ERLs studied here. The extension of the orbit to arbitrary paths is discussed in detail in the monograph by Berz (1999).

Let the reference orbit be the path $\mathbf{R}_0(s)$ in space parameterized by distance s , and define a basis vector $\mathbf{e}_s(s)$ as the unit tangent vector, given by

$$\mathbf{e}_s(s) \equiv \frac{d\mathbf{R}_0(s)}{ds}. \quad (2.1)$$

Now let two mutually perpendicular unit vectors $\mathbf{e}_x(s)$ and $\mathbf{e}_y(s)$ lie in the plane perpendicular to $\mathbf{e}_s(s)$, so that $\{\mathbf{e}_x(s), \mathbf{e}_y(s), \mathbf{e}_s(s)\}$ form a right-handed orthonormal frame. The curvilinear coordinates (x, y, s) therefore describe a point in space with position

$$\mathbf{r}(x, y, s) = \mathbf{R}_0(s) + x\mathbf{e}_x(s) + y\mathbf{e}_y(s). \quad (2.2)$$

We will say that $\mathbf{e}_x(s)$ and $\mathbf{e}_y(s)$ lie in the horizontal plane, so that the coordinates x and y describe the horizontal and vertical displacement from the reference

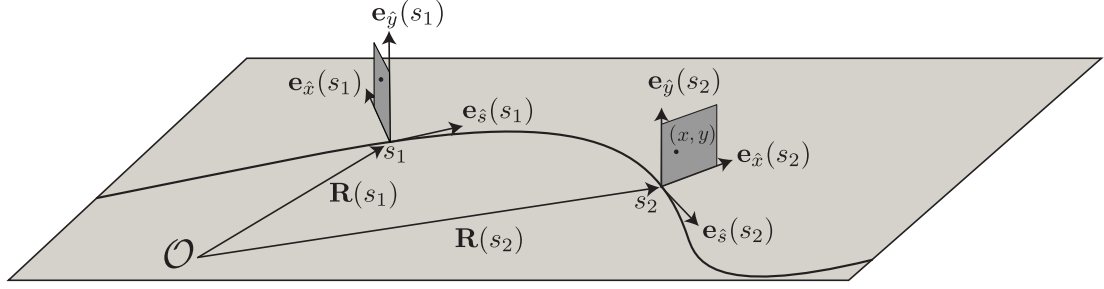


Figure 2.1: The accelerator coordinate system for a path in the horizontal plane. A particle's position is uniquely defined by its (x, y, s) coordinates.

orbit, respectively. This moving frame is illustrated in Fig. 2.1. The rotation of these basis vectors along the reference orbit is given by their derivatives

$$\frac{d\mathbf{e}_x(s)}{ds} = \kappa_0(s) \mathbf{e}_s(s), \quad (2.3)$$

$$\frac{d\mathbf{e}_y(s)}{ds} = 0, \quad (2.4)$$

$$\frac{d\mathbf{e}_s(s)}{ds} = -\kappa_0(s) \mathbf{e}_x(s). \quad (2.5)$$

Here $\kappa_0(s)$ is the curvature at s , and $1/\kappa_0(s)$ is the radius of curvature of the osculating circle at s .

Note that while (x, y, s) describe a unique point in space, the converse is only true for a path that is a straight line. However, if the points of interest always lie within a tube of radius $r < 1/\max|\kappa_0(s)|$ surrounding the reference orbit, then these points will have unique curvilinear coordinates. In practice this is almost always the case, because the radius of curvature will typically be on the order of meters, and the reference orbit is surrounded by a beam chamber with characteristic size on the order of centimeters.

For an arbitrary path parameterized by distance σ , the infinitesimal line

length $d\sigma$ is related to the curvilinear coordinates by

$$d\sigma^2 = dx^2 + dy^2 + [1 + \kappa_0(s)x] ds^2. \quad (2.6)$$

With the metric here one can write down all the usual vector calculus derivative operators and volume elements in curvilinear coordinates (see for example Gradshteyn & Ryzhik, 2000, section 10.51).

2.1.2 Equations of Motion

Now consider a point particle with charge q and mass m , and with curvilinear coordinates $x(t)$, $y(t)$, and $s(t)$ as a function of time t . While this is a perfectly good description, it will prove to be advantageous to use the longitudinal coordinate s , rather than time t , as the independent variable, so that $x(t) \rightarrow x(s)$ and $y(t) \rightarrow y(s)$. The particle then has position vector

$$\mathbf{x}(s) = \mathbf{R}_0(s) + x(s) \mathbf{e}_{\hat{x}}(s) + y(s) \mathbf{e}_{\hat{y}}(s) \quad (2.7)$$

at time $t(s)$. The velocity vector is

$$\mathbf{v}(s) = \dot{s} \frac{d\mathbf{x}}{ds} \quad (2.8)$$

$$= \dot{s} x' \mathbf{e}_{\hat{x}} + \dot{s} y' \mathbf{e}_{\hat{y}} + \dot{s} (1 + \kappa_0 x) \mathbf{e}_{\hat{s}} \quad (2.9)$$

with

$$\dot{s} = \left[\frac{\partial t(s)}{\partial s} \right]^{-1}, \quad (2.10)$$

and primes denote derivatives with respect to s , as in

$$x' \equiv \frac{dx}{ds}, \quad (2.11)$$

$$y' \equiv \frac{dy}{ds}. \quad (2.12)$$

It will be assumed that $\dot{s} > 0$, and each term is to be understood as a function of s . The magnitude of the velocity is

$$\begin{aligned}\|\mathbf{v}\| &= \dot{s} \left((1 + \kappa_0 x)^2 + x'^2 + y'^2 \right)^{1/2} \\ &\equiv \beta c.\end{aligned}\tag{2.13}$$

The regular momentum vector written in terms of the velocity vector is simply

$$\mathbf{p} = m \gamma \mathbf{v}\tag{2.14}$$

$$= p_x \mathbf{e}_{\hat{x}} + p_y \mathbf{e}_{\hat{y}} + p_s \mathbf{e}_{\hat{s}},\tag{2.15}$$

with magnitude

$$p = \sqrt{p_x^2 + p_y^2 + p_s^2}.\tag{2.16}$$

The corresponding mechanical energy of the particle is

$$\begin{aligned}\mathcal{E} &= \sqrt{(p c)^2 + m^2 c^4} \\ &= \gamma m c^2,\end{aligned}\tag{2.17}$$

where the relativistic factor $\gamma \equiv (1 - \beta^2)^{-1/2}$. The classical motion of such a particle in an external electric field \mathbf{E} and magnetic field \mathbf{B} , neglecting radiative losses, is governed by the Lorentz force equations:

$$\frac{d}{dt} \mathcal{E} = q \mathbf{v} \cdot \mathbf{E},\tag{2.18}$$

$$\frac{d}{dt} \mathbf{p} = q \mathbf{E} + q \mathbf{v} \times \mathbf{B}.\tag{2.19}$$

In terms of the moving frame, the fields are $\mathbf{E} = E^{\hat{x}} \mathbf{e}_{\hat{x}} + E^{\hat{y}} \mathbf{e}_{\hat{y}} + E^{\hat{s}} \mathbf{e}_{\hat{s}}$ and $\mathbf{B} = B^{\hat{x}} \mathbf{e}_{\hat{x}} + B^{\hat{y}} \mathbf{e}_{\hat{y}} + B^{\hat{s}} \mathbf{e}_{\hat{s}}$, where the components are understood to be functions of (x, y, t, s) . Inserting the energy and momenta into Eqs. (2.18–2.19) and equating

coefficients of the basis vectors gives the following relations

$$\frac{d\mathcal{E}}{ds} = x'q E^{\hat{x}} + y'q E^{\hat{y}} + (1 + \kappa_0 x) q E^{\hat{s}}, \quad (2.20)$$

$$\frac{dp_x}{ds} = \kappa_0 p_s + \frac{q}{\dot{s}} E^{\hat{x}} + y'q B^{\hat{s}} - (1 + \kappa_0 x) q B^{\hat{y}}, \quad (2.21)$$

$$\frac{dp_y}{ds} = \frac{q}{\dot{s}} E^{\hat{y}} + (1 + \kappa_0 x) q B^{\hat{x}} - x'q B^{\hat{s}}, \quad (2.22)$$

$$\frac{dp_s}{ds} = -\kappa_0 p_x + \frac{q}{\dot{s}} E^{\hat{s}} + x'q B^{\hat{y}} - y'q B^{\hat{x}}. \quad (2.23)$$

An alternate derivation of Eqs. (2.20–2.23) using the geodesic equations is given in Appendix A.

Similar to the way we introduced the curvilinear coordinate (x, y, s) to replace the Cartesian coordinates of a particle, we will introduce new phase space coordinates that are more suitable for charges in a particle accelerator. To begin, we define the **reference particle** to be a charged particle that always follows the reference orbit, and which defines the **reference time** $t_0(s)$ and **reference momentum** $p_0(s)$. Relative to this reference momentum, we define the **momentum deviation** δ of any other particle in terms of its total momentum p so that

$$\delta(s) \equiv \frac{p(s) - p_0(s)}{p_0(s)}, \quad (2.24)$$

which is the same as

$$p = (1 + \delta) p_0. \quad (2.25)$$

We will prefer this coordinate to p_s .

Associated with $\delta(s)$ is the longitudinal position $z(s)$ relative to the reference particle, which we will define in terms of the particle time $t(s)$ and reference time as

$$z(s) = -\beta(s) c [t(s) - t_0(s)], \quad (2.26)$$

with $\beta(s) c$ being the velocity at s . For example, suppose $t(s_1) > t_0(s_1)$, meaning that our particle arrives at $s = s_1$ at a later time than the reference particle.

Then, in the laboratory, when the reference particle is at s_1 , our particle is at a distance of approximately $\beta(s) c[t(s_1) - t_0(s_1)]$ behind the reference particle. We can therefore think of $z(s)$ as the longitudinal displacement of our particle when the reference particle is at s . The combination (z, δ) is therefore a point in the longitudinal phase space.

Now define new transverse momenta $a(s)$ and $b(s)$, which are normalized relative to the reference momentum, as in

$$a \equiv \frac{p_x}{p_0}, \quad (2.27)$$

$$b \equiv \frac{p_y}{p_0}, \quad (2.28)$$

so that a and b are the new horizontal and vertical momenta, respectively. In terms of the new momenta a, b , and δ , we have the relations

$$\beta = \left[1 + \left(\frac{m c}{(1 + \delta) p_0} \right)^2 \right]^{-1/2}, \quad (2.29)$$

$$\dot{s} = \beta c \frac{\sqrt{(1 + \delta)^2 - a^2 - b^2}}{(1 + \kappa_0 x)(1 + \delta)}. \quad (2.30)$$

To see the relationship between a and the slope x' , note that

$$a = \frac{p_x p_s}{p_s p_0}, \quad (2.31)$$

and from the velocity in Eq. (2.9) and the total momentum in Eq. (2.16)

$$\frac{p_x}{p_s} = \frac{x'}{1 + \kappa_0 x}, \quad (2.32)$$

$$\frac{p_s}{p_0} = \sqrt{(1 + \delta)^2 - a^2 - b^2}, \quad (2.33)$$

which lead to

$$\frac{dx}{ds} = \frac{(1 + \kappa_0 x) a}{\sqrt{(1 + \delta)^2 - a^2 - b^2}}. \quad (2.34)$$

Similarly the vertical direction gives

$$\frac{dy}{ds} = \frac{(1 + \kappa_0 x) b}{\sqrt{(1 + \delta)^2 - a^2 - b^2}}. \quad (2.35)$$

Using these new variables in Eqs. (2.21–2.23) yields

$$\frac{da}{ds} = -a \frac{p'_0}{p_0} + \kappa_0 \sqrt{(1 + \delta)^2 - a^2 - b^2} + \frac{q}{p_0} \left[\frac{1}{\dot{s}} E^{\hat{x}} + y' B^{\hat{s}} - (1 + \kappa_0 x) B^{\hat{y}} \right], \quad (2.36)$$

$$\frac{db}{ds} = -b \frac{p'_0}{p_0} + \frac{q}{p_0} \left[\frac{1}{\dot{s}} E^{\hat{y}} + (1 + \kappa_0 x) B^{\hat{x}} - x' B^{\hat{s}} \right], \quad (2.37)$$

$$\frac{d\delta}{ds} = -(1 + \delta) \frac{p'_0}{p_0} + \frac{q}{p_0} \left[\frac{y'}{\beta c} E^{\hat{y}} + \frac{x'}{\beta c} E^{\hat{x}} + \frac{1 + \kappa_0 x}{\beta c} E^{\hat{s}} \right]. \quad (2.38)$$

Differentiating Eq.(2.26) and using Eqs. (2.29–2.30) finally gives

$$\frac{dz}{ds} = \frac{z q}{m c^2 \beta^2 \gamma^3} \left[x' E^{\hat{x}} + y' E^{\hat{y}} + (1 + \kappa_0 x) E^{\hat{s}} \right] + \frac{\beta}{\beta_0} - \frac{(1 + \kappa_0 x)(1 + \delta)}{\sqrt{(1 + \delta)^2 - a^2 - b^2}}. \quad (2.39)$$

2.1.3 Accelerator Magnets

Due to the nature of the Lorentz force, in the absence of electric fields, particles traveling mainly in the longitudinal direction \mathbf{e}_s are primarily influenced by the transverse magnetic fields $B^{\hat{x}}$ and $B^{\hat{y}}$. For this reason, the magnets used to bend and focus the particle beam are typically designed to produce strong transverse fields, and often have well-defined multipole moments, which can be tuned independently by the operator of the machine.

Dipole magnets are the primary means by which the beam is bent along the reference orbit, and are also referred to as **bending magnets**. The fields in a dipole are of the form $\mathbf{B} = B_0^{\hat{x}} \mathbf{e}_{\hat{x}} + B_0^{\hat{y}} \mathbf{e}_{\hat{y}}$, where $B_0^{\hat{x}}$ and $B_0^{\hat{y}}$ are constants over the length of the magnet. Of course, any realistic magnet will have variations in the field strengths at its ends, called **fringe fields**, but for our purposes we will assume that the fringe fields cover zero extent. Such a simplification is called the **hard edge model**.

In such a magnet, consider the motion of a particle with $\delta = 0$ that instantaneously travels on the reference orbit at position s , so that $x(s) = 0$, $a(s) = 0$,

$y(s) = 0, b(s) = 0$, and therefore the velocity $\beta c = \dot{s}$. Equations (2.34-2.38) give

$$x'(s) = 0, \quad (2.40)$$

$$a'(s) = \kappa_0 - \frac{q}{p_0} B_0^{\hat{y}}, \quad (2.41)$$

$$y'(s) = 0, \quad (2.42)$$

$$b'(s) = \frac{q}{p_0} B_0^{\hat{x}}. \quad (2.43)$$

We require that such a particle remain on the reference orbit, meaning that $a' = 0$ and $b' = 0$, which imply

$$B_0^{\hat{x}} = 0, \quad (2.44)$$

$$B_0^{\hat{y}} = \frac{p_0}{q} \kappa_0(s). \quad (2.45)$$

Thus the reference orbit defines the necessary dipole fields. Conversely, the dipole fields along with a reference particle can be considered as defining the reference orbit. For simplicity, the curvature of the reference orbit $\kappa_0(s)$ will always be considered as a step function along s , and nonzero only in dipole magnets, so $\kappa_0' = 0$. The reference orbit then consists of straight lines and arcs of circles in the horizontal plane.

While the reference particle is guided along the accelerator with dipole magnets, other particles in its vicinity will not necessarily remain so well-controlled. In special circumstances a series of dipoles can be designed to manage such particles as well through symmetry and fringe field effects, but more often multipole magnets are employed to perform this duty.

Multipole expansions for static magnetic fields can be constructed from Apère's law and Gauss' law, which in regions without source currents or electric

fields are

$$\nabla \times \mathbf{B} = 0, \quad (2.46)$$

$$\nabla \cdot \mathbf{B} = 0. \quad (2.47)$$

These imply that the magnetic field can be described by a scalar function ψ so that

$$\mathbf{B} = -\nabla\psi, \quad (2.48)$$

with ψ satisfying Laplace's equation

$$\nabla^2\psi = 0. \quad (2.49)$$

In our curvilinear coordinates the Laplacian operator is

$$\nabla^2 = \frac{\partial^2}{\partial x^2} + \frac{\kappa_0}{1 + \kappa_0 x} \frac{\partial}{\partial x} + \frac{\partial^2}{\partial y^2} + \frac{1}{(1 + \kappa_0 x)^2} \frac{\partial^2}{\partial s^2}, \quad (2.50)$$

which contains some cumbersome factors of $1 + \kappa_0 x$. Fortunately, other than dipoles, we will nearly always be concerned with multipole fields in sections where the reference orbit is straight, *i.e.* $\kappa_0 = 0$. The Laplacian can then be written in cylindrical coordinates (r, θ, s) with $x = r \cos \theta$ and $y = r \sin \theta$, so that

$$\nabla^2 = \frac{1}{r} \frac{\partial}{\partial r} r \frac{\partial}{\partial r} + \frac{1}{r^2} \frac{\partial^2}{\partial \theta^2} + \frac{\partial^2}{\partial s^2}. \quad (2.51)$$

Neglecting the s dependence, in accordance with our hard edge model, a pure multipole potential of order n is the solution

$$\psi_n = -a_n r^n \sin(n\theta + \theta_n), \quad (2.52)$$

where a_n and θ_n are constants. A potential for a general transverse field is then a sum over multipole components, as in

$$\psi = \sum_{n=1}^{\infty} \psi_n, \quad (2.53)$$

Table 2.1: Field strengths for selected upright magnets

Type	$-\frac{q}{p_0}\psi$	$\frac{q}{p_0}B^x$	$\frac{q}{p_0}B^y$
Dipole	$k_0 y$	0	k_0
Quadrupole	$k_1 x y$	$k_1 y$	$k_1 x$
Sextupole	$\frac{1}{6} k_2 (3 x^2 y - y^3)$	$k_2 x y$	$\frac{1}{2} k_2 (x^2 - y^2)$
Octupole	$\frac{1}{6} k_3 (x^3 y - x y^3)$	$\frac{1}{6} k_3 (3 x^2 y - y^3)$	$\frac{1}{6} k_3 (x^3 - 3 x y^2)$

and is therefore completely described by the sets $\{a_n\}$ and $\{\theta_n\}$.

For planar accelerators, the most important magnets are ones that exhibit **midplane symmetry**. These magnets have $B^x = 0$ in the horizontal plane at $y = 0$, so that particles with trajectories in this plane are not deflected vertically, and are called **upright magnets**. They are described by a sum over multipole potentials in Eq. (2.52) with all $\theta_n = 0$. The coefficients a_n can be written in terms of derivatives of the magnetic field,

$$a_n = \frac{1}{n!} \left. \frac{\partial^{n-1} B^y}{\partial x^{n-1}} \right|_{\substack{x=0 \\ y=0}}, \quad (2.54)$$

and in terms of the reference particle we can define the upright multipole moments

$$\begin{aligned} k_n &\equiv (n+1)! \frac{q}{p_0} a_{n+1} \\ &= \frac{q}{p_0} \left. \frac{\partial^n B^y}{\partial x^n} \right|_{\substack{x=0 \\ y=0}}, \end{aligned} \quad (2.55)$$

which have units of $m^{-(n+1)}$. From before, we can identify $k_0 = \kappa_0$.

Table 2.1 lists the potentials and magnetic field components in (x, y) coordinates for a few of the lowest order upright multipoles. Figure 2.2 shows field patterns and equipotential lines for upright quadrupole and sextupole magnets.

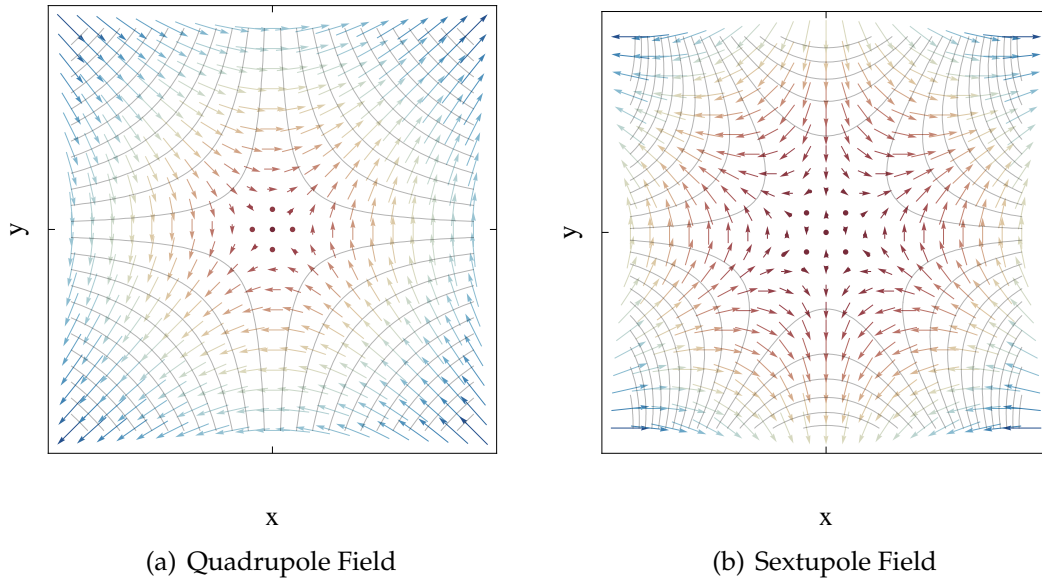


Figure 2.2: Magnetic field patterns and equipotential lines in quadrupole and sextupole magnets.

2.1.4 Accelerating Cavities

Of equal importance to the magnets in an accelerator are the accelerating structures that deliver and extract energy from the beam. For us, these elements will be a series of resonant cavities operating with standing waves at radio frequencies (RF). The design and manufacture of such devices is an active area of research, and the reader is referred to Chao & Tigner (2006) for technical details and references.

As a simple model of an accelerating cavity, consider a perfectly conducting cylinder aligned with the reference orbit that has an outer radius R and a length L . Electromagnetic boundary conditions restrict the possible fields, with the

lowest order TM_{010} fields being

$$\mathbf{E} = E_0 J_0 \left(j_{01} \frac{r}{R} \right) \cos(\omega_{010} t) \mathbf{e}_s, \quad (2.56)$$

$$\mathbf{B} = -\frac{E_0}{c} J_1 \left(j_{01} \frac{r}{R} \right) \sin(\omega_{010} t) \mathbf{e}_{\hat{\theta}}, \quad (2.57)$$

at the angular frequency $\omega_{010} = j_{01} c/R$. Here E_0 is the maximum electric field at $r = 0$, J_n is a Bessel function of the first kind, and $j_{01} \approx 2.4048255$ is the first root of J_0 (see, for example, section 8.7 of Jackson, 1999).

Now let a highly relativistic ($\beta \approx 1$) reference particle enter this cavity through a tiny hole on axis and exit through the opposite side. Assuming that it always maintains relativistic speeds, the energy gain of the particle through the cavity is

$$\begin{aligned} \Delta\mathcal{E} &= \int_{-L/2}^{L/2} ds qE_0 \cos(k_{\text{rf}}s + \phi_{\text{rf}}) \\ &= qE_0 \frac{2 \sin(k_{\text{rf}}L/2)}{k_{\text{rf}}} \cos(\phi_{\text{rf}}), \end{aligned} \quad (2.58)$$

where $k_{\text{rf}} = \omega_{010}/c$ is the angular wavenumber, and ϕ_{rf} is the phase when the particle is in the center of the cavity. The maximum acceleration is achieved when $\phi_{\text{rf}} = 0$ and $k_{\text{rf}}L = \pi$, so that the average energy change per unit length is $2qE_0/\pi$. This means that structures with lengths on the order of centimeters have optimal operating frequencies on the order of a GHz.

Modern accelerating elements can consist of several such cavities grouped together, with shapes and materials optimized to deliver a maximum accelerating field. Ultimately, however, they are designed to deliver effective accelerating voltages \hat{V} and therefore a particle with longitudinal displacement z from the reference particle will experience a change of energy of the form

$$\Delta\mathcal{E} = q\hat{V} \cos(\phi_{\text{rf}} - k_{\text{rf}}z). \quad (2.59)$$

We will usually consider particle bunches that are localized enough to be accelerated in the same RF wave, meaning that $|k_{\text{rf}} z| \leq \pi/2$. With $k_{\text{rf}} = 2\pi f_{\text{rf}}/c > 0$, this implies that $|z| \lesssim \frac{1}{4} \frac{c}{f_{\text{rf}}}$, which translates to $|z| \lesssim 8 \text{ cm}$ for $f_{\text{rf}} = 1 \text{ GHz}$.

2.1.5 Linear Optics

Up to this point, Eqs. (2.34-2.38) are exact in the sense of classical electrodynamics, and look rather complicated. Now several important approximations will be made that are relevant for particle accelerators which will allow us to use these equations to solve for the transverse motion of a charged test particle. The longitudinal phase space will then be treated and combined with the transverse motion to give the first order evolution of the six-dimensional phase space.

First, we will assume that the charges travel at relativistic speeds ($\gamma \gg 1$) primarily parallel to the reference orbit. This is called the **paraxial beam** approximation, or **small angle** approximation, which means that $|a| \ll 1$ and $|b| \ll 1$. Second, the transverse coordinates x and y are nearly always small relative to the size of the system, being on the order of millimeters compared with, for example, bending radii on the order of tens of meters. Third, the longitudinal coordinate z is typically on the order of millimeters and thus on the same order as x and y . Finally, the energies of all particles will be assumed to be similar to that of the reference particle, so that $|\delta| \ll 1$.

Now we can see the benefit of these special phase space coordinates: if each of x, a, y, b, z , and δ can be considered as “small”, then functions can be well approximated by simultaneous Taylor expansions in terms of them. In particular,

the horizontal and vertical slopes from Eq. (2.34) and Eq. (2.35) are

$$x' = a - \delta a + \kappa_0 x a + \mathcal{O}(\epsilon^3), \quad (2.60)$$

$$y' = b - \delta b + \kappa_0 x b + \mathcal{O}(\epsilon^3), \quad (2.61)$$

where ϵ^n is any combination of the phase space variables with (positive) powers summing to n . To first order $x' = a$ and $y' = b$, and therefore the pairs (x, x') and (y, y') are often referred to as the horizontal and vertical phase space, respectively, when discussing first order motion.

For now, we will specialize to regions with only static upright magnetic fields, expanded in terms of their multipole moments given in Tab. 2.1. Neglecting radiative losses, $\delta' = 0$ in such regions. Expanding Eqs. (2.36-2.38) and combining with Eqs. (2.60-2.61) then give

$$\frac{d}{ds} \begin{pmatrix} x \\ a \\ y \\ b \end{pmatrix} = \begin{pmatrix} a \\ \kappa_0 \delta - (\kappa_0^2 + k_1) x \\ b \\ k_1 y \end{pmatrix} + \mathcal{O}(\epsilon^2) \quad (2.62)$$

as the first order evolution of the transverse phase space. Reducing these to a pair of second order differential equations finally yields

$$x''(s) + [\kappa_0^2(s) + k_1(s)] x(s) = \kappa_0(s) \delta, \quad (2.63)$$

$$y''(s) - k_1(s) y(s) = 0. \quad (2.64)$$

These two equations form the basis for the linear optics. One now sees the use of upright dipole and quadrupole fields: they decouple the transverse equations of motion.

Hill's Equation

Equations (2.63-2.64) have the form of Hill's equation

$$x''(s) + K(s)x(s) = f(s), \quad (2.65)$$

for which, given an arbitrary function $K(s)$, it is impossible to write down a general solution analytically. For regions of constant K , however, the solutions are simple. In terms of the particle position and slope at $s = 0$, the homogeneous solutions are

$$x(s) = C_K(s)x(0) + S_K(s)x'(0), \quad (2.66)$$

$$x'(s) = C'_K(s)x(0) + S'_K(s)x'(0), \quad (2.67)$$

with the functions C_K and S_K defined as

$$\begin{bmatrix} C_K(s) \\ S_K(s) \end{bmatrix} \equiv \begin{cases} \begin{bmatrix} \cos(\sqrt{K}s) \\ \frac{1}{\sqrt{K}} \sin(\sqrt{K}s) \end{bmatrix} & \text{for } K > 0 \\ \begin{bmatrix} 1 \\ s \end{bmatrix} & \text{for } K = 0 \\ \begin{bmatrix} \cosh(\sqrt{|K|}s) \\ \frac{1}{\sqrt{|K|}} \sinh(\sqrt{|K|}s) \end{bmatrix} & \text{for } K < 0 \end{cases} \quad (2.68)$$

These solutions can also be written as a matrix equation

$$\begin{pmatrix} x(s) \\ x'(s) \end{pmatrix} = \mathbf{M}_K(s) \begin{pmatrix} x(0) \\ x'(0) \end{pmatrix}, \quad (2.69)$$

with the transformation matrix

$$\mathbf{M}_K(s) \equiv \begin{pmatrix} C_K(s) & S_K(s) \\ C'_K(s) & S'_K(s) \end{pmatrix}. \quad (2.70)$$

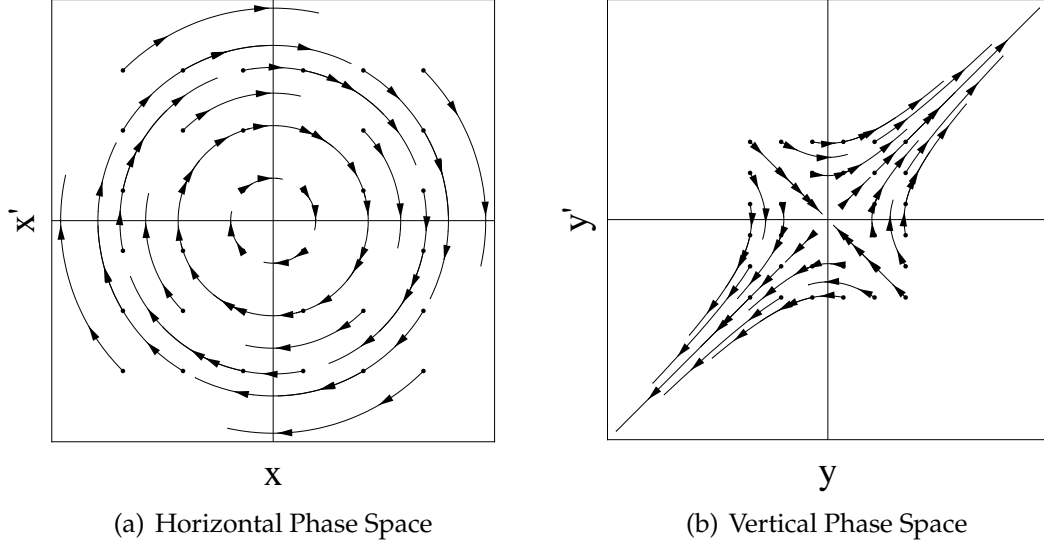


Figure 2.3: The action of a quadrupole with $k_1 > 0$ on an initial grid of points in (x, x') and (y, y') phase space.

Note that $dx dx'$ is an invariant volume element, because $\det \mathbf{M}_K = 1$. A particular solution with $f(s) \neq 0$ can then be formed from these solutions with

$$F(s) = \int_0^s ds' f(s') [C_K(s') S_K(s) - S_K(s') C_K(s)], \quad (2.71)$$

which satisfies

$$F''(s) + K(s) F(s) = f(s). \quad (2.72)$$

As an example, consider a particle with phase space coordinates x_0, x'_0, y_0, y'_0 , and $\delta = 0$ at the beginning of a quadrupole magnet with constant $k_1 > 0$ and length L . The coordinates at the end of the magnet are then

$$\begin{pmatrix} x \\ x' \end{pmatrix} = \begin{pmatrix} \cos(\sqrt{k_1} L) & \frac{1}{\sqrt{k_1}} \sin(\sqrt{k_1} L) \\ -\sqrt{k_1} \sin(\sqrt{k_1} L) & \cos(\sqrt{k_1} L) \end{pmatrix} \begin{pmatrix} x_0 \\ x'_0 \end{pmatrix}, \quad (2.73)$$

$$\begin{pmatrix} y \\ y' \end{pmatrix} = \begin{pmatrix} \cosh(\sqrt{k_1} L) & \frac{1}{\sqrt{k_1}} \sinh(\sqrt{k_1} L) \\ \sqrt{k_1} \sinh(\sqrt{k_1} L) & \cosh(\sqrt{k_1} L) \end{pmatrix} \begin{pmatrix} y_0 \\ y'_0 \end{pmatrix}. \quad (2.74)$$

Figure 2.3 illustrates the effect of this quadrupole on the transverse phase space. Now assume that this magnet is sufficiently short and weak, so that $\sqrt{k_1} L \ll 1$. The final coordinates are then approximately

$$\begin{pmatrix} x \\ x' \end{pmatrix} \approx \begin{pmatrix} 1 & L \\ -k_1 L & 1 \end{pmatrix} \begin{pmatrix} x_0 \\ x'_0 \end{pmatrix}, \quad (2.75)$$

$$\begin{pmatrix} y \\ y' \end{pmatrix} \approx \begin{pmatrix} 1 & L \\ k_1 L & 1 \end{pmatrix} \begin{pmatrix} y_0 \\ y'_0 \end{pmatrix}. \quad (2.76)$$

From the change in slopes, these equations have the form of linearly focusing and defocusing lenses in the horizontal and vertical directions with focal lengths $f = \pm 1/(k_1 L)$, respectively. Similarly, if we had used $k_1 < 0$, such a quadrupole would be defocusing in the the horizontal direction and focusing in the vertical direction. This brings up an important difficulty in beam optics: a single quadrupole magnet cannot simultaneously focus the beam in both the horizontal and vertical directions.

This matrix form suggests a way to extend such solutions to multi-element lattices. Consider $K(s)$ as a step function, which can be thought of as a sequence of elements starting at $s = 0$ with lengths L_i and values K_i for $i \in \mathbb{N}$. The solution within element N is therefore

$$\begin{pmatrix} x(s) \\ x'(s) \end{pmatrix} = \mathbf{M}_{K_N}(s - s_{N-1}) \cdot \mathbf{M}_{K_{N-1}}(L_{N-1}) \cdot \dots \cdot \mathbf{M}_{K_1}(L_1) \begin{pmatrix} x(0) \\ x'(0) \end{pmatrix}, \quad (2.77)$$

with $s_N \equiv \sum_{i=1}^N L_i$.

Identifying these K_i with $\kappa_0^2(s) + k_1(s)$ in the horizontal direction and $-k_1(s)$ in the vertical direction, assuming hard edge dipole and quadrupole magnets, this is therefore the solution to Eqs. (2.63-2.64) with $\delta = 0$. In other words, the phase space coordinates of a particle at s are linear functions of their values at 0, with

the transformation matrix being the concatenation of matrices corresponding to all of the elements between 0 and s .

Twiss Parameters

The individual particle trajectories can be utilized to characterize the evolution of a beam of particles through this system. To do this, we write the transverse coordinate in the form

$$x(s) = \sqrt{2J\beta_x(s)} \sin(\psi_x(s) + \phi). \quad (2.78)$$

The positive $\beta_x(s)$ is called the **beta function**, and $\psi_x(s) + \phi$ is called the **betatron phase**. The constants J and ϕ are called the **particle amplitude** and **particle phase**, respectively. The function $\psi_x(s)$ is chosen as

$$\psi_x(s) \equiv \int_0^s \frac{1}{\beta_x(s)} ds, \quad (2.79)$$

so that ϕ is the betatron phase at $s = 0$. Inserting Eq. (2.78) into Hill's equation, Eq. (2.65), gives

$$K = -\frac{1}{4\beta_x^2} (\beta'_x)^2 + \frac{1}{2\beta_x} \beta''_x - (\beta'_x)^{-2}. \quad (2.80)$$

The slope of the beta function defines another function

$$\alpha_x \equiv -\frac{1}{2}\beta'_x, \quad (2.81)$$

so now we have

$$\alpha_x^2 + \beta_x \alpha'_x - K (\beta_x)^2 + 1 = 0. \quad (2.82)$$

Finally, with the definition $\gamma_x \equiv K\beta_x - \alpha'_x$, we get

$$\gamma_x = \frac{1 + \alpha_x^2}{\beta_x}. \quad (2.83)$$

The functions $\beta_{x'}$, $\alpha_{x'}$, and γ_x are called **Twiss parameters**.

Differentiating Eq. (2.78), the particle's transverse phase space coordinates are related to the Twiss parameters by

$$\begin{pmatrix} x \\ x' \end{pmatrix} = \sqrt{2J} \begin{pmatrix} \sqrt{\beta_x} & 0 \\ -\frac{\alpha_x}{\sqrt{\beta_x}} & \frac{1}{\sqrt{\beta_x}} \end{pmatrix} \begin{pmatrix} \sin(\psi_x + \phi) \\ \cos(\psi_x + \phi) \end{pmatrix}. \quad (2.84)$$

This can also be written as

$$\begin{pmatrix} x(s) \\ x'(s) \end{pmatrix} = \mathbf{t}_x(s) \cdot \mathcal{R}(\psi_x) \cdot \sqrt{2J} \begin{pmatrix} \sin \phi \\ \cos \phi \end{pmatrix}, \quad (2.85)$$

where

$$\mathcal{R}(\theta) \equiv \begin{pmatrix} \cos \theta & \sin \theta \\ -\sin \theta & \cos \theta \end{pmatrix} \quad (2.86)$$

is a rotation matrix, and

$$\mathbf{t}_x(s) \equiv \begin{pmatrix} \sqrt{\beta_x(s)} & 0 \\ -\frac{\alpha_x(s)}{\sqrt{\beta_x(s)}} & \frac{1}{\sqrt{\beta_x(s)}} \end{pmatrix}. \quad (2.87)$$

The Twiss parameters can thus be used to form a transformation matrix that evolves a point in phase space with initial amplitude J and phase ϕ to a point at s , and therefore must be equivalent to the transformation matrix $\mathbf{M}_K(s)$. To see this, we insert Eq. (2.85) into Eq. (2.69), giving

$$\mathbf{t}_x(s) \cdot \mathcal{R}(\psi_x) = \mathbf{M}_K(s) \cdot \mathbf{t}_x(0). \quad (2.88)$$

Multiplying by the transpose gives

$$\mathbf{T}_x(s) = \mathbf{M}_K(s) \cdot \mathbf{T}_x(0) \cdot [\mathbf{M}_K(s)]^T, \quad (2.89)$$

with the Twiss matrix defined as

$$\begin{aligned} \mathbf{T}_x(s) &\equiv \mathbf{t}_x(s) \cdot [\mathbf{t}_x(s)]^T \\ &= \begin{pmatrix} \beta_x(s) & -\alpha_x(s) \\ -\alpha_x(s) & \gamma_x(s) \end{pmatrix}. \end{aligned} \quad (2.90)$$

So, if the Twiss parameters are known at any s , then the Twiss parameters at any other s can be determined from $\mathbf{M}_K(s)$.

As an example, consider the beta function in a drift. The transfer matrix in a drift ($K = 0$) is simply

$$\mathbf{M}_0(s) = \begin{pmatrix} 1 & s \\ 0 & 1 \end{pmatrix}. \quad (2.91)$$

If we assume that the Twiss parameters at the beginning of the drift are β_{x0} and α_{x0} , understanding that γ_x can be written in terms of these, Eq. (2.89) gives

$$\beta_x(s) = \beta_{x0} - 2\alpha_{x0}s + \frac{1 + \alpha_{x0}^2}{\beta_{x0}}s^2, \quad (2.92)$$

quadratic in s . As long as $\alpha_{x0} > 0$, the beta function will focus to a minimum at $s^* = \alpha_{x0}\beta_{x0}/(1 + \alpha_{x0}^2)$, with a value $\beta_x(s^*) = \beta_{x0}/(1 + \alpha_{x0}^2)$. Alternately written, the beta function in a drift given as the distance from the minimum at s^* with value β_x^* is

$$\beta_x(s - s^*) = \beta_x^* + \frac{(s - s^*)^2}{\beta_x^*}. \quad (2.93)$$

The shape of the beta function in a drift always has the form of a parabola.

The form of Eq. (2.84) also reveals an important relation. Multiplying by \mathbf{t}_x^{-1} and squaring both sides shows that

$$\beta_x x'^2 + 2\alpha_x x x' + \gamma_x x^2 = 2J \quad (2.94)$$

is a constant of motion, called the **Courant-Snyder invariant**. This equation has the form of an ellipse in (x, x') phase space, with dimensions shown in Fig. 2.4. Particles with the same amplitude J and various phases ϕ lie on this ellipse, while particles with smaller amplitude lie within. This is important, because a beam of particles is therefore completely characterized by a set of (J, ϕ) and initial Twiss parameters, with its evolution governed by \mathbf{M}_K .

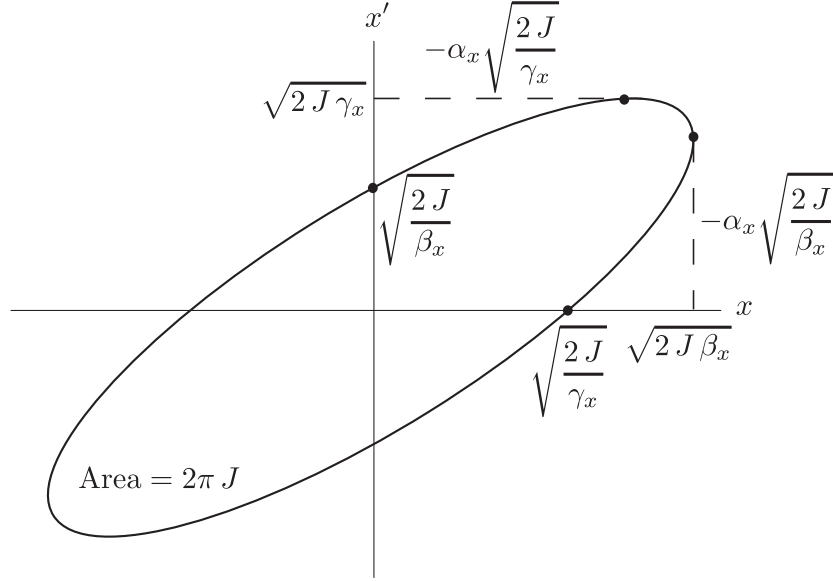


Figure 2.4: The phase space ellipse with a fixed amplitude J and all possible phases ϕ , according to Eq. (2.85) with Twiss parameters β_x , α_x , and $\gamma_x = (1 + \alpha_x^2)/\beta_x$. Particles distributed uniformly on this ellipse represent an emittance $\epsilon_x = J$.

For many particles, this set can be approximated by a density $\rho(J, \phi)$. Typically this density assumes a Gaussian distribution, modeled by

$$\rho_G(J, \phi) dJ d\phi = \frac{1}{2\pi\epsilon_x} e^{-J/\epsilon_x} dJ d\phi, \quad (2.95)$$

where ϵ_x is called the **emittance**. Using such a distribution, one can calculate the average amplitude of a particle

$$\begin{aligned} \langle J \rangle &= \int_0^\infty dJ \int_0^{2\pi} d\phi J \rho_G(J, \phi) \\ &= \epsilon_x. \end{aligned} \quad (2.96)$$

Similarly, the average position squared

$$\begin{aligned} \langle x^2 \rangle &= \int_0^\infty dJ \int_0^{2\pi} d\phi [2J \sin^2 \phi] \rho_G(J, \phi) \\ &= \epsilon_x \beta_x, \end{aligned} \quad (2.97)$$

the average slope squared

$$\begin{aligned}\langle x'^2 \rangle &= \int_0^\infty dJ \int_0^{2\pi} d\phi \frac{2J}{\beta_x} \left[\cos^2 \phi + \alpha_x^2 \sin^2 \phi - 2\alpha_x \cos \phi \sin \phi \right] \rho_G(J, \phi) \\ &= \epsilon_x \gamma_x,\end{aligned}\tag{2.98}$$

and the average correlation

$$\begin{aligned}\langle x x' \rangle &= \int_0^\infty dJ \int_0^{2\pi} d\phi 2J \left[\sin \phi \cos \phi - \alpha_x \sin^2 \phi \right] \rho_G(J, \phi) \\ &= -\epsilon_x \alpha_x.\end{aligned}\tag{2.99}$$

Identifying these terms in the average of Eq. (2.94) gives

$$\epsilon_x = \sqrt{\langle x^2 \rangle \langle x'^2 \rangle - \langle x x' \rangle^2}.\tag{2.100}$$

So, for this Gaussian distribution the emittance is the area in phase space circumscribed by a collection of particles with the average amplitude and which contains $(e - 1)/e \approx 63\%$ of the particles in the distribution. A collection of particles all with an amplitude $3 \epsilon_x$ circumscribes 95% of the distribution. This is useful because the various expectation values can be calculated for an arbitrary distribution, and then fit with such an ellipse.

When the emittance is calculated using Eq. (2.100) it is called the **geometric emittance**. During acceleration, however, our transverse momentum is reduced due by the reference momentum P_0 . To account for this, we define the **normalized emittance** as

$$\epsilon_N = \gamma \beta \epsilon,\tag{2.101}$$

which is invariant through acceleration.

From Eq. (2.97), we see that the root mean squared (RMS) width of the beam is $\sqrt{\epsilon_x \beta_x}$. Therefore the beta function describes the beam envelope, and must

be kept small enough to avoid colliding the outermost particles with the beam chamber. Fortunately, the the largest ERL emittance considered is on the order of a nm, which would give a beam width of 1 mm for a 1000 m beta function. However, if there are particles with more or less energy than the reference momentum, then the beam width can become larger where there is dispersion.

Dispersion

The preceding calculations are valid for $\delta = 0$. For nonzero δ the vertical equation of motion, Eq. (2.64), is unchanged because there are no vertical bends in this planar lattice, but the horizontal equation of motion, Eq. (2.63), has a right hand side $f(s) = \kappa_0 \delta$ within a bend. To account for this, we add the particular solution of Eq. (2.71) to the homogenous solution Eq. (2.66), which can be easily integrated for constant κ_0 and δ , giving

$$\delta D(s) = \delta \frac{1}{\kappa_0} [1 - \cos(\kappa_0 s)], \quad (2.102)$$

where $D(s)$ is called the **dispersion function**. The general solution for the horizontal coordinates of a particle in a bend is then, in matrix form,

$$\begin{pmatrix} x(s) \\ x'(s) \\ \delta \end{pmatrix} = \begin{pmatrix} \cos(\kappa_0 s) & \frac{1}{\kappa_0} \sin(\kappa_0 s) & \frac{1}{\kappa_0} [1 - \cos(\kappa_0 s)] \\ \kappa_0 \sin(\kappa_0 s) & \cos(\kappa_0 s) & \sin(\kappa_0 s) \\ 0 & 0 & 1 \end{pmatrix} \begin{pmatrix} x(0) \\ x'(0) \\ \delta \end{pmatrix}. \quad (2.103)$$

The dispersion function therefore represents an additional horizontal offset of an off-energy ($\delta \neq 0$) particle from the reference orbit, which arises from the fact that particles with higher energy than the reference particle are bent less (*i.e.* have a larger radius of curvature) in a dipole magnet, and vice versa, with the degree of offset proportional to their momentum deviation δ .

Due to the linearity of these equations, the dispersion can be thought of as separate from the motion of an otherwise on-energy ($\delta = 0$) particle, which evolves according to

$$\begin{pmatrix} D(s) \\ D'(s) \\ 1 \end{pmatrix} = \begin{pmatrix} C_K(s) & S_K(s) & \frac{1}{\kappa_0} [1 - \cos(\kappa_0 s)] \\ C'_K(s) & S'_K(s) & \sin(\kappa_0 s) \\ 0 & 0 & 1 \end{pmatrix} \begin{pmatrix} D(0) \\ D'(0) \\ 1 \end{pmatrix}, \quad (2.104)$$

and thus the dispersion through multiple lattice elements can be calculated by concatenating matrices, similar to the method in Eq. (2.77). The form of Eq. (2.104) also shows that while dispersion is “created” in bending magnets, it can be affected by quadrupole magnets as well, which will turn out to be useful.

The particle coordinate and slope in terms of beta function, phase, and dispersion are then

$$x(s) = x_\beta(s) + \delta D(s), \quad (2.105)$$

$$x'(s) = x'_\beta(s) + \delta D'(s), \quad (2.106)$$

with the definitions

$$x_\beta(s) \equiv \sqrt{2 J \beta_x(s)} \sin(\psi_x(s) + \phi), \quad (2.107)$$

$$x'_\beta(s) \equiv \sqrt{\frac{2 J}{\beta_x(s)}} [\cos(\psi_x(s) + \phi) - \alpha_x \sin(\psi_x(s) + \phi)] \quad (2.108)$$

coming directly from Eq. (2.84). In phase space, particles with the same amplitude and momentum deviation, but different phases still form an ellipse as in Fig. 2.4, but with the center shifted to $(\delta D(s), \delta D'(s))$. Sets of particles with different energies therefore separate in dispersive sections, which tends to increase the apparent size of the beam. When a section begins and ends with $D(s) = 0$ and $D'(s) = 0$, it is called **achromatic**.

Time of Flight

Thus far we have considered the transverse coordinates x, x', y, y' of a particle relative to the reference orbit, with momentum deviation δ relative to a reference particle on that orbit. The fifth coordinate to discuss is the longitudinal position $z(s)$ relative to the reference particle, which is also called the **time of flight** due to its relationship with $t(s)$ in Eq. (2.26).

In absence of electric fields, expanding Eq. (2.39) gives

$$\frac{dz}{ds} = -\kappa_0 x + \mathcal{O}(\epsilon^2), \quad (2.109)$$

noting that the ratio $\beta/\beta_0 = 1 + \mathcal{O}(\epsilon^3)$, because

$$\frac{\beta}{\beta_0} = 1 + \frac{\delta}{\gamma_0^2} - \frac{3}{2} \frac{\beta_0^2}{\gamma_0^2} \delta^2 + \dots \quad (2.110)$$

Integrating Eq. (2.109) then gives

$$z(s) = z(0) - \int_0^s \kappa_0(\tilde{s}) x(\tilde{s}) d\tilde{s} + \mathcal{O}(\epsilon^2). \quad (2.111)$$

Note that if we write the horizontal coordinate $x(s)$ in terms of Twiss parameters and dispersion function, as in Eq. (2.105), then the change in longitudinal coordinate is

$$z(s) - z(0) = - \int_0^s \kappa_0(\tilde{s}) \left[\sqrt{2 J \beta_x(\tilde{s})} \sin(\psi_x(\tilde{s}) + \phi) + D(\tilde{s}) \delta \right] d\tilde{s}. \quad (2.112)$$

Manipulation of the dispersion function within bends therefore allows the lattice designer to change the longitudinal phase space, and in particular bunch compression, discussed in Section 3.5.

The longitudinal coordinate to first order can only change within a bend, and we know the first order trajectory in a bend from the first row of Eq. (2.103),

$$x(s) = \cos(\kappa_0 s) x(0) + \frac{1}{\kappa_0} \sin(\kappa_0 s) x'(0) + \frac{1}{\kappa_0} [1 - \cos(\kappa_0 s)] \delta. \quad (2.113)$$

Using this in Eq. (2.111) gives

$$z(s) = z(0) - \sin(\kappa_0 s) x(0) + \frac{1}{\kappa_0} [\cos(\kappa_0 s) - 1] x'(0) + \left[\frac{1}{\kappa_0} \sin(\kappa_0 s) - s \right] \delta. \quad (2.114)$$

This result, combined with Eq. (2.103), the vertical motion, and the fact that δ is unchanged, gives the six-dimensional phase space evolution through a bending magnet in matrix form as

$$\begin{pmatrix} x(s) \\ x'(s) \\ y(s) \\ y'(s) \\ z(s) \\ \delta(s) \end{pmatrix} = \begin{pmatrix} \cos(\kappa_0 s) & \frac{1}{\kappa_0} \sin(\kappa_0 s) & 0 & 0 & 0 & \frac{1}{\kappa_0} [1 - \cos(\kappa_0 s)] \\ -\kappa_0 \sin(\kappa_0 s) & \cos(\kappa_0 s) & 0 & 0 & 0 & \sin(\kappa_0 s) \\ 0 & 0 & 1 & s & 0 & 0 \\ 0 & 0 & 0 & 1 & 0 & 0 \\ -\sin(\kappa_0 s) & \frac{1}{\kappa_0} [\cos(\kappa_0 s) - 1] & 0 & 0 & 1 & \frac{1}{\kappa_0} \sin(\kappa_0 s) - s \\ 0 & 0 & 0 & 0 & 0 & 1 \end{pmatrix} \begin{pmatrix} x(0) \\ x'(0) \\ y(0) \\ y'(0) \\ z(0) \\ \delta(0) \end{pmatrix}. \quad (2.115)$$

The six-dimensional transfer matrices for other common elements can be derived similarly, and are listed in Appendix B. In particular, the fifth element of the sixth column of these matrices is often called the first order **time of flight term** r_{56} , which is important in controlling the length of a bunch. When $r_{56} = 0$ for a section, it is called **isochronous** to first order. It and higher order time of flight terms are discussed in Section 2.1.6.

Acceleration

For simplicity we will model accelerating cavities as in section 2.1.4, which assumes that particles are sufficiently relativistic with velocity $v \approx c$ so that they travel essentially with the accelerating wave. If $\mathcal{E}(0)$ is the energy of a particle at the beginning of a cavity, then the energy of the particle at the end of the cavity,

according to Eq. (2.59), is

$$\mathcal{E}(L) = \mathcal{E}(0) + q\hat{V} \cos[\phi_{\text{rf}} - k_{\text{rf}} z(0)], \quad (2.116)$$

where $q\hat{V}$ is the maximum energy that the cavity can deliver over its length L . Also in this relativistic assumption, the longitudinal coordinate is approximately unchanged, as in $z(L) = z(0)$. Because the energy through many cavities is simply accumulated, the passage of a particle through many adjacent cavities with energies $q\hat{V}_1, q\hat{V}_2$, etc., the final energy through N such cavities is given by Eq. (2.116) with $q\hat{V} = \sum_{n=1}^N q\hat{V}_n$, so long as the phases ϕ_{rf} are the same.

For particles with momentum $p \gg mc$, the momentum deviation δ is approximately the same as the **energy deviation**

$$\frac{\mathcal{E} - \mathcal{E}_0}{\mathcal{E}_0} \approx \frac{p - p_0}{p_0}, \quad (2.117)$$

where \mathcal{E} is the energy of the particle and \mathcal{E}_0 is the energy of the reference particle. For example, an electron with energy 11 MeV has a momentum deviation of $\delta = 0.10025$ compared to a reference electron at energy 10 MeV, and because the machines considered will operate at energies above 10 MeV, the terms energy deviation and momentum deviation will be used interchangeably.

Now let the reference particle enter the cavity with energy \mathcal{E}_0 , so that its energy at the end of the cavity $\mathcal{E}_1 = \mathcal{E}_0 + q\hat{V} \cos \phi_{\text{rf}}$. For a particular particle, rearranging Eq. (2.116) gives the energy deviation at the end of the cavity

$$\delta(L) = \left\{ 1 - \frac{\mathcal{E}_0}{\mathcal{E}_1} \right\} \left\{ \frac{\cos[\phi_{\text{rf}} - k_{\text{rf}} z(0)]}{\cos \phi_{\text{rf}}} - 1 \right\} + \frac{\mathcal{E}_0}{\mathcal{E}_1} \delta(0). \quad (2.118)$$

The cosine term expanded in small z is

$$\frac{\cos[\phi_{\text{rf}} - k_{\text{rf}} z]}{\cos \phi_{\text{rf}}} - 1 = k_{\text{rf}} z \tan \phi_{\text{rf}} - \frac{1}{2} (k_{\text{rf}} z)^2 - \frac{1}{6} (k_{\text{rf}} z)^3 \tan \phi_{\text{rf}} + \mathcal{O}(z^4). \quad (2.119)$$

This gives the first order transfer matrix for the longitudinal phase space as

$$\begin{pmatrix} z(L) \\ \delta(L) \end{pmatrix} = \begin{pmatrix} 1 & 0 \\ [1 - \mathcal{E}_0/\mathcal{E}_1] k_{\text{rf}} \tan \phi_{\text{rf}} & \mathcal{E}_0/\mathcal{E}_1 \end{pmatrix} \begin{pmatrix} z(0) \\ \delta(0) \end{pmatrix}. \quad (2.120)$$

With these explicit formulas it is possible to calculate the longitudinal phase space density ρ_1 at the end of a linac given the density ρ_0 at the beginning. This is done by first writing the initial phase space coordinates (z_0, δ_0) in terms of the final phase space coordinates (z_1, δ_1) , as in

$$z_0(z_1, \delta_1) = z_1, \quad (2.121)$$

$$\delta_0(z_1, \delta_1) = \left[1 - \frac{\mathcal{E}_1}{\mathcal{E}_0} \right] \left[\frac{\cos(\phi_{\text{rf}} - k_{\text{rf}} z_1)}{\cos \phi_{\text{rf}}} - 1 \right] + \frac{\mathcal{E}_1}{\mathcal{E}_0} \delta_1. \quad (2.122)$$

Simply changing variables gives

$$\rho_0(z_0, \delta_0) dz_0 d\delta_0 = \rho_0(z_0(z_1, \delta_1), \delta_0(z_1, \delta_1)) \begin{vmatrix} \frac{\partial z_0}{\partial z_1} & \frac{\partial z_0}{\partial \delta_1} \\ \frac{\partial \delta_0}{\partial z_1} & \frac{\partial \delta_0}{\partial \delta_1} \end{vmatrix} dz_1 d\delta_1, \quad (2.123)$$

and we can therefore identify

$$\rho_1(z_1, \delta_1) = \rho_0(z_0(z_1, \delta_1), \delta_0(z_1, \delta_1)) \frac{\mathcal{E}_1}{\mathcal{E}_0}, \quad (2.124)$$

where the Jacobian factor has been calculated. Typically the standard deviation of z and δ using such densities are called the **bunch length** and **energy spread**, respectively.

To illustrate the effect of a linac, consider a bunch with an initial Gaussian distribution in z and δ ,

$$\rho_0(z, \delta) = \frac{\exp\left(\frac{-z^2}{2\sigma_z^2}\right) \exp\left(\frac{-\delta^2}{2\sigma_\delta^2}\right)}{\sqrt{2\pi}\sigma_z \sqrt{2\pi}\sigma_\delta}, \quad (2.125)$$

with bunch length σ_z , energy spread σ_δ , and energy $\mathcal{E}_0 = 10 \text{ MeV}$ shown in Fig. 2.5(a). It is then sent through a linac with $\phi_{\text{rf}} = 0$ and accelerated to an

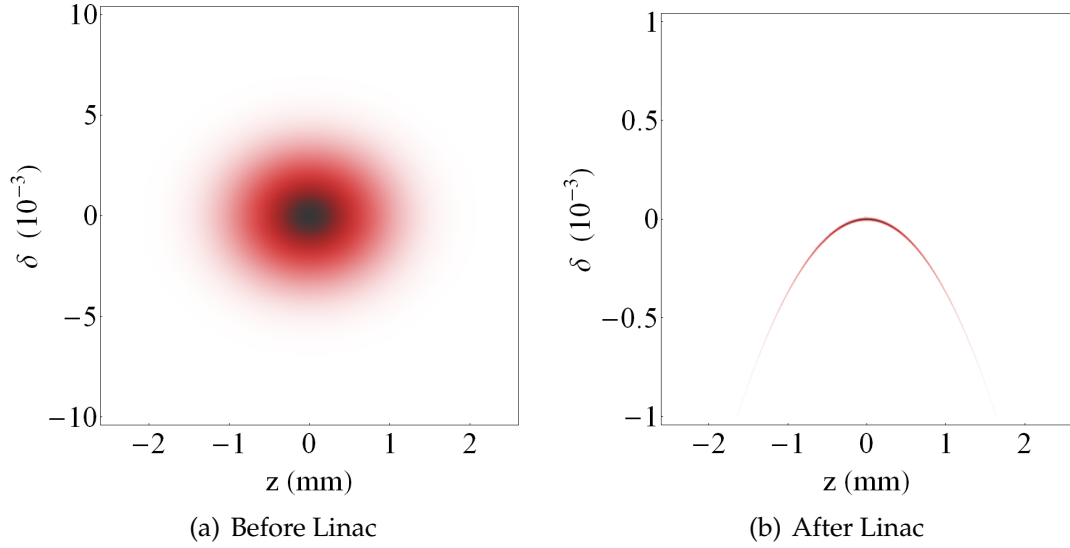


Figure 2.5: The longitudinal phase through a linac. The bunch begins with a Gaussian density according to Eq. (2.125) with bunch length $\sigma_z = 0.6$ mm, energy spread $\sigma_\delta = 2 \times 10^{-3}$, and energy $\mathcal{E}_0 = 10$ MeV, and is accelerated through a linac with $\phi_{\text{rf}} = 0$ and $f_{\text{rf}} = 1.3$ GHz to an energy of $\mathcal{E}_1 = 5$ GeV, according to Eq. (2.124) combined with Eqs. (2.121–2.122).

energy $\mathcal{E}_1 = 5$ GeV, shown in Fig. 2.5(b). There one sees that the final energy spread is dominated by the cosine-like curvature of the density, with the initial energy spread giving little contribution.

For an arbitrary ϕ_{rf} , the variance of z_1 and δ_1 at the end of a linac can be calculated exactly using the distribution in Eq. (2.125), yielding

$$\sigma_{z1}^2 = \sigma_{z0}^2, \quad (2.126)$$

$$\sigma_{\delta1}^2 = \left(1 - \frac{\mathcal{E}_0}{\mathcal{E}_1}\right)^2 \frac{e^{-2\epsilon} (e^\epsilon - 1) (e^\epsilon - \cos 2\phi_{\text{rf}})}{2 \cos^2 \phi_{\text{rf}}} + \left(\frac{\mathcal{E}_0}{\mathcal{E}_1}\right)^2 \sigma_{\delta0}^2, \quad (2.127)$$

where $\epsilon \equiv (k_{\text{rf}} \sigma_{z0})^2$. The bunch length σ_z is unchanged by the linac. Typically ϵ is small, so expanding Eq. (2.127) gives

$$\sigma_{\delta1}^2 \approx \left(1 - \frac{\mathcal{E}_0}{\mathcal{E}_1}\right)^2 \left[(k_{\text{rf}} \sigma_{z0} \tan \phi_{\text{rf}})^2 + \left(\frac{\cos 2\phi_{\text{rf}}}{\cos^2 \phi_{\text{rf}}} - \frac{1}{2}\right) (k_{\text{rf}} \sigma_{z0})^4 + \dots \right] + \left(\frac{\mathcal{E}_0}{\mathcal{E}_1}\right)^2 \sigma_{\delta0}^2. \quad (2.128)$$

The energy spread for **on-crest** acceleration ($\phi_{\text{rf}} = 0$) of a Gaussian bunch is

therefore approximately $\sigma_{\delta 1} \approx \frac{1}{\sqrt{2}}(k_{\text{rf}} \sigma_{z0})^2$, and for sufficient **off-crest** acceleration ($\phi_{\text{rf}} \neq 0$) it is approximately $\sigma_{\delta 1} \approx |k_{\text{rf}} \sigma_{z0} \phi_{\text{rf}}|$.

The evolution of the transverse phase space in an accelerating cavity is worked out in Rosenzweig & Serafini (1994), and for completeness we give their result here. The transfer matrix is

$$\mathbf{M}_{\text{rf}} = \begin{pmatrix} \cos \alpha - \sqrt{2} \cos \Delta\phi \sin \alpha & A 2 \sqrt{2} \cos \Delta\phi \sin \alpha \\ -\frac{\sin \alpha}{A} \left[\frac{1}{\sqrt{2}} \cos \Delta\phi + \frac{1}{2 \sqrt{2} \cos \Delta\phi} \right] & B \left[\cos \alpha + \sqrt{2} \cos \Delta\phi \sin \alpha \right] \end{pmatrix}, \quad (2.129)$$

with parameters written in our terms as

$$\Delta\phi \equiv \phi_{\text{rf}} - k_{\text{rf}} z(0), \quad (2.130)$$

$$A \equiv \left[\frac{1 + \delta(0)}{\mathcal{E}_1/\mathcal{E}_0 - 1} \right] \left[\frac{\cos \phi_{\text{rf}}}{\cos \Delta\phi} \right] L, \quad (2.131)$$

$$B \equiv \frac{A}{A + L}, \quad (2.132)$$

$$\alpha \equiv \frac{1}{2 \sqrt{2} \cos \Delta\phi} \log B. \quad (2.133)$$

The transverse coordinates at the end of the cavity are then

$$\begin{pmatrix} x(L) \\ x'(L) \end{pmatrix} = \mathbf{M}_{\text{rf}} \begin{pmatrix} x(0) \\ x'(0) \end{pmatrix}, \quad (2.134)$$

$$\begin{pmatrix} y(L) \\ y'(L) \end{pmatrix} = \mathbf{M}_{\text{rf}} \begin{pmatrix} y(0) \\ y'(0) \end{pmatrix}. \quad (2.135)$$

2.1.6 Nonlinear Optics

The motion in a classical deterministic system can be completely predicted given the fields and initial phase space points, and the six-dimensional transfer matrices of this form give the full first-order classical motion in the accelerator.

For compactness, we will call the vector of phase space coordinates \vec{z} , with an arrow to distinguish it from the coordinate $z(s)$. The components \vec{z}^i of \vec{z} are numbered according to

$$\left(\vec{z}^1, \vec{z}^2, \vec{z}^3, \vec{z}^4, \vec{z}^5, \vec{z}^6\right) \equiv (x, a, y, b, z, \delta). \quad (2.136)$$

Equations like Eq. (2.115) can then be written as

$$\vec{z}^i(s) = R^i_{j(s)} \vec{z}^j(0) + \mathcal{O}(\epsilon^2), \quad (2.137)$$

with i and j numbering the row and column of an element of the the transfer matrix, respectively. Repeated indices are summed from 1 to 6 according to the Einstein summation convention. Similar to Eq. (2.77), the phase space coordinates the end of the n^{th} element with position $s = s_n$ given the phase space coordinates at the beginning of the first element at $s = 0$ are

$$\vec{z}^i(s_n) = R^i_{(n)j_n} R^{j_n}_{(n-1)j_{n-1}} \dots R^{j_3}_{(2)j_2} R^{j_2}_{(1)j_1} \vec{z}^{j_1}(0) + \mathcal{O}(\epsilon^2), \quad (2.138)$$

associating $R^i_{(m)j}$ with the components of the transfer matrix for the m^{th} element.

The first order particle motion can thereafter be used to calculate higher order motion. The reader may be familiar with this method from perturbation theory in quantum mechanics (see for example Landau & Lifschitz Vol. 3, 2002). Let \mathcal{M} be the exact map of phase space coordinates, so that $\vec{z}^i(0)$ at $s = 0$ is mapped to $\vec{z}^i(s)$ through a portion of the accelerator according to

$$\vec{z}^i(s) = \mathcal{M}^i(\vec{z}(0), s) \quad (2.139)$$

$$= R^i_{j(s)} \vec{z}^j(0) + T^i_{jk(s)} \vec{z}^j(0) \vec{z}^k(0) + U^i_{jkl(s)} \vec{z}^j(0) \vec{z}^k(0) \vec{z}^l(0) + \mathcal{O}(\epsilon^4), \quad (2.140)$$

where the map has been Taylor expanded about $\vec{z}^i = 0$, the reference particle coordinates. The matrix $R^i_{j(s)}$ is the first order map which we have solved for

in terms of individual elements, as in Eq. (2.138). The coefficients $T^i_{jk}(s)$ and $U^i_{jkl}(s)$ represent the second and third order motion, respectively.

Phase space coordinates evolve according to the first order differential equation

$$\frac{d}{ds} \vec{z}^i(s) = f^i(\vec{z}, s), \quad (2.141)$$

where the functions f^i have been calculated at the end of Section 2.1.2. Alternatively, they can be found from the Hamiltonian \mathcal{K} of the system, by

$$(f^1, f^2, f^3, f^4, f^5, f^6) = \left(\frac{\partial \mathcal{K}}{\partial a}, -\frac{\partial \mathcal{K}}{\partial x}, \frac{\partial \mathcal{K}}{\partial b}, -\frac{\partial \mathcal{K}}{\partial y}, \frac{\partial \mathcal{K}}{\partial \delta}, -\frac{\partial \mathcal{K}}{\partial z} \right). \quad (2.142)$$

In fact, all analysis could start with such a Hamiltonian, as shown in Courant & Snyder (1958).

Now Taylor expand f about $\vec{z} = 0$, so that

$$\frac{d}{ds} \vec{z}^i = L^i_j \vec{z}^j + \mathcal{N}^i(\vec{z}, s) \quad (2.143)$$

$$= L^i_j \vec{z}^j + N^i_{jk} \vec{z}^j \vec{z}^k + N^i_{jkl} \vec{z}^j \vec{z}^k \vec{z}^l + \mathcal{O}(\epsilon^4), \quad (2.144)$$

where L^i_j are the linear terms, \mathcal{N}^i are all of the nonlinear terms, and the N are expansions of the nonlinear terms of f . For example, given a horizontal trajectory within static upright magnetic fields we have

$$\frac{d}{ds} \begin{pmatrix} x \\ a \\ y \\ b \\ z \\ \delta \end{pmatrix} = \begin{pmatrix} a \\ \kappa_0 \delta - (\kappa_0^2 + k_1) x \\ b \\ k_1 y \\ -\kappa_0 x \\ 0 \end{pmatrix} + \begin{pmatrix} \kappa_0 x a - a \delta \\ -(\kappa_0 k_1 + \frac{1}{2} k_2) x^2 - \frac{1}{2} \kappa_0 a^2 + \frac{1}{2} k_2 y^2 - \frac{1}{2} \kappa_0 b^2 \\ \kappa_0 x b - b \delta \\ (\kappa_0 k_1 + k_2) x y \\ -\frac{1}{2} (\kappa_0 x)^2 - \frac{1}{2} a^2 - \frac{1}{2} b^2 \\ 0 \end{pmatrix} + \mathcal{O}(\epsilon^3), \quad (2.145)$$

where the first vector on the r.h.s. contains the first order terms L^i_j , and the second vector on the r.h.s. contains the second order terms N^i_{jk} . Along with this, write \vec{z} as

$$\vec{z}^i = \vec{z}_{[1]}^i + \vec{z}_{[2]}^i + \vec{z}_{[3]}^i + \mathcal{O}(\epsilon^4), \quad (2.146)$$

where terms up to $\vec{z}_{[n]}$ represent the n^{th} order solution to Eq. (2.144). The first order equation

$$\frac{d}{ds} \vec{z}_{[1]}^i = L^i_j \vec{z}_{[1]}^j \quad (2.147)$$

has already been solved, with solution

$$\vec{z}_{[1]}^i(s) = R^i_j(s) \vec{z}_{[1]}^j(0). \quad (2.148)$$

This is equivalent to

$$\frac{d}{ds} R^i_j = L^i_k R^k_j. \quad (2.149)$$

The second order equation is

$$\frac{d}{ds} (\vec{z}_{[1]}^i + \vec{z}_{[2]}^i) = L^i_j (\vec{z}_{[1]}^j + \vec{z}_{[2]}^j) + N^i_{jk} \vec{z}_{[1]}^j \vec{z}_{[1]}^k. \quad (2.150)$$

Subtracting off the first order Eq. (2.147) and some manipulation gives

$$\frac{d}{ds} \left[(R^{-1})^i_j \vec{z}_{[2]}^j \right] = (R^{-1})^i_k N^k_{lm} \vec{z}_{[1]}^l \vec{z}_{[1]}^m, \quad (2.151)$$

where R^{-1} is the inverse matrix of R . With the definitions $\vec{z}_{[n]}(0) = 0$ for $n \geq 2$, integrating Eq. (2.151) gives

$$\vec{z}_{[2]}^j(s) = R^i_j(s) \int_0^s d\tilde{s} \left[R^{-1}(\tilde{s}) \right]^j_k N^k_{lm}(\tilde{s}) \vec{z}_{[1]}^l(\tilde{s}) \vec{z}_{[1]}^m(\tilde{s}) \quad (2.152)$$

$$= T^i_{jk}(s) \vec{z}^j(0) \vec{z}^k(0), \quad (2.153)$$

where the coefficients T^i_{jk} are given explicitly in terms of R^i_j and N^i_{jk} by

$$T^i_{jk}(s) = R^i_a(s) \int_0^s d\tilde{s} \left[R^{-1}(\tilde{s}) \right]^a_b N^b_{cd}(\tilde{s}) R^c_j(\tilde{s}) R^d_k(\tilde{s}). \quad (2.154)$$

Because $T_{jk}^i = T_{kj}^i$, it is more convenient in practice to refer to symmetrized versions of nonlinear terms, defined as

$$t_{ijk} \equiv \begin{cases} T_{jk}^i & \text{for } j = k \\ 2T_{jk}^i & \text{for } j \neq k \end{cases}, \quad (2.155)$$

and similarly for higher orders. Also define

$$r_{ij} \equiv R_j^i. \quad (2.156)$$

Note that the dispersion $D = r_{16}$, and its slope $D' = r_{26}$. This method can be similarly continued to higher orders.

Sextupole Magnet

As an example, consider the motion in an upright sextupole magnet with length L and sextupole moment k_2 . The first order transfer matrix $R_j^i(s)$ is simply that of a drift given by Eq. (B.1). The phase space coordinates at the entrance of the sextupole at $s = 0$ are

$$\vec{z}_{[1]}^i(0) = \begin{pmatrix} x_0 \\ a_0 \\ y_0 \\ b_0 \\ z_0 \\ \delta \end{pmatrix}. \quad (2.157)$$

Multiplying by the transfer matrix and inserting the solution into the second term on the r.h.s. of Eq. (2.145) gives the second order terms

$$N_{lm}^k(\tilde{s}) \vec{z}_{[1]}^l(\tilde{s}) \vec{z}_{[1]}^m(\tilde{s}) = \begin{pmatrix} -\delta a_0 \\ -\frac{1}{2}k_2(x_0 + \tilde{s}a_0)^2 + \frac{1}{2}k_2(y_0 + \tilde{s}b_0)^2 \\ -\delta b_0 \\ k_2(x_0 + \tilde{s}a_0)(y_0 + \tilde{s}b_0) \\ -\frac{1}{2}a_0^2 - \frac{1}{2}b_0^2 \\ 0 \end{pmatrix}. \quad (2.158)$$

Multiplying by transfer matrices and integrating as in Eq. (2.152) finally gives

$$\vec{z}_{[2]}(L) = \begin{pmatrix} k_2 L^4 \left[-\frac{1}{4} \left(\frac{x_0}{L} \right)^2 - \frac{1}{2} \left(\frac{x_0}{L} \right) a_0 - \frac{1}{24} a_0^2 + \frac{1}{6} \left(\frac{y_0}{L} \right) b_0 + \frac{1}{24} b_0^2 \right] - L a_0 \delta \\ k_2 L^3 \left[-\frac{1}{2} \left(\frac{x_0}{L} \right)^2 - \frac{1}{2} \left(\frac{x_0}{L} \right) a_0 - \frac{1}{6} a_0^2 + \frac{1}{2} \left(\frac{y_0}{L} \right) b_0 + \frac{1}{6} b_0^2 \right] \\ k_2 L^4 \left[\frac{1}{2} \left(\frac{x_0}{L} \right) \left(\frac{y_0}{L} \right) + \frac{1}{6} \left(\frac{y_0}{L} \right) a_0 + \frac{1}{6} \left(\frac{x_0}{L} \right) b_0 + \frac{1}{12} a_0 b_0 \right] - L b_0 \delta \\ k_2 L^3 \left[\left(\frac{x_0}{L} \right) \left(\frac{y_0}{L} \right) + \frac{1}{2} \left(\frac{y_0}{L} \right) a_0 + \frac{1}{2} \left(\frac{x_0}{L} \right) b_0 + \frac{1}{3} a_0 b_0 \right] \\ -\frac{1}{2} L (a_0^2 + b_0^2) \\ 0 \end{pmatrix}. \quad (2.159)$$

From this one is able to read off all of the second order terms. For example, $t_{126} = -L$ and $t_{244} = \frac{1}{6}k_2 L^3$.

By definition, a sextupole moment can only affect the second order motion and higher of a particle. This is useful for the lattice designer, because once the first order optics have been determined then sextupole magnets can be introduced and tuned. In particular, they are useful for controlling the second order dispersion.

It should be noted that, in practice, the nonlinear transfer map terms are calculated numerically using techniques from differential algebra, and with great efficiency. For an overview, see section 2.3.7 of Chao & Tigner (2006).

Nonlinear Dispersion and Time of Flight

In general, the **dispersive orbit** is the result of mapping a particle that has phase space coordinates all zero except for a finite momentum deviation. In other words, if \mathcal{M} is a phase space map, then the dispersive orbit through the map is given by

$$\begin{pmatrix} x_\delta \\ a_\delta \\ y_\delta \\ b_\delta \\ z_\delta \\ \delta \end{pmatrix} = \mathcal{M} \circ \begin{pmatrix} 0 \\ 0 \\ 0 \\ 0 \\ 0 \\ \delta \end{pmatrix}, \quad (2.160)$$

where the subscript δ is a reminder of the δ dependence. For horizontal reference orbit we always have $y_\delta = 0$ and $b_\delta = 0$, because there are no vertical bends to create vertical dispersion. Expanding these functions in δ gives

$$x_\delta(s) = D(s) \delta + t_{166}(s) \delta^2 + \mathcal{O}(\epsilon^2), \quad (2.161)$$

$$a_\delta(s) = D'(s) \delta + t_{266}(s) \delta^2 + \mathcal{O}(\epsilon^2), \quad (2.162)$$

$$z_\delta(s) = r_{56}(s) \delta + t_{566}(s) \delta^2 + \mathcal{O}(\epsilon^2), \quad (2.163)$$

revealing the first order dispersion function $D(s)$ and its slope $D'(s)$. The time of flight term $r_{56}(s)$ can be found using Eq. (2.111), giving

$$r_{56}(s) = - \int_0^s \kappa_0(\tilde{s}) D(\tilde{s}) d\tilde{s}. \quad (2.164)$$

The dispersive orbit is dependant on the reference location, chosen here to be at $s = 0$. For example, suppose that the map from $s = 0$ to $s = s_1$ is known to second order, and that we have a sextupole magnet with length L and sextupole

moment k_2 beginning at $s = s_1$. The dispersive orbit at $s_2 = s_1 + L$, the end of this element, is then

$$\begin{pmatrix} x_\delta(s_2) \\ a_\delta(s_2) \\ z_\delta(s_2) \\ \delta \end{pmatrix} = \begin{pmatrix} D(s_1) + L D'(s_1) \\ D'(s_1) \\ r_{56}(s_1) \\ 1 \end{pmatrix} \delta + \begin{pmatrix} t_{166}(s_2) \\ t_{266}(s_2) \\ t_{566}(s_2) \\ 0 \end{pmatrix} \delta^2 + \mathcal{O}(\delta^3), \quad (2.165)$$

with the second order terms

$$\begin{aligned} t_{166}(s_2) = & t_{166}(s_1) + L t_{266}(s_1) - \frac{1}{4} k_2 L^2 [D_0(s_1)]^2 \\ & - \frac{1}{2} k_2 L^3 D(s_1) D'(s_1) - \frac{1}{24} k_2 L^4 [D'(s_1)]^2 - L D'(s_1), \end{aligned} \quad (2.166)$$

$$t_{266}(s_2) = t_{266}(s_1) - \frac{1}{2} k_2 L [D(s_1)]^2 - \frac{1}{2} k_2 L^2 D(s_1) D'(s_1), \quad (2.167)$$

$$t_{566}(s_2) = t_{566}(s_1) - \frac{1}{2} L [D'(s_1)]^2. \quad (2.168)$$

This shows that a sextupole must be in a section with nonzero first order dispersion in order to affect the second order dispersion, and that, roughly speaking, sextupole strengths can be weakened as the first order dispersion is strengthened.

2.2 Radiative Emittance Growth

When a bunch is accelerated, each particle can emit photons by synchrotron radiation, which perturb the orbits of these particles and can result in an increase in emittance. The following argument, which originated in Sands (1970), gives an estimate for this emittance growth.

Suppose that a particle with energy \mathcal{E}_0 is traveling in a dipole magnet with horizontal position $x(s)$ and slope $x'(s)$ at s , and emits a photon with energy \mathcal{E}_γ .

Neglecting the opening angle of this radiation, the particle's position and slope are approximately unchanged, but its energy has been lowered, and therefore according to Eqs. (2.105–2.106) its position and slope due to betatron motion are changed by

$$\Delta x_\beta(s) = D(s) \frac{\mathcal{E}_\gamma}{\mathcal{E}_0}, \quad (2.169)$$

$$\Delta x'_\beta(s) = D'(s) \frac{\mathcal{E}_\gamma}{\mathcal{E}_0}, \quad (2.170)$$

which corresponds to a variation in amplitude

$$2 \Delta J = \beta_x \Delta(x_\beta'^2) + 2 \alpha_x \Delta(x_\beta x'_\beta) + \gamma_x \Delta(x_\beta^2). \quad (2.171)$$

The variation in x_β^2 is calculated as

$$\begin{aligned} \Delta(x_\beta^2) &= (x_\beta + \Delta x_\beta)^2 - x_\beta^2, \\ &= 2 x_\beta \Delta x_\beta + (\Delta x_\beta)^2, \\ &= 2 x_\beta D \frac{\mathcal{E}_\gamma}{\mathcal{E}_0} + D^2 \frac{\mathcal{E}_\gamma^2}{\mathcal{E}_0^2}, \end{aligned} \quad (2.172)$$

and similarly

$$\Delta(x_\beta x'_\beta) = x_\beta D' \frac{\mathcal{E}_\gamma}{\mathcal{E}_0} + x'_\beta D \frac{\mathcal{E}_\gamma}{\mathcal{E}_0} + D D' \left(\frac{\mathcal{E}_\gamma}{\mathcal{E}_0} \right)^2, \quad (2.173)$$

$$\Delta(x_\beta'^2) = 2 x'_\beta D' \left(\frac{\mathcal{E}_\gamma}{\mathcal{E}_0} \right) + D'^2 \left(\frac{\mathcal{E}_\gamma}{\mathcal{E}_0} \right)^2. \quad (2.174)$$

Factoring out the energies, we have

$$2 \Delta J = \mathcal{H}(s) \left(\frac{\mathcal{E}_\gamma}{\mathcal{E}_0} \right)^2, \quad (2.175)$$

$$\mathcal{H}(s) \equiv \beta_x(s) [D'(s)]^2 + 2 \alpha_x(s) D(s) D'(s) + \gamma_x(s) [D(s)]^2. \quad (2.176)$$

Averaging over the synchrotron radiation power spectrum and integrating through a distance L in the lattice gives the change in normalized emittance as

$$\Delta \epsilon_N = \frac{55}{48 \sqrt{3}} \frac{r_c \hbar c}{m c^2} \int_0^L \mathcal{H}(s) |\kappa(s)|^3 \gamma^6 ds. \quad (2.177)$$

This formula is especially useful for lattice design, because it is written in terms of the Twiss parameters and dispersion.

2.3 Accelerator Simulation

In the previous sections we have seen how the evolution of a beam through an individual element can be understood through the linear and nonlinear maps of phase space coordinates through that element, and we have seen how to calculate these maps. The transportation of a beam through a lattice is then understood through the concatenation of individual element maps.

For lattices of few elements or high symmetry it can occasionally be enlightening to do such calculations by hand. Realistic accelerators, however, are often described by complicated lattices with many elements, and the modeling of these machines requires the inclusion of many effects beyond the single particle equations of motion, for example coherent synchrotron radiation, described in Chapter 5. Furthermore, lattices often need to be designed to provide certain beam characteristics, such as beta functions at a point, by simultaneously tuning attributes of several elements, such as quadrupole moments, and these characteristics often depend on the element attributes in highly nonlinear ways. For these reasons the aid of a computer is necessary in the design and simulation of modern particle accelerators.

Many different codes are in use, with some in more active development than others. A table of some of the more easily available ones is shown in section 2.2.7 of Chao & Tigner (2006). Many are derived from *MAD* (Methodical Accelerator Design), which is perhaps the most commonly known program (Grote & Iselin,

1991). The work in this dissertation is primarily done using a code called *Bmad* .

2.3.1 *Bmad* & *Tao*

Bmad is a set of subroutine libraries for simulating relativistic charged beams in a particle accelerator, and has been in development and use at Cornell University since 1996 (for a brief introduction see Sagan, 2006). It is written in a modular fashion, primarily in Fortran 90, so that a user may relatively easily build a custom program to perform a particular simulation. A lattice in *Bmad* is described by a text file written in an extended form of the *MAD* syntax, and can describe an arbitrary arrangement of common accelerator elements, *e.g.* bends, quadrupole magnets, and accelerating cavities.

The capabilities of *Bmad* include essentially all of the calculations described in this chapter. Once a lattice is loaded, it can compute Twiss parameters and dispersion through multiple elements, calculate and manipulate Taylor maps to arbitrary order, integrate emittance growth formulas such as Eq. (2.177), and calculate a myriad of other important accelerator physics quantities not discussed here. In particular, *Bmad* has the ability to track point particles through the lattice and apply effects to these particles along the way.

Designing and testing accelerator lattices is such a common use for *Bmad* that Sagan, along with Jeffrey Smith, created the *Tao* (Tool for accelerator optimization) program, which is now in active development along with *Bmad* . *Tao* is an interactive command-line environment (along with a plot window) that calls *Bmad* routines to perform lattice and beam calculations. Many of the plots in Chapters 3 and 4 were generated using *Tao* .

The main capability of *Tao* is multi-dimensional optimization of an accelerator lattice. Optimization in general is an important mathematical topic in the field of operations research, and has a wide variety of applications ranging from stock portfolio allocation to the timing of traffic lights in a city. In optimization, one is concerned with a system \mathcal{S} that is determined by a set of independent variables \mathcal{V}_m , and a merit function \mathcal{M} that somehow encapsulates the overall quality of \mathcal{S} . This merit function is typically composed of out of a set of constraints C_n with the form

$$\mathcal{M} = \sum_n w_n C_n^2. \quad (2.178)$$

Each constraint represents some property of \mathcal{S} that should be minimized, and the set of weights w_n determines the relative importance each constraint. A constraint is typically of the form

$$C = X(\mathcal{S}) - \hat{X}, \quad (2.179)$$

where X is a number that can be computed from \mathcal{S} , and \hat{X} is the desired value for that number. For example, if \mathcal{S} is an accelerator lattice, then X could be the horizontal beta function β_x in meters at the center of an undulator, and $\hat{X} = 2.5$ could be a value specified by a beamline user. Constraints occasionally have the form of

$$C = \max [X(\mathcal{S}) - \bar{X}, 0], \quad (2.180)$$

which is zero as long as $X(\mathcal{S})$ is less than \bar{X} . For example, $X(\mathcal{S})$ could be the maximum beta function in meters through a section of the lattice, and $\bar{X} = 100$ could be the maximum allowed.

An optimizer is an algorithm that takes an initial set \mathcal{V}_m and varies each to find a minimum for \mathcal{M} . An optimizer generally knows nothing of the underlying logic or physics that determines the merit function, and can often be

treated as a ‘black box’ for solving complicated systems. *Tao* incorporates a variety of optimizers, but typically only two are needed for lattice design. One is the Differential Evolution (Price *et al.*, 2005) method, which is a heuristic algorithm inspired by evolutionary biology. It works by taking an initial random population of variables $\{\mathcal{V}_i\}$ corresponding to a set of merit functions $\{\mathcal{M}\}$, and combines and alters them to produce a new population of variables with lower associated merit functions. It is a very effective global optimizer. The other is the Levenberg–Marquardt algorithm, which is a modified method of steepest descent (see for example Press *et al.*, 2007). It takes an initial \mathcal{V}_n and varies each variable to calculate a local derivative of the merit function, and steps the solution accordingly. This algorithm is especially useful when the initial solution is close to the desired solution, meaning that it is a good local optimizer. It can also be surprisingly good even when the solution seems to not be very local.

2.3.2 Optimization Example

As an example of a typical optimization, consider a section of an accelerator at the end of a linac in Fig. 2.6, which shows all of the constraints for the section. Particles exit the linac at 5 GeV, and must have a specified width in undulator, which translates into the constraints $\beta_x = \beta_y = 2.5$ m and $\alpha_x = \alpha_y = 0$ in the center of the undulator. The dispersion and its slope must also be zero in the undulator, but that is automatically satisfied because there is no dispersion exiting the linac. A first optimization uses the five quadrupole strengths prior to the first undulator as variables with a merit function composed of these constraints, and results in the beta functions plotted.

Following the undulator is a three bend isochronous achromat, which must end with $D = 0$, $D' = 0$, and $r_{56} = 0$. Because the section begins with $D = 0$ and $D' = 0$, and is symmetric about the center bend, the achromatic condition can be satisfied by using a constraint of $D' = 0$ in the middle of the center bend, and varying quadrupole strengths in pairs about this point. Also because of the symmetry, using $r_{56} = 0$ at this point will satisfy the isochronous condition, and using the constraints that $\alpha_x = \alpha_y = 0$ at this point will result in beta functions that lead into the second undulator with the same Twiss parameters as the first undulator. Finally these presence of bends will result in radiative emittance growth $\Delta\epsilon_N$ according to Eq. (2.177), so this is used as constraint with the form in Eq. (2.180). A second optimization thus varies the quadrupole strengths between the undulators symmetrically, resulting in the beta functions and dispersion plotted.

The second order dispersion is required to give $t_{266} = 0$ and $t_{566} = 0$ in the middle of the second undulator. Using the four sextupole strengths as variables and a merit function with these constraints, a third optimization results in the second order dispersion t_{166} plotted.

In principle all three optimizations could be combined, using all of the constraints mentioned and varying all of the quadrupole and sextupole strengths. In practice, such an approach can be very time consuming, with the optimization taking perhaps days to complete on modern computer hardware. Instead, an intelligent partitioning of this optimization, and recognizing the symmetries, can reduce the computation time to be on the order of minutes.

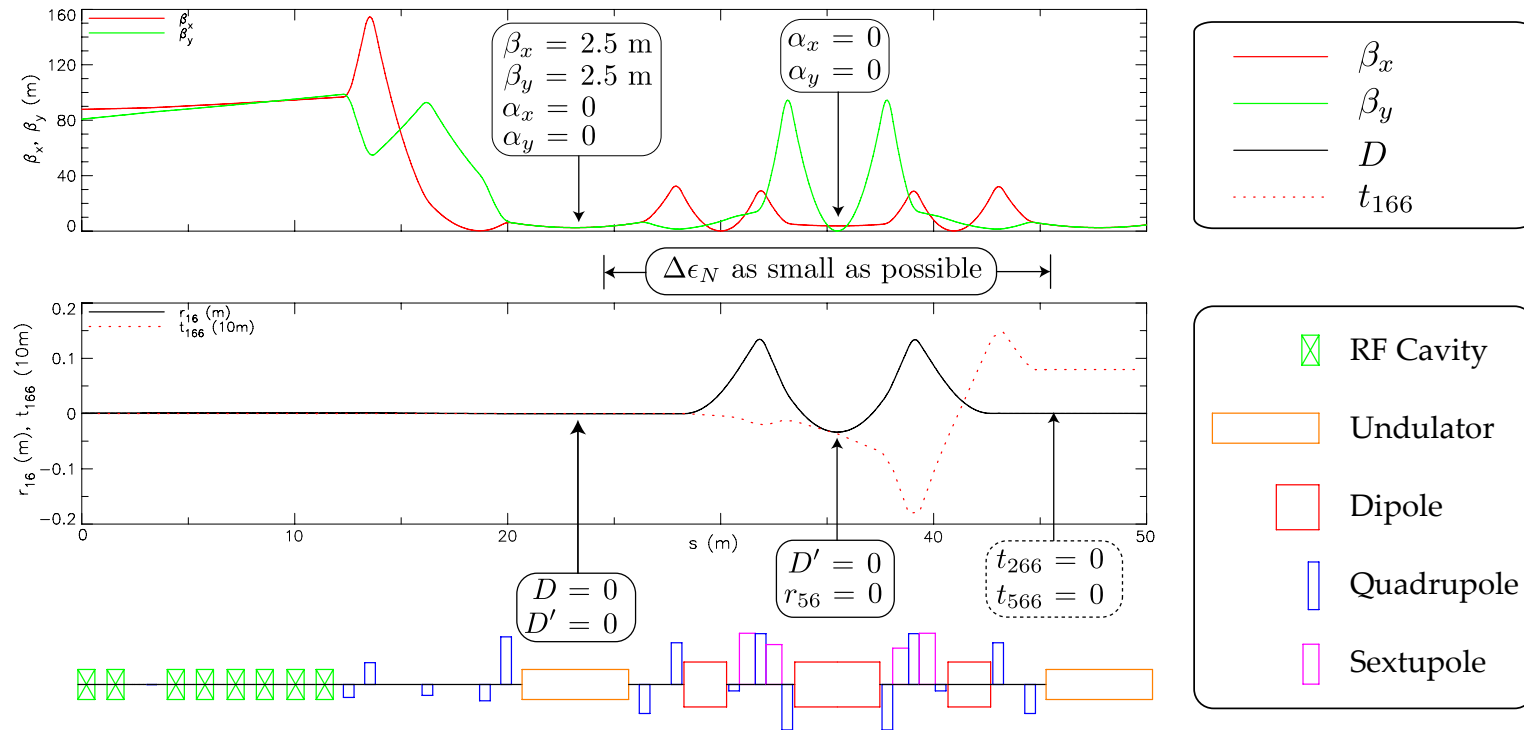


Figure 2.6: Example of the optimization of a section following a linac. The constraints at different points are indicated by the arrows. The vertical size of the quadrupole and sextupole magnets represents their k_1 and k_2 strengths, respectively. This section is identical to one later shown in Section 3.2.3.

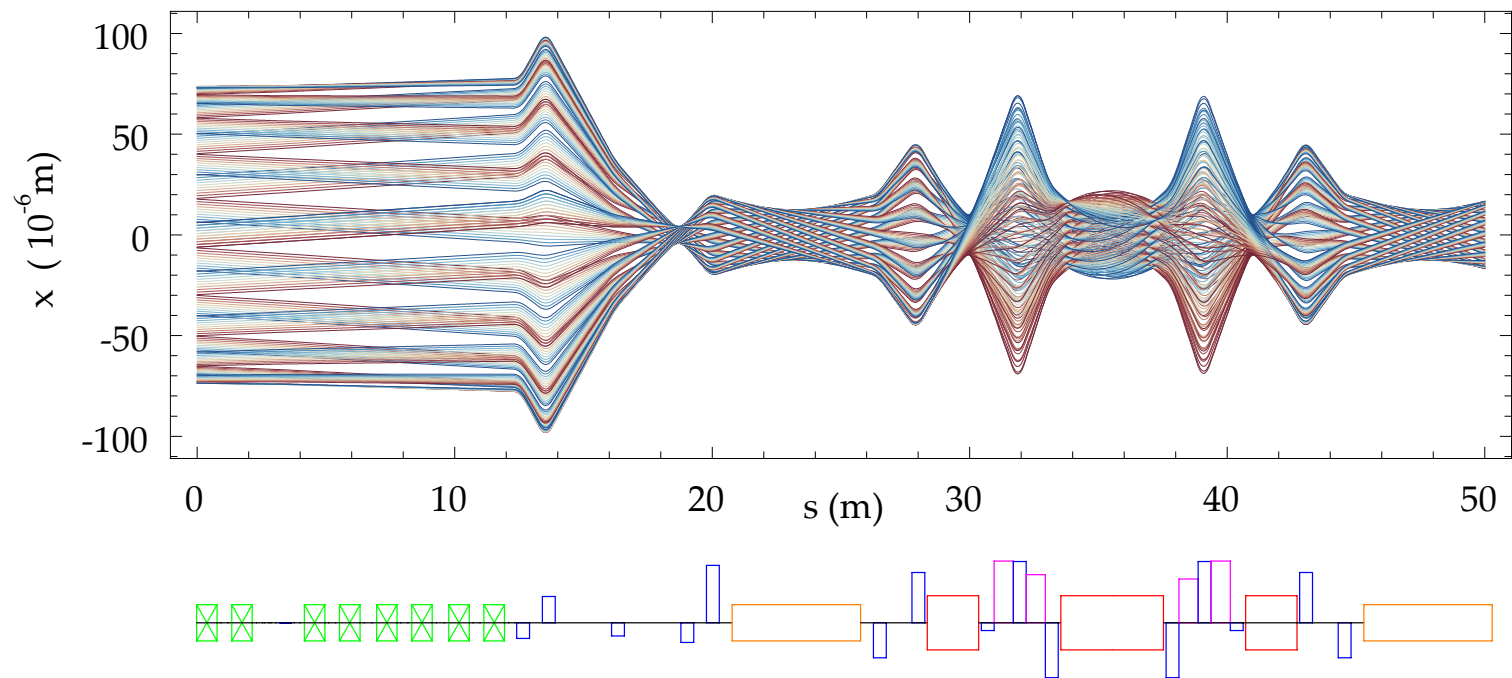


Figure 2.7: Trajectories of particles in the horizontal plane using the Twiss parameters and dispersion from Fig. 2.6. The particles are initially distributed with the same amplitude and different phases and energies shown in Fig. 2.8(a), and represent a normalized emittance of 0.3 mm-mrad at 5 GeV and momentum deviations $\delta \epsilon \left[-2 \times 10^{-4}, 2 \times 10^{-4} \right]$.

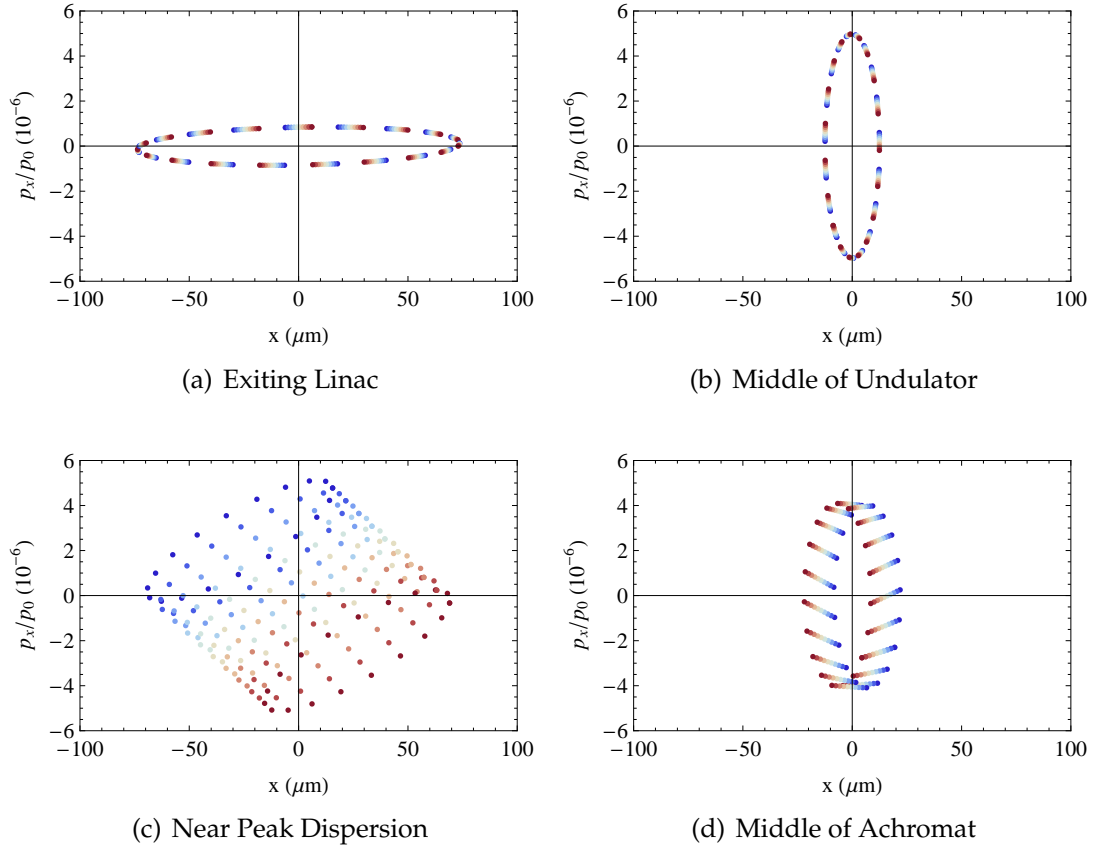


Figure 2.8: Particles in the horizontal phase space at selected points in Fig. 2.7. The colors represent different momentum deviations δ , with blue representing positive δ , and red representing negative δ . They all have the same amplitude J with different phases ϕ .

Finally, to illustrate what the result of these optimizations will do to a beam, individual particle trajectories in the horizontal plane are shown in Fig. 2.7. They are calculated using the Twiss parameters and dispersion from Fig. 2.6 according to Eqs. (2.105–2.106). The initial distribution of particles is a matched ellipse shown in Fig. 2.8(a). This ellipse contains particles with different energies. Manipulation by the first five quadrupole magnets brings this distribution to have a small width shown in Fig. 2.8(b). At the point where the dispersion is largest, ellipses with different energies separate, shown in Fig. 2.8(c). The distribution in the center of the achromat is shown in Fig. 2.8(d).

CHAPTER 3

MINIMAL ERL

3.1 Introduction & Layout

The Minimal ERL (MERL) is a realistic lattice and layout for a high energy ERL X-ray light source. It is used to show all of the major issues that one must analyze when designing an ERL. The layout is especially designed to be as compact as possible given practical attributes for typical beam transport elements, without reference to any particular topography. It is highly symmetric, which greatly simplified the amount of effort needed to design and optimize the beam optics. This machine is essentially a simplification of Cornell ERL described in Chapter 4, and uses many of the same operating parameters as that design. In particular, it uses the same operating modes for particle bunches, as listed in Tab. 3.1.

The MERL is primarily a light source, and has space for 18 insertion devices. In order to produce high quality X-rays, it must:

- Accelerate particles from 10 MeV to 5 GeV
- Send bunches with low emittance through 18 insertion devices
- Control bunch length

We will assume the existence of a injector that can merge bunches of 10 MeV electrons into the main linacs of the MERL. In the default operating mode (Mode A), these bunches will have 77 pC of charge and will occur at a repetition rate of 1.3 GHz, which corresponds to an average current of 100 mA.

Table 3.1: MERL & CERL operating modes at 5 GeV

	Mode A	Mode B	Mode C	
\mathcal{E}	5	5	5	GeV
I	100	25	1	mA
Q	77	19	1000	pC
$\epsilon_{N,x}, \epsilon_{N,y}$	0.3	0.08	5.0	mm-mrad
ϵ_{x}, ϵ_y	31	8.2	511	pm
σ_z/c	2000	2000	100	fs
σ_δ	2	2	30	10^{-4}

As mentioned in Chapter 1, such a high current and energy would require an unreasonable amount of electrical power for a linear machine, so the MERL recovers energy from these bunches. In order to operate as an ERL, the machine must then:

- Ensure the survival of all particles
- Decelerate and recover 4.990 GeV per particle (minus radiative losses)
- Discard 10 MeV particles

Here we assume the existence of a dump that can extract and absorb 10 MeV electrons.

The MERL layout is divided into six sections, shown in Fig. 3.1. The injector (IN) delivers a 10 MeV beam into Linac A (LA), which accelerates it to 2.505 GeV. The beam then goes through a Turnaround Arc (TA) and connects to Linac B (LB), which further accelerates it to 5 GeV. It then traverses a Return Arc (RA) containing eighteen insertion devices. The beam is then reintroduced to the beginning of LA at the decelerating phase and returns 2.495 GeV per particle to the RF cavities. Now at 2.505 GeV, the beam goes through the same TA, and then into LB where 2.495 GeV per particle is recovered. Finally, the 10 MeV beam is

sent to the dump (DU) at the end of LB.

The dimensions of this machine are primarily governed by the lengths of the linacs and the number and lengths of the insertion devices. The linacs are each taken to be 318 m long, based on the Cornell ERL designs, and all 18 insertion devices are taken to be 5 m long undulators. Allotting a minimal amount of space for dipole, quadrupole, and sextupole magnets, with suitable drifts in between leads to a 465 m long RA containing the undulators, which lies roughly on a circle with a 122 m radius. The TA is designed to be as short as possible with special consideration given to the heat load on the chamber wall. In general, the power per unit length radiated on the beam chamber wall in a dipole magnet due to incoherent synchrotron radiation is given by

$$\left\langle \frac{P}{L} \right\rangle = \frac{2}{3} r_c m c^2 \beta^3 \gamma^4 \kappa^2 \frac{I}{q}, \quad (3.1)$$

where I is the average current, q is the elementary charge, and $1/\kappa$ is the magnet bending radius. Here the bends are chosen to give ≈ 750 W/m for 200 mA electron beam in the TA, and allotting for focusing elements makes it 116 m long. Incidentally, Eq. (3.1) gives ≈ 500 W/m for a 100 mA electron beam in the RA. The total length of the machine is then 1217 m.

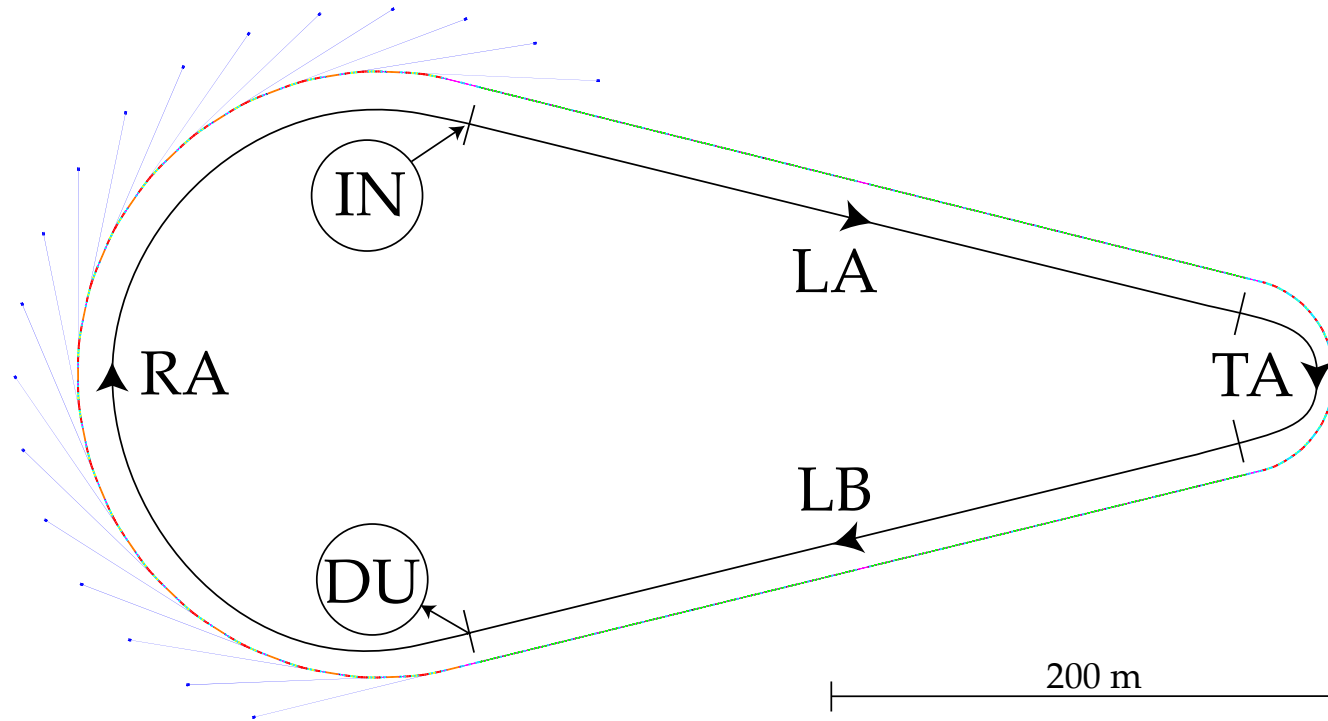


Figure 3.1: The MERL layout with section labels. A bunch is accelerated to 10 MeV in the injector (IN), and injected into the beginning of Linac A (LA), which accelerates it to 2.5 GeV. The bunch traverses Turnaround A (TA), and gains another 2.5 GeV through Linac B (LB). At 5 GeV, the bunch travels through 18 undulators in the Return Arc (RA). It then reenters LA off phase, which decelerates it to 2.5 GeV, enters Turnaround B (TB), and is decelerated to 10 MeV through LB. Finally it is extracted and sent to the Dump (DU).

3.2 Optics

The majority of the optics design is focused on the linear optics. The selection and ordering of dipole magnets and quadrupole magnets is chosen with this in mind. Once the lengths of drifts and strengths of bends have been settled upon, fixing the layout, the optics optimization typically then only involves choosing the quadrupole strengths. Second order effects can be adjusted separately by sextupole strengths.

The optics in the MERL must be tuned to be in accordance with the X-ray and ERL requirements described above. For the X-ray requirements, this means that the initially injected bunch emittance must be preserved through the linacs and through TA, which amounts to minimizing the radiative emittance growth given by Eq. (2.177). Additionally, the beta functions and dispersion in the undulators determine the X-ray source spot size, and must be well controlled throughout the entire machine. Controlling the bunch length amounts to controlling time of flight terms and linac phases, and is further discussed in Section 3.5. For the ERL requirements, the linac optics must be able control two beams of different energies, and nonlinear effects must be controlled to insure that all particles survive their passage through the machine. Finally, the time of flight terms need to be controlled to minimize the energy spread at the dump.

The following sections describe the choice and optimization of the optics for each of the major sections. By design, each of these sections can be optimized separately and pieced together to form the total optics solution. The complete solution for the beta functions and dispersion is shown in Fig. 3.3. The radiative emittance growth is shown in Fig. 3.2.

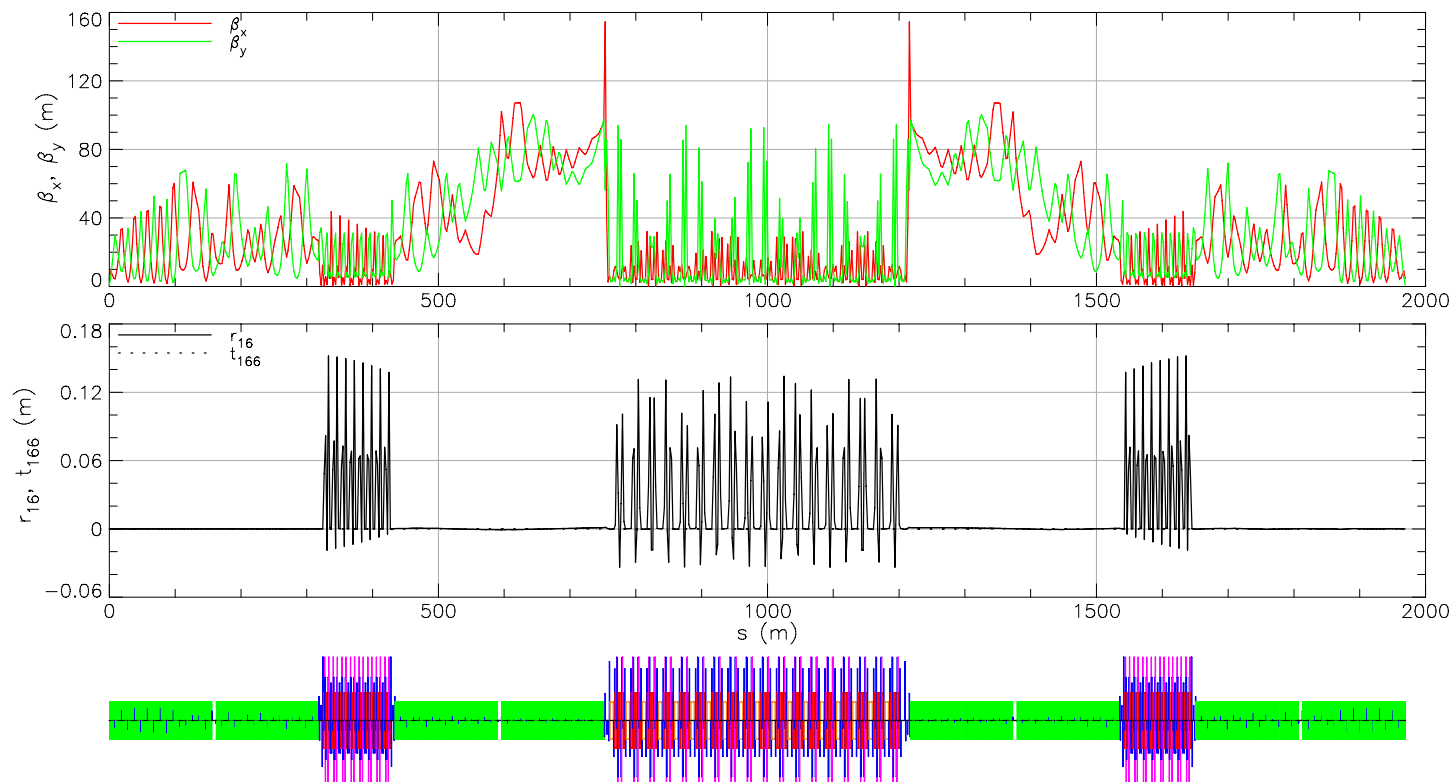


Figure 3.2: Beta functions and dispersion for the MERL, including the energy recovery pass.

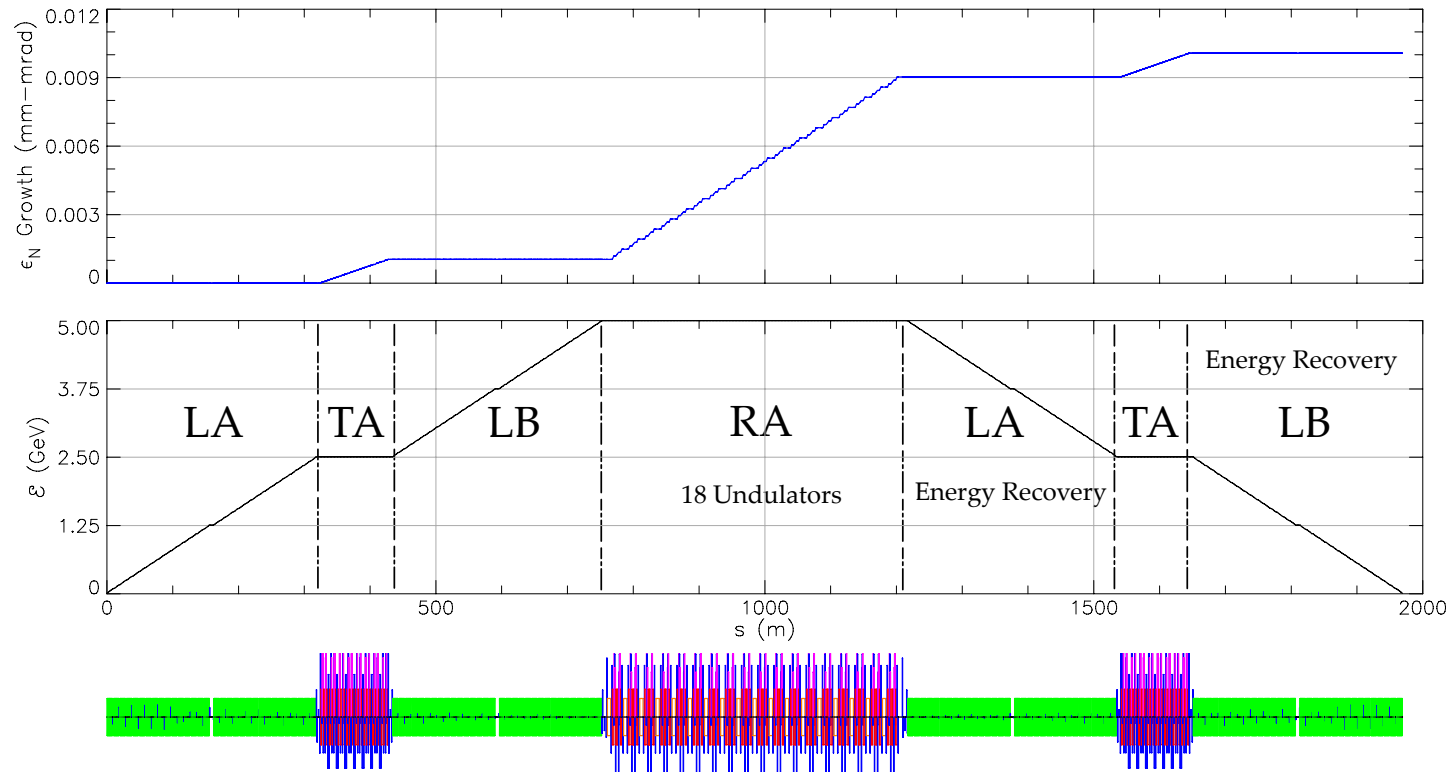


Figure 3.3: Radiative emittance growth ϵ_N and total energy \mathcal{E} in the MERL, including the energy recovery pass.

3.2.1 Linacs

The linacs are the engines of an ERL lightsource. The linacs in the MERL consist of 64 identical cryomodules, each of which can give or take approximately 78 MeV to or from the beam, and operate at a fundamental frequency of $f_{\text{rf}} = 1.3$ GHz. Each cryomodule contains one quadrupole magnet. Because these are similar to those of the CERL, they are further described in Section 4.3.1.

The main optics requirement in a linac section is to keep the beta functions as small as possible for both the accelerating and decelerating beams. This is done primarily to suppress the effect of wakefields in the accelerating cavities, which can result in the beam breakup instability (see for example section 4.3 of Chao & Tigner, 2006). Additionally, the Twiss parameters must be matched to the adjacent sections. In particular, the Twiss parameters at the end of LA must be the same for both beams, and similarly must be the same at the beginning of LB, in order to have a single set of optics in the TA. There is no dispersion in the linacs. Some optics guidelines for ERL linacs can be found in Douglas (2000) and Bazarov *et al.* (2001).

A solution satisfying these constraints is sought by varying the quadrupole fields. Due to the symmetry in the layout, a good solution for both LA and LB can be found by finding a solution for one linac, and mirroring the quadrupole strengths in the other. Such a scheme is shown in Fig 3.4. In this case it is simplest to optimize LB by varying the 32 quadrupole gradients as well as the beginning Twiss parameters, set to be the same for both beams.

The difficulty in this optimization is due to the presence of two beams of different energies. In nearly all other sections the quadrupole strength k_1 is

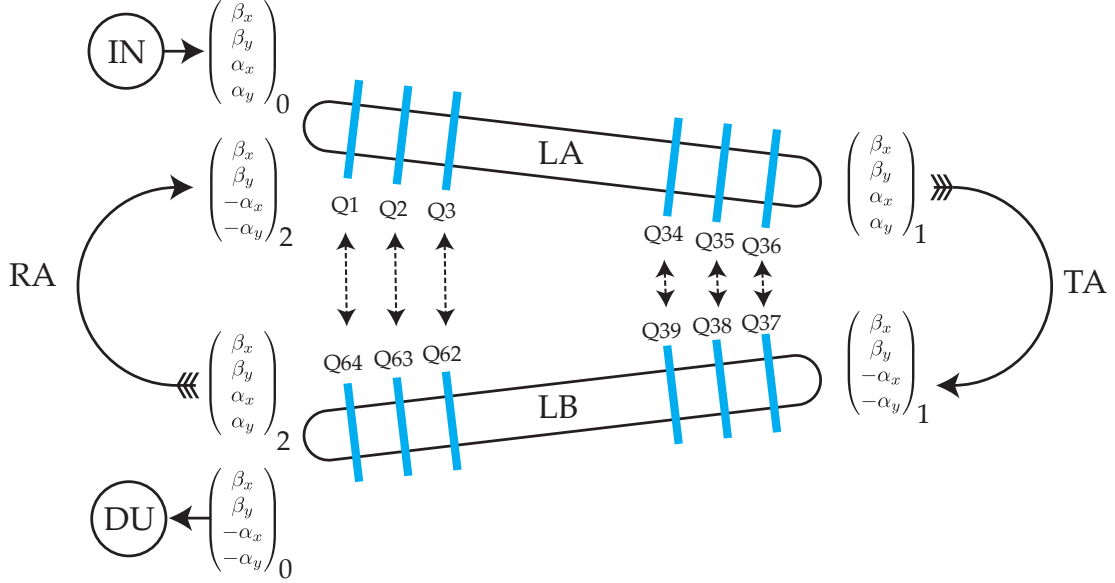


Figure 3.4: A mirroring scheme for the MERL linac optics. Different Twiss parameters from the IN and RA converge to a single set at the entrance of the TA. The TA optics reverse the signs of α_x and α_y to enter into LB. Similarly, the RA optics reverse the signs of α_x and α_y from the high energy beam at the end of LB.

treated as a variable, as that is the quantity that affects linear optics. Multipole strengths, however, are normalized by the reference particle momentum according to Eq. (2.55), so here we vary the physical magnetic field gradient instead. This means that the ratio of the quadrupole strengths seen by the beams is inversely proportional to the ratio of their momenta, as in

$$[k_1]_d = \frac{[p_0]_a}{[p_0]_d} [k_1]_a, \quad (3.2)$$

in which the subscripts a and d denote the decelerating and accelerating beams, respectively. For example, in the first quadrupole magnet in the first cryomodule of LA, where the accelerating beam is at $(10 + 78)$ MeV and the decelerating beam is at $(5000 - 78)$ MeV, we have the quadrupole strength $[k_2]_d \simeq [k_2]_a / 56$. The resulting strengths for all 64 quadrupole magnets seen by the different beams are shown in Fig 3.5. Both beams have the same energy at the end of LA. Because quadrupole gradients at the beginning of LA and end of LB must be weak

enough so as to not over-focus the low energy beam, it becomes difficult for them to focus the high energy beam.

The beta functions for the first pass (accelerating) beam and energy recovery (decelerating) beam in LB are shown in Fig. 3.6. Near the entrance to this section the beams are at similar energies, and the beta functions are therefore similar. Near the end, where the beam energies are the most different, so are the beta functions. There is no known rule for finding good solutions in this situation, though in practice it has been found that alternating positive and negative quadrupole strengths gives a good starting point. In this solution, we see that the end of LB for the second pass beam has very regularly focusing and defocusing beta functions, while the beta functions for the first pass beam behave similar to those in a long drift. The optics for LA are shown in Fig. 3.7.

The relative effectiveness of quadrupole magnets on the different beams happens to be a virtue for matching from the IN and to the DU, because quadrupole fields near those sections can be tuned for the low energy beam with little effect on the high energy beam. Therefore matching from the IN and to the DU is relatively simple compared to the overall optimization. For simplicity, they are just taken to be the same in this design.

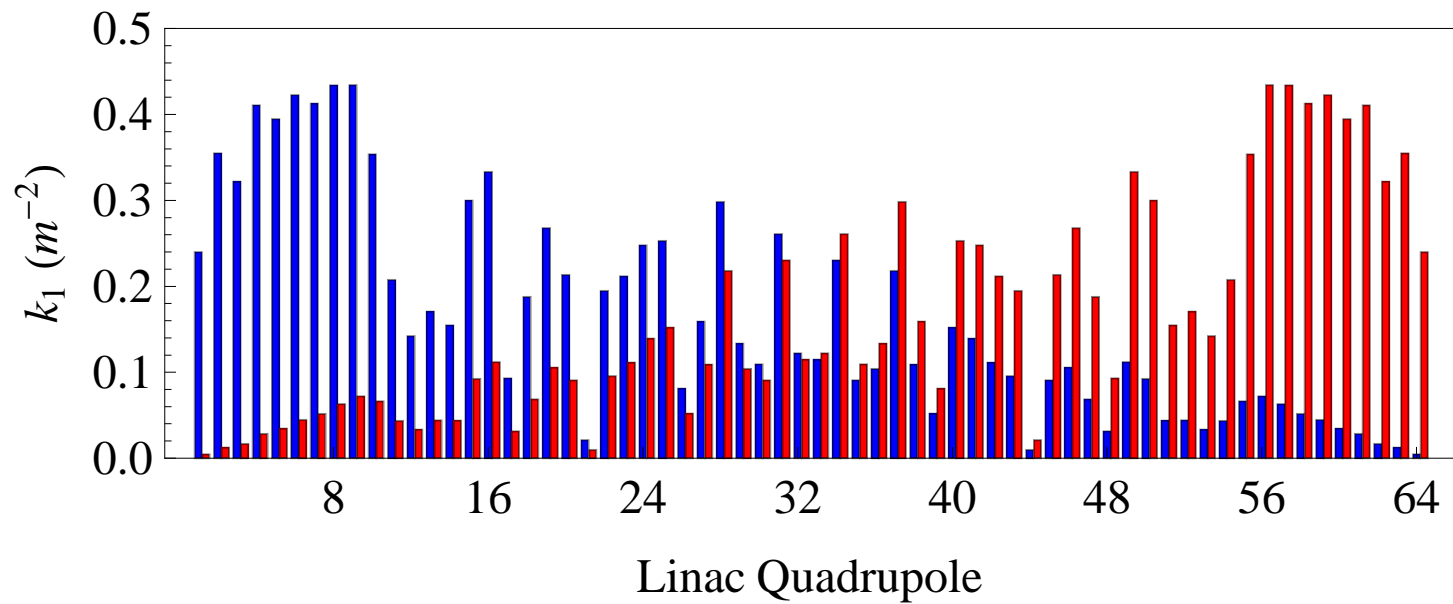


Figure 3.5: Quadrupole k_1 strengths seen by the accelerating beam (blue bars) and decelerating beam (red bars). Because of the mirroring scheme shown in Fig. 3.4, these strengths are symmetric between quadrupoles 32 and 33.

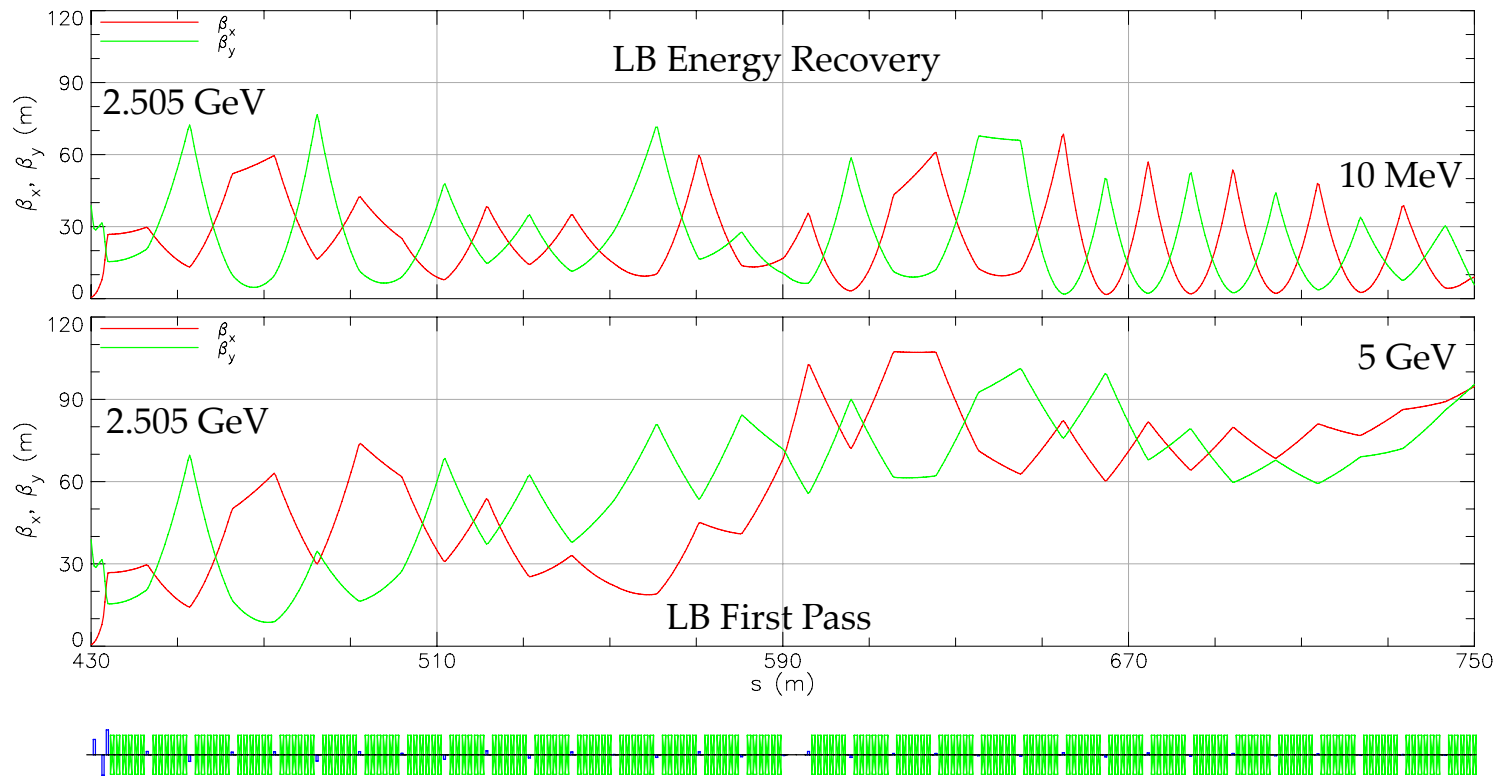


Figure 3.6: Beta functions for the first pass (accelerating) beam and energy recovery (decelerating) beam in LB. The optimization criteria are to keep the beta functions as small as possible and to match the low energy beam at $s = 0$ to the Twiss parameters from the IN.

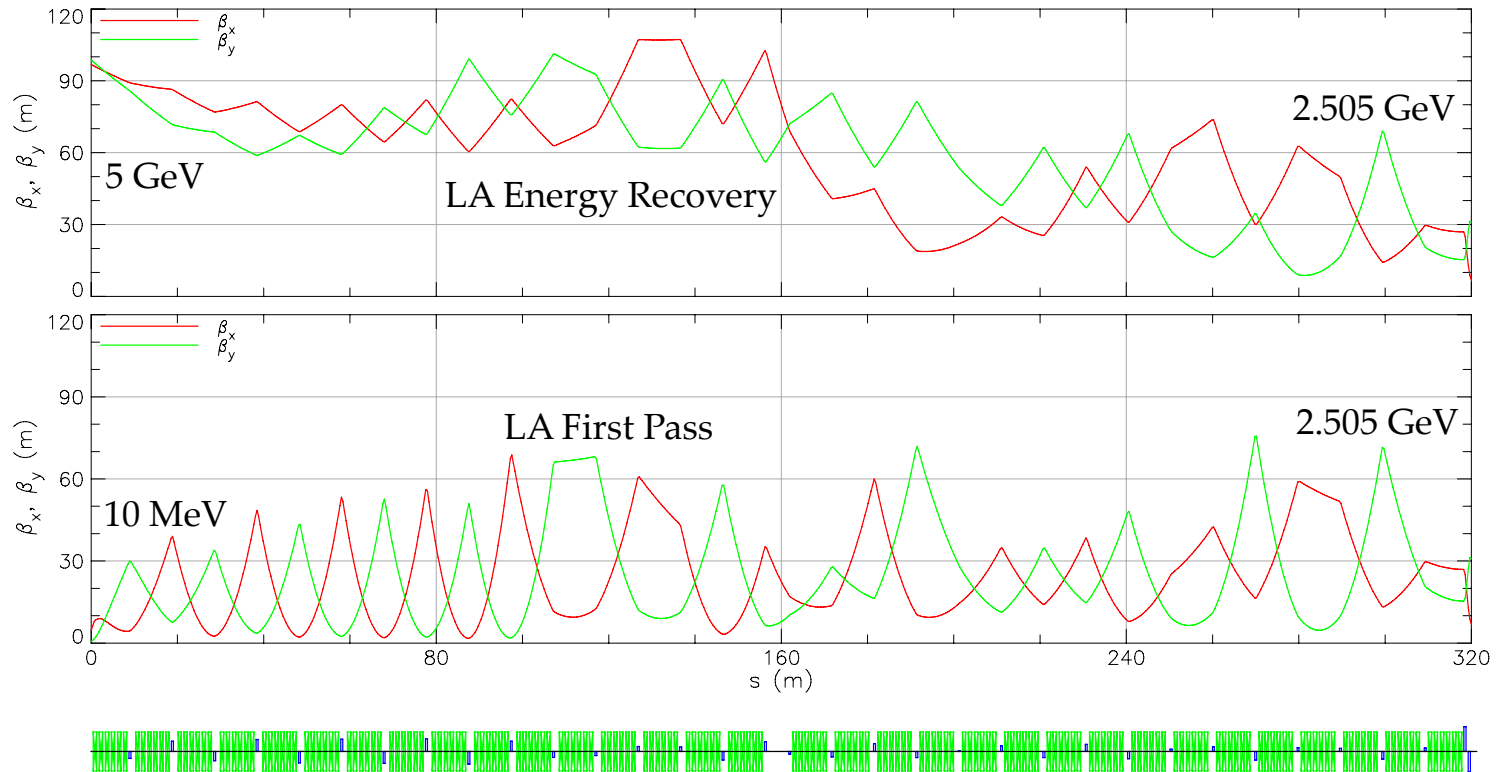


Figure 3.7: Beta functions for the first pass (accelerating) beam and energy recovery (decelerating) beam in LA. This is essentially the mirror image of the optics for LB shown in Fig. 3.6

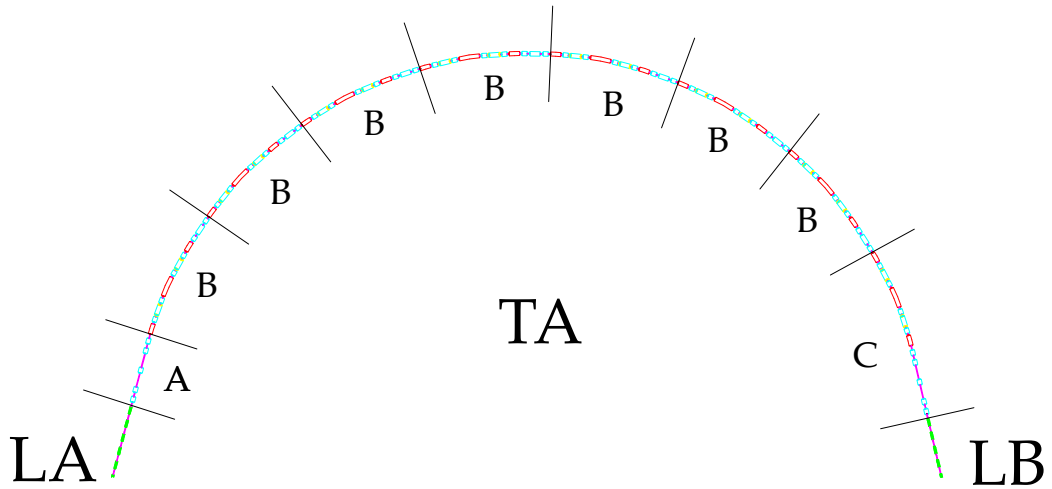


Figure 3.8: Layout for the TA. This section is divided into three

3.2.2 Turnaround Arc

The purpose of the TA is to connect LA to LB and reverse the slope of the beta functions, according to the scheme in Fig 3.4. In order to deliver zero dispersion to LB, this section is made to be achromatic to second order. Additionally, to control the bunch length and to aid efficient energy recovery (further described in Section 3.4), the time of flight terms r_{56} and t_{566} are set to zero, making the section isochronous to second order.

The TA layout is shown in Fig. 3.8. It is partitioned into three types of sections, called Cells:

Cell A Straight section with five quadrupole magnets, matches Twiss parameters from LA into Cell B

Cell B Periodic section containing a three-bend isochronous achromat – occurs seven times

Cell C The mirror image of Cells A and B, matches Twiss parameters into LB

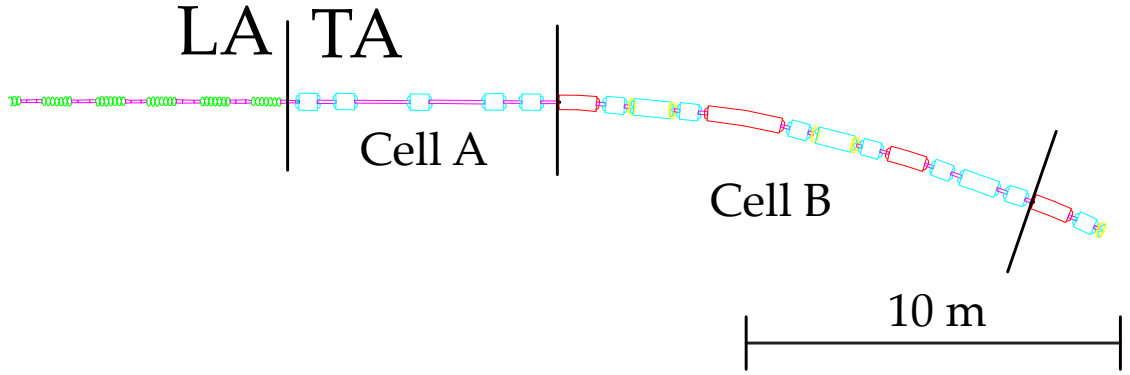


Figure 3.9: The layout for the beginning of the MERL TA, showing the cell partitions.

The bulk of the TA is built out of Cell B sections, so most of the effort in optimizing the TA is focused a single such section. The beta functions are required to be periodic, so that many sections can be linked together. Once a good Cell B optics is found, the five quadrupole strengths in Cell A are varied to match the Twiss parameters from LA into the first Cell B. Because of the symmetry, Cell C quadrupole strengths can be set to the mirror image of those from Cell A and the first Cell B, and will automatically end with the correct Twiss parameters for LB. Note that there are a total of eight sets of three-bend isochronous achromats in the TA.

The layout and optics for Cell A and the first Cell B are shown in Fig. 3.9 and Fig. 3.10, respectively. The linear optics in Cell B are optimized by varying the nine quadrupole strengths. For simplicity these strengths are varied in pairs symmetric about the center bend, so effectively there are only five variables. To make the section achromatic, we demand that the dispersion $r_{16} = 0$ and its slope $r_{26} = 0$ at the end of the third bend. To make the section isochronous, we demand that $r_{26} = 0$ and $r_{56} = 0$ in the center of the middle bend. Finally, we demand that the radiative emittance growth, described by Eq. (2.177), be as small as possible.

Also shown in Fig. 3.10 is the second order dispersion t_{166} . This is manipulated by varying the four sextupole strengths in Cell B, and is related to the second order time of flight t_{566} . It would be simplest to make a single Cell B isochronous to second order ($t_{566} = 0$) and achromatic to second order ($t_{166} = 0$, $t_{266} = 0$), but it was found that such constraints demanded very large sextupole strengths. These strengths need not be as large if the achromatic constraint is relaxed for the cell, and so these constraints are replaced by the demand that $t_{266} = 0$ in the center of the eighth quadrupole magnet. Because the layout and strengths are symmetric about this point, sextupole strengths in the following Cell B can be set to those in the reverse ordering of those in the first Cell B, automatically making a pair of Cell B sections isochronous and achromatic to second order.

The optics for the entire TA are shown in Fig. 3.11. There one can see the pairing of the Cell B sections as related to the second order dispersion. The radiative emittance growth and time of flight terms are shown in Fig. 3.12.

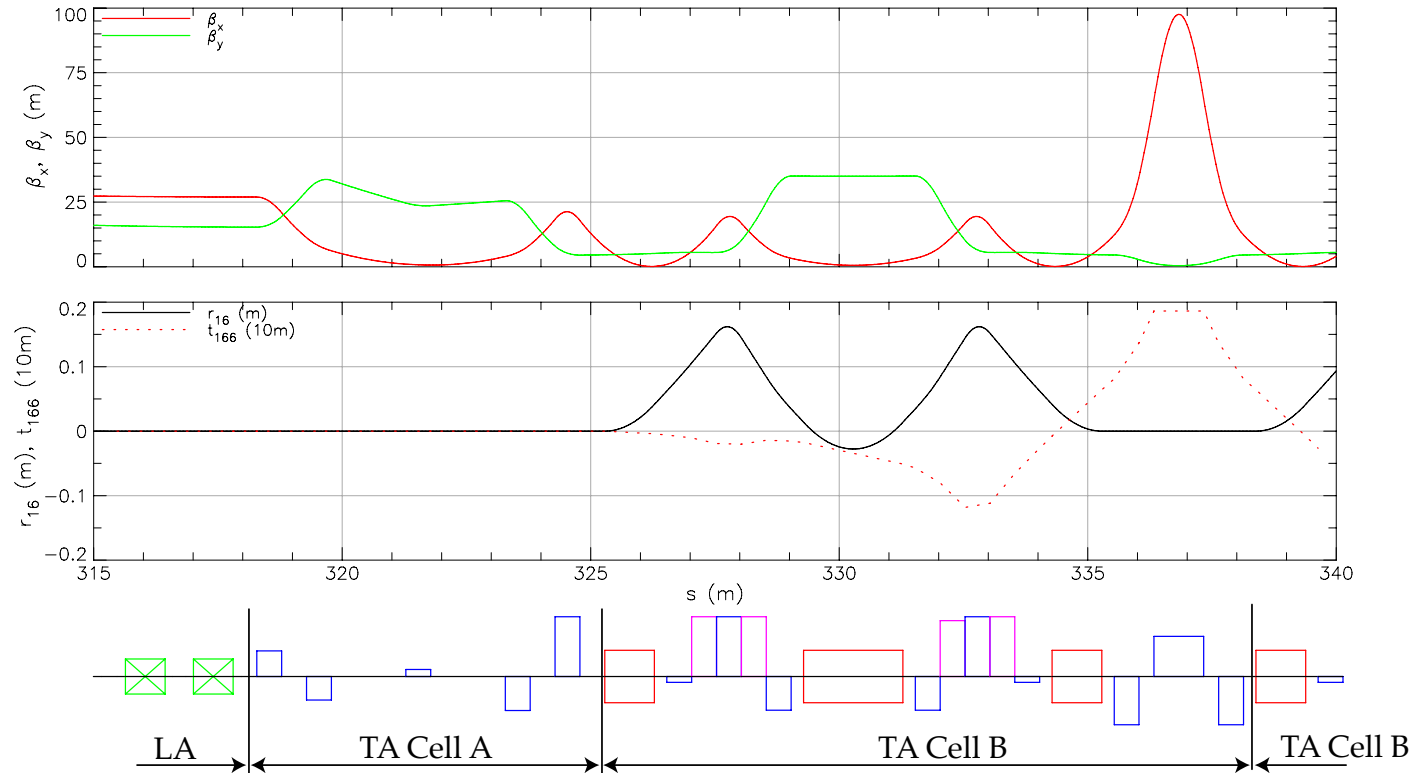


Figure 3.10: Optics for the MERL TA Cell A and first Cell B. Cell B is optimized to have periodic beta functions, to be isochronous, to be achromatic, and to minimize radiative emittance growth by varying nine quadrupole strengths symmetrically about the center of the center dipole magnet. It is made to be isochronous to second order by varying four sextupole strengths, and a pair of Cell B sections is made to be achromatic to second order by making $t_{266} = 0$ in the center of the eight quadrupole, and mirroring sextupole strengths for the following Cell B.

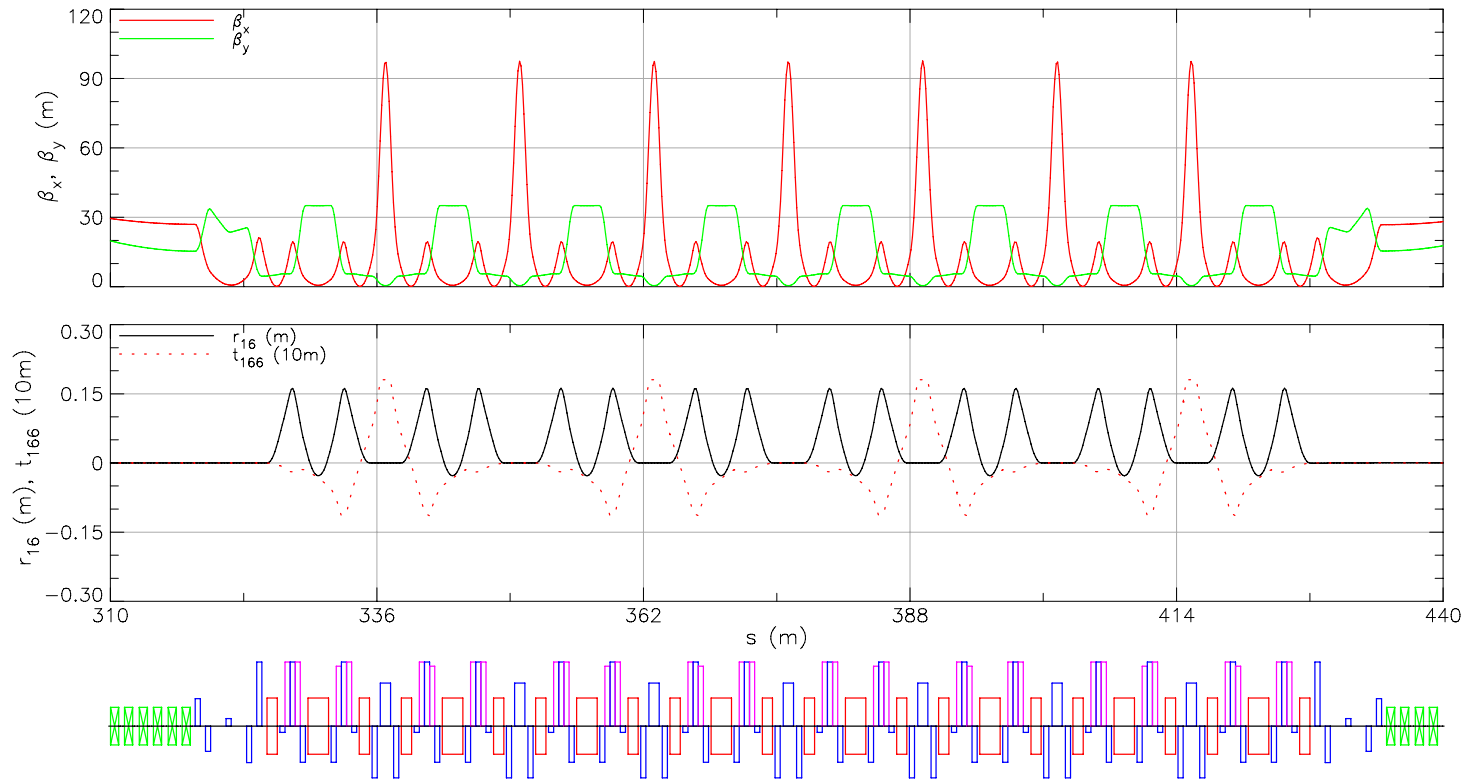


Figure 3.11: Optics for the full MERL TA section. Here one can see that each Cell B is achromatic to first order, and that pairs of Cell B sections are achromatic to second order. One also sees that the exiting beta functions have reversed slopes relative to the entering beta functions, as required by the linac optics scheme in Fig. 3.4.

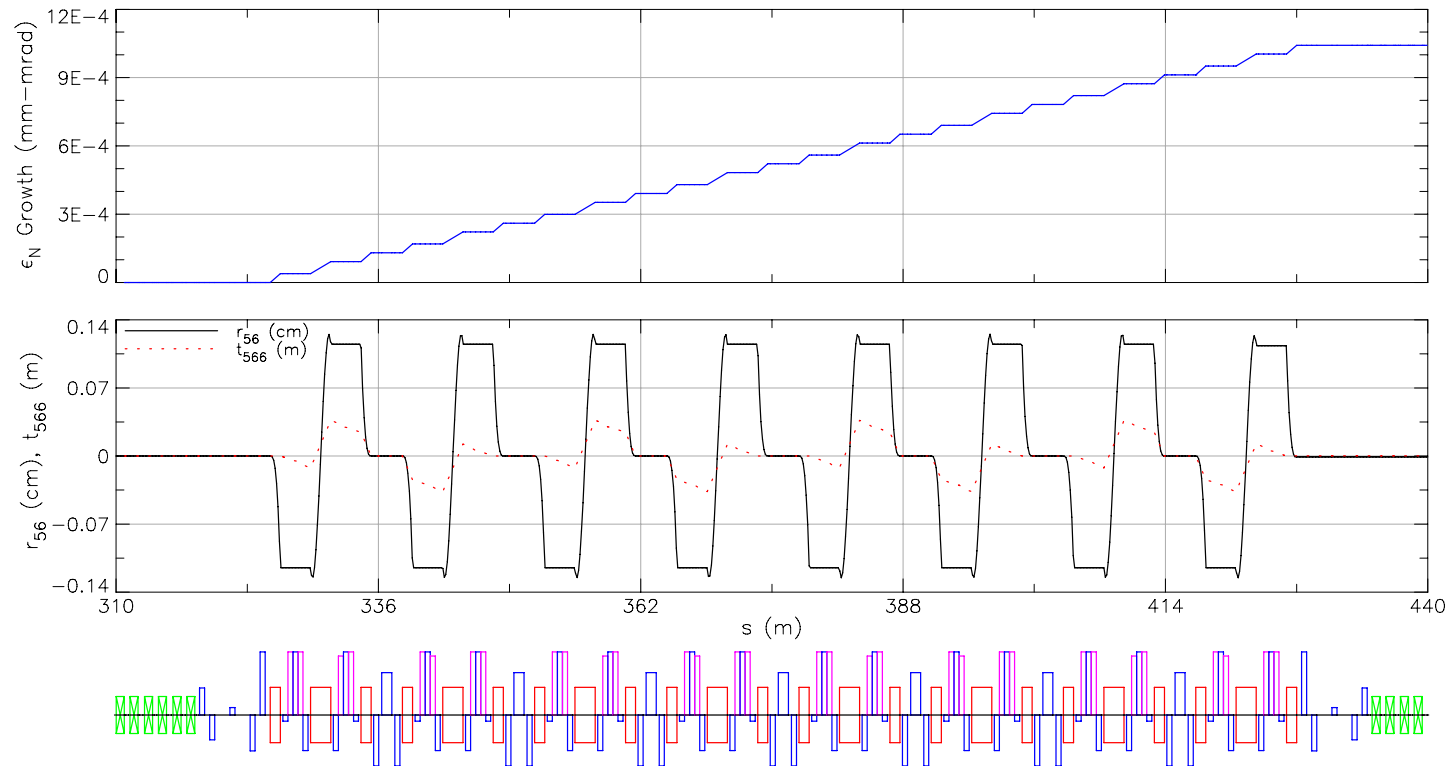


Figure 3.12: Radiative emittance grown and time of flight terms in the full MERL TA section. Here one can see that each Cell B is isochronous to second order. This emittance growth is very small compared to the initial Mode B normalized emittance of 8×10^{-2} mm-mrad.

3.2.3 Return Arc

The RA optics, similar to the TA optics, need to accept the Twiss parameters from LB and reverse the signs of α_x and α_y from the entrance to the end, and furthermore need to be isochronous and achromatic. This section houses all 18 undulators, and the beam quality needs to be preserved through each of them. Additionally, in order to recover the energy from this 5 GeV beam, the total time for the center of a bunch to traverse the RA needs to be adjustable by one period of the fundamental mode of the linacs ($1/f_{\text{rf}}$), so that it will arrive out of phase with LA by π radians. The TA avoids such a problem because the RF phase of LB can be chosen relative to the RF phase of LA. We will assume that these technical challenges will be solved in the machine operation.

The beginning of the RA layout is shown in Fig. 3.8. It is divided into three types of cells:

Cell A Straight section with five quadrupole magnets, matches Twiss parameters from LB into Cell B

Cell B Periodic section containing a three-bend isochronous achromat – occurs eighteen times

Cell C The mirror image of Cell A, matches Twiss parameters into LA for energy recovery

Note that this is similar to the partitioning in the TA, and the same symmetries exist.

The RA Cell B is essentially the same as the TA Cell B, except that the dipole magnet lengths are doubled from (1 m, 2 m, 1 m) to (2 m, 4 m, 2 m), respectively,

in order to reduce the radiation load on the wall. Additionally, a 5 m undulator with quadrupole magnets at the ends replaces the eighth quadrupole magnet, and some of the drifts have changed lengths. The optimization criteria are also nearly the same: $r_{16} = 0$ and $r_{26} = 0$ at the end of the third bend, and $r_{26} = 0$ and $r_{56} = 0$ in the center of the second bend. The second order dispersion is also controlled symmetrically over two cells by sextupole magnets. Note that this is the same section used as an example in Section 2.3.2.

The beta functions are periodic, but unlike the TA Cell B, the RA Cell B has fixed entering Twiss parameters. This is because the Twiss parameters in the undulator are chosen by the X-ray user. For baseline values we will assume them to be half the length of the undulator; that is, $\beta_x = \beta_y = 2.5$ m and $\alpha_x = \alpha_y = 0$ in the center of the undulator. Because the undulator to first order basically behaves like a drift, these values can be propagated to the beginning of the cell using Eq. (2.93), giving the entering Twiss parameters as $\beta_x = \beta_y = 6.1$ m and $\alpha_x = \alpha_y = 1.2$.

The optics for Cell A and two Cell B sections are shown in Fig. 3.14. The optics for the entire RA are shown in Fig. 3.15, with the radiative emittance growth and time of flight terms shown in Fig. 3.16.

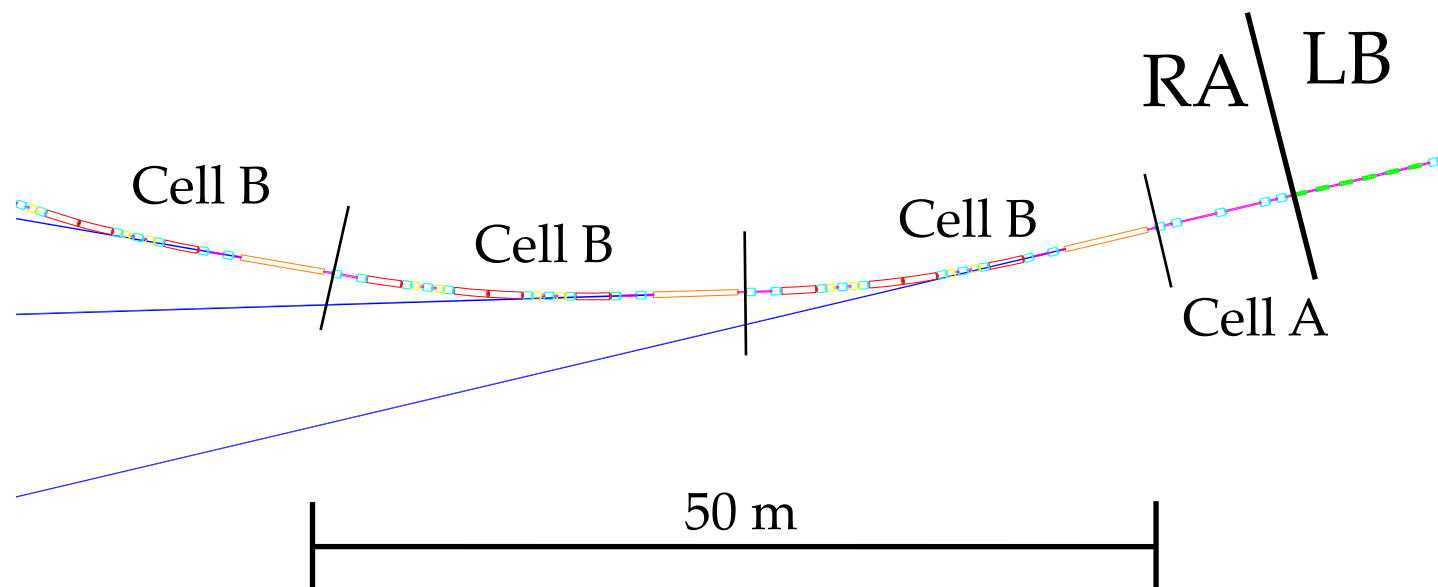


Figure 3.13: The layout for the beginning of the MERL RA, which contains 18 undulators. The blue lines are 80 m long and represent the X-ray beamlines projecting out of the undulators.

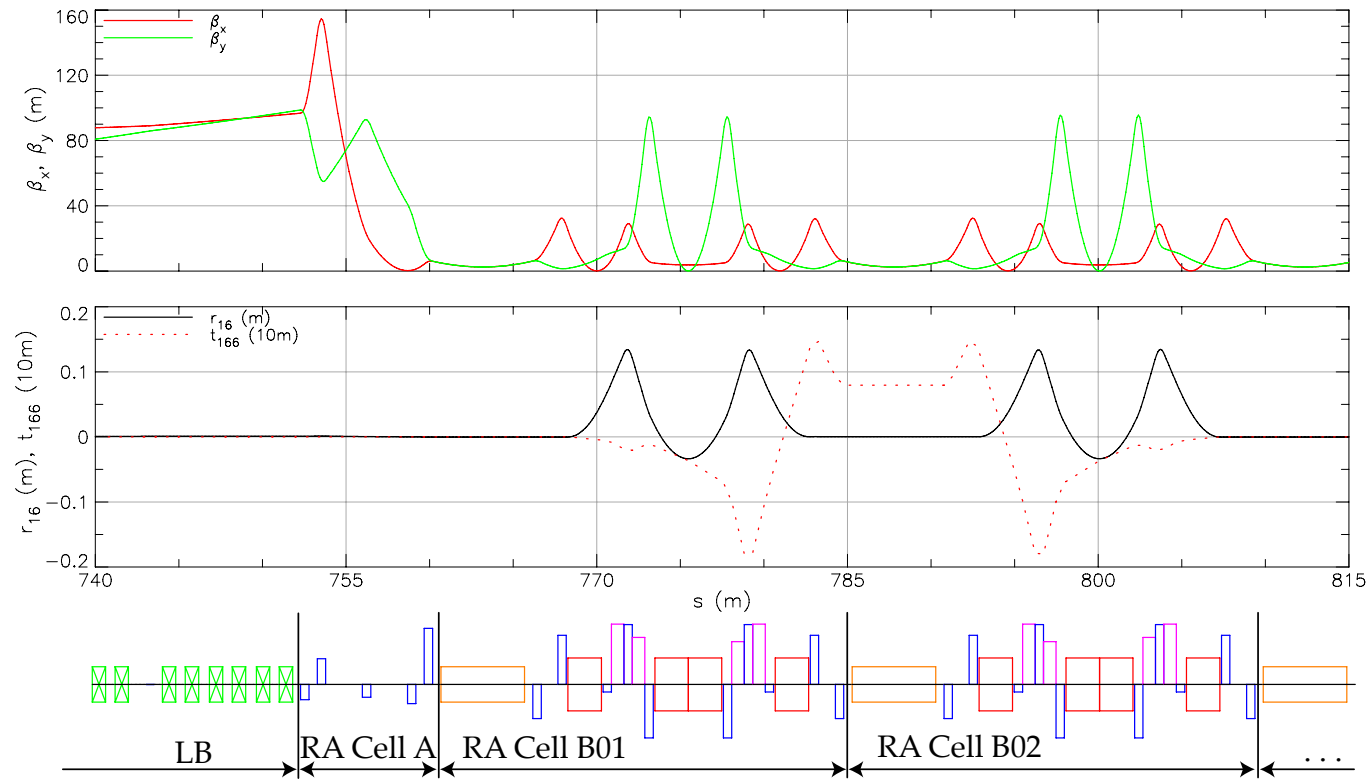


Figure 3.14: Optics for the MERL RA Cell A and two Cell B sections. The five quadrupole magnets in Cell A are used to match the exiting Twiss parameters from LB into Cell B. The Twiss parameters in the beginning and end of Cell B are fixed by the Twiss parameters in the center of the undulator. Cell B is further made to be achromatic and isochronous by requiring that $r_{56} = 0$ and $D' = 0$ in the center of the center bend, and mirroring quadrupole strengths about this point. The second order dispersion is controlled by the sextupole magnets to make a pair of Cell B sections achromatic and isochronous to second order.

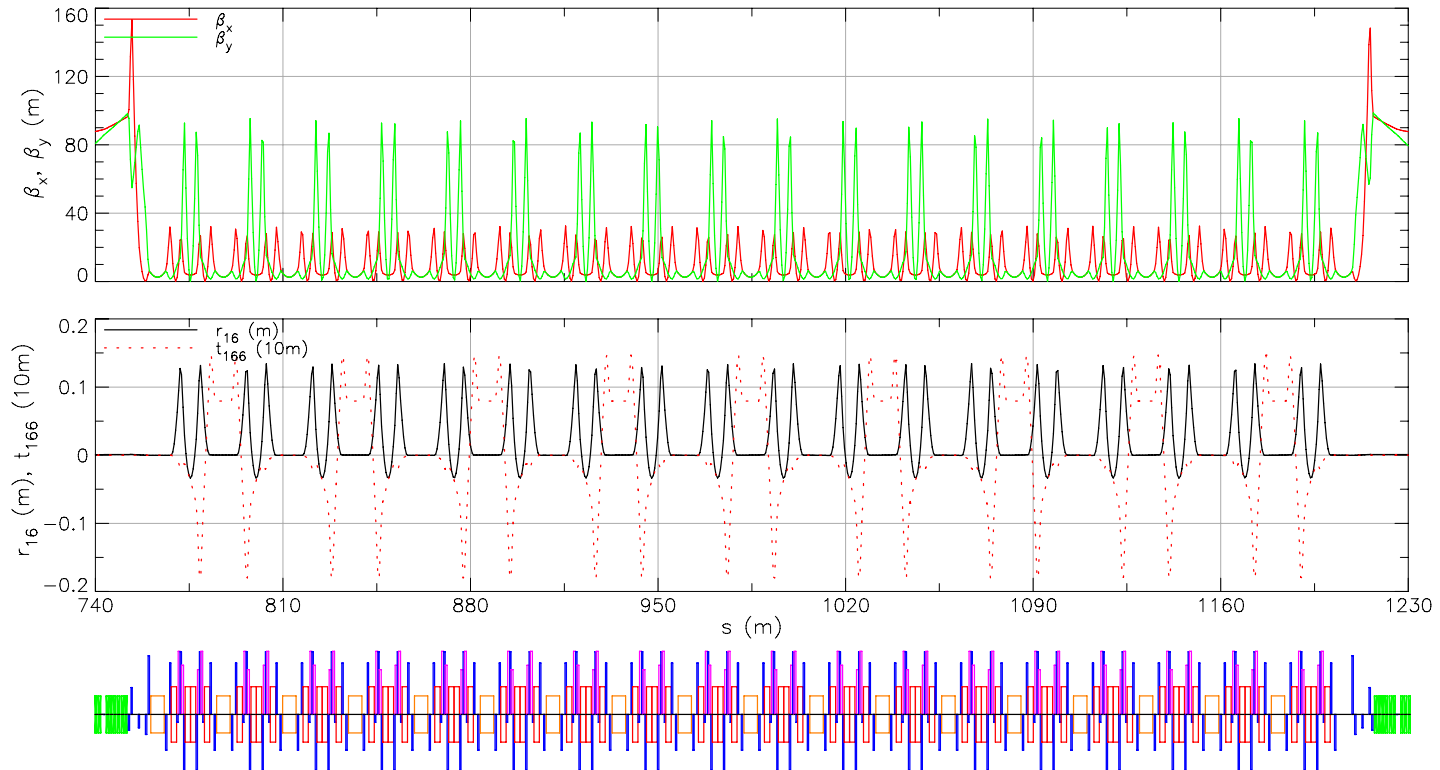


Figure 3.15: Optics for the MERL Return Arc

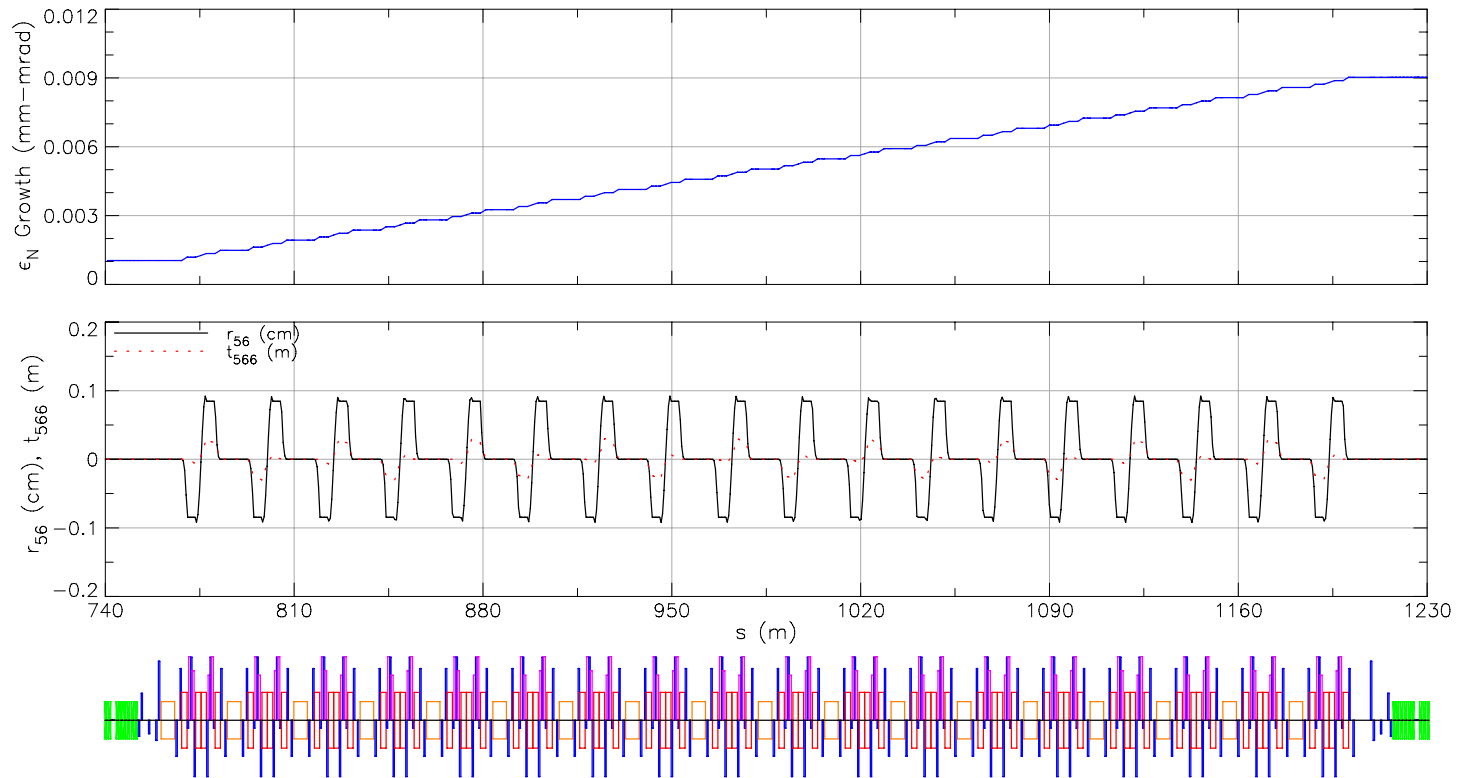


Figure 3.16: Radiative Emittance Growth and Time of Flight terms in the MERL RA.

3.3 Particle Tracking

Much effort has been taken in designing a lattice that controls the Twiss parameters, dispersion, and time of flight terms in the lattice. The emittance in Eq. (2.100), however, is only invariant for linear transformations. To verify that nonlinear terms do not ruin the initial emittance, we employ the method of tracking particles through the lattice.

As mentioned in Section 2.3.1, *Bmad* has the ability to track particles element by element through the lattice. Each element is treated as a truncated Taylor map of phase space coordinates, and particles are propagated through these elements by applying the maps in the appropriate order. At each element, statistics such as emittance and bunch length are computed and saved.

The initial distribution, for simplicity, is taken to be a Gaussian in the horizontal, vertical, and longitudinal phase space planes. Each transverse phase space is furthermore generated to match the phase space ellipse shown in Fig. 2.4 for the appropriate Twiss parameters.

In practice, it is impossible to simulate all of the particles in a typical bunch, the number of which can be on order of billions. Therefore we take a fraction of these particles to represent a bunch. This can be either be done by taking equally weighted particles and distributing them in phase space randomly according to the desired distribution, or by placing particles in phase space, and then differently weighting them according to the distribution. Both methods are useful, but the latter has the advantage of sampling more of the outlying particles. Such a method is shown in Fig. 3.17, in which particles in the horizontal, vertical, and longitudinal phase spaces are placed on discrete ellipses sampling

the bunch out to three standard deviations in each dimension.

These particles at the beginning and end of the RA are shown in Fig. 3.18. At the beginning of the RA, we see that the longitudinal phase space takes on the characteristic shape of an on-crest distribution through a linac, previously seen in Fig. 2.5. The horizontal phase space looks relatively unperturbed, while the vertical phase space shows the signs of **chromaticity**, meaning that particles with different energies have different phase advances. Particles at the end of the RA are more noticeably disturbed, indicating that there may be some emittance growth.

The calculated horizontal and vertical widths σ_x and σ_y for these particles through the RA are shown in Fig. 3.20, along with the normalized horizontal and vertical emittances. These quantities show some marginal increases as particles advance through the arc, with the vertical phase space suffering slightly more than the horizontal phase space. Normalized emittances and energy spread through the entire MERL are shown in Fig. 3.21. The bunch widths and length are shown in Fig. 3.22.

The particles at the end of the MERL are shown in Fig. 3.19, calculated with and without the sextupole magnets turned on. Here we pleasantly find that turning off the sextupole magnets results in negligible emittance growth through the lattice. The cost is a small increase in energy spread.

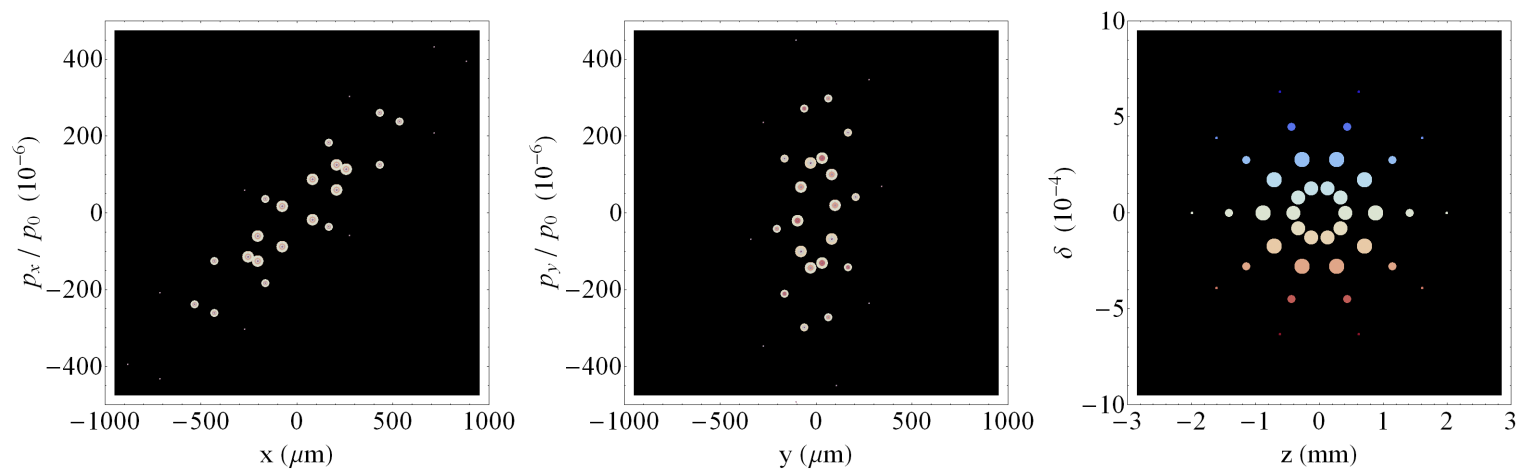


Figure 3.17: Phase space slices of the initial particle distribution used in the MERL. The colors represent different energies, with blue being higher and red being lower than the reference particle energy. The sizes of the particles in these plots are indicative of their sampling weight. Note that particles “overlap” in these plots, masking the fact that there are 36,000 particles present.

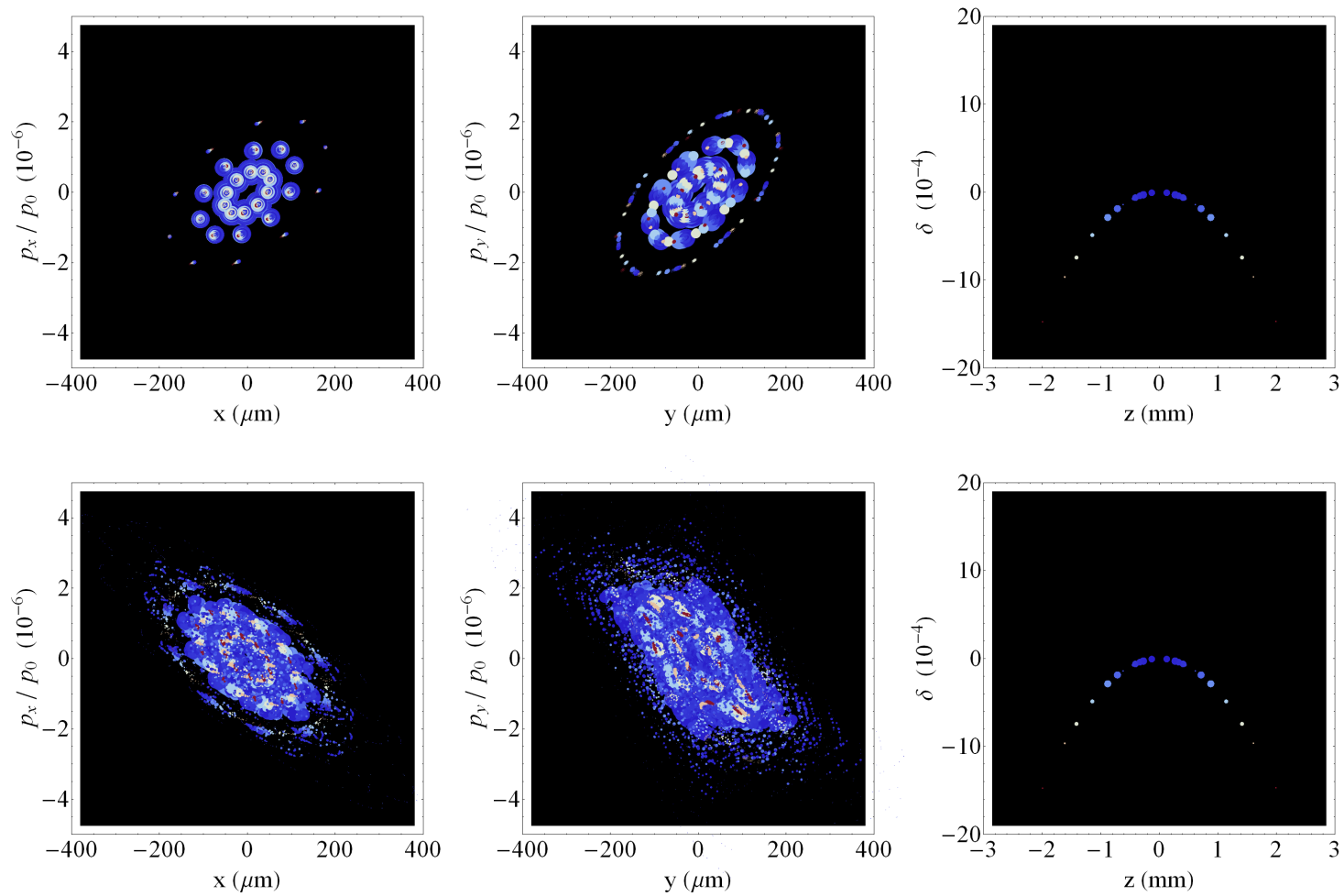


Figure 3.18: MERL Mode A phase space slices for particles at the beginning of the RA (top row), and at the end of the RA (bottom row).

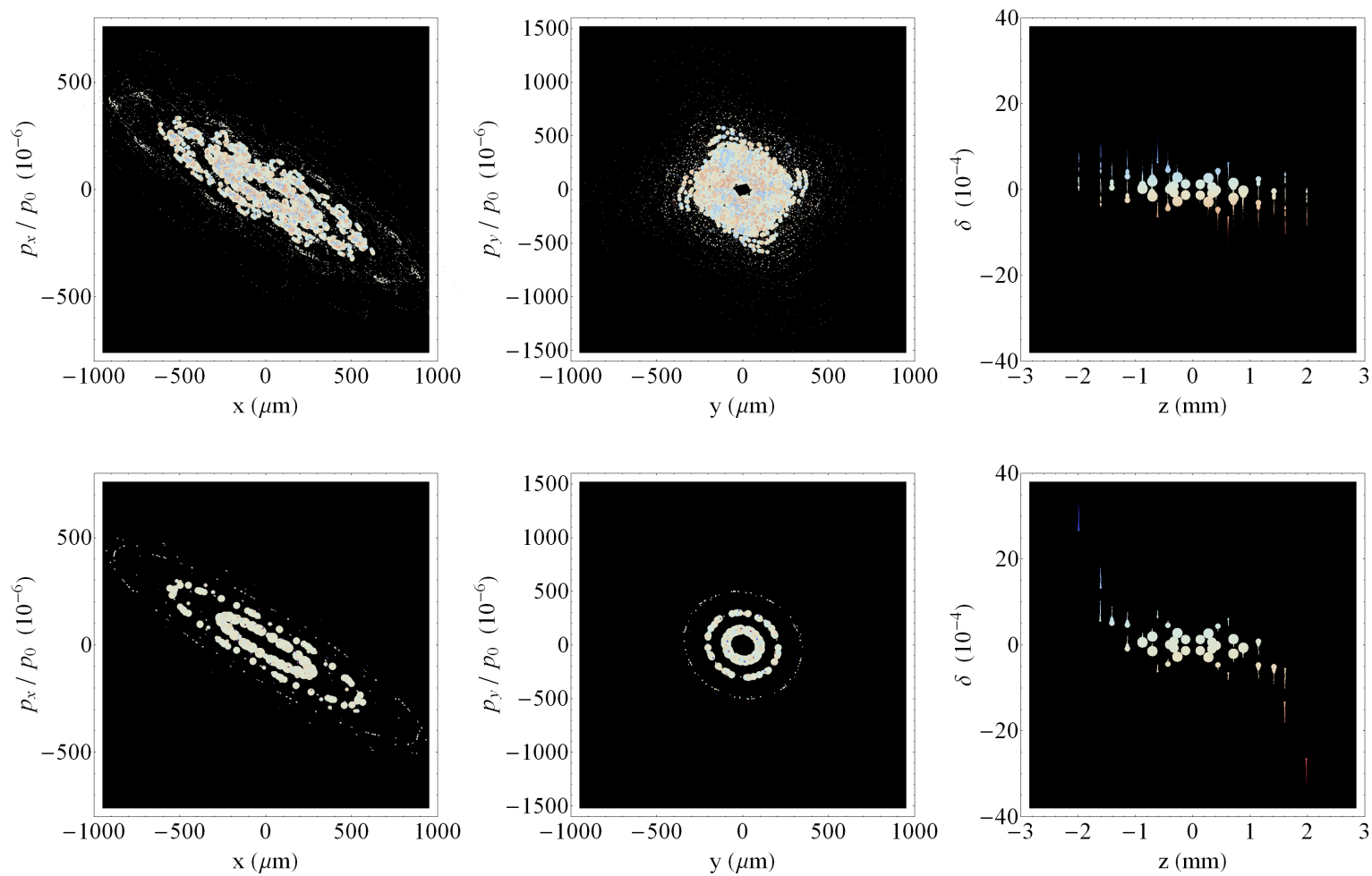


Figure 3.19: Particles at the end of the MERL. The top row is with sextupoles on, and the bottom row is with sextupoles off.

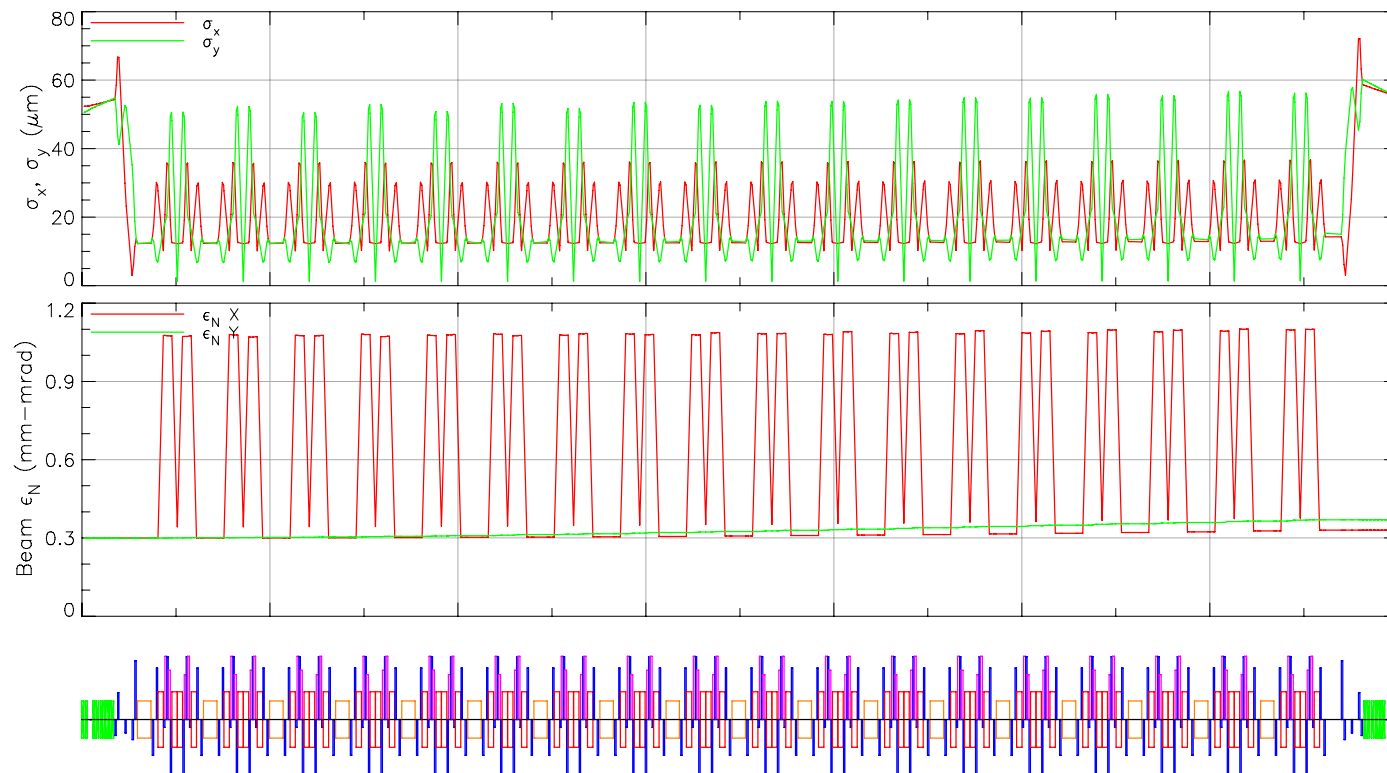


Figure 3.20: Bunch widths and normalized emittances through the RA, calculated using an initial distribution shown in Fig. 3.17.

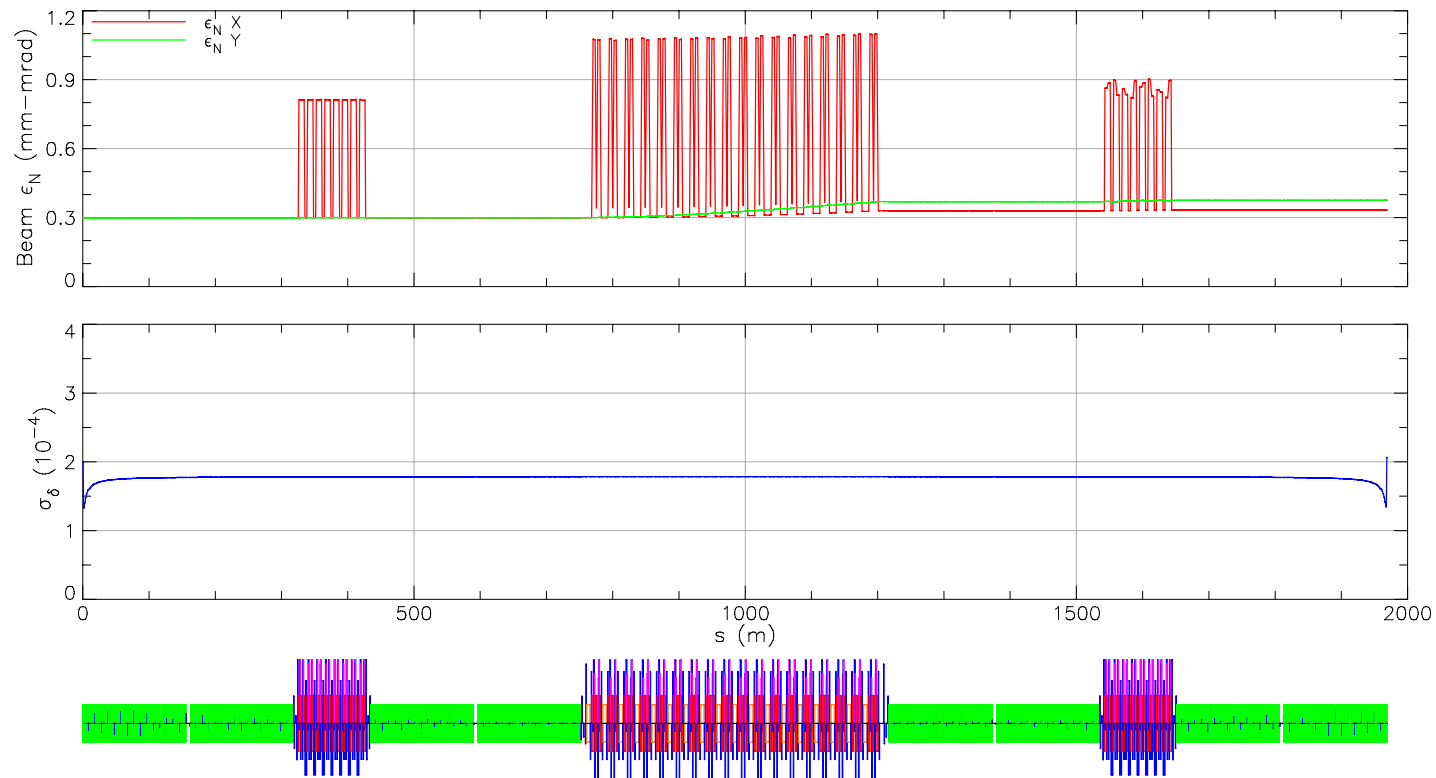


Figure 3.21: MERL normalized emittances and energy spread from particle tracking, using an initial distribution shown in Fig. 3.17.

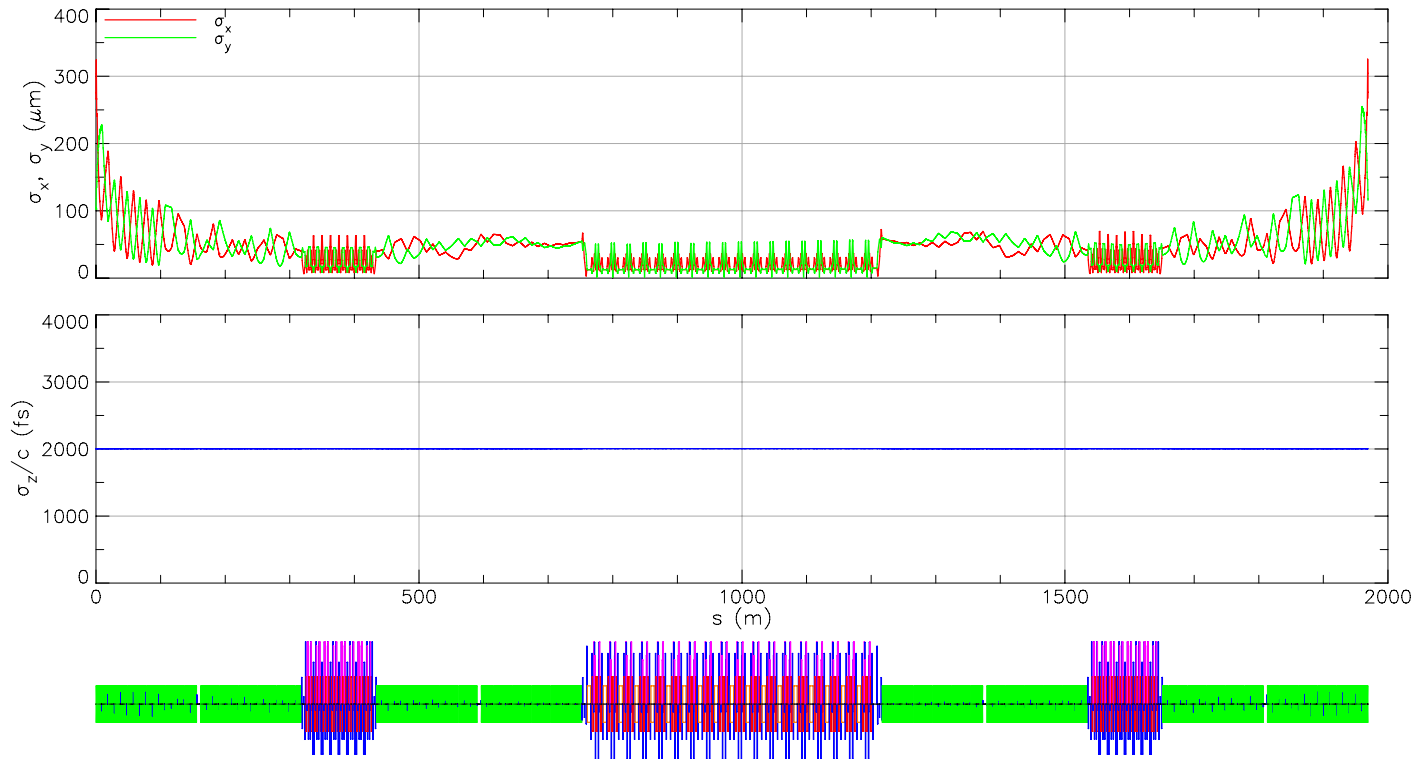


Figure 3.22: MERL bunch widths and bunch length from particle tracking, using an initial distribution shown in Fig. 3.17.

3.4 Time of Flight in ERL Arcs

A linac does not accelerate all particles uniformly, and likewise does not decelerate particles uniformly. When an ERL is built out of linacs connected by arcs, care must be taken to insure that all particles in a bunch arrive at the beginning of each linac with the correct phases in order to achieve maximum efficiency. To make this happen, the TA and RA are ideally isochronous, and designed to be so to second order in Sections 3.2.2 and 3.2.3. This section will examine how precisely isochronous these arcs must be.

From Eq. (2.118), the longitudinal phase space coordinates (z_1, δ_1) at the end of a linac given initial coordinates (z_0, δ_0) at the beginning of the linac are

$$z_1 = z_0, \quad (3.3)$$

$$\delta_1 = \left[1 - \frac{\mathcal{E}_0}{\mathcal{E}_1} \right] \left[\frac{\cos(\phi_{\text{rf}} - k_{\text{rf}} z_0 + \phi_{\text{error}})}{\cos \phi_{\text{rf}}} - 1 \right] + \frac{\mathcal{E}_0}{\mathcal{E}_1} \delta_0, \quad (3.4)$$

where a possible phase error ϕ_{error} has been added, representing an error in the arrival time of the center of a bunch with respect to the ideal accelerating wave. An arc, on the other hand, evolves initial coordinates (z_0, δ_0) according to Eq.(2.163) as

$$z_1 = z_0 + r_{56} \delta_0 + t_{566} \delta_0^2 + u_{5666} \delta_0^3 + \dots, \quad (3.5)$$

$$\delta_1 = \delta_0, \quad (3.6)$$

which includes a possible third order time of flight term u_{5666} . Synchrotron radiation losses have been neglected for simplicity.

Successful energy recovery can be quantified by requiring the distribution of energy deviations to have $\max |\delta| < 0.5$ at the dump. These energy deviations are straightforwardly calculated by successive maps of Eqs. (3.3–3.4) through

the linacs and Eqs. (3.5–3.6) through the arcs, starting with coordinates $(z, \delta)_{\text{IN}}$ at the injector and ending with coordinates $(z, \delta)_{\text{DU}}$ at the dump. When there are no linac phase errors, and the arcs are isochronous to all orders, then this map is simple: $(z, \delta)_{\text{DU}} = (z, \delta)_{\text{IN}}$. The maximum absolute energy deviation will then be on the order of $3 \times \sigma_{\delta 0}$, where $\sigma_{\delta 0}$ is the injected energy spread.

In the MERL, all bunches are to be injected with a bunch length $\sigma_{z0} = (2c)$ ps and energy spread $\sigma_{\delta 0} = 2 \times 10^{-4}$. Perfect linac phases and perfectly isochronous arcs therefore result in final energy deviations well within the 50% range at the dump. When the arcs are imperfectly isochronous, the energy deviation at the dump can be expanded for small injected particle position z_{IN} and small ϕ_{rf} , giving

$$\delta_{\text{DU}} = \left[\left(\frac{\mathcal{E}_{\text{TA}}}{\mathcal{E}_{\text{IN}}} + \frac{\mathcal{E}_{\text{IN}}}{\mathcal{E}_{\text{TA}}} - 2 \right) k_{\text{rf}} r_{\text{TA}} + \left(\frac{\mathcal{E}_{\text{RA}}}{\mathcal{E}_{\text{IN}}} + \frac{\mathcal{E}_{\text{IN}}}{\mathcal{E}_{\text{RA}}} - 2 \right) \frac{1}{2} k_{\text{rf}} r_{\text{TA}} \right] \times \left[3 \phi_{\text{rf}} k_{\text{rf}}^2 z_{\text{IN}}^2 - k_{\text{rf}}^3 z_{\text{IN}}^3 \right] + \dots, \quad (3.7)$$

where r_{TA} and r_{RA} represent the r_{56} terms for the linear maps of the TA and RA, respectively. The ratio $\mathcal{E}_{\text{RA}}/\mathcal{E}_{\text{TA}} \simeq 2$, and the ratio $\mathcal{E}_{\text{RA}}/\mathcal{E}_{\text{IN}} \gg 1$, so this equation is approximately

$$\delta_{\text{DU}} \simeq \frac{1}{2} \frac{\mathcal{E}_{\text{RA}}}{\mathcal{E}_{\text{IN}}} (k_{\text{rf}} r_{\text{RA}} + k_{\text{rf}} r_{\text{TA}}) \left(3 \phi_{\text{rf}} k_{\text{rf}}^2 z_{\text{IN}}^2 - k_{\text{rf}}^3 z_{\text{IN}}^3 \right) \quad (3.8)$$

This implies that particles with $|z_{\text{IN}}| \leq 3 \times \sigma_{z0}$ will end up within the 50% energy spread range at the dump as long as

$$|r_{\text{TA}} + r_{\text{RA}}| \lesssim \frac{1}{54} \frac{\mathcal{E}_{\text{IN}}}{\mathcal{E}_{\text{RA}}} \frac{1}{k_{\text{rf}}^3 \sigma_{z0}^2 (|\phi_{\text{rf}}| + k_{\text{rf}} \sigma_{z0})} \quad (3.9)$$

Note that $k_{\text{rf}} \sigma_{z0} \approx 1.6 \times 10^{-2}$ corresponding to approximately 0.94° , and $\mathcal{E}_{\text{IN}}/\mathcal{E}_{\text{RA}} = 1/500$. When all bunches are synchronized with $\phi_{\text{rf}} = 0$ for both linacs, then Eq. (3.9) implies that $|r_{\text{RA}} + r_{\text{TA}}| \lesssim 31$ cm. This can be seen in Fig. 3.23,

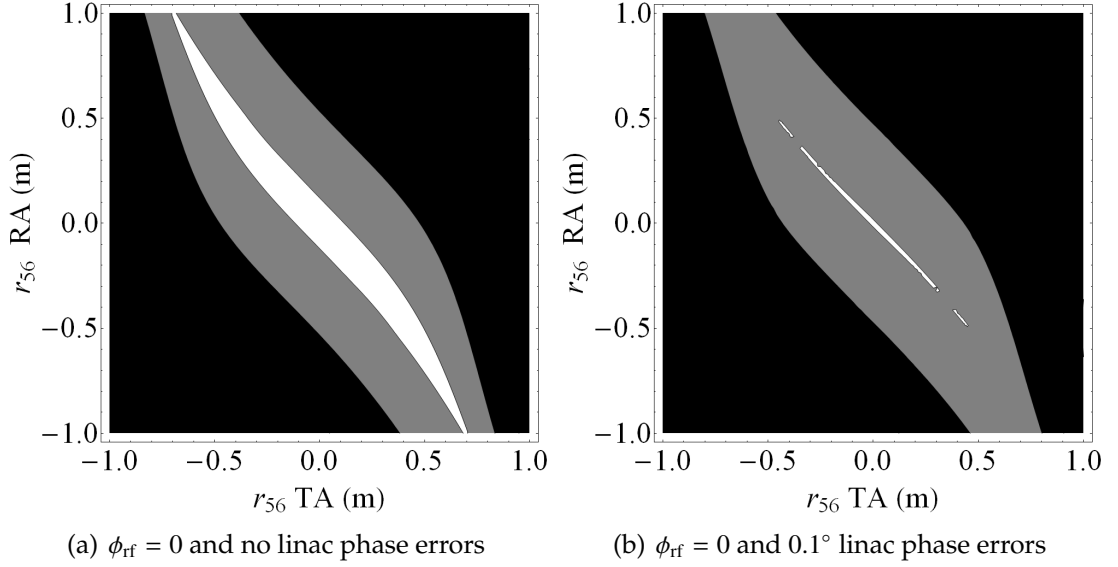


Figure 3.23: Maximum absolute energy deviation at the dump for combinations of r_{56} in the TA and RA, assuming an injected bunch with particles $z_{IN} \in [-3\sigma_{z0}, 3\sigma_{z0}]$. The white area indicates $\max |\delta_{DU}| < 0.1$, the gray area indicates $0.1 < \max |\delta_{DU}| < 0.5$, and the black area indicates $\max |\delta_{DU}| > 0.5$. Figure 3.23(a) is without linac phase errors, and Fig. 3.23(b) is with all possible combinations of 0.1° phase errors, defined in Eq. (3.4).

which shows the maximum energy deviations for different combinations of r_{RA} and r_{TA} with no higher order time of flight terms. This figure also includes the possibility of 0.1° phase errors in all both passes of a bunch through the linacs. When both $r_{RA} = 0$ and $r_{TA} = 0$, one must examine the degree that the second order time of flight terms need to be controlled. This is shown for $\phi_{rf} = 0$ in Fig. 3.24, which is essentially the same as Fig. 3.23 but for t_{566} instead of r_{56} terms. This indicates that t_{566} terms should be controlled to be within 150 m. A separate calculation shows that we must have all $\phi_{error} \lesssim 0.6^\circ$ even when the arcs are perfectly isochronous.

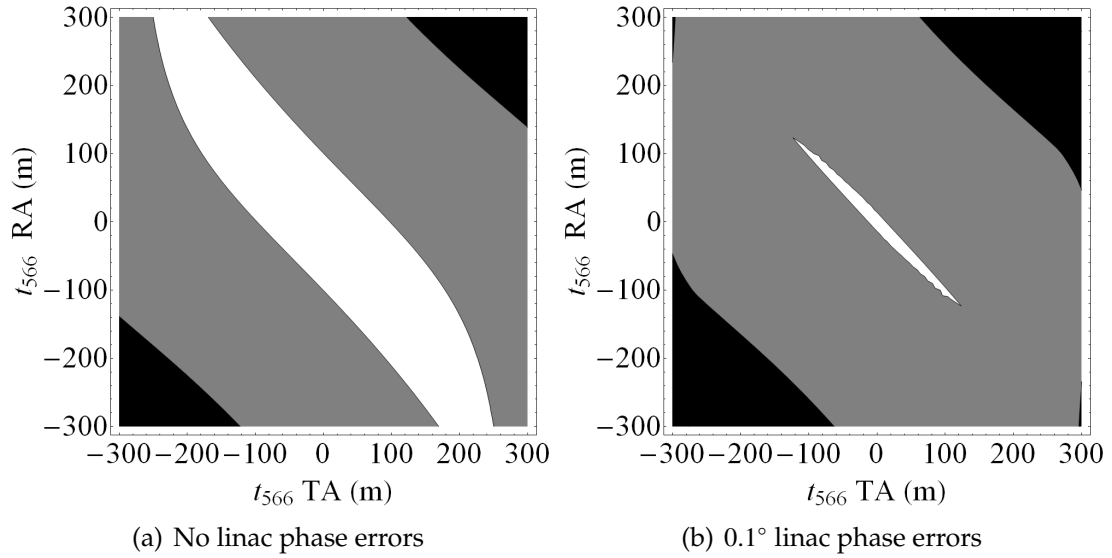


Figure 3.24: Similar to Fig. 3.23, but for t_{566} terms in the TA and RA, assuming all $r_{56} = 0$.

When operating at $\phi_{rf} \neq 0$, the range of allowed time of flight terms in the arcs becomes more restricted. Figure 3.25 shows the allowed ranges for r_{56} and t_{566} in the TA and RA for $\phi_{rf} = 9^\circ$. Equation (3.9) implies that $|r_{RA} + r_{TA}| \lesssim 3$ cm, and the more exact calculation shown in the figure indicates that this absolute sum should be less than 2 cm. When phase errors $\phi_{error} = 0.1^\circ$ are introduced, this value should be less than 0.5 cm.

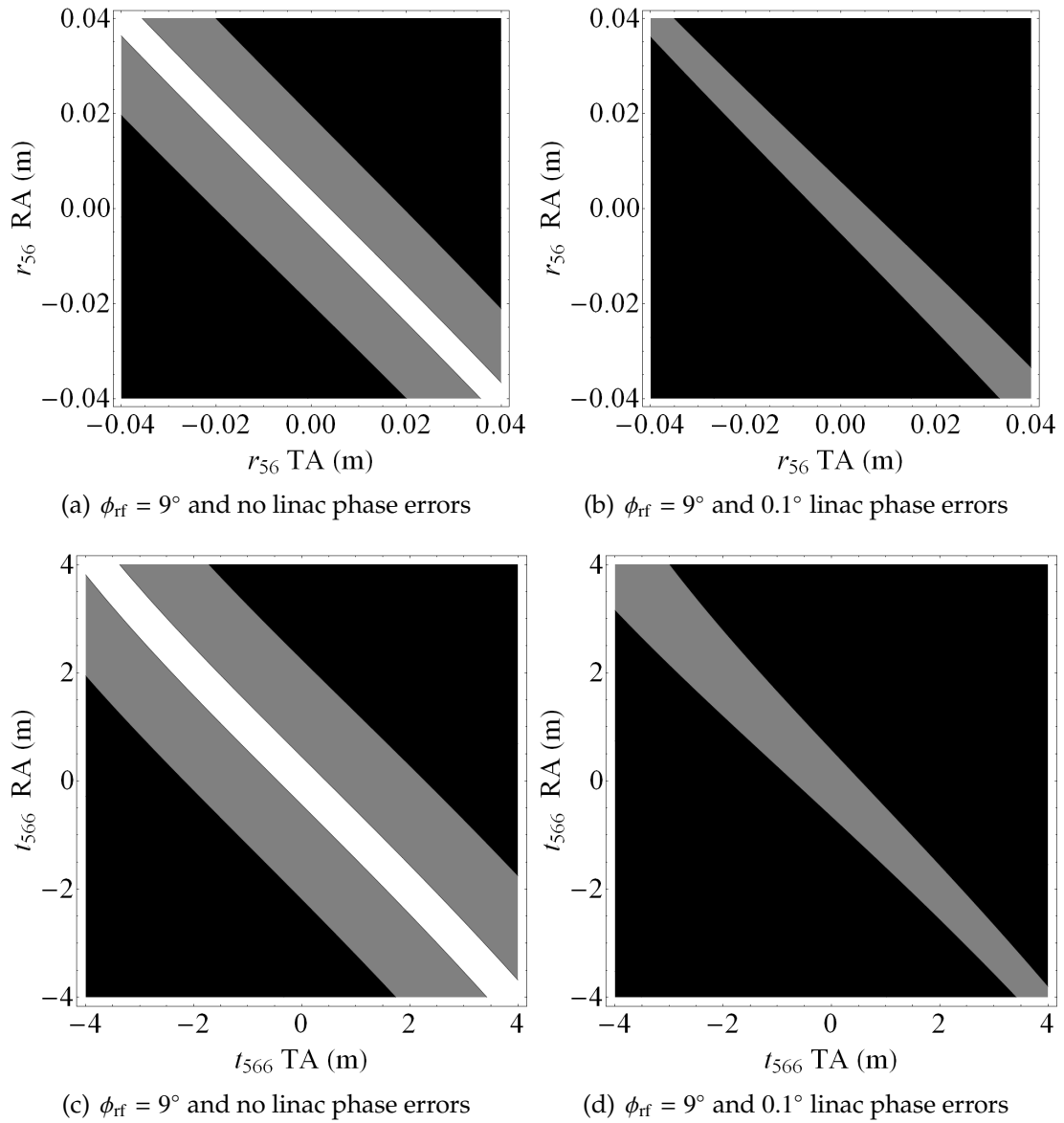


Figure 3.25: The same as Figs. 3.23–3.24, but with $\phi_{rf} = 9^\circ$. Note the much more restricted range of possible r_{56} and t_{566} terms in the TA and RA.

3.5 Bunch Compression

Accelerating bunches off-crest increases the energy spread, requires a higher peak accelerating voltage, and restricts time of flight terms in the TA and RA versus on-crest acceleration. However, off-crest acceleration creates a correlation between z and δ in the longitudinal phase space, which can be taken advantage of with nonzero time of flight terms in an arc to compress the bunch. When sent through undulators, these short bunches emit short pulses of X-rays. This technique is well known, and similar formulas can be found in Bazarov & Hoffstaetter (2003).

To see how this works, consider a single linac and a single arc. The energy deviations at the end of the linac are, according to Eq. (3.4),

$$\delta_1 \simeq \frac{\cos(\phi_{\text{rf}} - k_{\text{rf}} z_0)}{\cos \phi_{\text{rf}}} - 1, \quad (3.10)$$

assuming that $\mathcal{E}_0/\mathcal{E}_1 \ll 0$. Sending these particles through an arc gives modifies the longitudinal positions according to Eq. (3.5) as

$$z_2 \simeq z_1 + r_{56} \left[\frac{\cos[\phi_{\text{rf}} - k_{\text{rf}} z_0]}{\cos \phi_{\text{rf}}} - 1 \right] + t_{566} \left[\frac{\cos[\phi_{\text{rf}} - k_{\text{rf}} z_0]}{\cos \phi_{\text{rf}}} - 1 \right]^2 + \dots \quad (3.11)$$

Now assume that the initial distribution is a Gaussian according to Eq. (2.125), which has moments

$$\langle z_0^2 \rangle = \sigma_{z_0}^2, \quad (3.12)$$

$$\langle z_0^4 \rangle = 3 \sigma_{z_0}^4, \quad (3.13)$$

$$\langle z_0^6 \rangle = 15 \sigma_{z_0}^6 \quad (3.14)$$

⋮

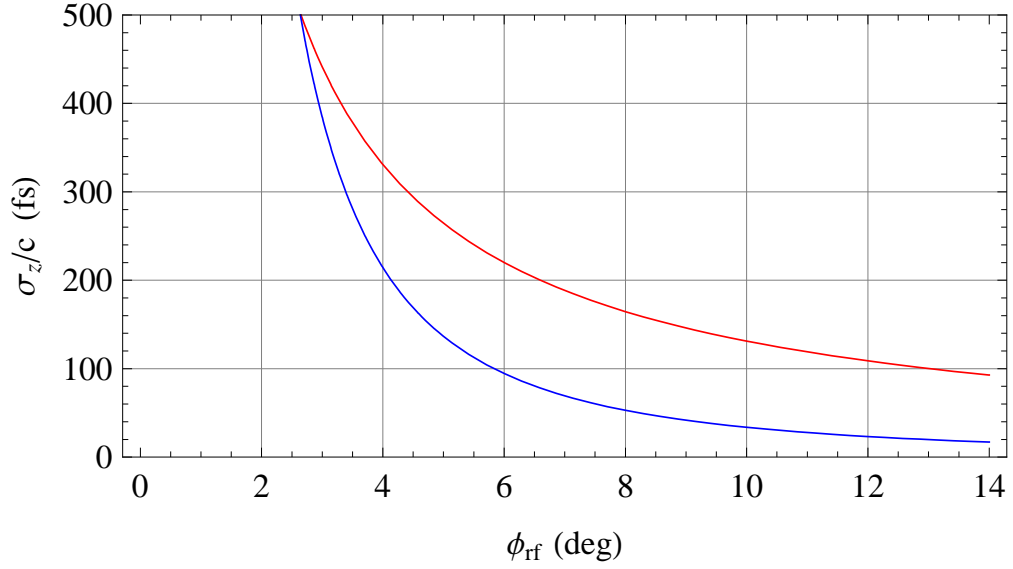


Figure 3.26: The minimum possible bunch length for first order compression (red) and second order compression (blue), assuming that all higher order time of flight terms are zero, versus ϕ_{rf} . The initial distribution has $\sigma_z/c = 2$ ps and the linac operates at $f_{rf} = 1.3$ GHz.

The variance of z_2 in Eq. (3.11) can then be calculated by expanding and averaging in z_0 , resulting in

$$\begin{aligned}
\sigma_{z_2}^2 = & \sigma_{z_0}^2 [1 + k r \tan \phi]^2 \\
& + \sigma_{z_0}^4 \frac{3}{2} k^3 [k r^2 - 2(r + 6 t) \tan \phi - 2 k r (r + 8 t) \tan^2 \phi \\
& + 12 u \tan^3 \phi + 4 k (t^2 + 3 r u) \tan^4 \phi] \\
& + O(\sigma_{z_0}^6)
\end{aligned} \tag{3.15}$$

in which k , ϕ , r , t , u , and are abbreviations for k_{rf} , ϕ_{rf} , r_{56} , t_{566} , and u_{5666} , respectively. One can then choose $r_{56} = -k_{rf}^{-1} \cot \phi_{rf}$ to eliminate the leading term, resulting in a bunch length compressed to first order with a new leading term

$$[\sigma_{z_2}]_{\min 1} \simeq \sqrt{3} k_{rf} \sigma_{z_0}^2 \left| \frac{1}{2} \cot \phi_{rf} + k_{rf} t_{566} \tan^2 \phi_{rf} \right|. \tag{3.16}$$

To compress to second order, one can then choose $t_{566} = -\frac{1}{2 k_{rf}} \cot^3 \phi_{rf}$, resulting in a new

$$[\sigma_{z_2}]_{\min 2} \simeq \sqrt{15} k_{rf}^2 \sigma_{z_0}^3 \left| \frac{1}{6} + \frac{1}{2} \cot^2 \phi_{rf} + k_{rf} u_{5666} \tan^3 \phi_{rf} \right|, \tag{3.17}$$

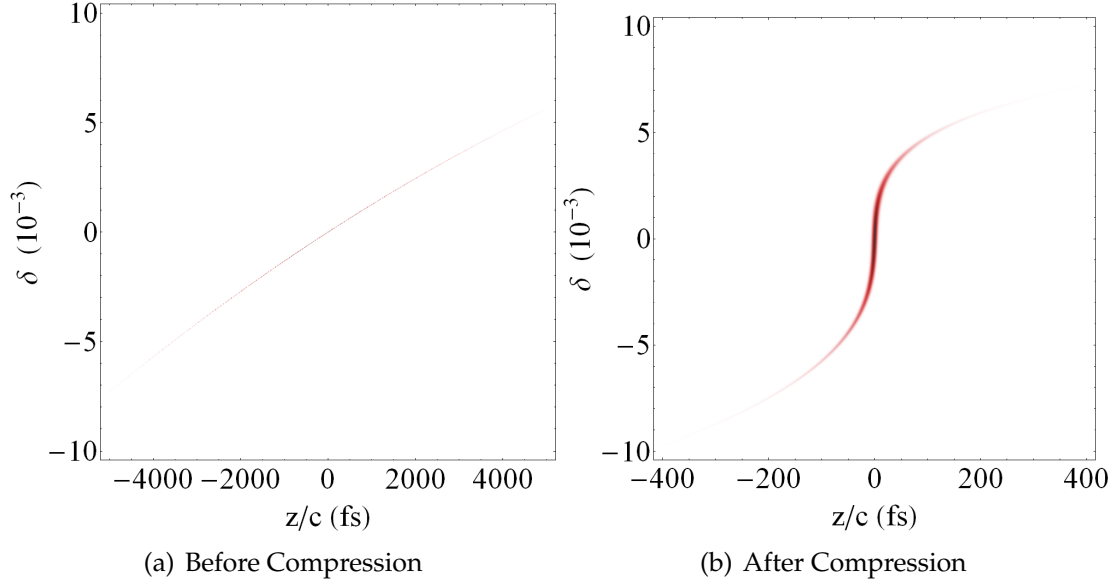


Figure 3.27: Longitudinal phase space before and after second order compression for $\phi_{\text{rf}} = 9^\circ$. The bunch length in Fig. 3.27(a) is 2000 fs, while the bunch length in Fig. 3.27(b) is 100 fs.

and so on. These minimum lengths, assuming $t_{566} = 0$ in Eq. (3.16) and $u_{5666} = 0$ in Eq. (3.17) for MERL parameters are compared in Fig. 3.26.

Similar to Fig. 2.5, the longitudinal phase space density for a compressed bunch can be calculated by inverting $z_2(z_0, \delta_0)$ and $\delta_2(z_0, \delta_0)$, and using Eq. (2.124). The results of the inversion are

$$z_0(z_2, \delta_2) = z_2 - r_{56} \delta_2 - t_{566} \delta_2^2 - u_{5666} \delta_2^3, \quad (3.18)$$

$$\delta_0(z_2, \delta_2) = \frac{\mathcal{E}_1}{\mathcal{E}_0} \delta_2 - \left[\frac{\cos(\phi_{\text{rf}} - k_{\text{rf}}(z_2 - r_{56} \delta_2 - t_{566} \delta_2^2 - u_{5666} \delta_2^3))}{\cos \phi_{\text{rf}}} - 1 \right]. \quad (3.19)$$

This is shown in Fig. 3.27 for $\phi_{\text{rf}} = 9^\circ$ off-crest acceleration, and full compression to second order.

The short bunch mode in the MERL is Mode C from Tab. 3.1, which has $\sigma_z/c = 100$ fs. According to Fig. 3.26, this requires the linac phase to be at least 6° . We will choose $\phi_{\text{rf}} = 9^\circ$, which allows for a range in combinations of r_{56}

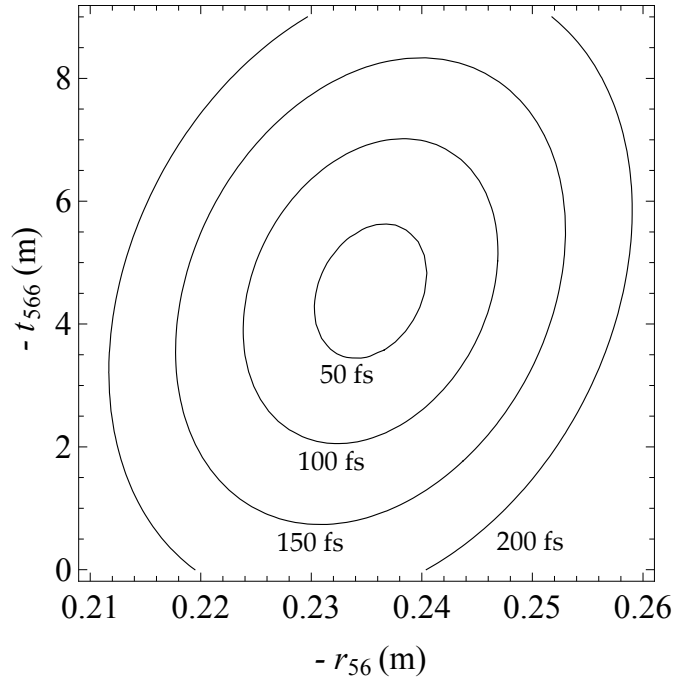


Figure 3.28: Contours of bunch lengths for combinations of r_{56} and t_{566} terms, given the parameters in Fig. 3.26.

and t_{566} terms in an arc to compress the bunch, shown in Fig. 3.28. Practically speaking, it is often easiest to optimize for time of flight terms near zero, so we will choose a point on the bottom left of the 100 fs contour that has $r_{56} = -0.225$ m and $t_{566} = -2.9$ m.

The first four Cell B sections in the RA can be used as a bunch compressor by optimizing them to provide these special time of flight values. This requires large dispersion, because r_{56} is proportional to the integral of the dispersion over the bending radius from Eq. (2.164). The sextupole strengths can further be changed to adjust t_{566} . The eleven undulators following the bunch compression section will then ideally receive the short bunches. To have energy recovery, the last four Cell B sections of the RA must decompress the bunch by exactly reversing the time of flight terms to make the whole of the RA isochronous.

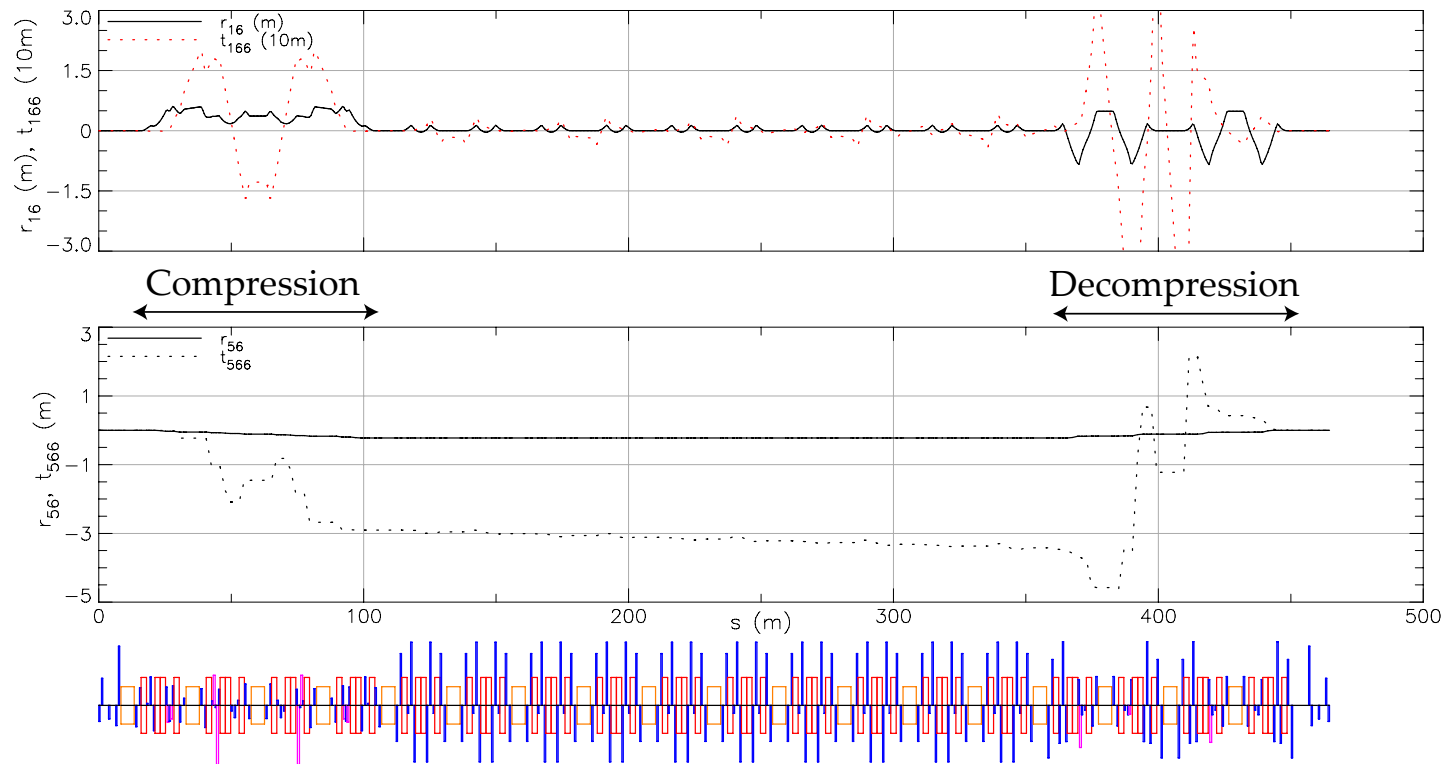


Figure 3.29: Dispersion and time of flight terms in the RA for Mode C bunch compression.

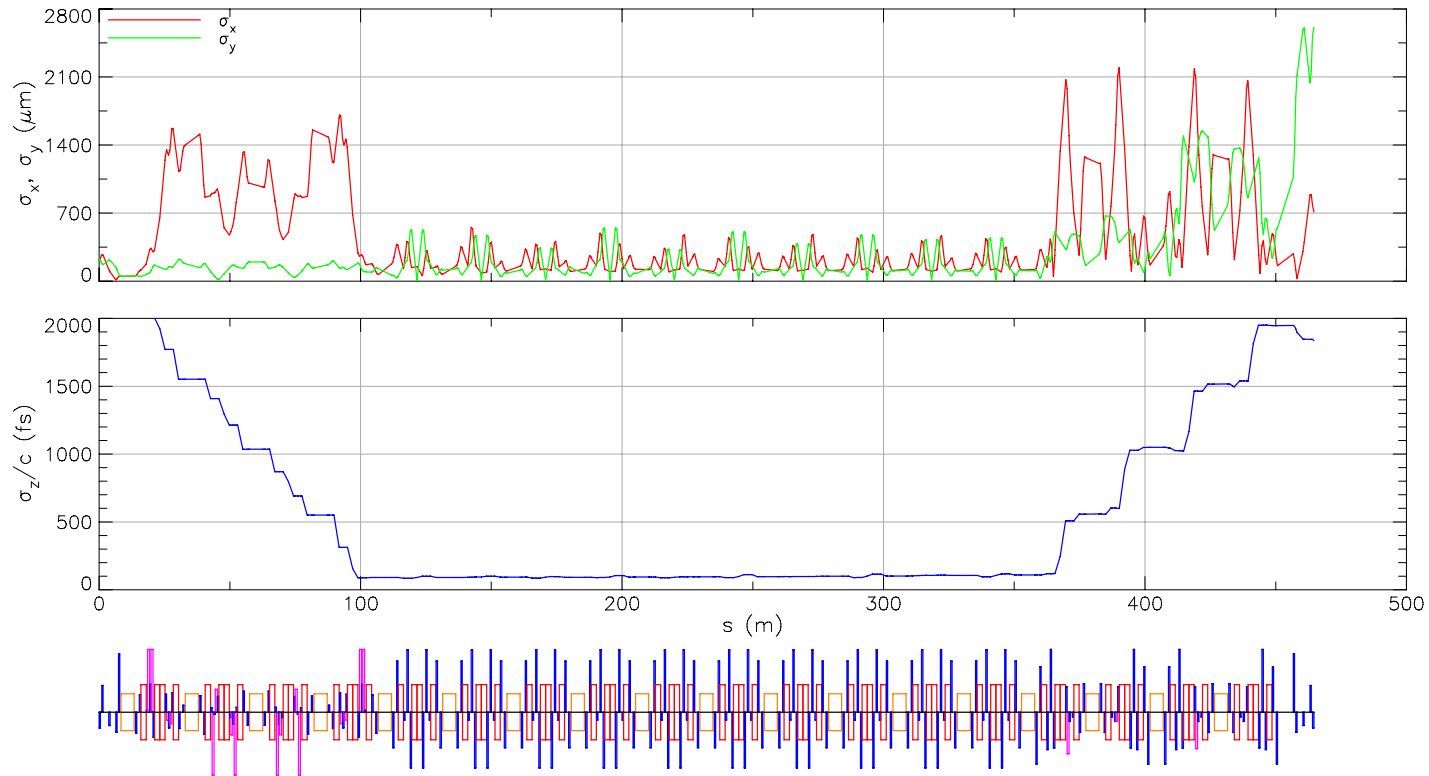


Figure 3.30: Bunch widths and length in the RA for Mode C bunch compression. The minimum bunch length in the middle eleven undulators is approximately $\sigma_z/c = 100$ fs.

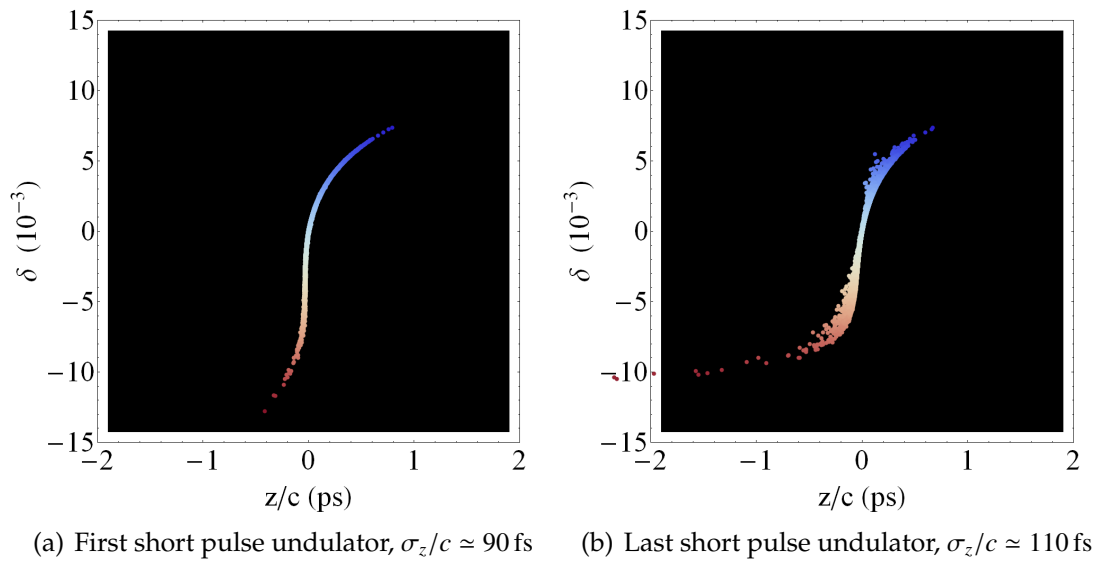


Figure 3.31: Longitudinal phase space in the first undulator after compression and in the last undulator before decompression in the MERL RA.

The resulting first and second order dispersion from this optimization are shown in Fig. 3.29, along with the first and second order time of flight terms. This compression is tested by tracking particles, with the resulting bunch widths and length shown in Fig. 3.30. It was found in this tracking that the sextupole strengths in the middle cells did more harm than good, so they are set to zero here, resulting in a marginal degradation in the bunch length. The longitudinal phase space in the first and last undulators that have short bunches are shown in Fig. 3.31. It should be noted that the decompression in this solution is not perfect, as the bunch does not exactly return to its original length at the end of the arc, and also the bunch widths become relatively large.

CHAPTER 4

CORNELL ERL

4.1 Site

The development of an ERL at Cornell presents many unique challenges in addition to those for the Minimal ERL. Primarily, the Cornell ERL (CERL) is planned to make as much use as possible from the existing facilities at the Wilson Synchrotron Laboratory, which include the Cornell Electron Storage Ring (CESR), the Cornell High Energy Synchrotron Source (CHESS) G-line beamline, and the Wilson Lab building. Because the CESR components were designed to sustain 8 GeV electrons, this section can comprise part of the 5 GeV return arc.

The location of Wilson Lab, shown in red in Fig. 4.1, lies on a hillside between the Cornell campus and Cascadilla creek. The CESR tunnel is approximately 15 meters below the soccer field to the north. Early designs for an ERL at Cornell extended CESR to the north by twin linacs that avoided buildings, but it was found that these linacs were too short to deliver the full 5 GeV energy given current technology. With the creek to the south and buildings to the west and the north, the ERL linacs must then connect to CESR and extend to the east. Several possibilities have been considered, all of which utilized a single tunnel to house the two linacs, with a small turnaround loop to the east. It was found that the bending radius of this loop was too small for any modern tunneling machine to dig, and that it would be more cost effective for the linacs to occupy their own tunnels, with the turnaround being a simple arc. Additionally, in order to have separate control over accelerating and decelerating beams, the linacs are to run at different energies, so that the turnaround can house two

beam transport lines, one for each energy.

The most current design, as of the writing of this document, is shown in Fig. 4.1. The logic in choosing this design is discussed in the following sections. The layout is divided into nine discrete sections, shown in Fig. 4.2, roughly in accordance with their function: The injector (IN) delivers a 10 MeV beam into Linac A (LA), which accelerates it to 2.8 GeV. This beam feeds into Turnaround A (TA), which bends it around to connect to Linac B (LB). The beam is accelerated through LB to 5 GeV into the South Arc (SA) containing up to fourteen undulators, which connects to part of CESR (CE), which connects to the North Arc (NA) containing eight more undulators. The NA connects back into LA, which decelerates the beam to 2.2 GeV, recovering 2.8 GeV. A demerging dipole separates this beam from the 2.8 GeV accelerating beam into TB. Thereafter a merging dipole combines this decelerating beam with the accelerating beam from TA and directs it into LB, where it is decelerated to 10 MeV, recovering 2.2 GeV. Finally the beam is sent to the Dump (DU).

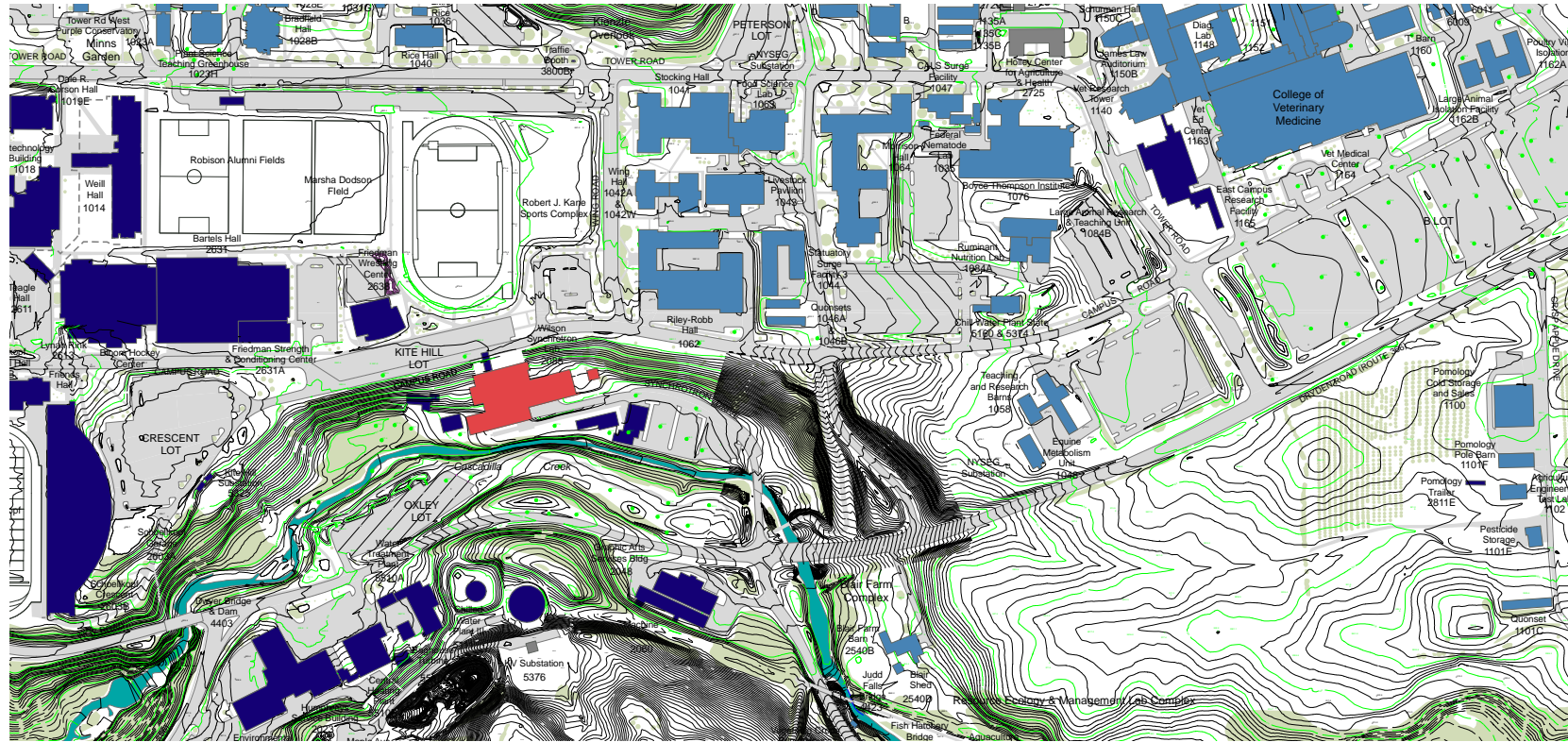


Figure 4.1: The Cornell campus map in the area immediately surrounding Wilson Lab, shown in red. Other buildings are shown in blue. The CESR tunnel lies 15 meters below the soccer field to the north. Due to the length of the linacs required for a 5 GeV ERL, the only viable direction to build is to the east.

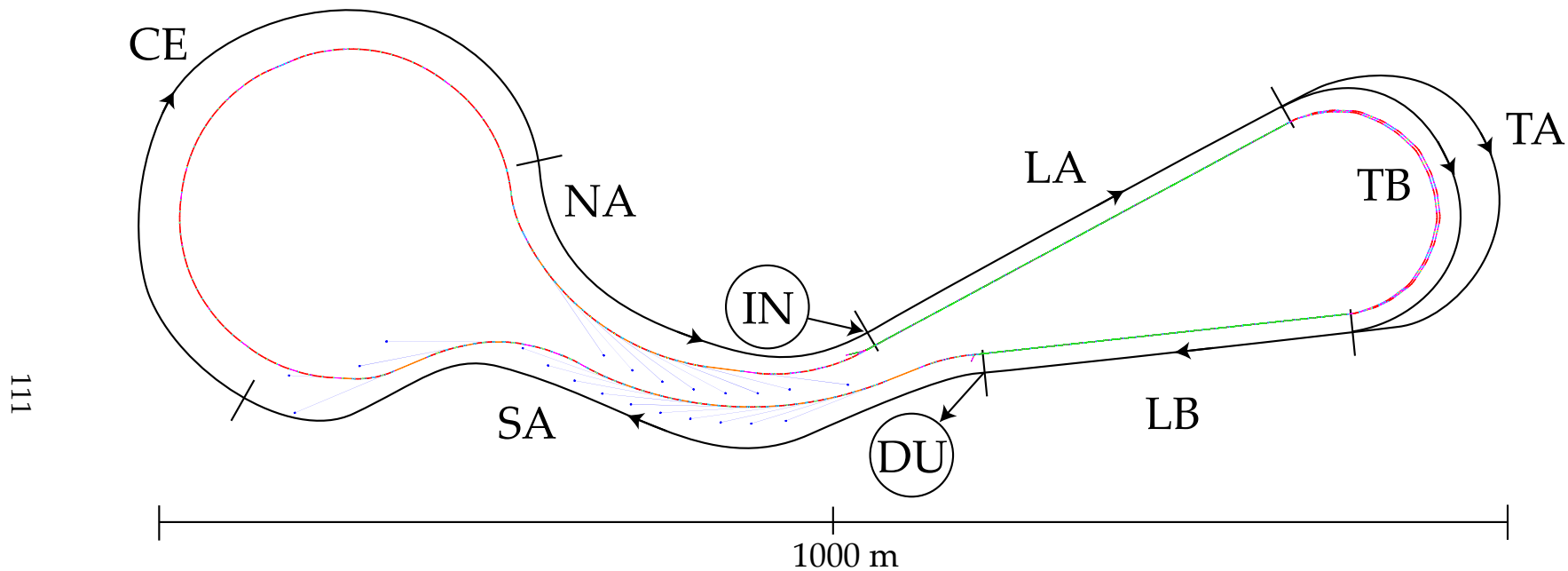


Figure 4.2: The CERL layout with section labels. A bunch is accelerated to 10 MeV in the injector (IN), and injected into the beginning of Linac A (LA), which accelerates it to 2.8 GeV. The bunch traverses Turnaround A (TA), and gains another 2.2 GeV through Linac B (LB). At 5 GeV, the bunch travels through undulators in the South Arc (SA), the CESR tunnel (CE), and undulators in the North Arc (NA). It then reenters LA off phase, which decelerates it to 2.2 GeV, enters Turnaround B (TB), and is decelerated to 10 MeV through LB. Finally it is extracted and sent to the Dump (DU).

4.2 Layout

In order to be a competitive and cost-effective light source, it has been determined that the CERL must:

- Utilize as much of CESR as possible
- Provide at least 18 X-ray beamlines with easy access
- Have a single building to house all X-ray beamlines outside of Wilson Lab, as well as the injector and dump
- Accommodate at least two 25 m long undulators
- Include the CHESS G-line beamline

As mentioned before, the natural extension of the CERL from CESR is to the east. Taking advantage of the curved hillside in this direction, the South Arc is shaped to conform to the terrain, with the North Arc beamlines terminating as close as possible to this arc, which can be seen in Fig. (SA and NA). In this manner, beamlines from both arcs can be housed in a single building. Space has been allotted for four beamlines in Wilson lab, including G-line and a 25 m undulator, with the new building containing up to eighteen beamlines. Of these beamlines, up to ten are from the South Arc and up to eight are from the North Arc, with each contributing a long undulator. Thus the CERL can accommodate three 25 m undulators and nineteen 5 m undulators.

Tunneling technology requires the bending radius of the turnaround tunnel to be at least 250 feet, and this minimum is used in the design. The bends and the beginning of the SA and the end of the NA are adjusted so that, when connected via the linacs, the turnaround loop is a pure arc. The linacs then have a relative

angle of approximately 22 degrees, and therefore TA and TB bend the beam by approximately 202 degrees.

Bends in the CERL are designed so that:

- The angle between undulators is large enough to be able to place the first optical element, outside the shielding wall, at approximately 30 m down the X-ray line after the end of the undulator
- The radiation load on the beam chamber does not exceed 1 kW/m

All undulators are separated by two-bend achromatic sections that satisfy the first constraint. For the second constraint, from Eq. (3.1), the average power per unit length lost on the beam chamber walls in a magnet with radius of curvature ρ is, in practical units,

$$\left\langle \frac{P}{L} \right\rangle \simeq 14.08 \frac{\text{W}}{\text{m}} \left(\frac{\mathcal{E}}{\text{GeV}} \right)^4 \left(\frac{I}{\text{mA}} \right) \left(\frac{\rho}{\text{m}} \right)^{-2}, \quad (4.1)$$

where \mathcal{E} is the beam energy and I is the average current. For a 100 mA beam, this implies that bends in the SA, CE, and NA must have a minimum radius of curvature of approximately 30 m. The bends in TA and TB must have a minimum radius of curvature of 10 m and 6 m, respectively, which are easily satisfied given the dimensions of the turnaround tunnel.

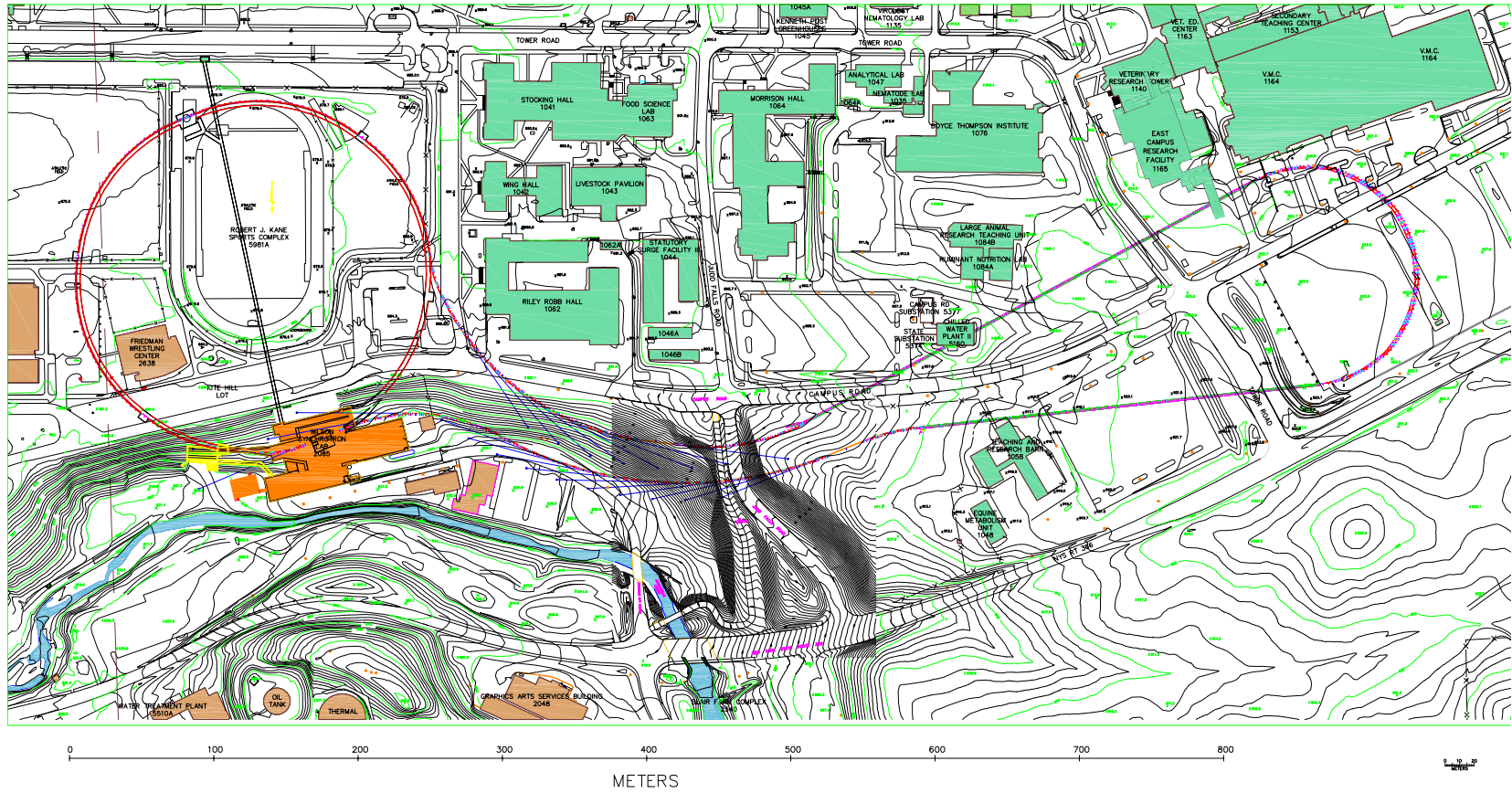


Figure 4.3: The CERL on the campus map

4.3 Optics

In order to deliver a high quality beam to the undulators and perform energy recovery, the optics in the CERL must overall:

- Accommodate simultaneously accelerating and decelerating beams in the LA and LB sections
- Accommodate one high energy beam in the SA, CE, and NA sections
- Limit radiative emittance growth as much as possible prior to undulators

The bulk of TA and TB maneuver the accelerating and decelerating beams separately, and the SA, CE, and NA sections only manage the high energy beam, so the only sections that must handle both beams are LA, LB, and the ends of TA and TB. The optimization of these sections is challenging, and discussed in sections 4.3.1 and 4.3.2. Emittance growth occurs in every bending magnet due to the quantum nature of synchrotron radiation, at a rate given by Eq. (2.177). It must be controlled everywhere, especially in TA and between the SA undulators. Unfortunately, the CESR magnet arrangement reused in CE does not admit a low emittance solution, and therefore the emittance in the NA is relatively large. For this reason, an upgrade option to CE is given in section 4.3.4.

In order to provide the desired transverse beam size and length to undulators, and to avoid nonlinearities in magnets, the linear optics are subject to the following:

- Flexible time of flight term r_{56} for each turnaround loop
- Zero time of flight term in the return arc, *i.e.* $r_{56} = 0$ from the end of the LB section to the beginning of the LA section
- Tunable r_{56} within subsections
- Flexible beta functions and zero dispersion in all undulators
- Beta functions must be less than 100 m everywhere

In general, the time of flight term r_{56} and the phase of the accelerating cavities can be used to manipulate the longitudinal phase space, as described in Section 3.5. In particular, r_{56} must be zero from the end of LB to the beginning in LA in order for the energy spread profile to correctly match the decelerating RF voltage and therefore perform energy recovery, as described in Section 3.4.

The beta functions in all undulators must be flexible in order to satisfy the requirements of individual users of these devices. The dispersion is zero in undulators to avoid an apparent increase in beam size. As a rule of thumb, the beta functions are also kept below 100m as much as possible to limit their sensitivity to field errors in magnets, and it is generally advantageous to keep them small in order to limit emittance growth.

For further refinement of the transverse beam size and length, the nonlinear optics are subject to the following:

- Zero second order dispersion t_{166} in all undulators
- All sections achromatic to second order, i.e. $t_{166} = 0$ and $t_{266} = 0$ from the beginning to end of each section
- Flexible second order time of flight term t_{566} in all sections, close to zero

Similar to the first order dispersion, the zero second order dispersion in undulators avoids an apparent increase in beam size. As a rule of thumb, it is often easiest to control second order dispersion when $t_{166} = 0$ and $t_{266} = 0$ for every subsection.

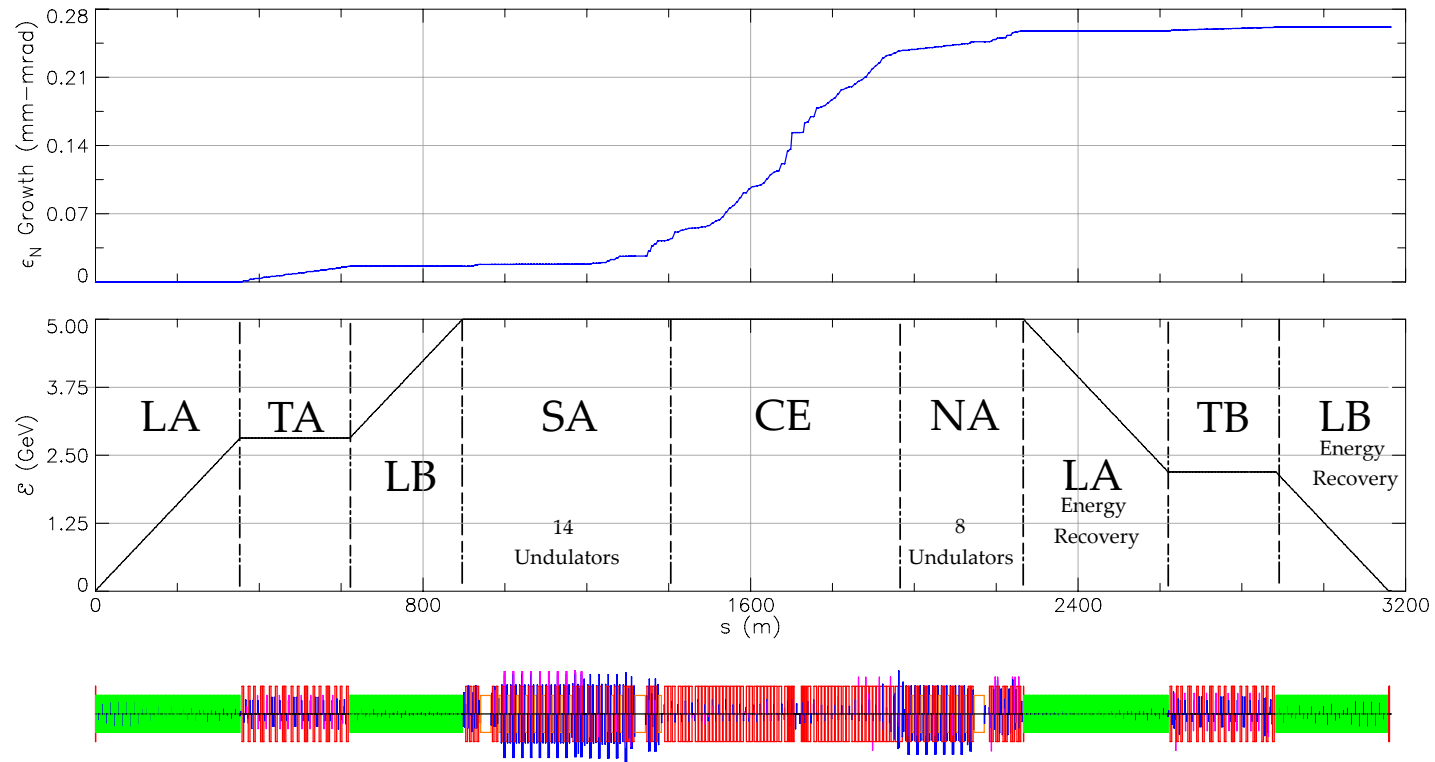


Figure 4.4: Radiative emittance growth ϵ_N and total energy \mathcal{E} in the CERL, including the energy recovery pass.

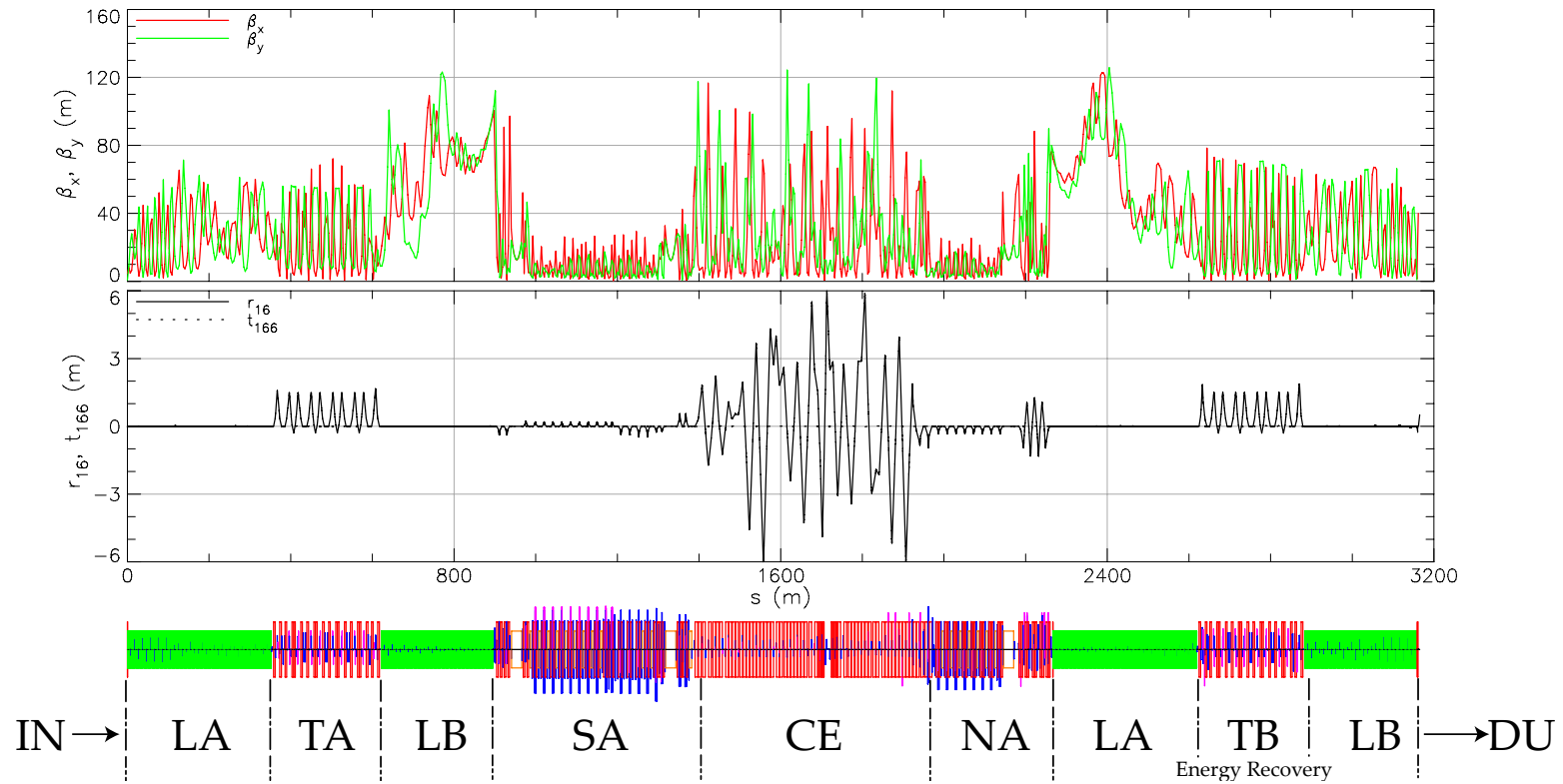


Figure 4.5: Beta functions and dispersion for the CERL, including the energy recovery pass.

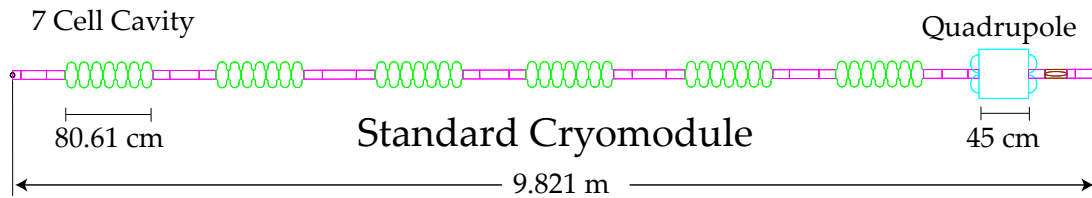


Figure 4.6: The standard CERL cryomodule.

4.3.1 LA & LB – Linac A and B

The CERL linacs consist of 64 identical cryomodule cells divided among LA and LB, with the layout for the standard CERL cryomodule shown in Fig. 4.6. Each cryomodule contains six superconducting accelerating cavities and a single quadrupole magnet, along with other elements, *e.g.* higher order mode absorbers, gate valves, and beam position monitors, that can be considered to be drifts for purposes of the beam optics. Some technical details regarding the development of such cryomodules and cavities can be found in McIntosh *et al.* (2006). Each cavity contains seven elliptical cells operating at the fundamental frequency $f_{\text{rf}} = 1.3 \text{ GHz}$, which corresponds to $k_{\text{rf}} \approx 27.25 \text{ m}^{-1}$ and a wavelength $\lambda_{\text{rf}} = 23.06 \text{ cm}$. They are designed to deliver accelerating gradients in the range of 15-20 MV/m for currents up to 100 mA. Using the dimensions in Fig. 4.6, in order to bring a 10 MeV beam to 5 GeV, each cavity must provide an average energy gradient of 16.12 MeV/m, and therefore a single cryomodule can give or take 78 MeV to or from a beam.

Because the CERL has two turnaround loops TA and TB operating at different energies, one linac needs to be longer than the other. In general, for N_A and N_B standard cryomodules in LA and LB, respectively, the changes in energy of the beam in these linacs are

$$\Delta\mathcal{E}_{LA} = \frac{N_A}{N_A + N_B} (\mathcal{E}_{\max} - \mathcal{E}_{\min}), \quad (4.2)$$

$$\Delta\mathcal{E}_{LB} = \mathcal{E}_{\max} - \mathcal{E}_{\min} - \Delta\mathcal{E}_{LA}, \quad (4.3)$$

where \mathcal{E}_{\min} is the injection energy and \mathcal{E}_{\max} is the full operating energy of the ERL. For $N_A = 36$ and $N_B = 28$, with energies $\mathcal{E}_{\min} = 10$ MeV and $\mathcal{E}_{\max} = 5$ GeV, we get $\Delta\mathcal{E}_{LA} = 2.806875$ GeV and $\Delta\mathcal{E}_{LB} = 2.183125$ GeV. The beam in TA is therefore has an energy of $\mathcal{E}_{\min} + \Delta\mathcal{E}_{LA} = 2.816875$ GeV, and the beam in TB has an energy of $\mathcal{E}_{\max} - \Delta\mathcal{E}_{LA} = 2.193125$ GeV, which will often be abbreviated as 2.8 GeV and 2.2 GeV, respectively.

The beam optics in the linacs must satisfy the following criteria:

- Zero dispersion
- Keep beta functions as small as possible for both accelerating and decelerating beams

- Accept Twiss parameters from the IN for LA
- Provide correct Twiss parameters for the DU from LB

The adjacent sections provide zero dispersion to LA and LB, and because there are no bends within the linacs there can be no creation of dispersion. The beta functions are manipulated by the 36 and 28 quadrupole magnets in LA and LB, respectively.

The optimization of the Twiss parameters in LA and LB is very similar to the MERL linac optimization described in Section 3.2.1. Here, however, the existence of two turnaround loops means that the two beams do not need to have the same Twiss parameters as they enter the turnaround tunnel, and are thus more flexible. Nevertheless, the MERL LA and LB solutions can still be used as a starting point. The resulting quadrupole strengths seen by each beam are shown in Fig. 4.7. The optics are shown in Figs. 4.8–4.9.

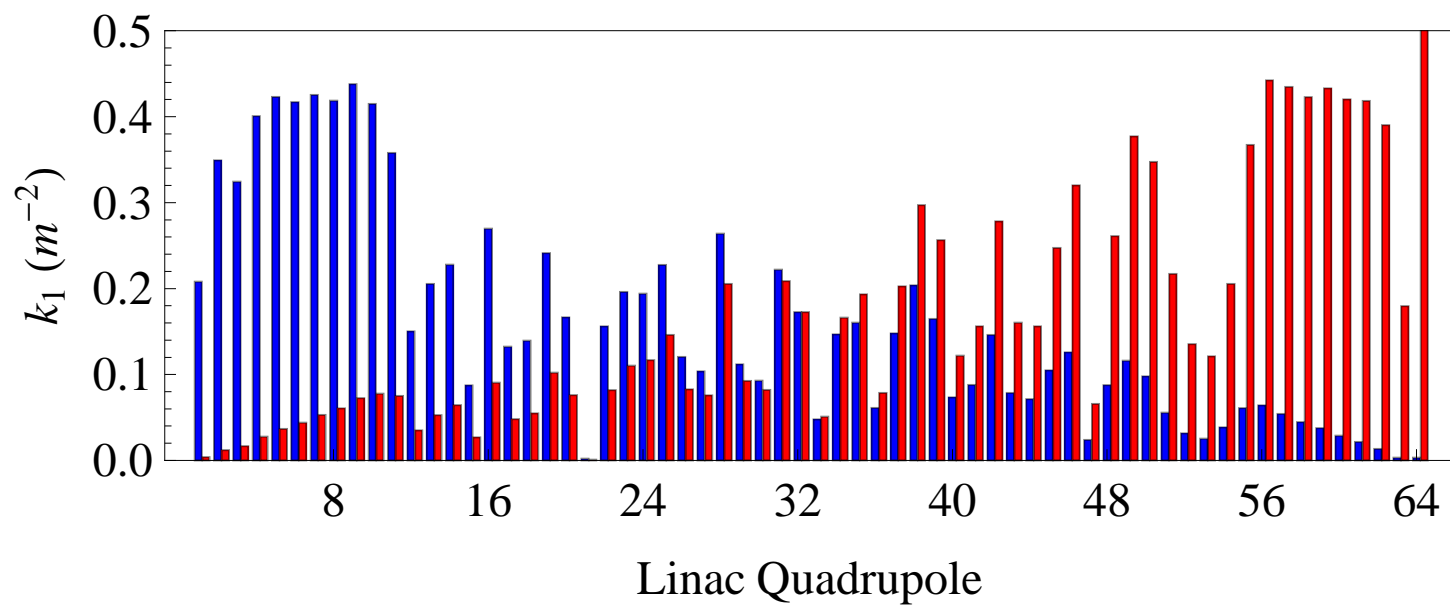


Figure 4.7: Quadrupole k_1 strengths seen by the accelerating beam (blue bars) and decelerating beam (red bars) in the CERL linacs.

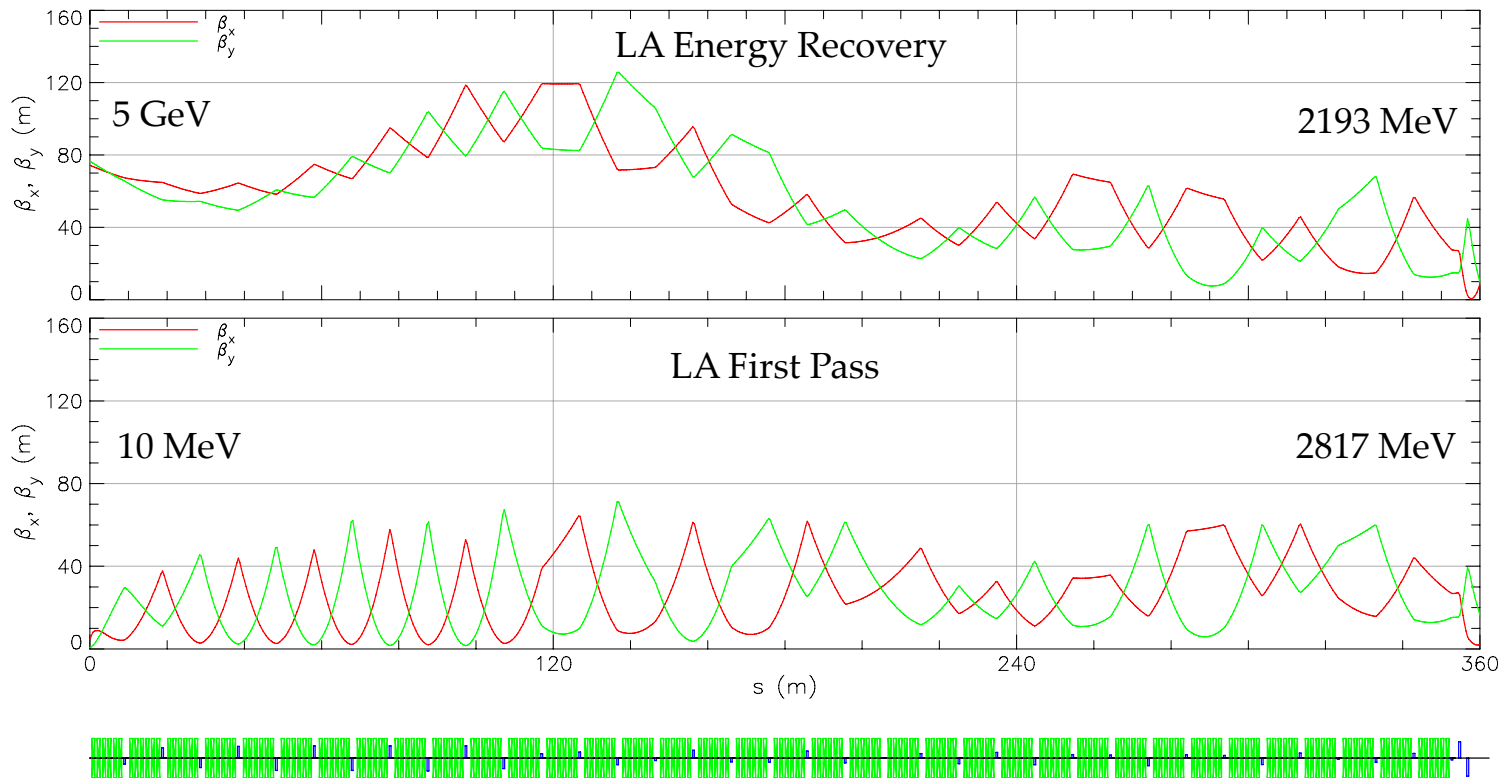


Figure 4.8: Beta functions for the first pass (accelerating) beam and energy recovery (decelerating) beam in LA. The optimization criteria are to keep the beta functions as small as possible and to match the low energy beam at $s = 0$ to the Twiss parameters from the IN. This section is most effectively optimized by propagating the beta functions “backwards” from the end of LA by varying β_x and β_y there along with the 36 quadrupole fields.

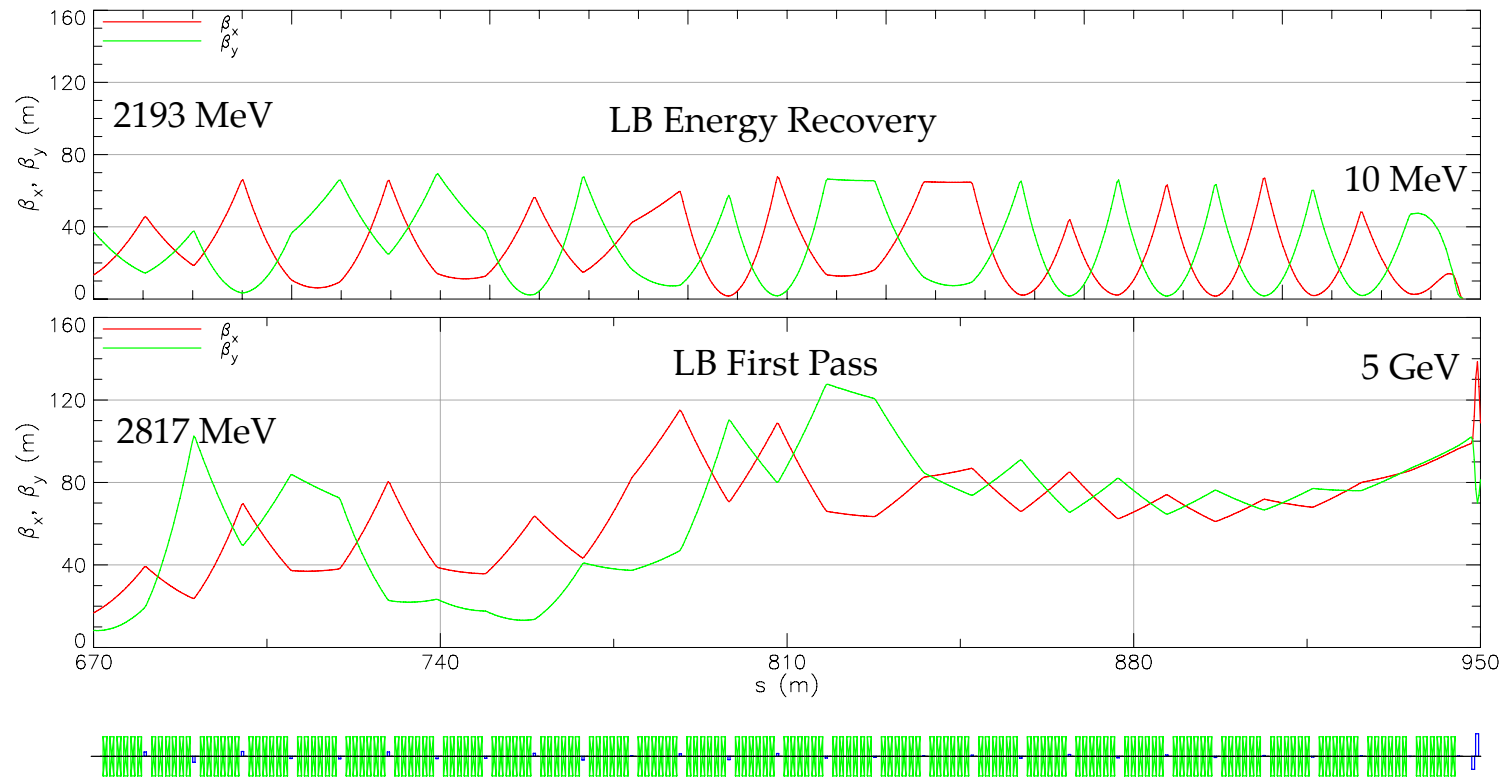


Figure 4.9: Beta functions for the first pass (accelerating) beam and energy recovery (decelerating) beam in LB. Optimization is similar to that in LA described in Fig. 4.8

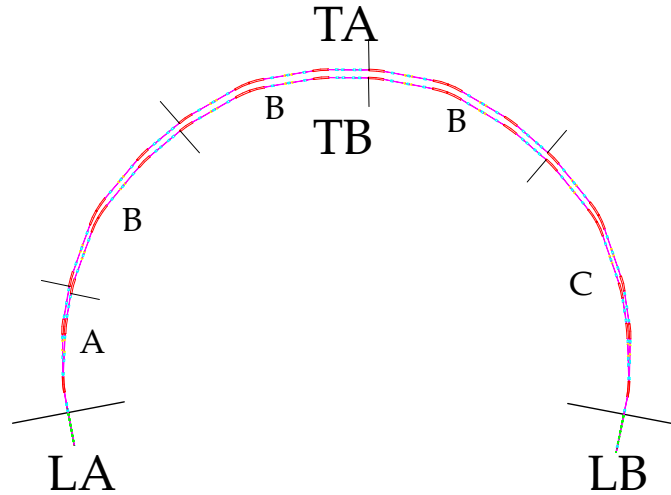


Figure 4.10: Layout for the TA and TB sections showing the partitions into Cells A, B, and C.

4.3.2 TA & TB – Turnaround A and B

Two turnaround arcs provide an additional level of flexibility in the optics relative to the single turnaround in the MERL. In particular, having two turnarounds allows for the compensation of wake-fields by tuning time of flight terms, a scheme described in Hoffstaetter & Lau (2008). First pass particles exit LA at 2.8 GeV, and follow TA. The second pass beam exits LA at 2.2 GeV, and follows TB.

TA is divided into five cell types:

Cell A Controls and separates the two beams after LA

Cell B Periodic section containing 4 bends and 4 quadrupole magnets for beam transport – occurs three times

Cell C Similar to the reverse of Cells A and B, matches Twiss parameters into LB for both beams

These cells are shown in Fig. 4.10. Cells for TB are very similar to those of TA.

The bulk of TA (and similarly TB) is built out of four three-bend achromats, described in a Cell B section. These are similar to the MERL achromats in Section 3.2.2, except that the bends and drifts are much longer. The beginning of Cell A for each turnaround contains shared elements, including a demerging bend, shown in Fig. 4.11. This bend is part of a two-bend achromat for each Cell A, which give fixed r_{56} and t_{566} time of flight terms.

We would like both TA and TB to be isochronous, so the interior Cell B sections are optimized to compensate for the fixed time of flight terms in Cells A and C. The optics for the TA Cell B are shown in Fig. 4.12. In addition to the time of flight contributions, this cell is optimized for periodic Twiss parameters, low radiative emittance growth, and to be achromatic by varying the quadrupole strengths. The second order dispersion and time of flight are optimized by varying the sextupole strengths.

With these periodic beta functions at hand, the TA and TB Cell A sections are optimized simultaneously to match into their respective Cell B sections. The optics for these cells are shown in Fig. 4.13. Additionally, radiative emittance growth is controlled.

The optics for all of TA are shown in Fig. 4.14. The TA radiative emittance growth and time of flight terms are shown in Fig. 4.15. There one sees how the interior cells compensate for the outer cells to make all of TA achromatic and isochronous to second order. Note that the radiative emittance growth is approximately 20% of the Mode B normalized emittance.

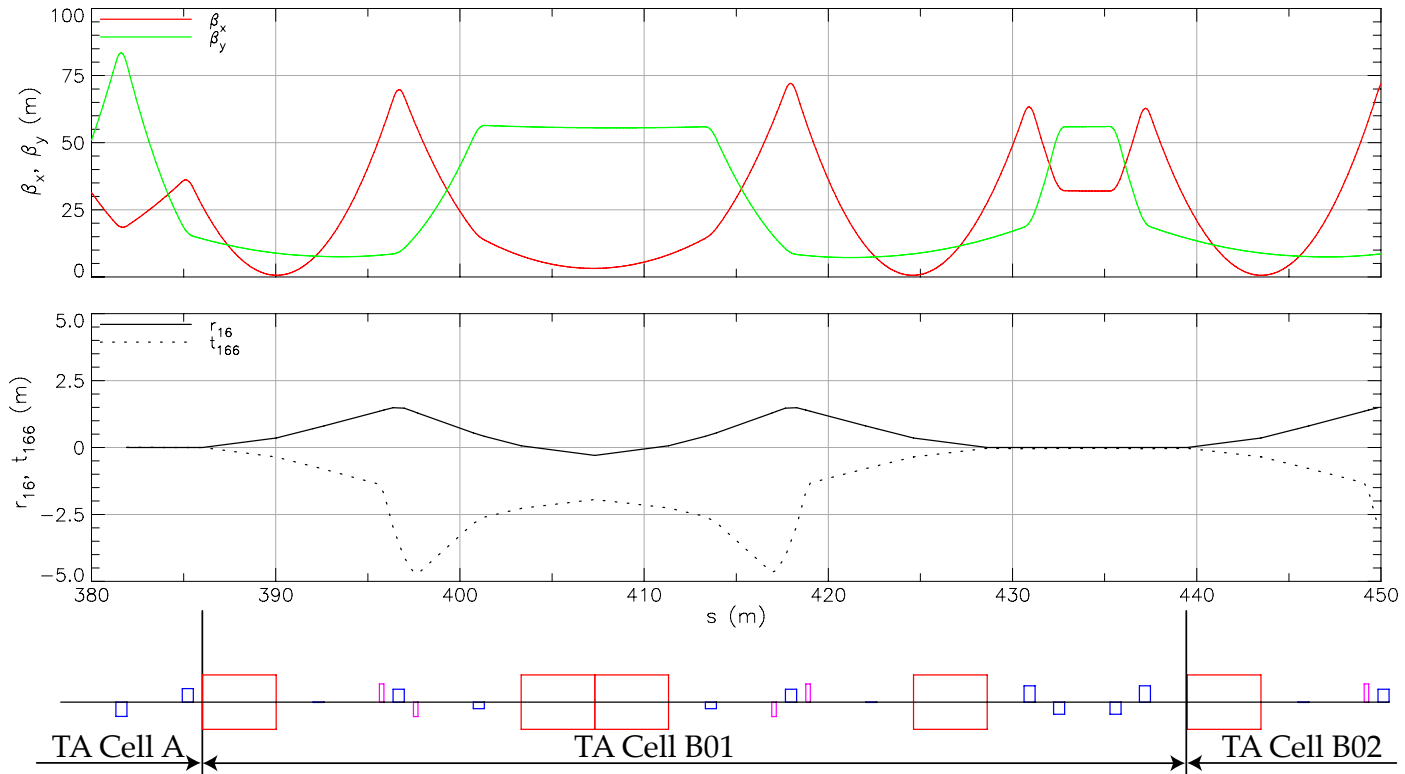


Figure 4.12: Optics for the first TA Cell B. This section is optimized for periodic beta functions and low radiative emittance growth. The dispersion and its slope are brought to zero at the end of the third bend, making the section achromatic.

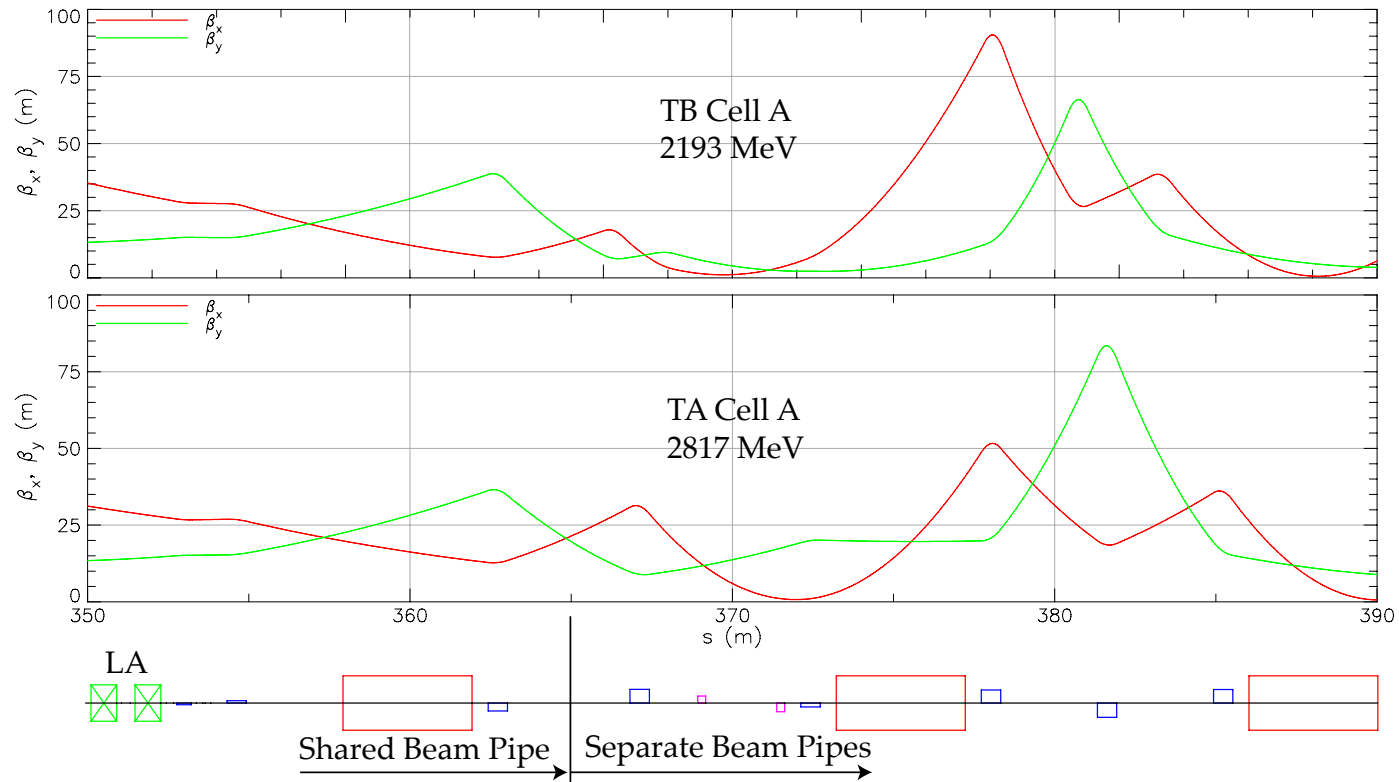


Figure 4.13: Beta functions for the TA Cell A and TB Cell A. These sections need to be optimized simultaneously to match Twiss parameters into the next cells.

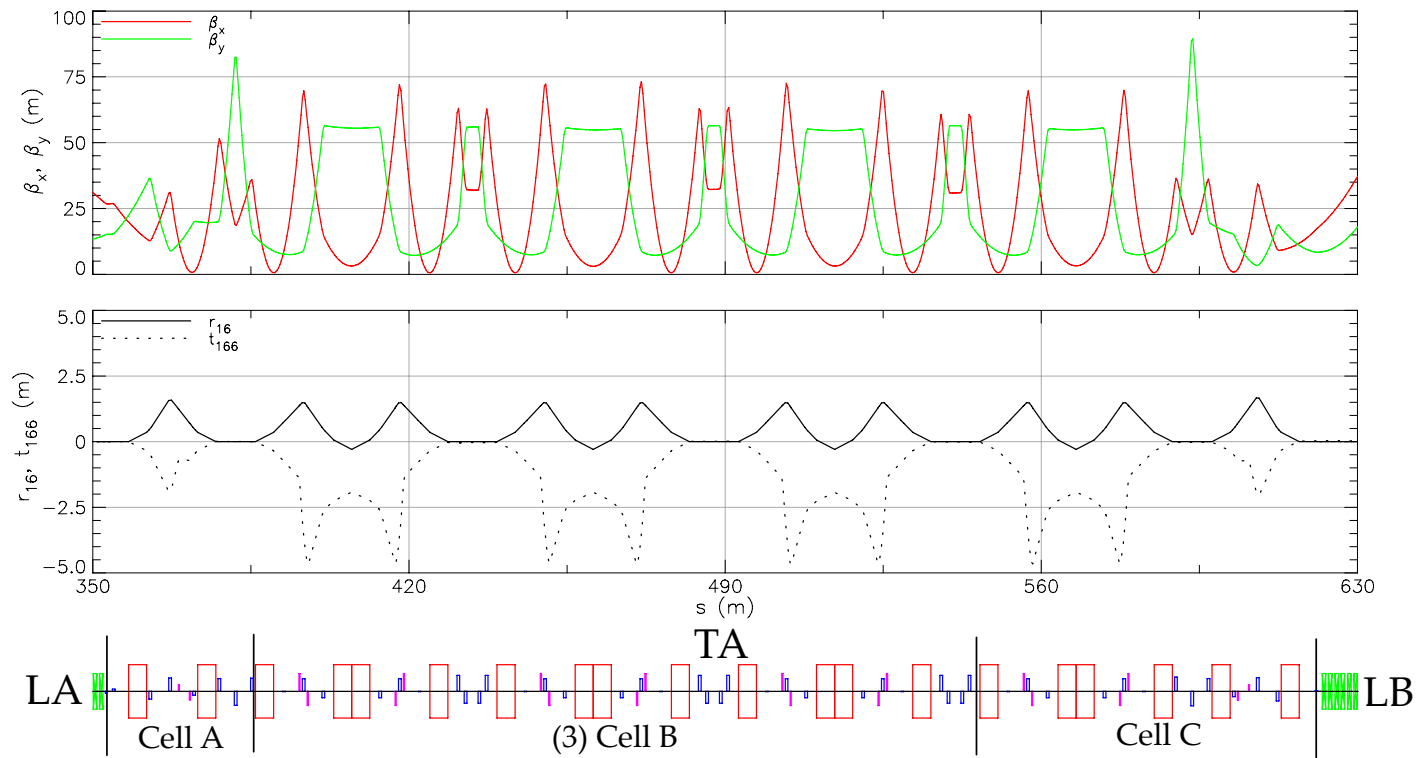


Figure 4.14: Optics for the entire TA section

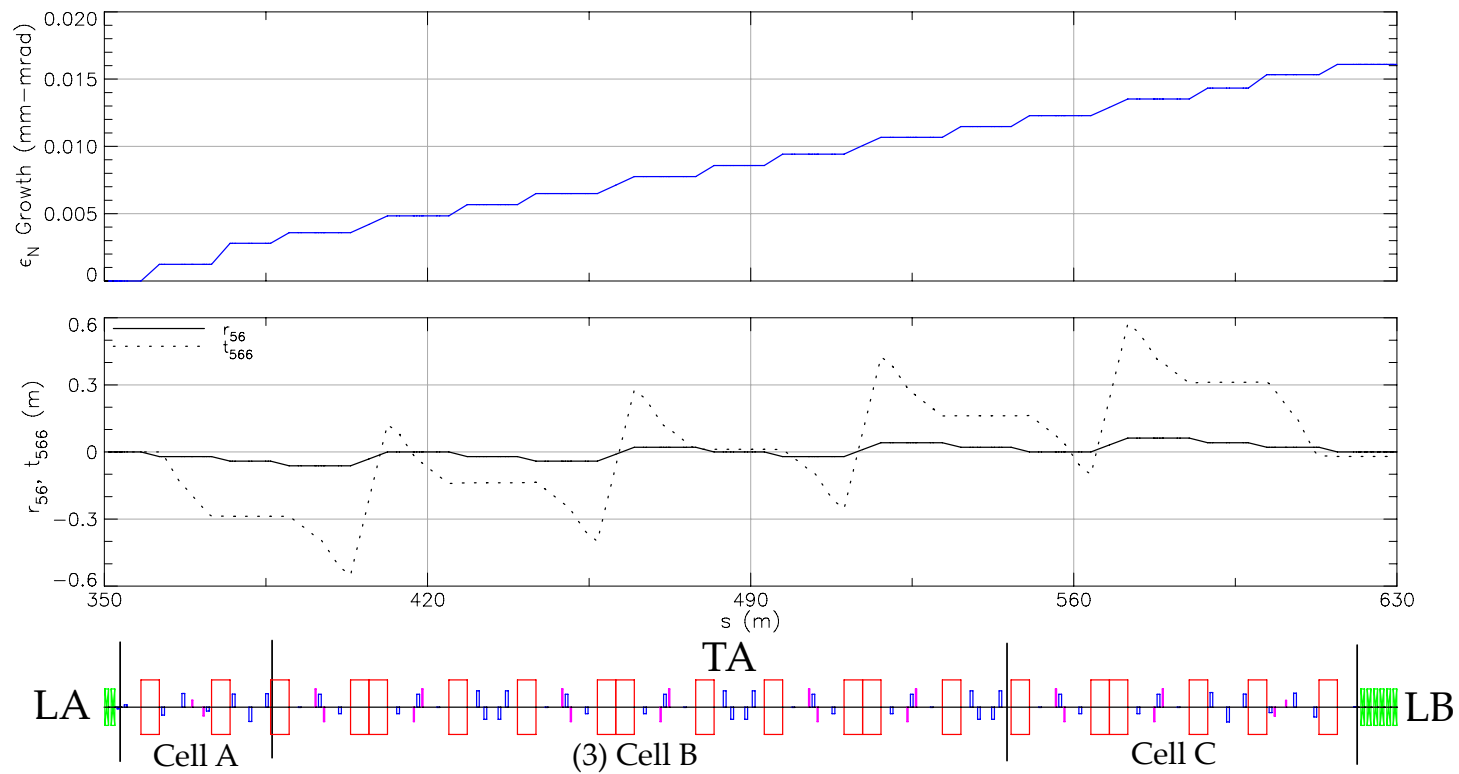


Figure 4.15: Radiative emittance growth and time of flight terms r_{56} and t_{566} for the entire TA section.

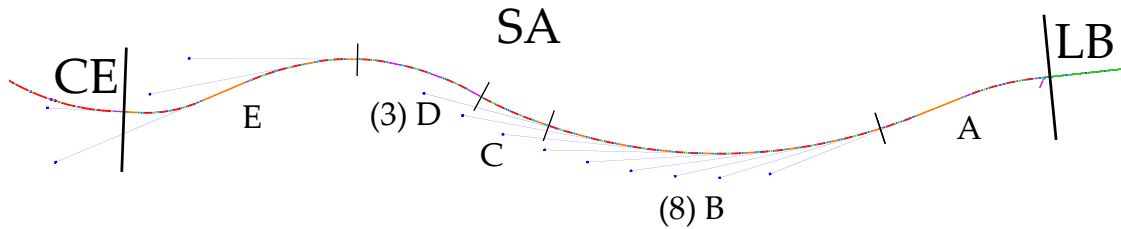


Figure 4.16: Layout showing the SA.

4.3.3 SA – South Arc

The SA section, shown in Fig. 4.16, is approximately 500 m long and contains the majority of undulators in the CERL. It is the first section after the beam has been accelerated to 5 GeV by LB, and therefore receives bunches with the lowest possible emittance. It is divided into five cell types:

Cell A Matches Twiss parameters from LB into Cell B and contains a 25 m undulator

Cell B Periodic section containing a 5 m undulator and a two-bend achromatic section – occurs eight times

Cell C Matches Twiss parameters from the last Cell B into the first Cell D

Cell D Periodic section consisting of a two-bend achromat for beam transport only – occurs three times

Cell E Matches Twiss parameters from Cell D into four undulators, and ends with the 6 m G-line undulator.

The layout for the beginning of the SA is shown in Fig. 4.17 with Cell A and the first three Cell B sections. The first four bends comprise a pair of two-bend

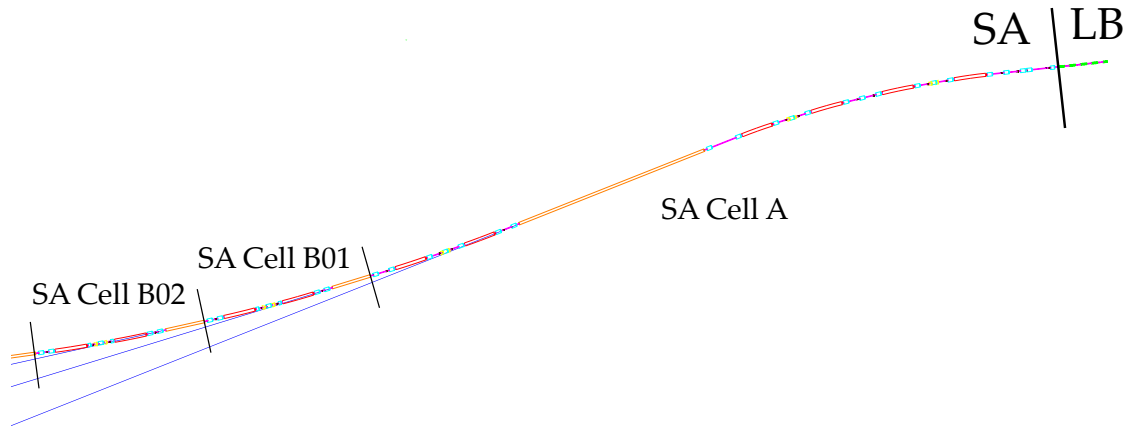


Figure 4.17: The layout for the beginning of the SA section, showing Cell A with the long undulator and two Cell B sections, each with an undulator. The beam moves to the left from the end of LB.

achromatic sections that serve to rotate the linacs and turnaround to the south, and thus avoid tunneling under the College of Veterinary Medicine. The first 25 m undulator follows, and that is followed by a single two-bend achromat to match into the first Cell B.

The linear optics for Cell A are shown in Fig. 4.19. Because the beta functions exiting LB are large, five quadrupole magnets are used to focus them down to manageable values. The following four bends direct the beam into the 25 m undulator, with quadrupole magnets interspersed to give $\alpha_x = 0$, $\alpha_y = 0$, and specified values for the beta functions in the center of this undulator. Additionally the the quadrupole magnets between the first two bends focus the dispersion and its slope to zero at the end of the second bend, and similarly for the third and fourth bends. After the undulator a two-bend achromat matches Twiss parameters into the undulator in the first Cell B. With the Twiss parameter and dispersion constraints satisfied, the quadrupole strengths are further optimized to reduce the radiative emittance growth as much as possible.

The second order dispersion, also in the figure, is manipulated by six sextupole magnets. Four sextupole magnets placed in areas of large dispersion are used to make $t_{166} = 0$ and $t_{266} = 0$ from the beginning of the first bend to the end of the fourth bend. Similarly, two sextupole magnets at the end of the section make $t_{166} = 0$ and $t_{266} = 0$ from the beginning of the fifth bend to the end of the sixth bend, making the last two bends achromatic to second order.

The linear optics for Cell B are shown in Fig. 4.20. The cell consists of a 5 m undulator followed by a two-bend achromat, and occurs eight times. The bends provide an angle between the beginning and end of the cell so that the beam-lines emitted from the undulators of consecutive cells have sufficient clearance after 30 m. The Twiss parameters at the beginning and the end of the cell are fixed by the requirements of the undulators at the beginning of the cell and the beginning of the next cell. Seven quadrupole magnets, arranged symmetrically about the center of the achromat, are used to match these requirements, with the center three additionally used to focus the dispersion and its slope to zero at the end of the second bend. As with the previous sections, emittance growth is reduced as much as possible while maintaining the Twiss parameter and dispersion requirements. Two sextupole magnets placed symmetrically about the center of the achromat are used to set $t_{166} = 0$ and $t_{266} = 0$ through the two bends.

Cells C and D serve as beam transport lines between the last Cell B and the first undulator in Cell E. Both are very similar to Cell B without an undulator. The linear and nonlinear optics are thus treated similarly.

Cell E contains the four Wilson lab undulators, including G-line, and connects to CE. The optics are shown in Fig. 4.21. The first two undulators are of the same type as in Cell B, separated by the same type of two-bend achromat

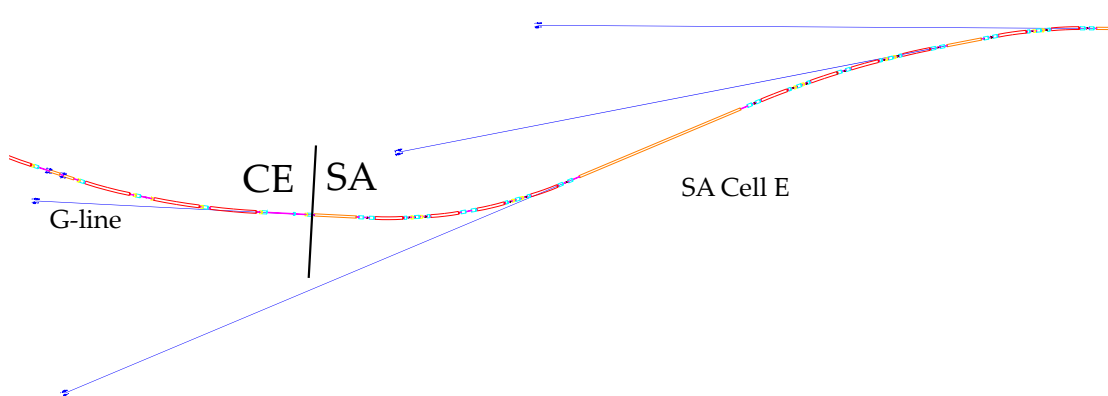


Figure 4.18: The layout for the end of the SA showing Cell E lying within Wilson Lab with four undulators. The G-line beamline radiates from the leftmost undulator. Beyond that one sees the first magnets of CE

and optimized similarly. A pair of two-bend achromats follow the second undulator, and are optimized similarly to the beginning of Cell A to provide specified beta functions and $\alpha_x = \alpha_y = 0$ in the center of the 25 m undulator. Finally, another pair of two-bend achromats focus the beam into the 6 m G-line undulator. The second order dispersion is controlled by sextupole magnets similarly to the previous sections.

The optics for the entire SA section are shown in Fig. 4.22. Radiative emittance growth and time of flight terms r_{56} and t_{566} are shown in Fig. 4.23. One sees that the emittance growth is dominated by portions of Cell E. This is due to the relatively strong bends needed to place the undulators appropriately in Wilson lab.

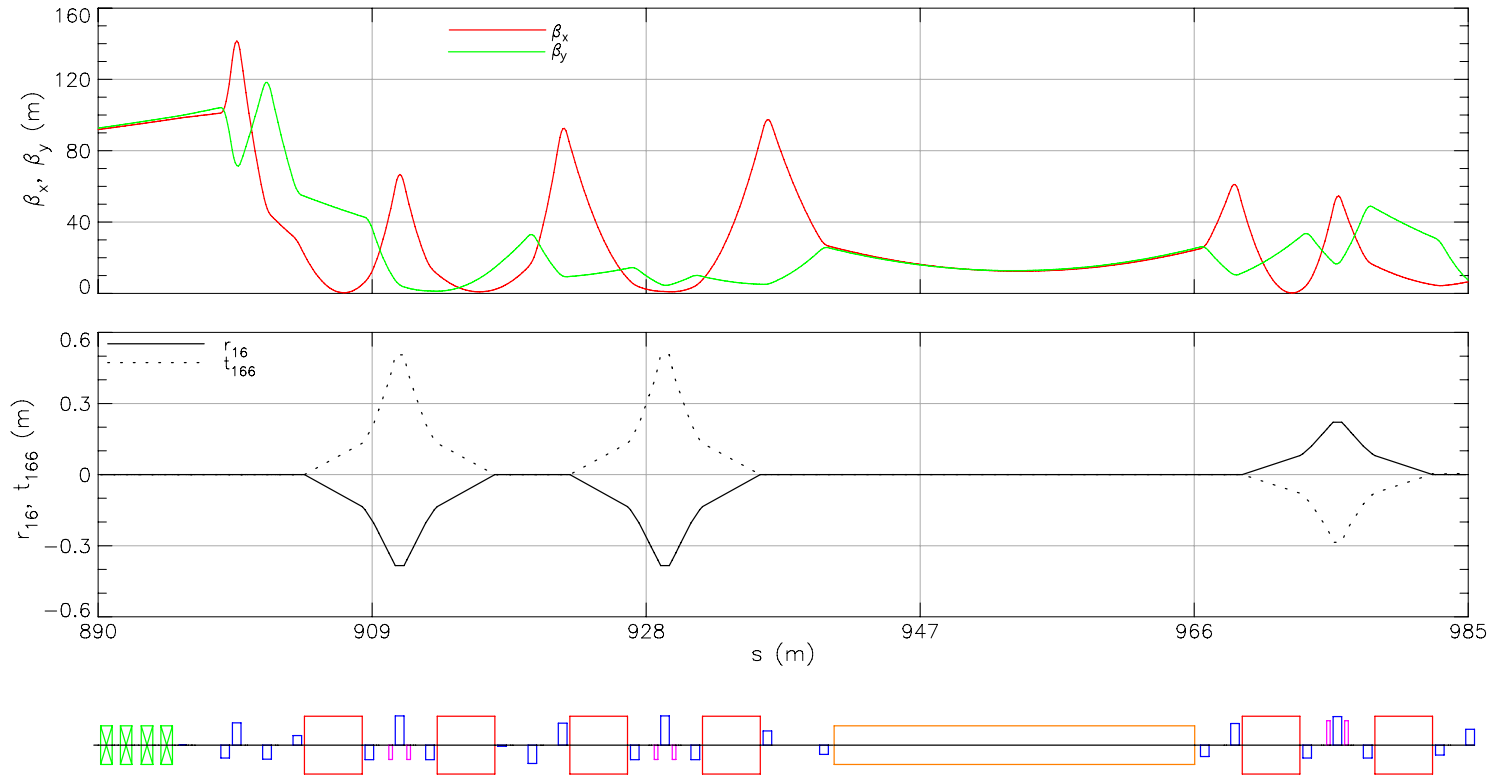


Figure 4.19: Optics for Cell A in the SA. Five quadrupole magnets focus the large beta functions exiting LB down to manageable values. The first sixteen quadrupole strengths are varied to match $\alpha_x = \alpha_y = 0$, $\beta_x = \beta_y = 12.5$ m in the center of the 25 m undulator, as well as $r_{16} = 0$ and $r_{26} = 0$ at the ends of the second and fourth bends, all while attempting to keep the beta functions below 100 m and minimizing emittance growth. Then the last seven quadrupole strengths are varied to provide $r_{16} = 0$ and $r_{26} = 0$ at the end of the last bend and to match into the Twiss parameters for the undulator in the following Cell B. Sextupole magnets placed in dispersive sections serve to set $t_{166} = 0$ and $t_{266} = 0$ between the first and fourth bends, and between the fifth and sixth bends, making this section achromatic to second order.

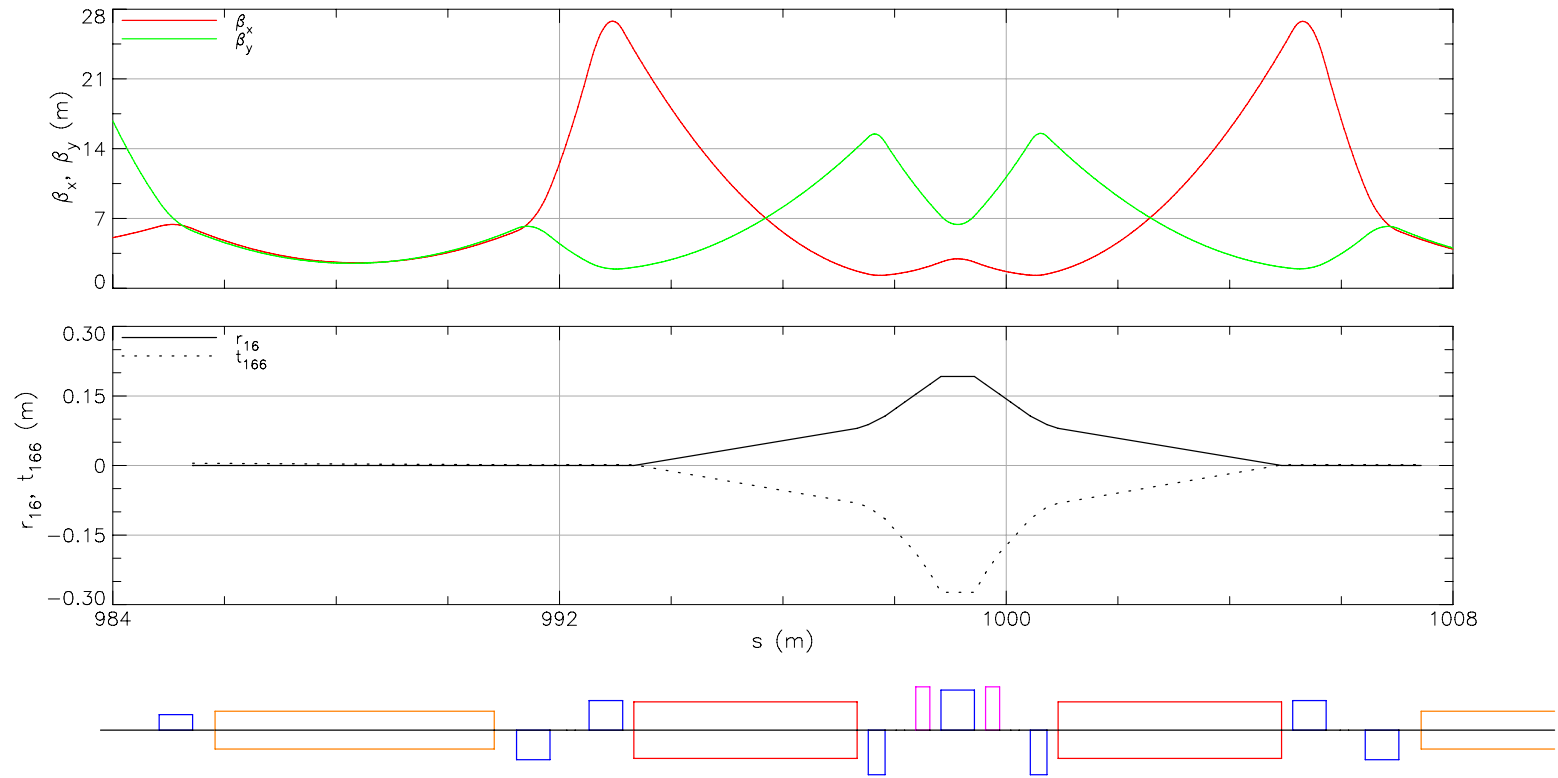


Figure 4.20: Optics for the first SA Cell B, which consists of a 5 m undulator followed by a two-bend achromat. The undulator at the beginning of the next Cell B is seen to the right. Here $\beta_x = \beta_y = 2.5$ m and $\alpha_x = \alpha_y = 0$ in the center of both undulators, and the dispersion and its slope are brought to zero at the end of the second bend. Due to the symmetry, this system can be optimized by varying quadrupole strengths symmetrically about the center of the achromat. Two sextupole magnets placed symmetrically about the center of the achromat provide $t_{166} = 0$ and $t_{266} = 0$ from the beginning of the first bend to the end of the second, making these bends achromatic to second order.

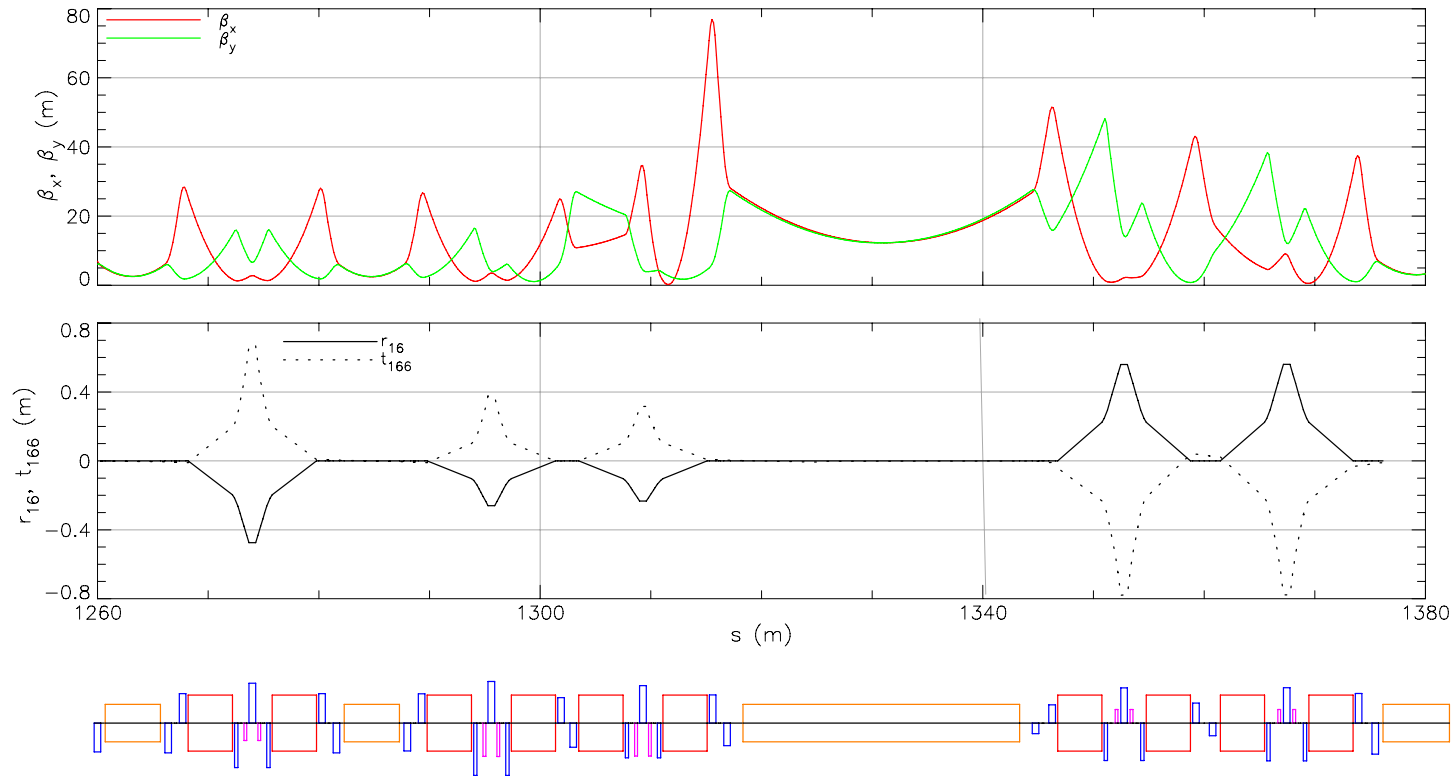


Figure 4.21: Optics for the SA Cell E section. The quadrupole strengths between the first two undulators are optimized similarly to Cell B. The following pair of two-bend achromats and 25 m undulator are very similar to the beginning of Cell A, so the quadrupole strengths are optimized in the same way to provide $\alpha_x = \alpha_y = 0$, $\beta_x = \beta_y = 12.5$ m in the center of this undulator. The final pair of two-bend achromats focus the beam into the 6 m G-line undulator. The second order dispersion is controlled by sextupole magnets in the same way as portions of Cells A and B.

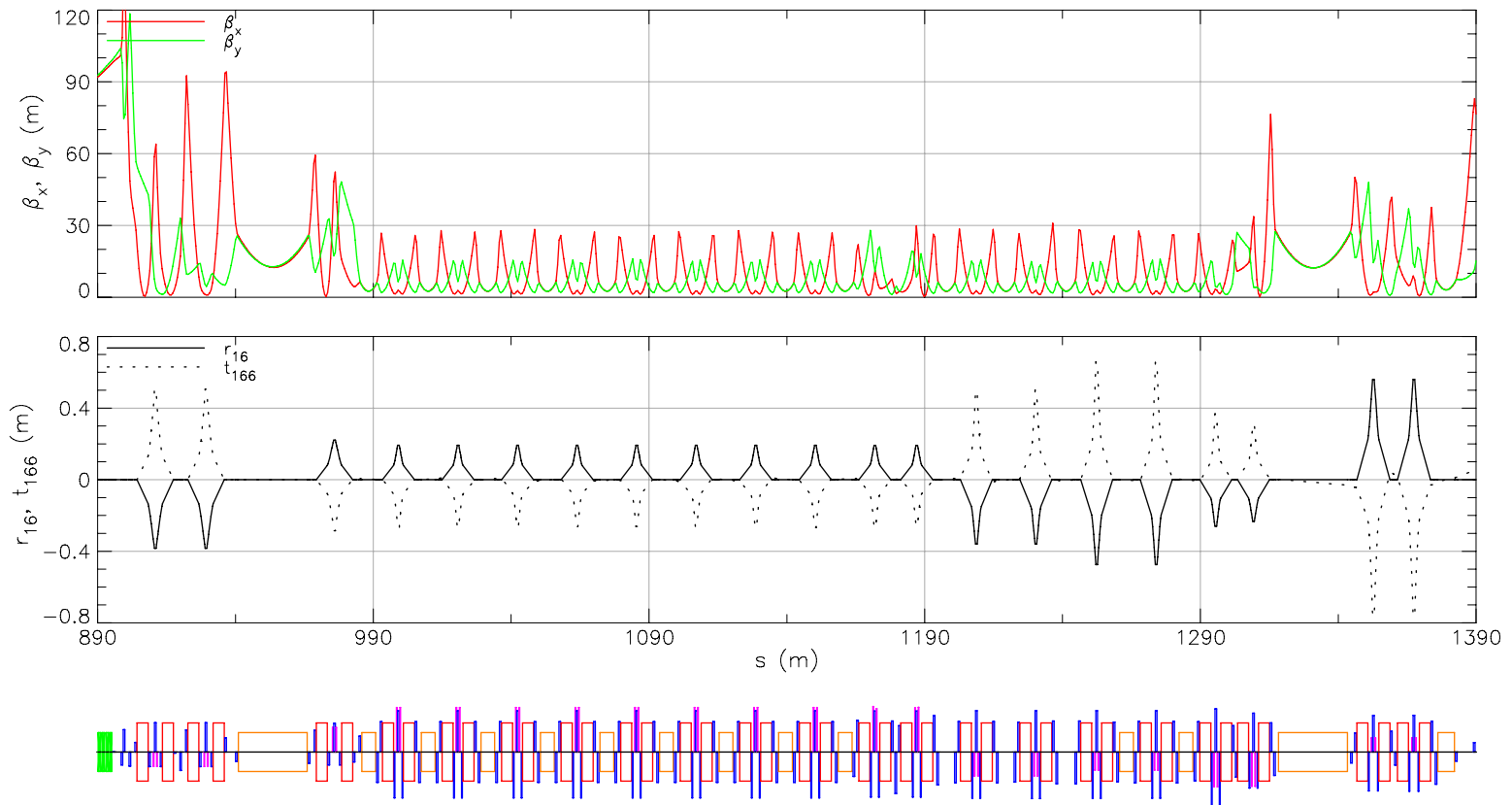


Figure 4.22: Optics for the entire SA section.

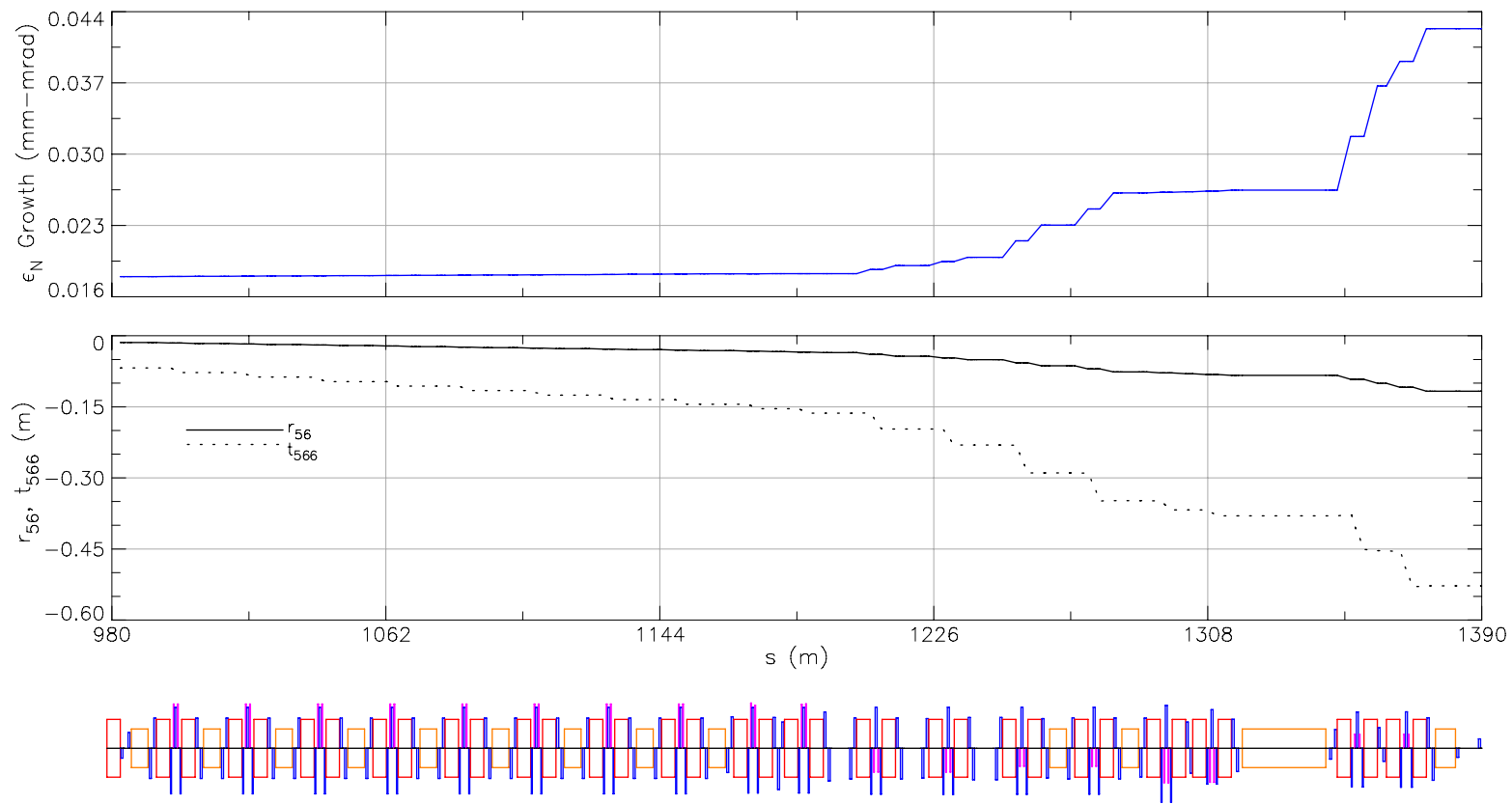


Figure 4.23: Normalized radiative emittance growth ϵ_N and time of flight terms r_{56} and t_{566} for the SA. Emittance growth for this section is dominated by relatively strong bends in Cell E.

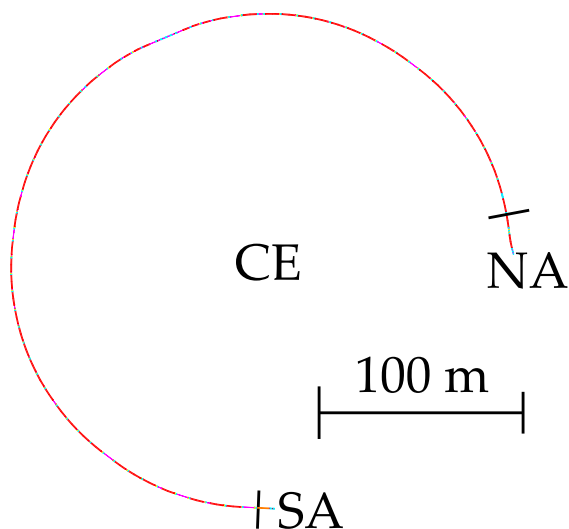


Figure 4.24: Layout for the CE section.

4.3.4 CE – CESR

The CERL baseline design intends to reuse most of the currently existing CESR elements. The layout for the CE is shown in Fig. 4.24. This section is approximately 540 m long, containing 58 dipole magnets, 72 quadrupole magnets, and 60 sextupole magnets. It is configured in an alternating dipole-quadrupole (FODO) arrangement.

Unfortunately, this configuration is not completely regular, and it does not lend itself to periodic cells as in the other sections. Therefore it is optimized as a whole for controlled beta functions and emittance growth, as well as controlled time of flight terms, by varying all quadrupole strengths for the linear optics, and all sextupole strengths for the second order optics. These optimizations were performed by James Crittenden and Carol Johnstone, with the optics shown in Fig. 4.25, and the radiative emittance growth and time of flight terms are shown in Fig. 4.26.

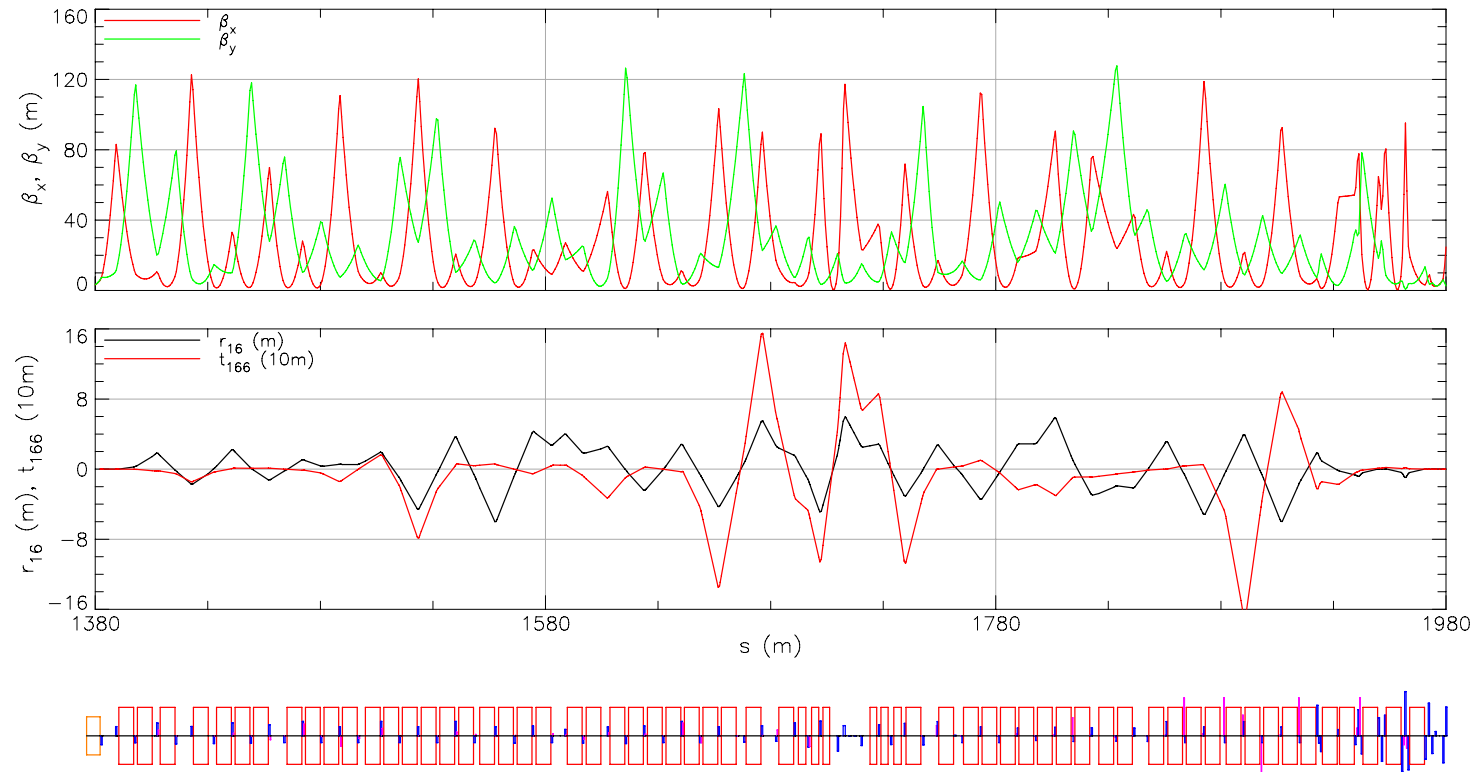


Figure 4.25: Optics for the entire CE section.

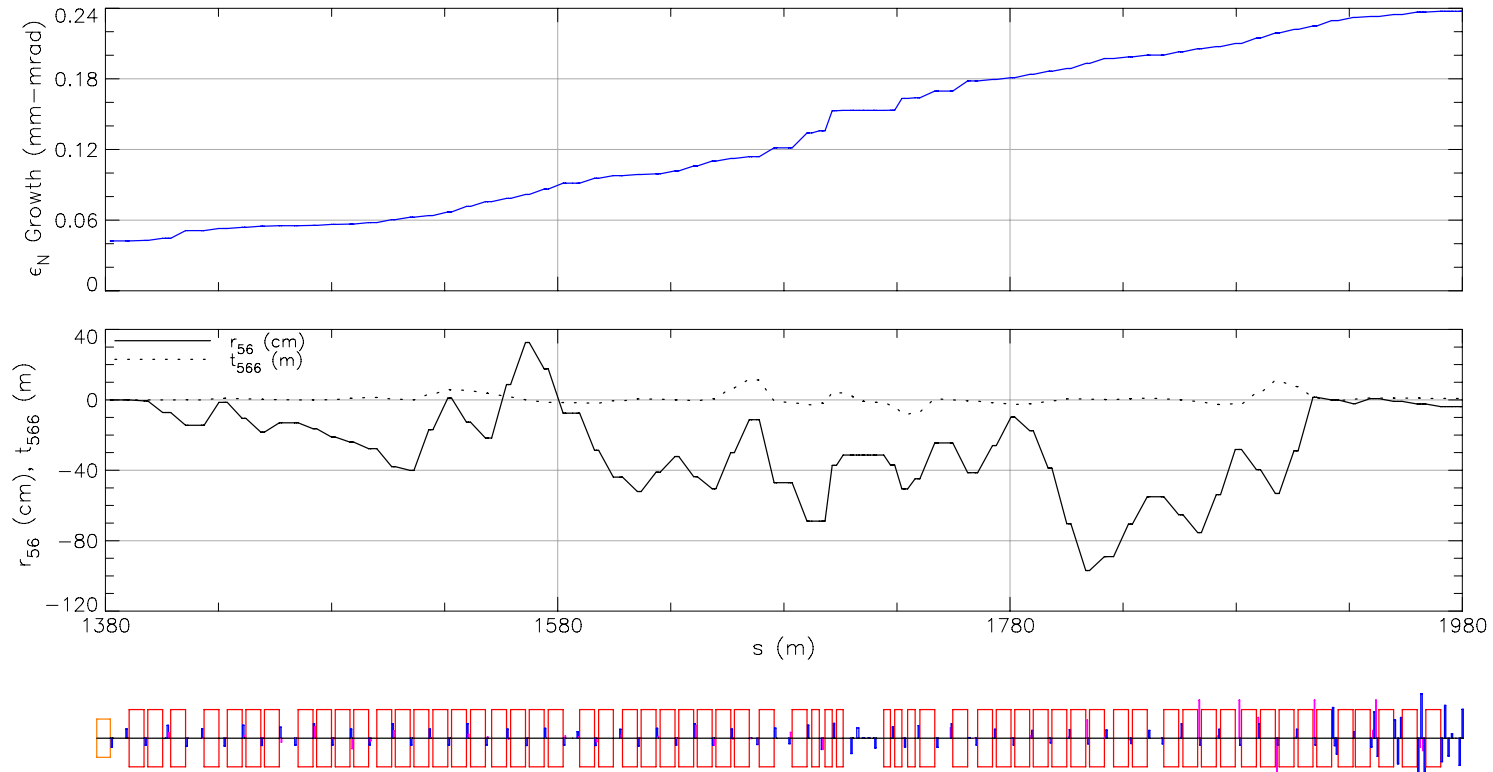


Figure 4.26: Normalized radiative emittance growth ϵ_N and time of flight terms r_{56} and t_{566} (note the scaling) for CE.

Roughly speaking, the reason for the poor emittance growth is that there are not enough quadrupole magnets per dipole magnet to simultaneously control the beta functions and dispersion enough to minimize Eq. (2.177).

Low Emittance Upgrade

The CESR magnets can effectively transport the beam from the SA to the NA, but they contribute to the vast majority of the emittance growth in the CERL. Here an upgrade option for the CE section is presented that provides very low emittance growth. It uses the same 6.57 m long dipole magnets as in the CESR, with the addition of quadrupole and sextupole magnets.

The CESR tunnel is a mixture of pure arcs connected by straight sections. In this upgrade, the CESR dipole magnets are rearranged to span the arcs by periodic cells containing two bends. The straight sections are drifts with three quadrupole magnets. For optimization, CE is divided into seven cell types:

Cell P Periodic cell with two bends – Occurs twenty times

Cell A Matches optics from the SA into the first Cell P

Cell B, C, D, E Matches optics from a Cell P to a Cell P

Cell F Matches optics from the last Cell P into the NA

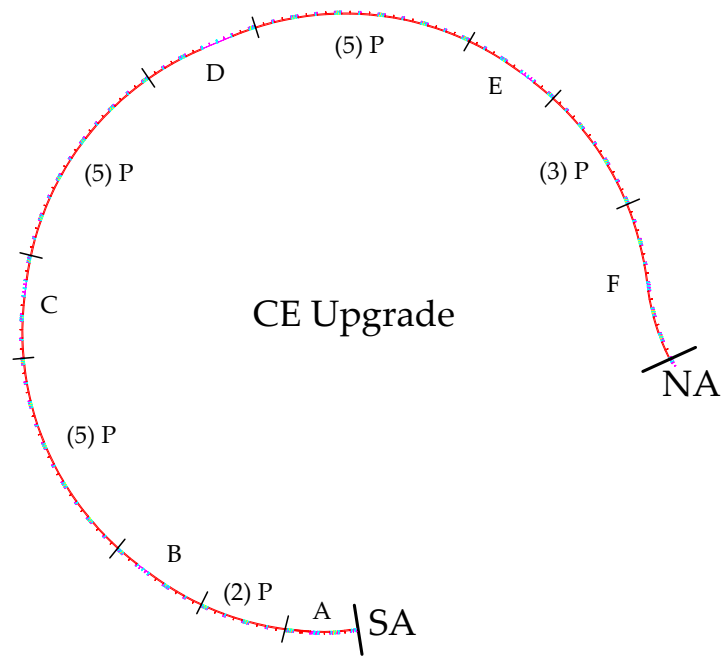


Figure 4.27: Layout for a low emittance upgrade for the CE section.

The positions of these cells are shown in Fig.4.27. Essentially multiple Cell P sections comprise most of CE, with matching cells A and F for connecting to the SA and the NA, respectively. Cells B, C, D, and E account for the straight sections in the tunnel. Each is similar to two Cell P sections, with an extended drift and extra quadrupole magnets between the third and fourth bends.

The beta functions and first and second order dispersion in Cell P are shown in Fig. 4.28. The four quadrupole strengths are optimized to produce periodic beta functions and first order dispersion that yield a specified value for the r_{56} contribution and low radiative emittance growth. Those quantities can be seen in Fig. 4.29. Next the two sextupole strengths are optimized to produce a specified value for the t_{566} contribution, also seen in Fig. 4.29.

The optics for Cell B are shown in Fig. 4.30. Due to symmetry, it is sufficient

to optimize the section by setting the Twiss parameters and dispersion at the entrance to those of the end of Cell P, and vary quadrupole strengths symmetrically about the center quadrupole magnet in the straight section to produce $\alpha_x(s_c) = 0$, $\alpha_y(s_c) = 0$, and $D'(s_c) = 0$, with $s = s_c$ in the center of that magnet. The value of $D(s_c)$ can be chosen freely, and therefore the r_{56} contribution by the section is adjustable. The two sextupole strengths are optimized symmetrically to match $t_{266}(s_c) = 0$.

Cells C and E are practically identical to Cell B, all having a 6.3 m straight section. Cell D has a longer straight section of 12.2 m, but the optimization strategy is the same as that of Cell B.

The optics for the matching Cells A and F can be seen in Fig. 4.31 and Fig. 4.32, respectively. There are enough quadrupole and sextupole magnets in these sections to match Twiss parameters between the adjacent sections, and to fine tune the total r_{56} and t_{566} contributions by CE. The resulting optics for all of CE are shown in Fig. 4.33. Radiative emittance growth and time of flight terms are shown in Fig. 4.34. There one sees that, due to the similarity of all the cells, emittance growth is very regular and relatively small in the bulk CE.

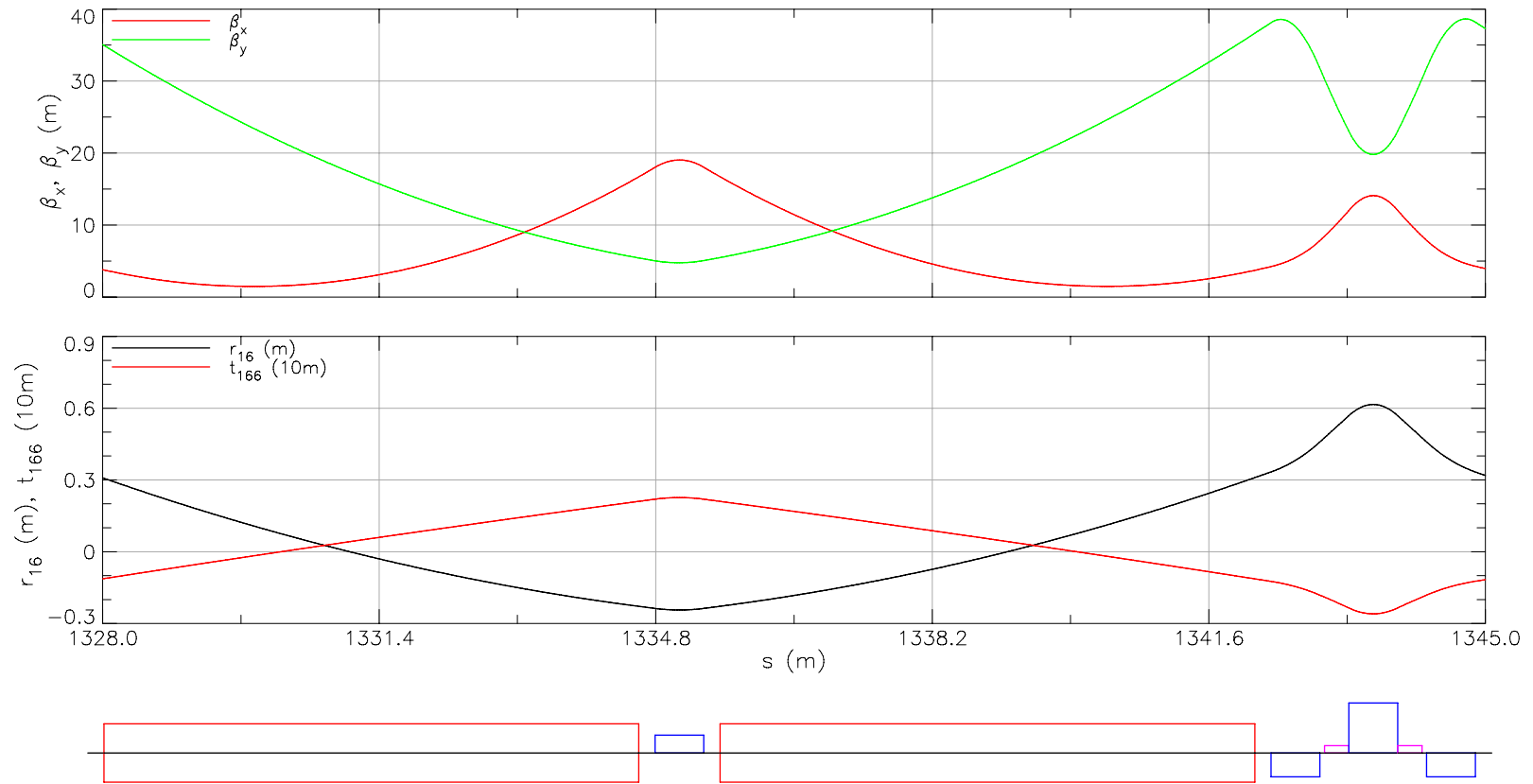


Figure 4.28: Optics for the CE Upgrade Cell P section. The four quadrupole strengths are varied to produce periodic beta functions and dispersion with a specified contribution time of flight term r_{56} (in this case near zero) and as low as possible radiative emittance growth. The two sextupole strengths are then optimized to produce periodic section order dispersion with a specified time of flight term t_{566} contribution.

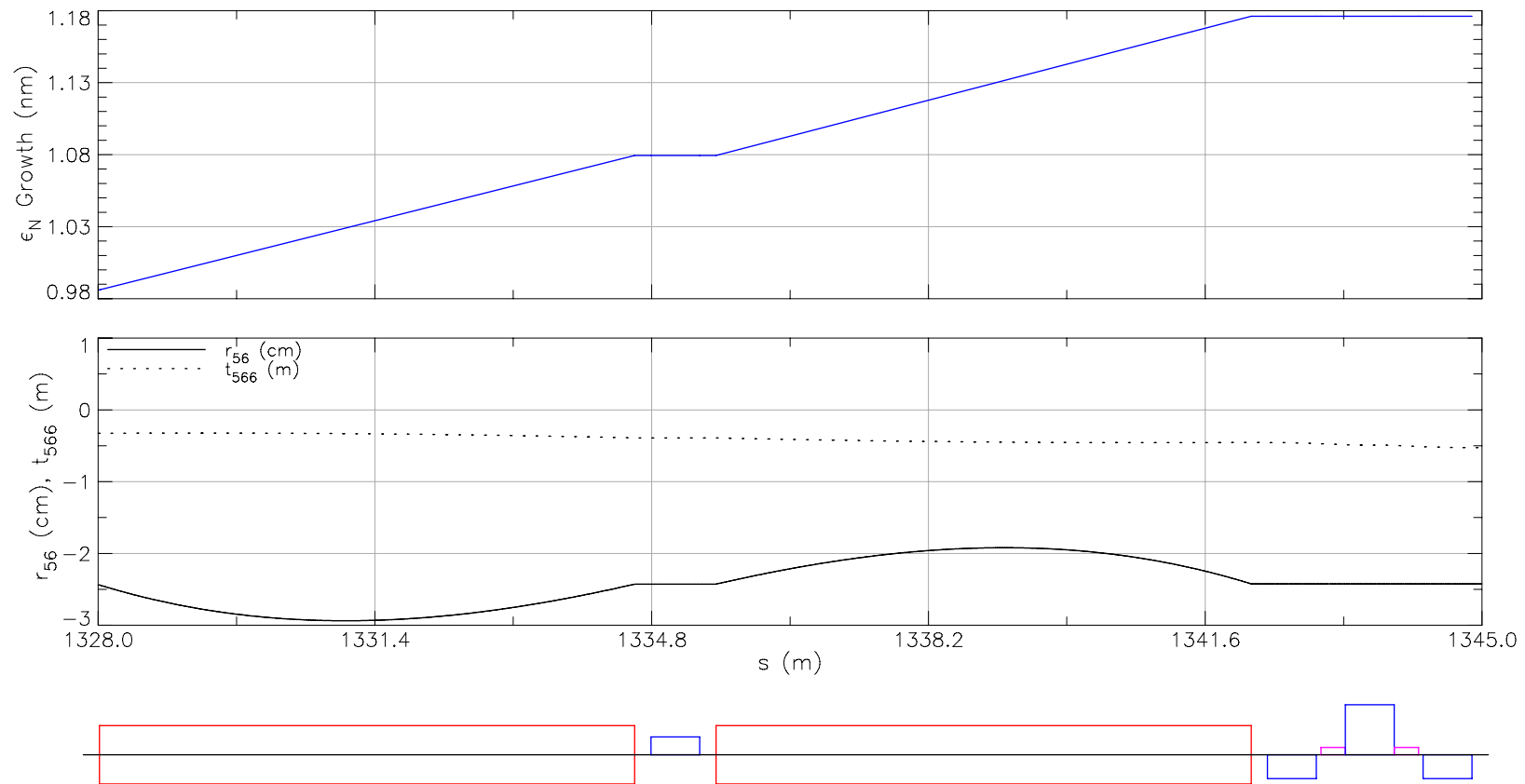


Figure 4.29: Normalized radiative emittance growth ϵ_N and time of flight terms r_{56} and t_{566} for the CE Upgrade Cell P section.

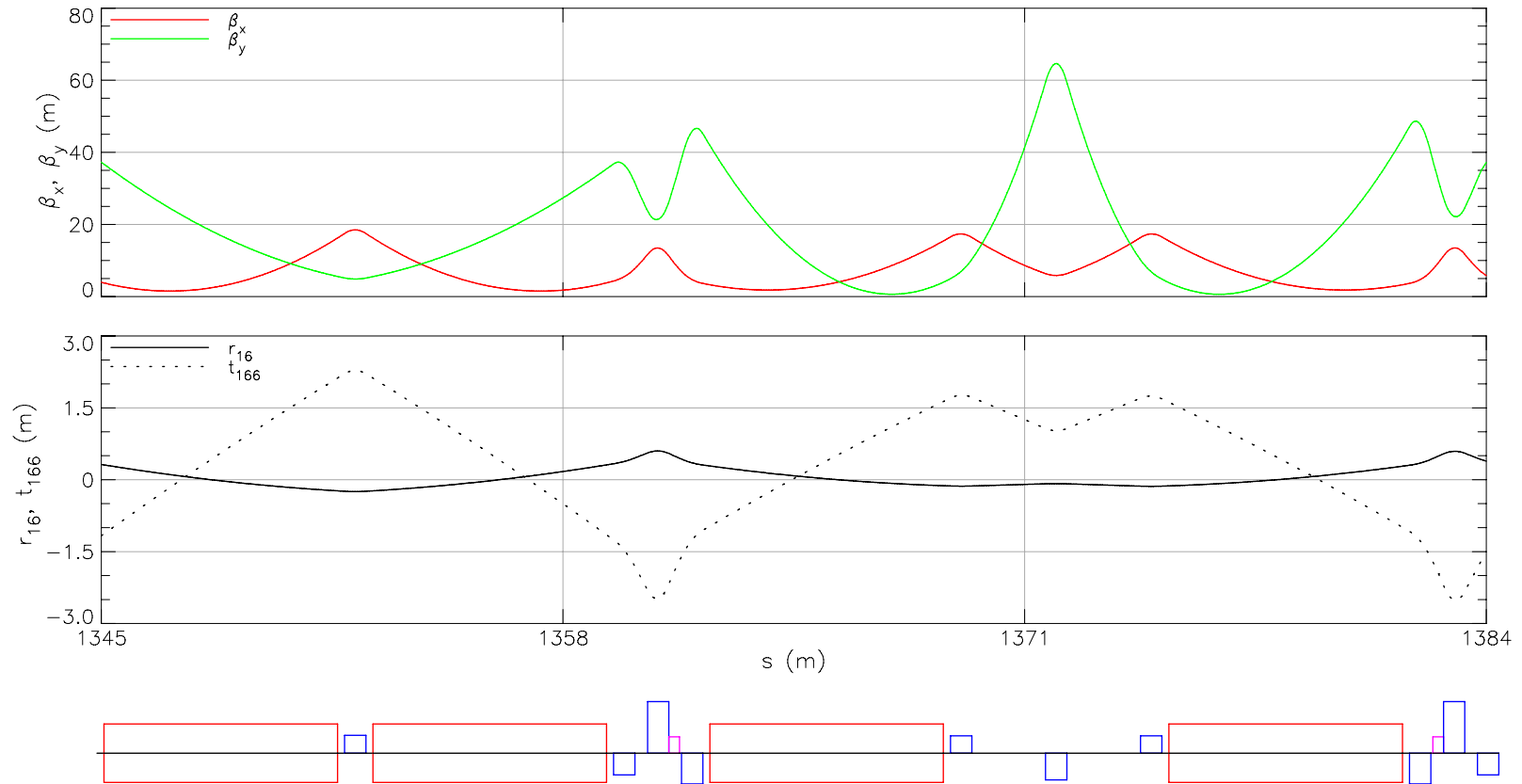


Figure 4.30: Optics for the CE Upgrade Cell B section. This section begins with Twiss parameters and dispersion from a Cell P. Quadrupole strengths are varied symmetrically about the quadrupole magnet in the center of the 6.2m straight section to produce $\alpha_x(s_c) = 0$, $\alpha_y(s_c) = 0$, and $D'(s_c) = 0$, with $s = s_c$ in the center of that magnet. Additionally the dispersion is adjusted to produce a specified value for the r_{56} contribution by the cell. Sextupole strengths are varied symmetrically to produce $t_{266}(s_c) = 0$. Cells C,D, and E are optimized similarly.

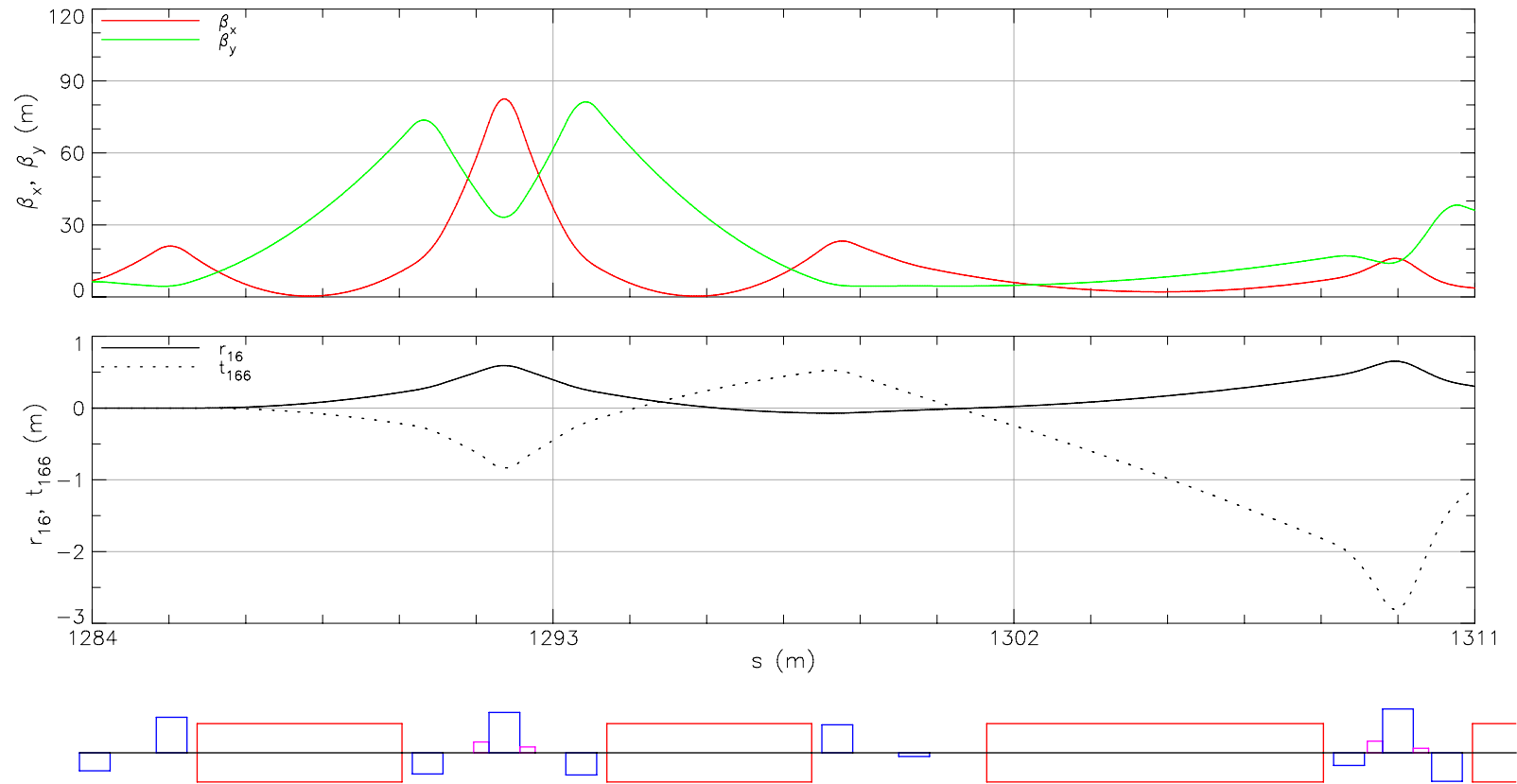


Figure 4.31: Optics for the CE Upgrade Cell A section, which matches Twiss parameters and dispersion from the end of the SA into the first CE Cell P section. All quadrupole and sextupole strengths are varied independently to achieve this matching, with the additional constraints of providing specified time of flight terms and as low as possible radiative emittance growth.

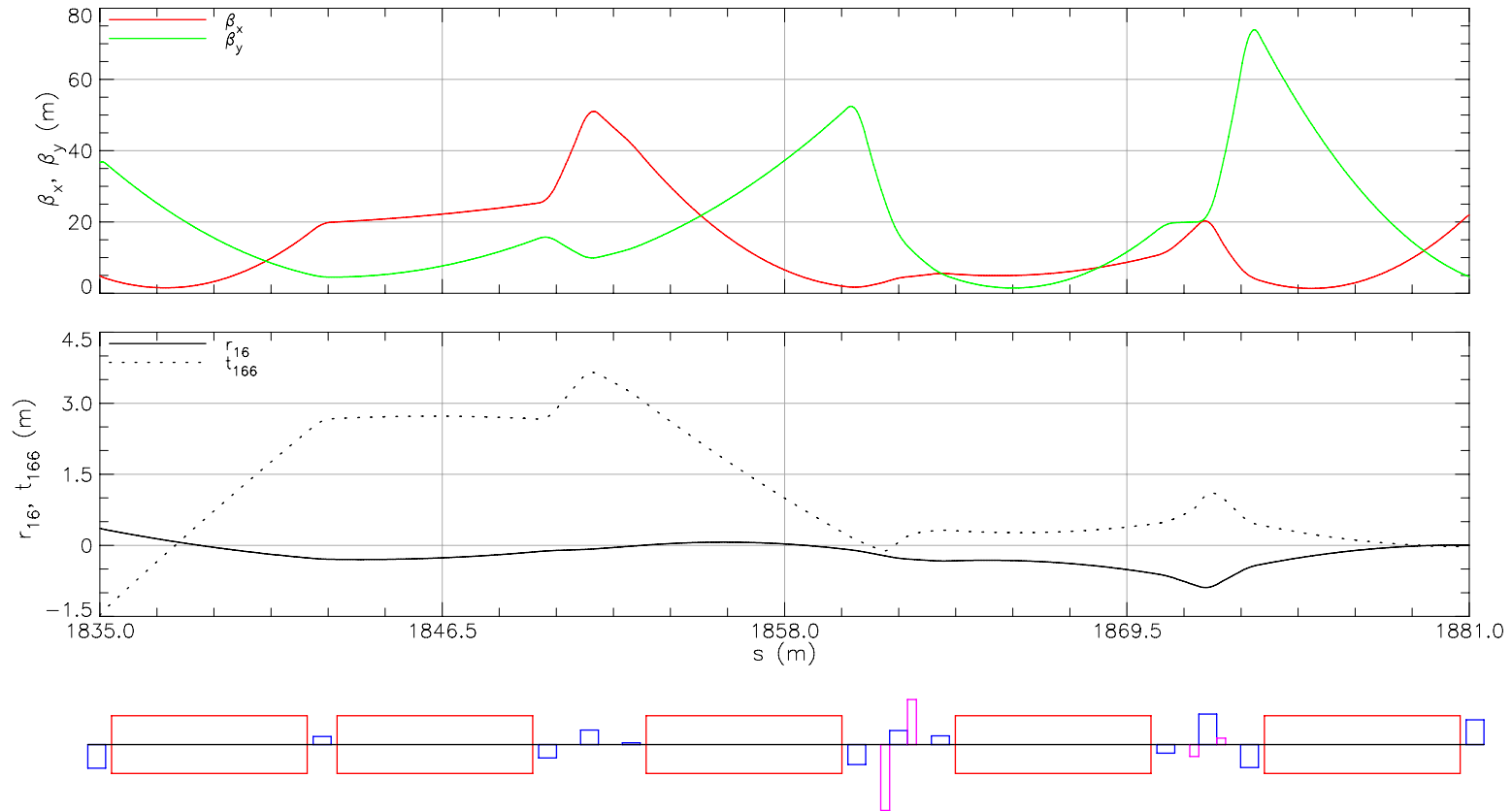


Figure 4.32: Optics for the CE Upgrade Cell F section, which matches Twiss parameters and dispersion from the last CE Cell P section into the NA. All quadrupole and sextupole strengths are varied independently to achieve this matching, with the additional constraints of providing specified time of flight terms and as low as possible radiative emittance growth.

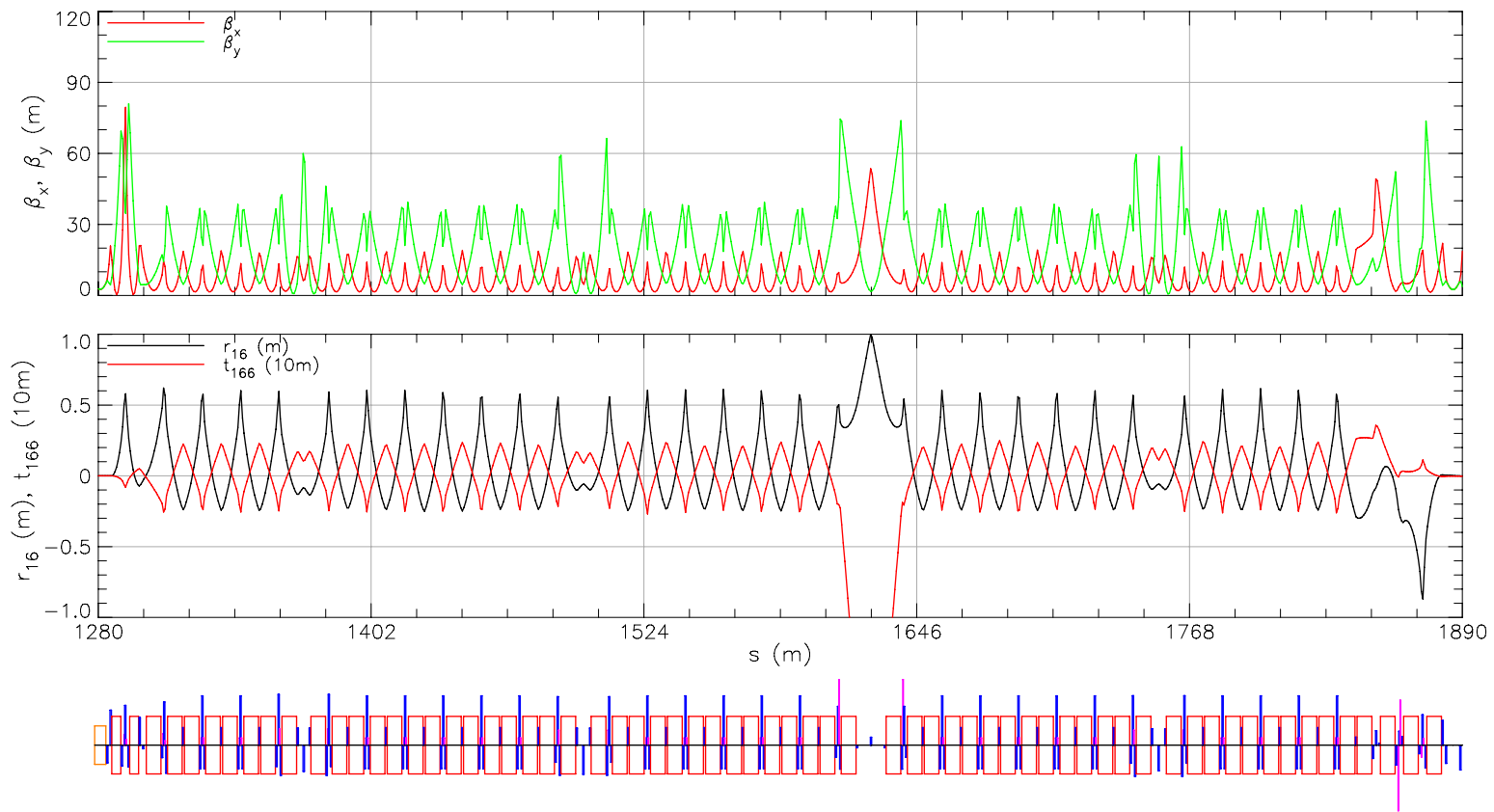


Figure 4.33: Optics for the entire CE Upgrade section.

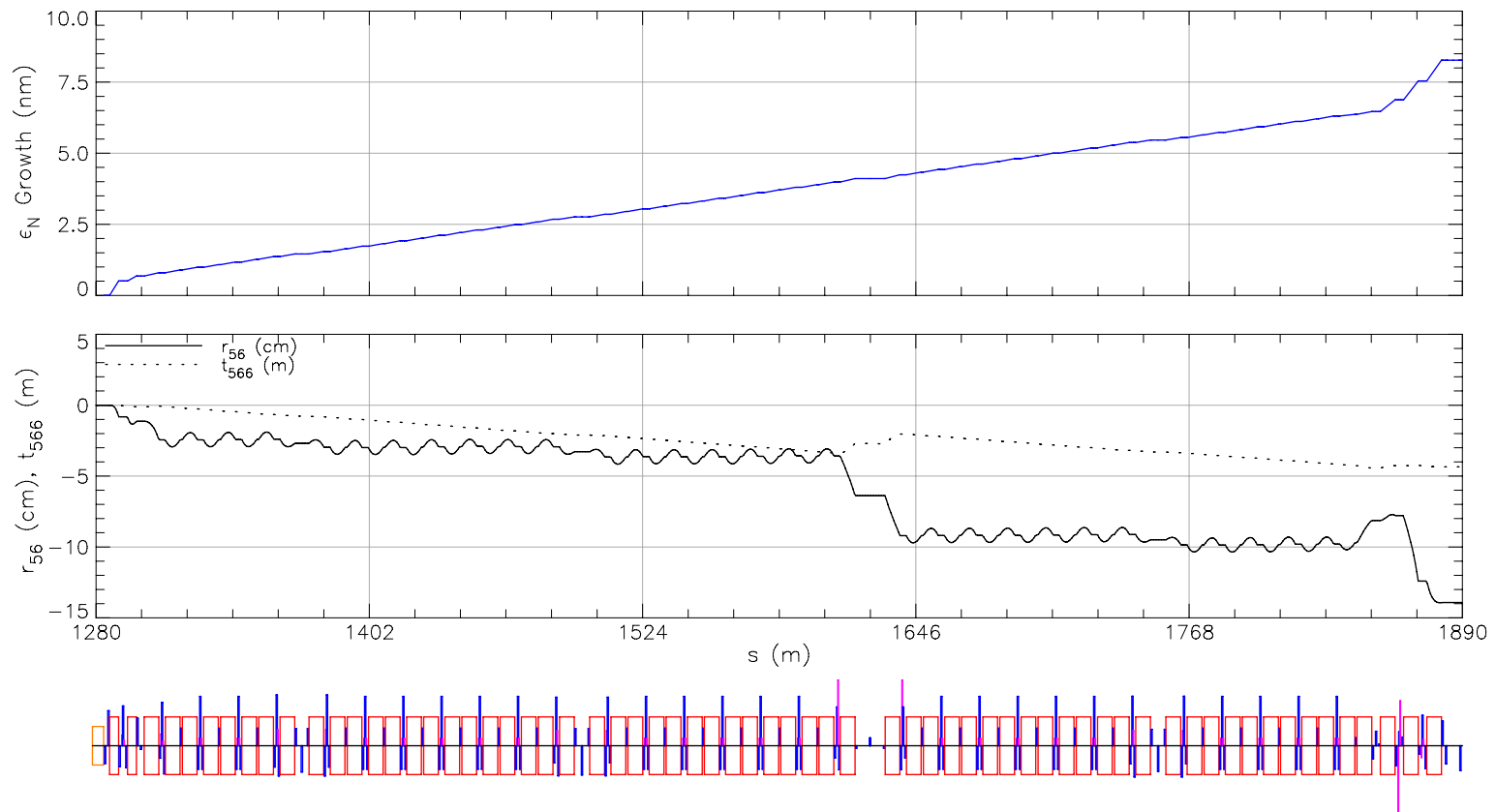


Figure 4.34: Normalized radiative emittance growth ϵ_N and time of flight terms r_{56} and t_{566} for the entire CE Upgrade section.

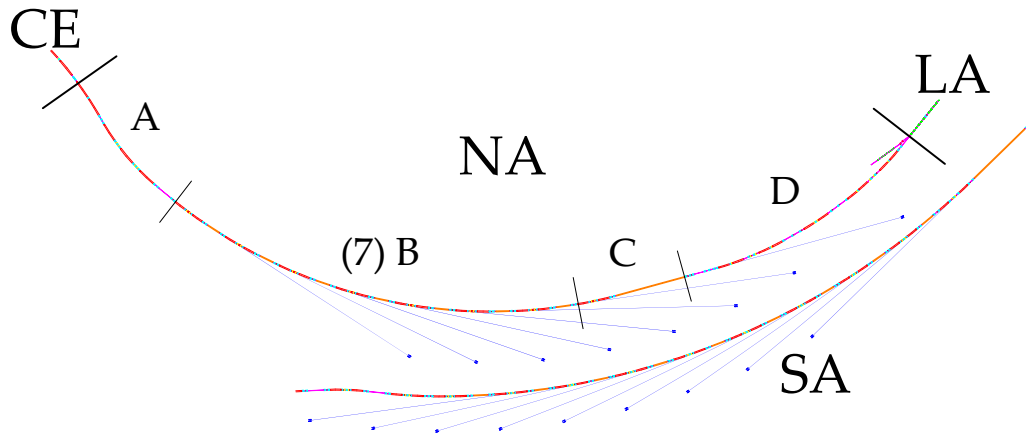


Figure 4.35: Layout for the NA section. Part of the SA is shown for reference.

4.3.5 NA – North Arc

The NA is approximately 354 m long and contains the final set of seven 5 m undulators and a single 25 m undulator before energy recovery in LA. It is divided into four cell types:

Cell A Matches optics from CE into Cell B

Cell B Periodic section containing a three-bend isochronous achromat and a 5 m undulator – occurs seven times

Cell C Matches optics from the last Cell B into a 25 m undulator

Cell D Bunch decompression section, matches optics into LA for energy recovery

The layout for these cells is shown in Fig. 4.35.

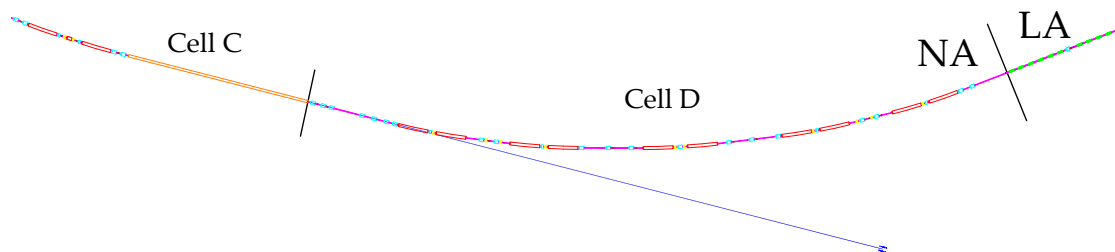


Figure 4.36: Layout showing the NA Cell D.

In the bunch compression mode, where CE compresses the bunch, it is necessary to keep the bunch short in all undulators. Therefore, in addition to being achromatic, the bends between all undulators are also isochronous. This is achieved by adding a short “negative” bend between the two long bends in an achromat, which can be seen in all Cell B and Cell C sections. This short bend is also designed to produce an adjustable quadrupole moment.

Besides this short bend, all Cell B sections have the same layout as the SA Cell B sections, with altered drift lengths and bend strengths, and each begins with the bends as opposed to an undulator. Cell C is similar to a Cell B section, except with a longer 25 m undulator. Optimization for these cells is therefore similar to the method described in Section 4.3.3 for SA Cell B, with the additional constraint that $r_{56} = 0$ through a cell. Two sextupole magnets make the section achromatic to second order. The resulting optics for these sections are shown in Figs. 4.37-4.38.

The NA Cell A section matches Twiss parameters and dispersion from CE into the first NA Cell B. Optics for this cell are shown in Fig. 4.39. The first and second order dispersion are fine tuned to give the desired r_{56} and t_{566} terms from the beginning of CE to the beginning of the first NA undulator.

After the 25 m undulator, the NA ends with a ten bend arc that connects the beam back into LA for energy recovery, shown in Fig. 4.36. In the mode where the bunch arrives compressed, this section serves to decompress the bunch by providing rather large dispersion through the central bends and correspondingly large r_{56} compensation. The optics for this cell are shown in Fig. 4.40, with the resulting time of flight terms shown in Fig. 4.41.

Optics for the entire NA section are shown in Fig. 4.42, with radiative emittance growth and time of flight terms shown in Fig. 4.43. Because the time of flight terms are calculated starting at the beginning of the SA, one sees that they indeed go to zero at the end of the NA and thus the SA-CE-NA sections together are achromatic and isochronous to second order.

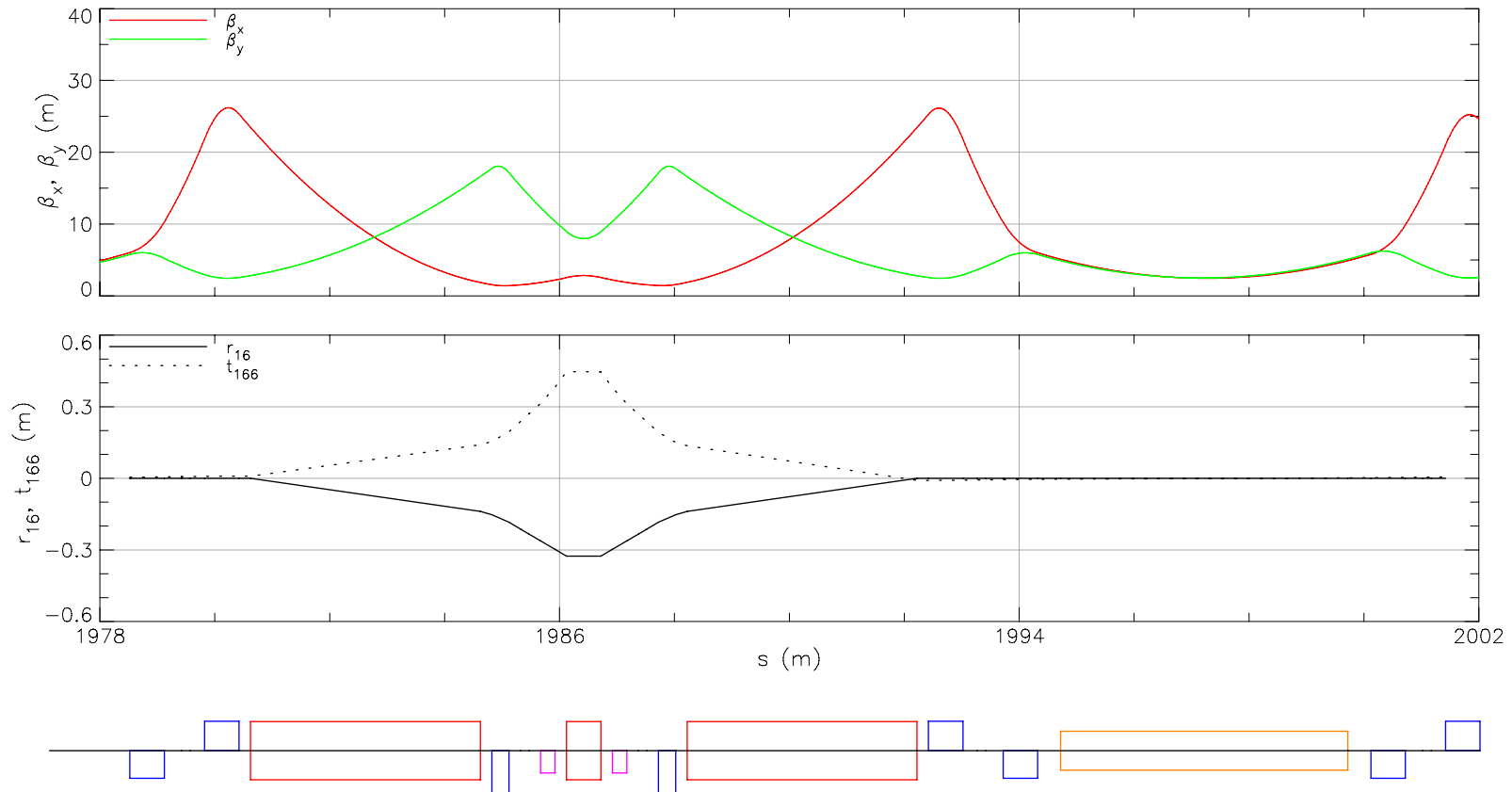


Figure 4.37: Optics for the first NA Cell B section. The layout is the same as the SA Cell B section, shown in Fig. 4.20, with the addition of a short “negative” bend between the 4 m dipole magnets, which allows the section to be isochronous. Optimization is therefore the same as in the SA Cell B, with the additional constraint that $r_{56} = 0$ through the bends.

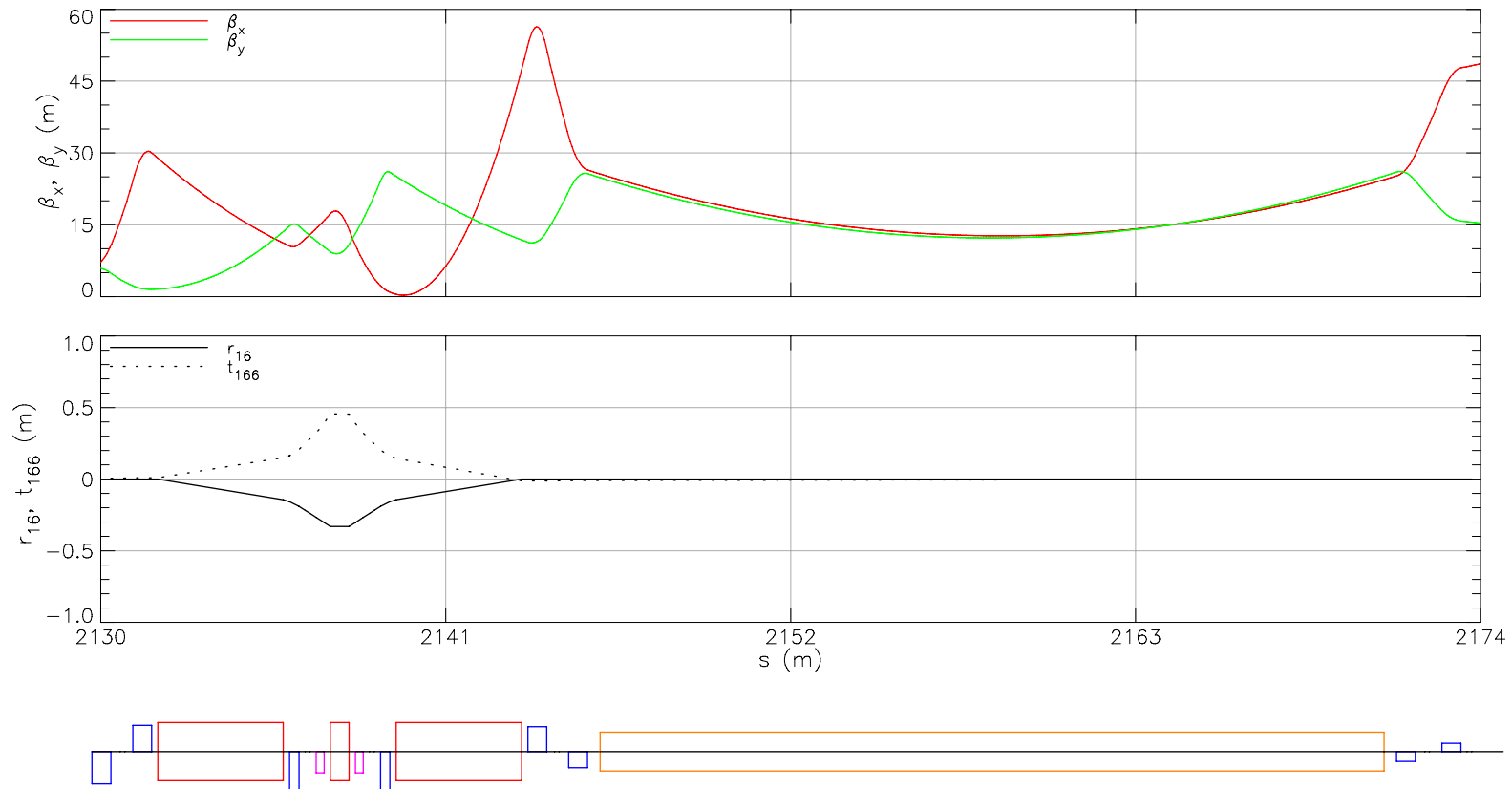


Figure 4.38: Optics for the NA Cell C section. This section is very similar to the NA Cell B section shown in Fig. 4.37, except with a longer 25 m undulator.

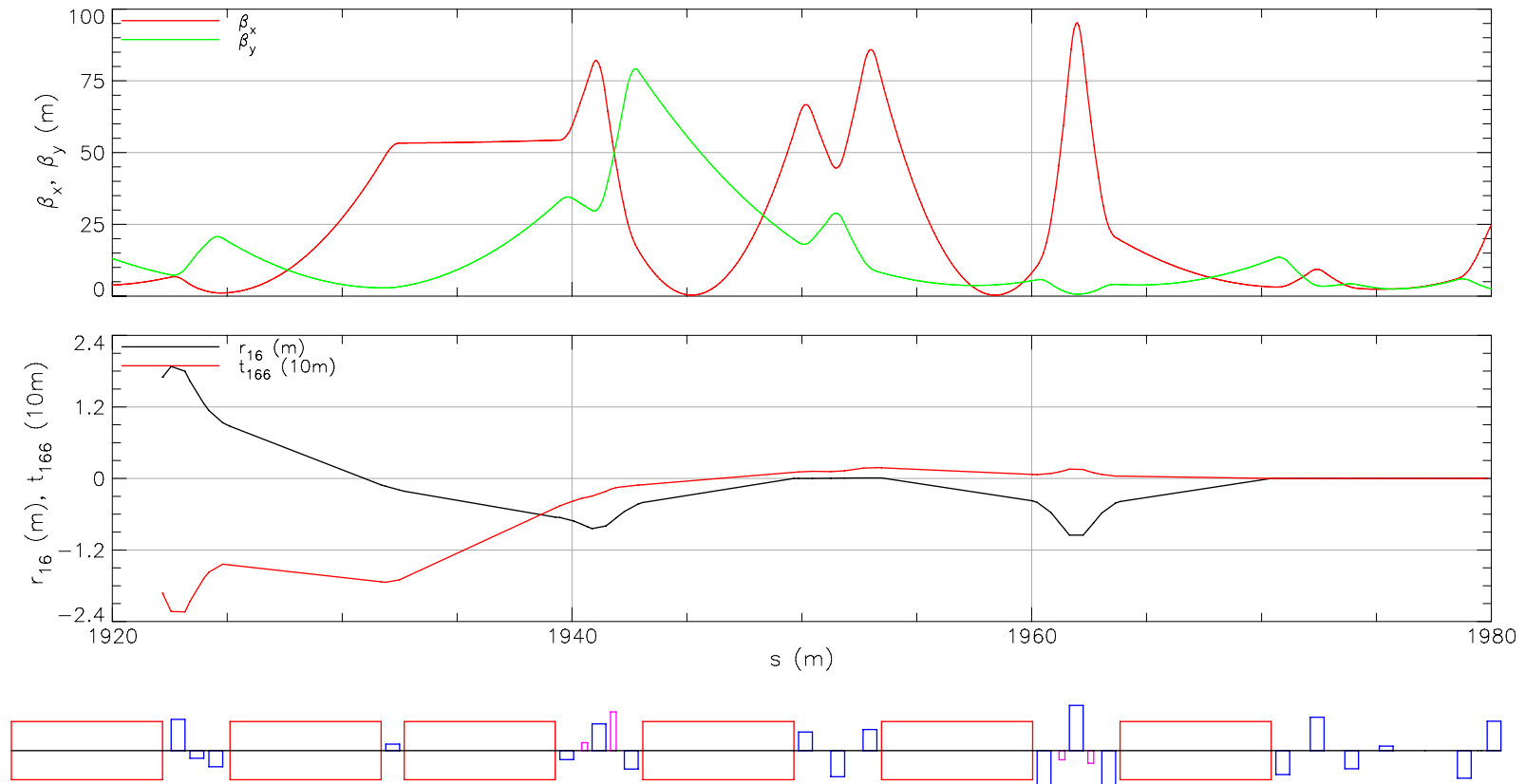


Figure 4.39: Optics for the NA Cell A section. This section accepts Twiss parameters and dispersion from the end of CE, and matches them to the first NA Cell B section. Additionally the time of flight terms r_{56} and t_{566} are fine tuned when the ERL is operating in bunch compression mode. All quadrupole and sextupole strengths are varied independently to satisfy these constraints.

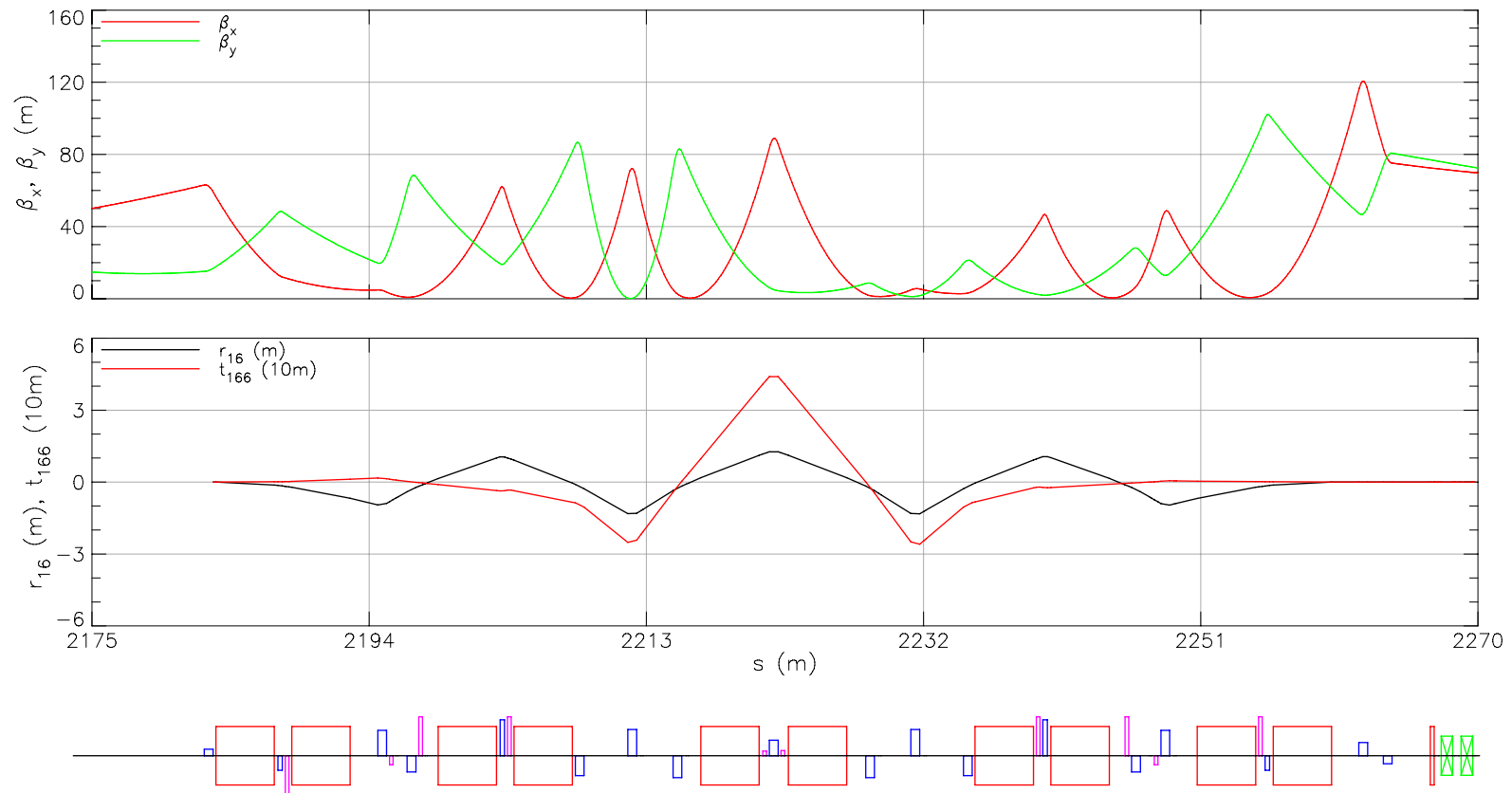


Figure 4.40: Optics for the NA Cell D section. Because there are many quadrupole magnets in this section, the optimization of the beta functions and dispersion is greatly simplified by varying the quadrupole strengths symmetrically about the quadrupole between the 5th and 6th bends in the section, and requiring that $\alpha_x(s_c) = 0$, $\alpha_y(s_c) = 0$, and $D'(s_c) = 0$, with $s = s_c$ located in the center of that quadrupole magnet. Once a solution is found with the desired r_{56} contribution, the last few quadrupole strengths are varied independently to match Twiss parameters into LA for energy recovery. Sextupole strengths are finally adjusted to provide $t_{166} = 0$, $t_{266} = 0$, and a specified t_{566} through the section.

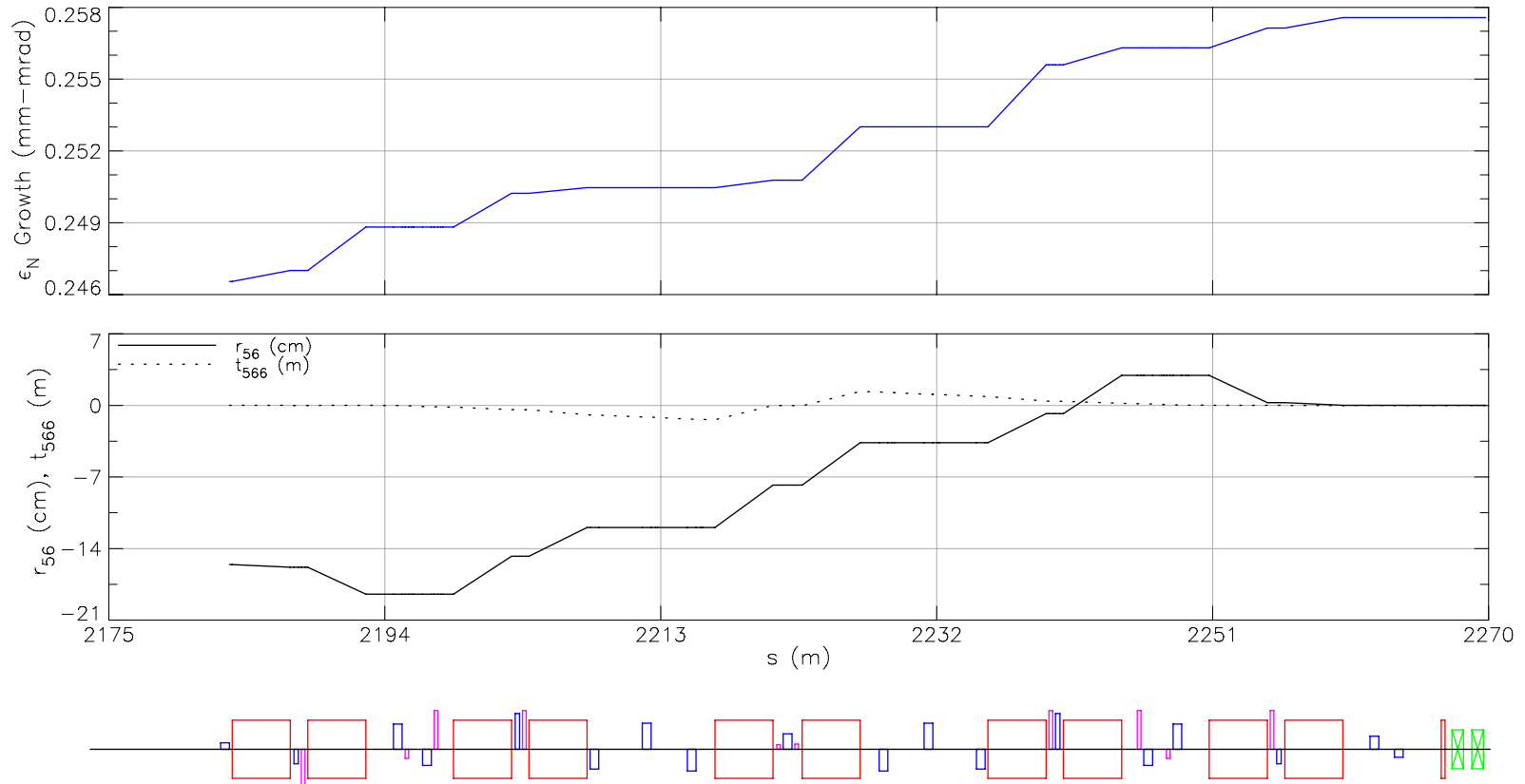


Figure 4.41: Normalized radiative emittance growth ϵ_N and time of flight terms r_{56} and t_{566} for the NA Cell D. The time of flight terms are calculated relative to the beginning of the SA, so here one sees how they are adjusted to make $r_{56} = 0$ and $t_{566} = 0$ at the end of the section.

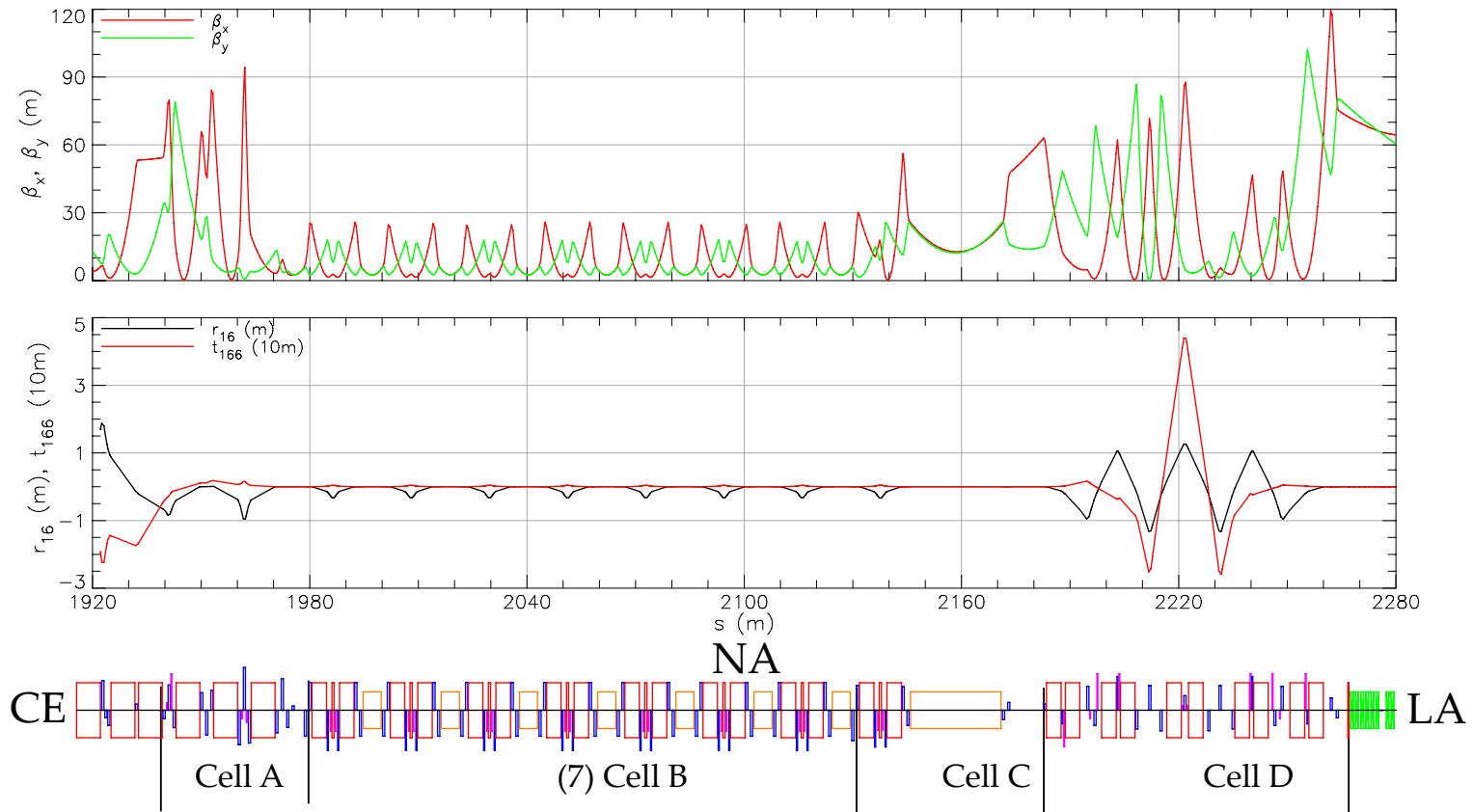


Figure 4.42: Optics for the entire NA section.

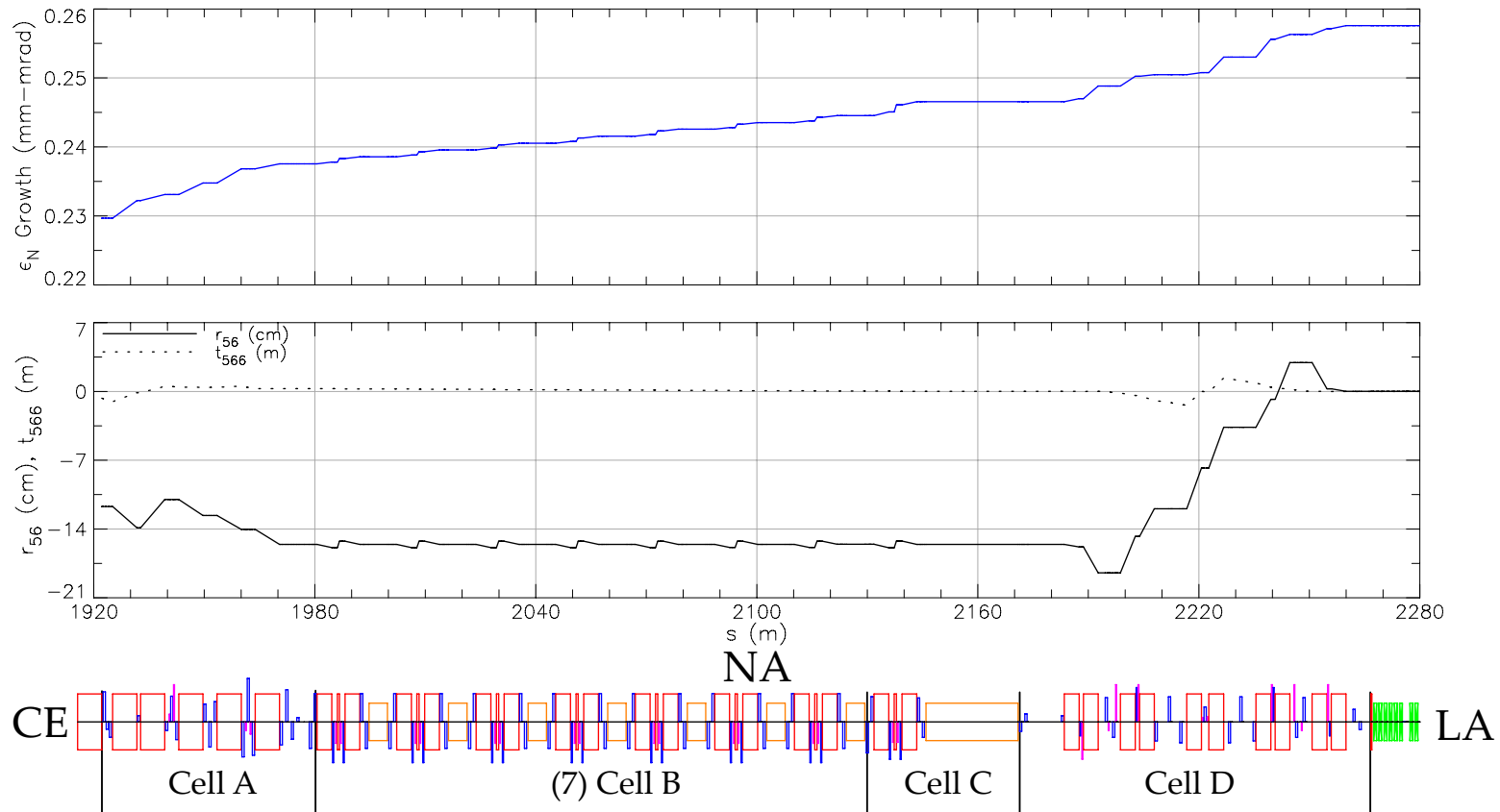


Figure 4.43: Normalized radiative emittance growth ϵ_N and time of flight terms r_{56} and t_{566} for the entire NA section.

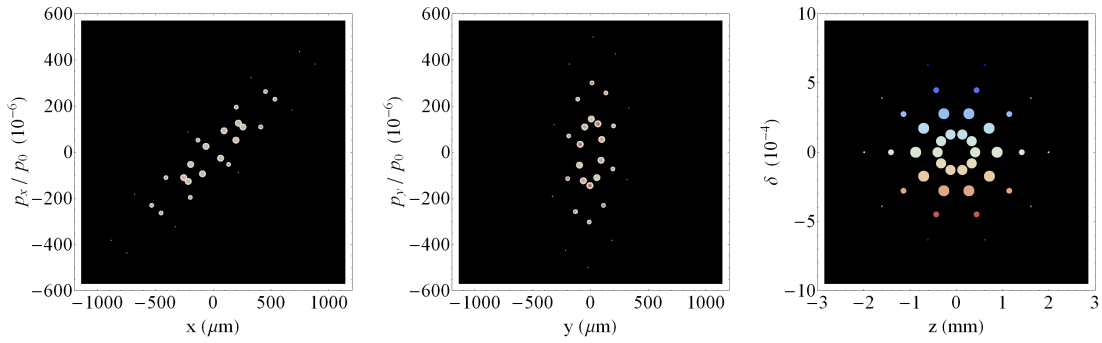


Figure 4.44: Phase space slices of the initial particle distribution used in the CERL. The colors represent different energies, with blue being higher and red being lower than the reference particle energy. The sizes of the particles in these plots are indicative of their sampling weight.

4.4 Particle Tracking

Just as with the MERL, our efforts in designing the CERL lattice are tested by tracking particles through the lattice. The initial distribution is in accordance with the Mode A parameters shown in Tab. 3.1, and is accelerated on-crest with $\phi_{rf} = 0$. It is very similar to the MERL one, only matched to different incoming Twiss parameters, shown in Fig. 4.44.

Particles at the beginning and end of the SA are shown in Fig. 4.45. There it is evident that the TA does a good job in preserving the transverse phase space. The end of the SA shows some chromaticity, but negligible emittance growth. Transportation through CE does disturb the transverse phase space, with particles in the first NA wiggler shown in Fig. 4.46. Notice that the longitudinal phase space has been sheared due to time of flight terms in the SA and NA. The end of the NA corrects for this, as seen in the same figure.

The calculated horizontal and vertical widths σ_x and σ_y for these particles through the SA are shown in Fig. 4.48, along with the normalized horizontal

and vertical emittances. Although it is difficult to see in the figure, the emittance shows negligible increase in emittance through the SA. The same quantities are shown through the NA in Fig. 4.49. Even though the particles in Fig. 4.46 look distorted, it turns out that the emittance growth is negligible through CE and the NA.

Normalized emittances and energy spread through the entire CERL are shown in Fig. 4.50. The bunch widths and length are shown in Fig. 4.51. There one sees that the bunch width in the horizontal plane becomes very wide in CE due to the large dispersion there.

The particles at the end of the CERL are shown in Fig. 4.47, calculated with and without the sextupole magnets turned on. Here we see that the CERL does not fare well with sextupole magnets turned off, showing a large increase in energy spread. Additionally the normalized beam emittance in CE is increased from 0.3 mm-mrad to approximately 0.6 mm-mrad when sextupoles are off (not plotted).

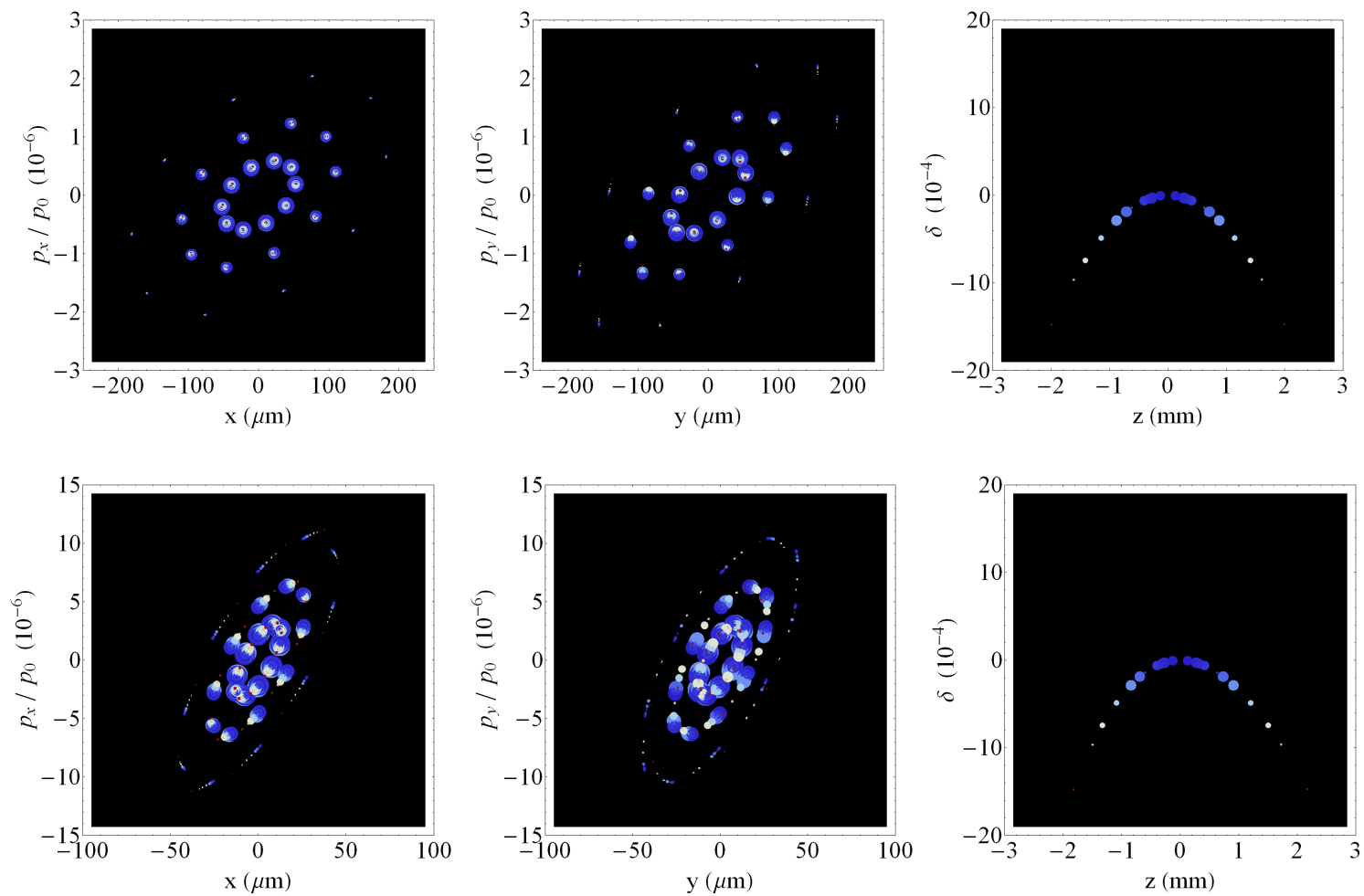


Figure 4.45: Particles at the beginning (top row) and end (bottom row) of the SA for Mode A.

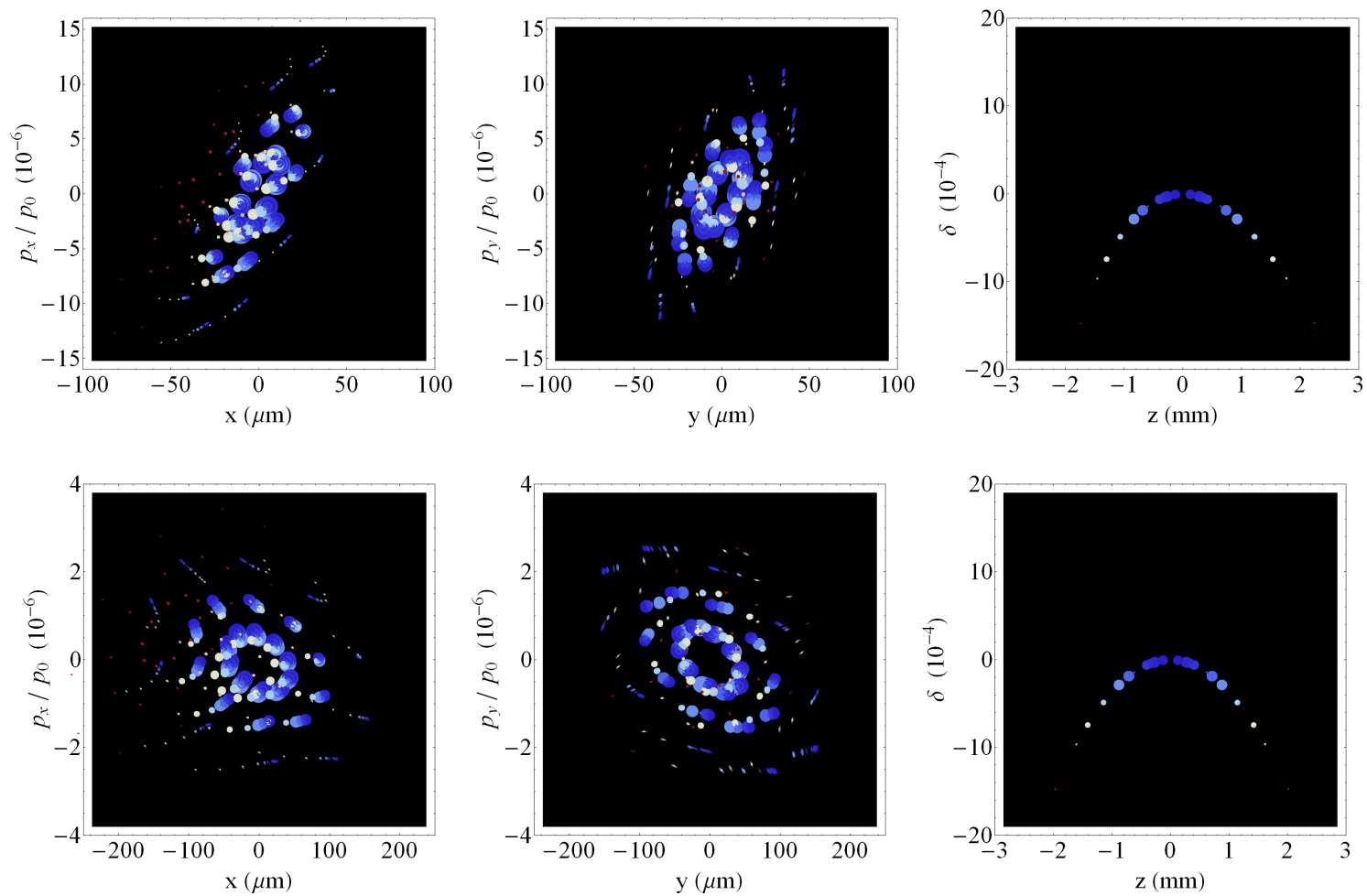


Figure 4.46: Particles at the beginning (top row) and end (bottom row) of the NA for Mode A.

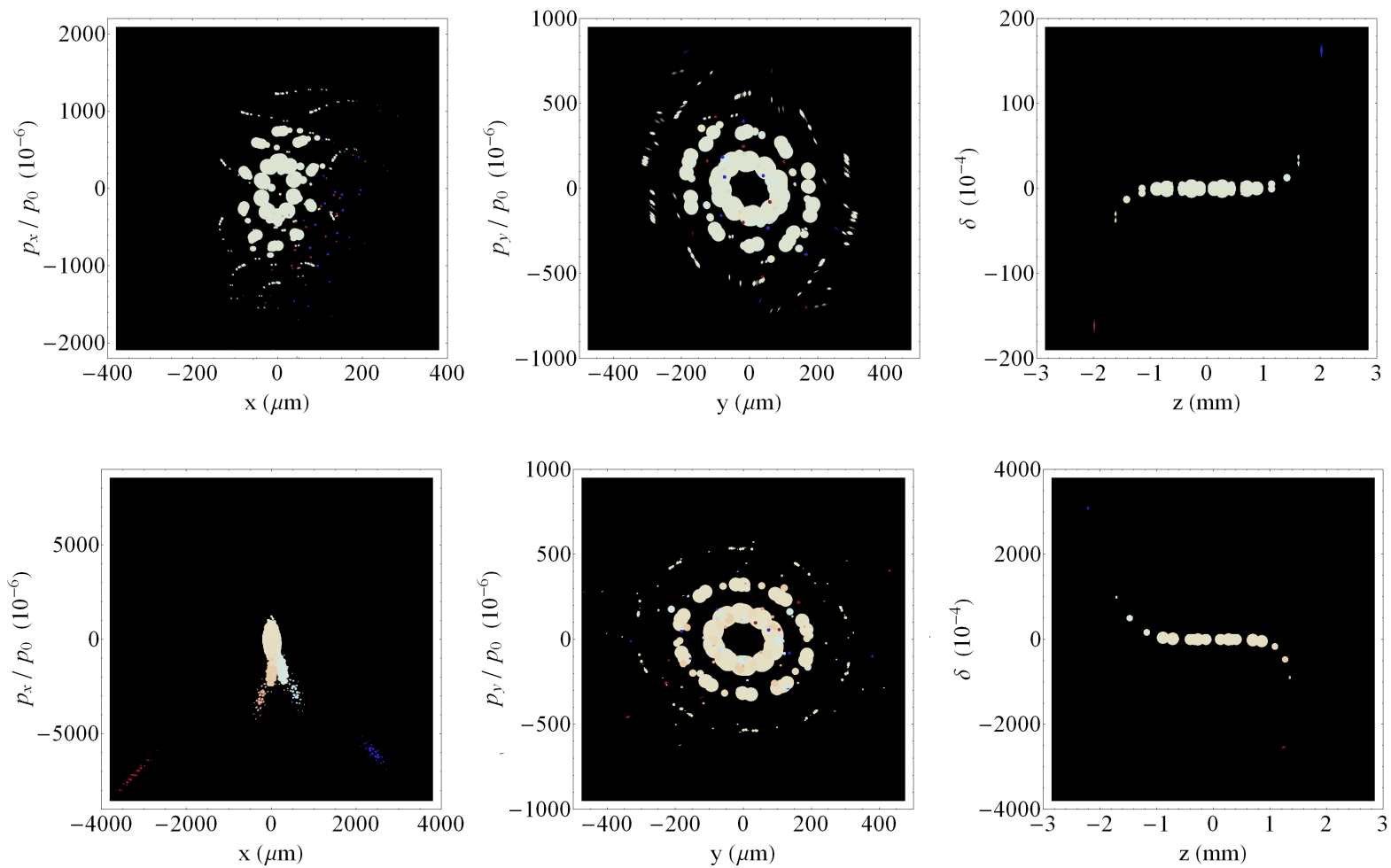


Figure 4.47: Particles at the end of the CERL. The top row is with sextupoles on, and the bottom row is with sextupoles off.

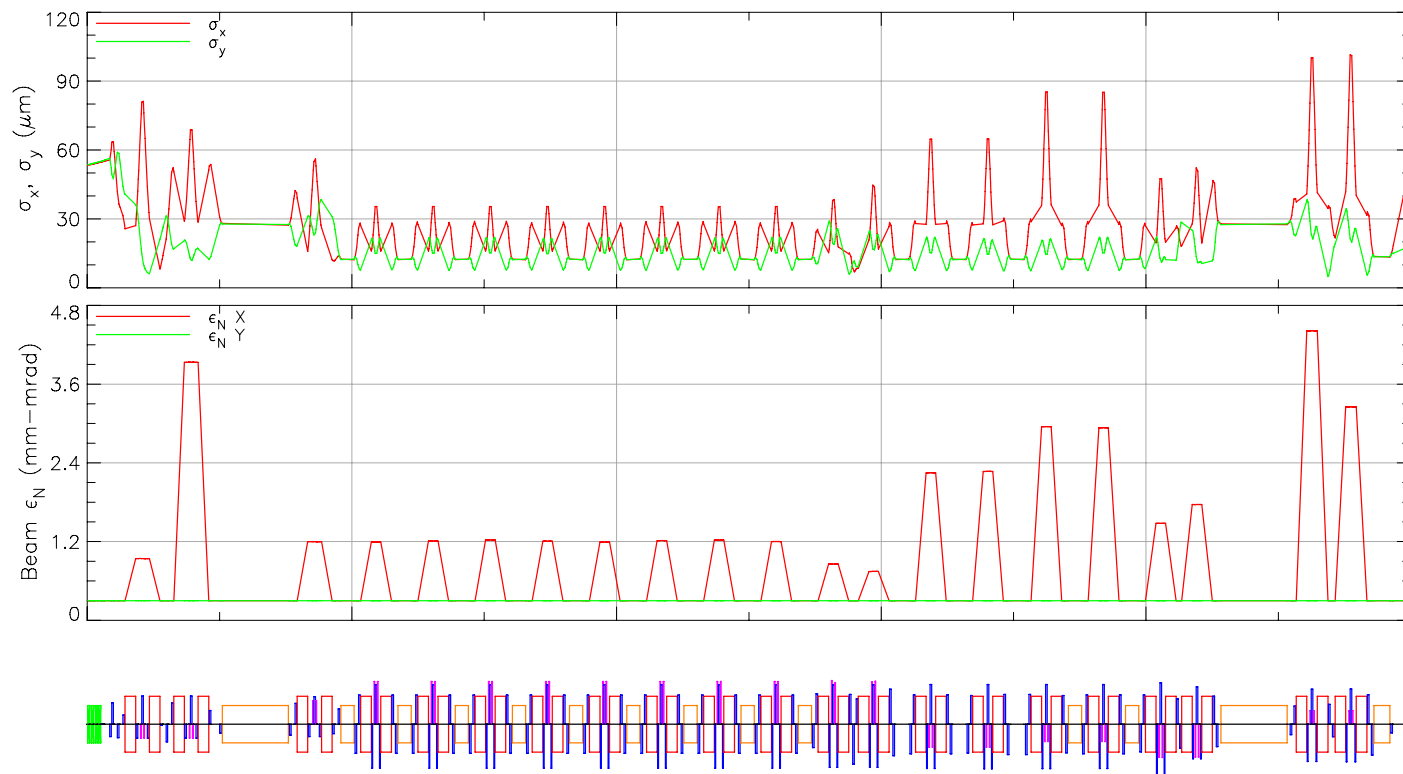


Figure 4.48: Mode A bunch widths and normalized emittances through the SA, calculated using an initial distribution shown in Fig. 4.44.

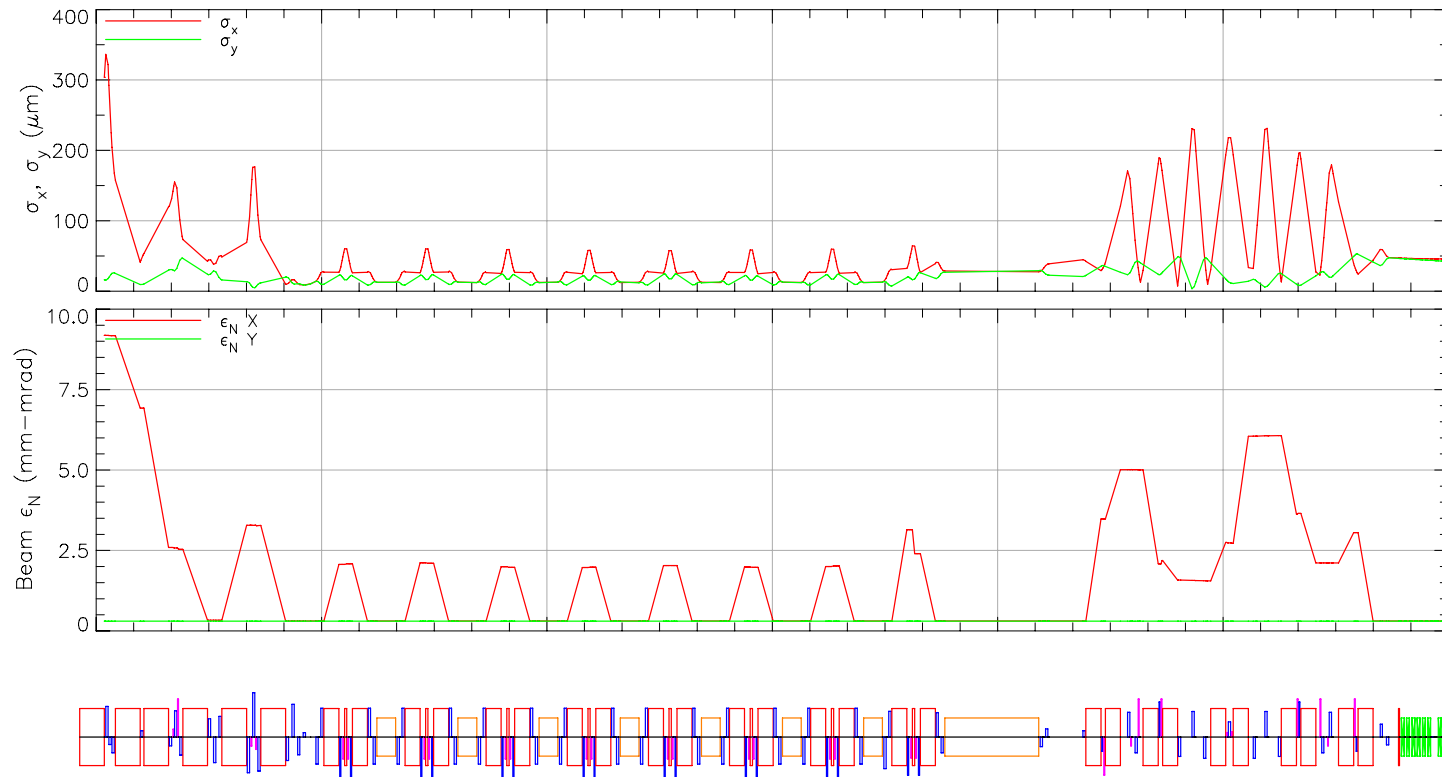


Figure 4.49: Mode A bunch widths and normalized emittances through the NA, calculated using an initial distribution shown in Fig. 4.44. The normalized emittance at the end is marginally larger than the initial 0.3 mm-mrad emittance.

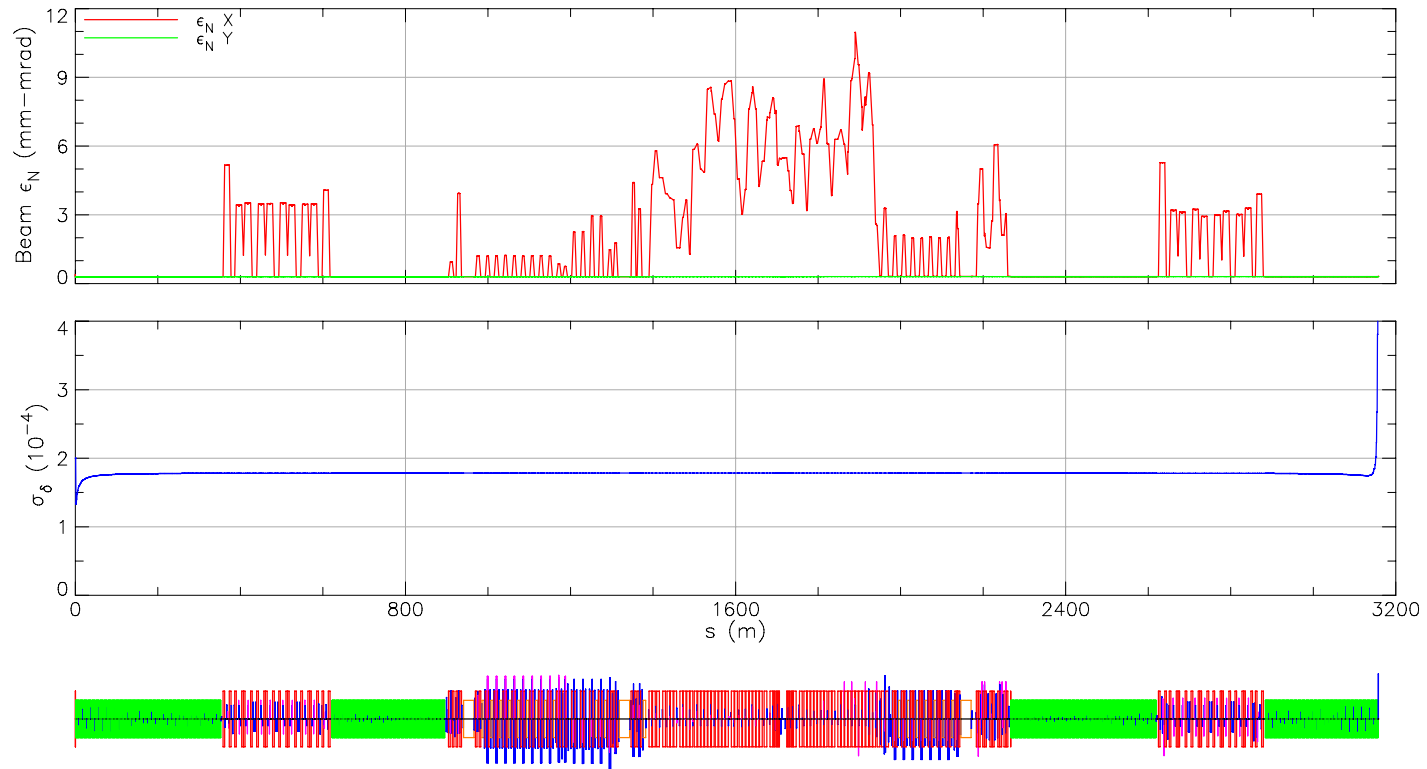


Figure 4.50: CERL Mode A normalized emittances and energy spread from particle tracking, using an initial distribution shown in Fig. 4.44.

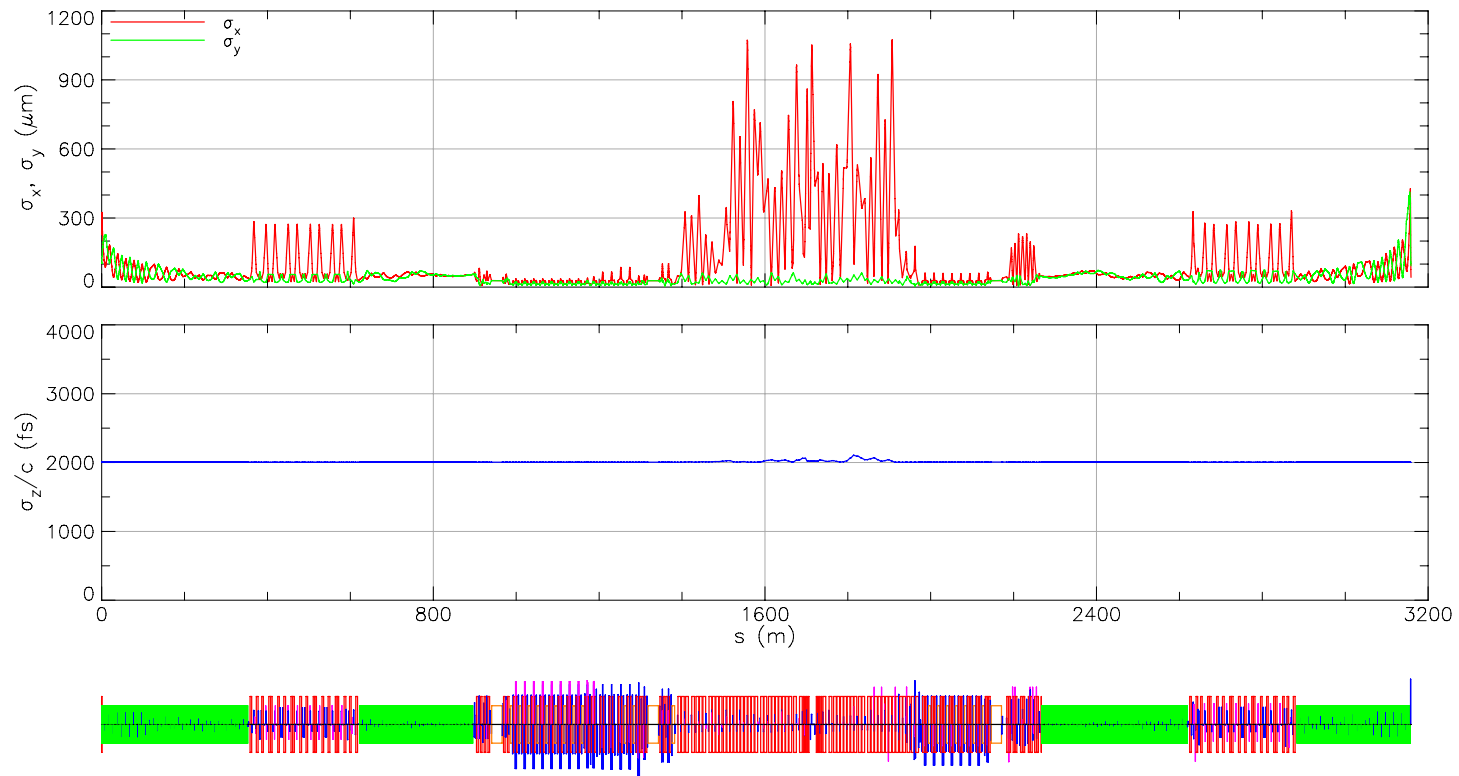


Figure 4.51: CERL Mode A bunch widths and bunch length from particle tracking, using an initial distribution shown in Fig. 3.17.

4.5 Bunch Compression

Bunch compression, described in Section 3.5, can be performed when there is a correlation in (z, δ) phase space that can be manipulated by time of flight terms. This correlation is created by sending bunches off-crest through the linacs, and optimizing the r_{56} and t_{566} terms in an arc.

Mode C in Tab. 3.1 is the bunch compression mode for the CERL. Just as in the MERL, we choose $\phi_{rf} = 9^\circ$, along with $r_{56} = -0.225$ m and $t_{566} = -2.9$ m in order to compress the bunch to $\sigma_z/c = 100$ fs at the end of CE. The optimized dispersion and time of flight terms that give these values are shown in Fig. 4.52.

This compression is tested by tracking particles. Unfortunately, even with r_{56} and t_{566} properly tuned, the bunch is unable to achieve the desired compressed length, shown in Fig. 4.53. This is due to the third order time of flight term u_{5666} , which becomes large at the end of CE. Perhaps equally troublesome is an erratic bunch length through CE in which, unintentionally, the first and second order time of flight terms occasionally conspire to give a 150 fs length.

Fortunately, the upgraded CE lattice fares much better, and is able to achieve 100 fs lengths through the NA undulators. This is shown in Fig. 4.54, along with u_{5666} , which remains small through the compression, and only grows in the decompression section at the end of the NA.

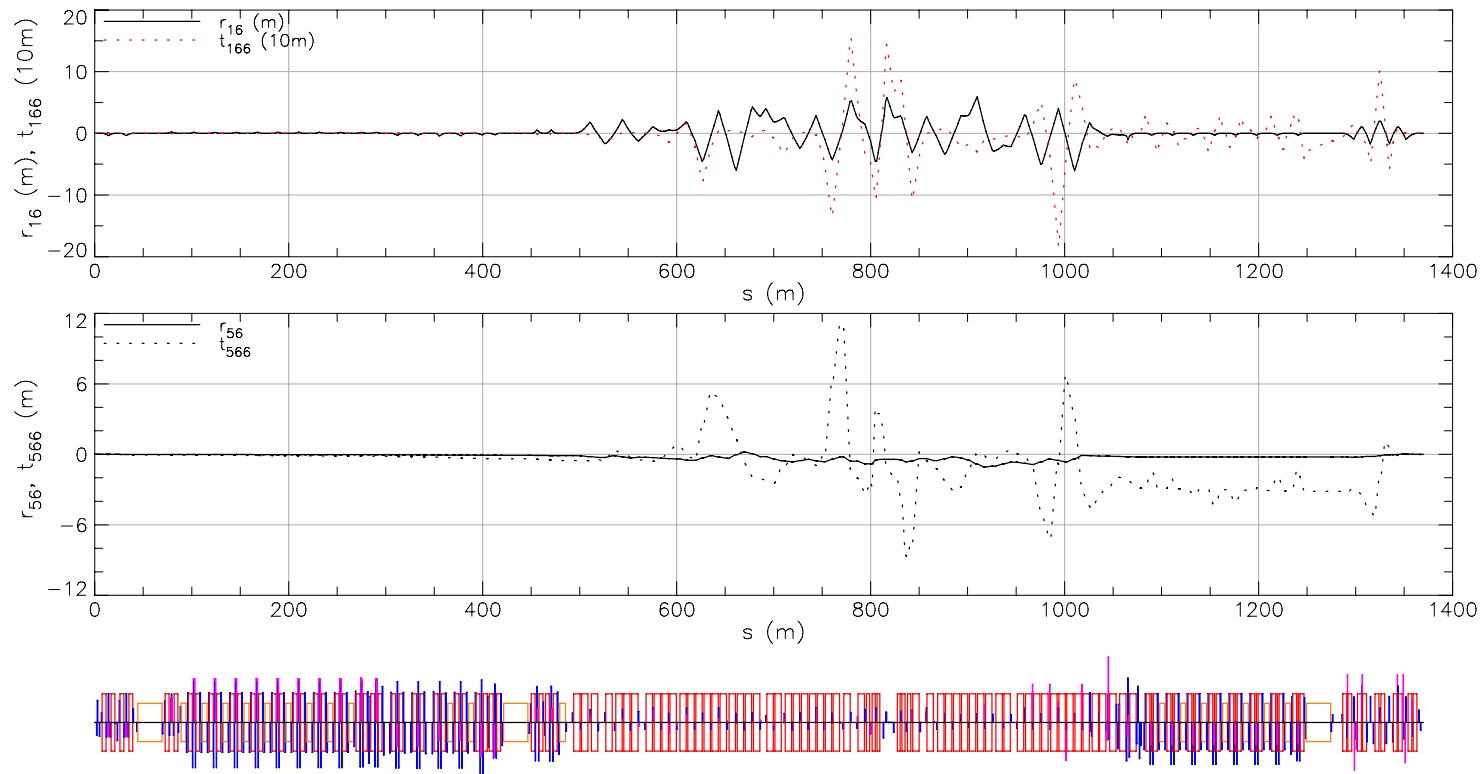


Figure 4.52: CERL Mode C (bunch compression) dispersion and time of flight terms through the SA, CE, and NA sections.

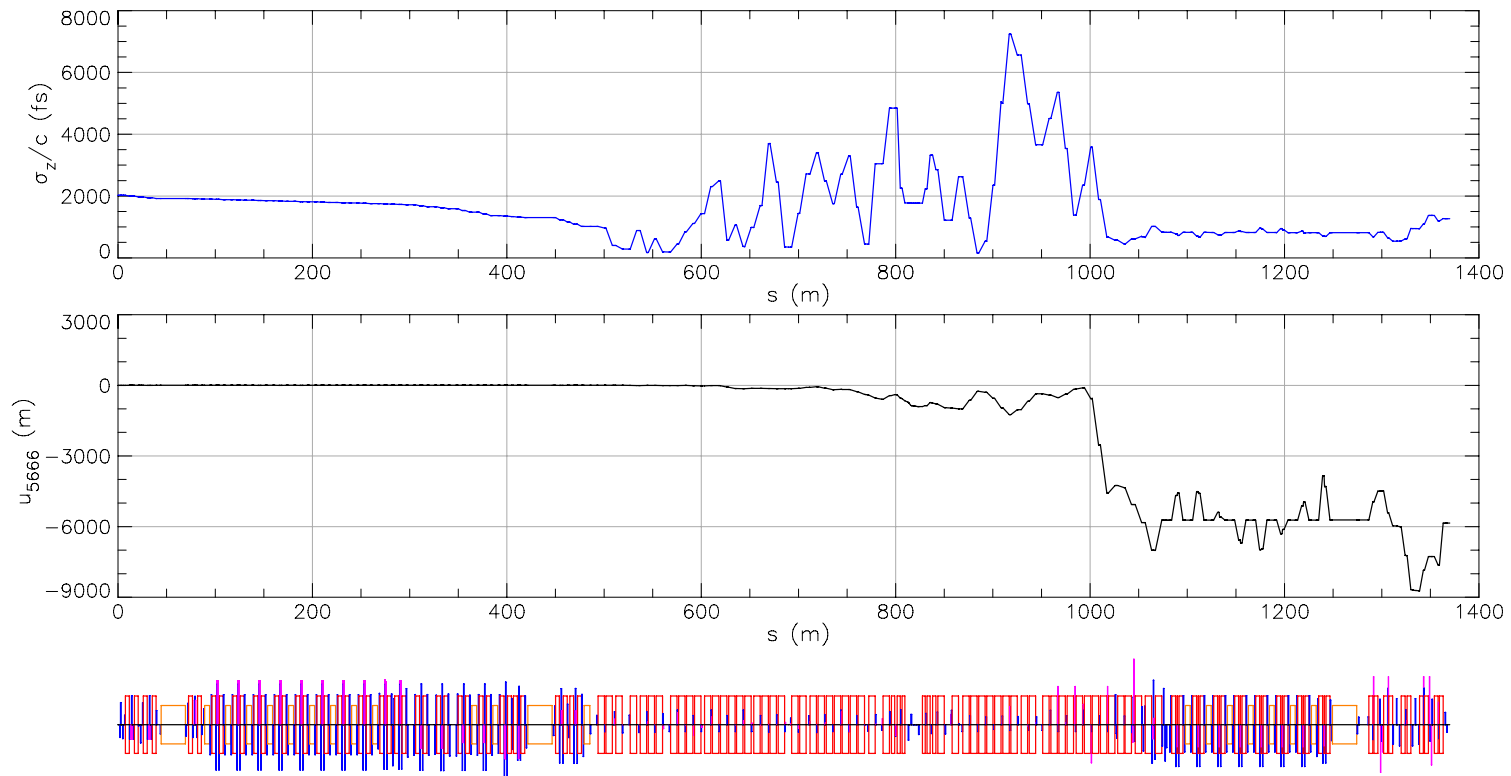


Figure 4.53: CERL Mode C bunch length and third order time of flight term u_{5666} through the SA, CE, and NA sections. Due to the difficult to control time of flight terms using the existing CESR magnets, the bunch unintentionally becomes short ($\sigma_z/c = 150$ fs) near the beginning of CE. The final compressed length in the NA undulators is 800 fs, which is very different from the intended 100 fs length due to the large u_{5666} .

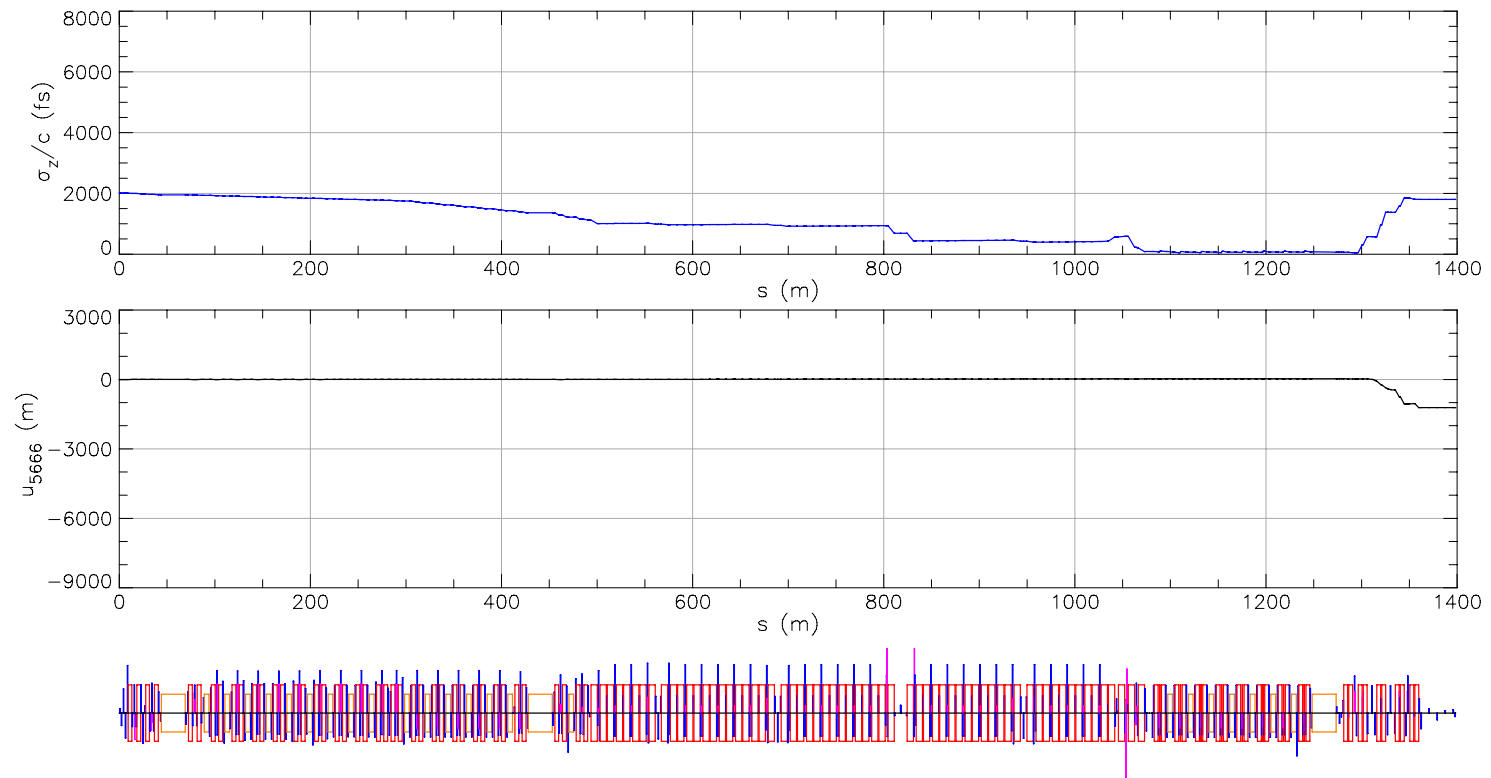


Figure 4.54: The same as Fig. 4.53, but with the upgraded CE lattice. The additional quadrupole magnets in CE aid in controlling the time of flight terms, so that the bunch attains and maintains the intended 100 fs length through the NA undulators.

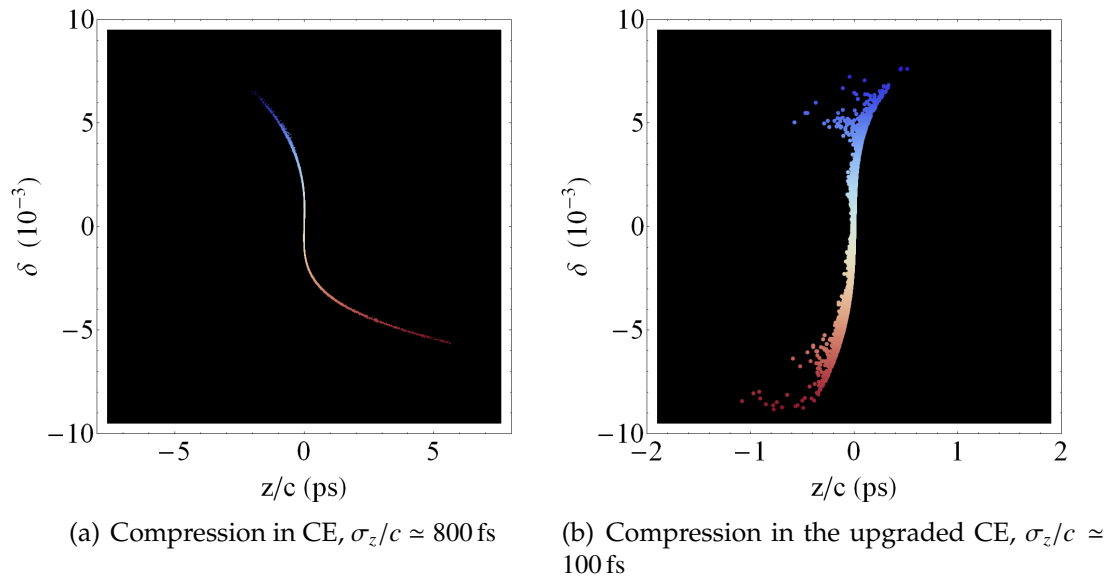


Figure 4.55: Longitudinal phase space in the first undulator after compression with the existing CESR magnets and the upgraded CESR magnets.

The longitudinal phase space in the first NA undulator using the non-upgraded CE is shown in Fig. 4.55(a). High order time of flight terms shear this phase space at relatively large δ and spoil the intended bunch length. The corresponding phase space using the upgraded CE is shown in Fig. 4.55(b). There the bunch is properly compressed to second order without noticeable contributions from higher order time of flight terms.

CHAPTER 5
COHERENT SYNCHROTRON RADIATION

This final chapter examines the effect of Coherent Synchrotron Radiation (CSR) in a particle accelerator. It uses the less widely known Jefimenko forms of Maxwell's equations (Jackson, 1999), which allow one to calculate electromagnetic fields by directly using the evolving charge and current densities, and which internally incorporate all retardation effects. These equations are related to forms used in Derbenev *et al.* (1995) and Warnock *et al.* (2006). This is in contrast to the usual Liénard-Wiechert approach, which gives fields due to charges at their retarded times t' and positions $\mathbf{x}(t')$, and one must invert equations of the form $t - t' = |\mathbf{x}(t') - \mathbf{x}_o|/c$ for the retarded time t' , where \mathbf{x}_o is an observation point at a later time t and c is the speed of light. While this latter method has proven useful in deriving equations for (incoherent) synchrotron radiation of single particles, the former is found to be useful for the coherent fields of particle distributions.

5.1 Exact 1D model for CSR

In general, for given charge and current densities $\rho(\mathbf{x}, t)$ and $\mathbf{J}(\mathbf{x}, t)$ at position \mathbf{x} and time t , the electric field $\mathbf{E}(\mathbf{x}, t)$ can be calculated using Jefimenko's form of Maxwell's equations (Jackson, 1999)

$$\mathbf{E}(\mathbf{x}, t) = \frac{1}{4\pi\epsilon_0} \int d^3x' \left[\frac{\mathbf{r}}{r^3} \rho(\mathbf{x}', t') + \frac{\mathbf{r}}{c r^2} \partial_{t'} \rho(\mathbf{x}', t') - \frac{1}{c^2 r} \partial_{t'} \mathbf{J}(\mathbf{x}', t') \right]_{t'=t-r/c}, \quad (5.1)$$

in which $\mathbf{r} \equiv \mathbf{x} - \mathbf{x}'$, $r \equiv \|\mathbf{r}\|$, ϵ_0 is the vacuum permittivity and t' is the retarded time. In this formulation, the retarded points \mathbf{x}' and times t' are independent

variables, so there are no functions that need to be inverted. Therefore, if one knows $\rho, \dot{\rho}$, and $\dot{\mathbf{J}}$ at all points in space \mathbf{x}' and times $t' \leq t$, with a dot denoting the time derivative, then this formula gives the electric field by direct integration.

Now consider a line charge distribution, which follows a path $\mathbf{X}(s)$ parameterized by distance s , has a unit tangent $\mathbf{u}(s) = d\mathbf{X}(s)/ds$, and moves with constant speed βc along this path. A bunch with total charge Q and normalized line density λ therefore has one-dimensional charge density and current

$$\begin{aligned}\rho(s, t) &= Q \lambda(s - s_b - \beta ct), \\ \mathbf{J}(s, t) &= Q \beta c \mathbf{u}(s) \lambda(s - s_b - \beta ct),\end{aligned}\tag{5.2}$$

where s_b is the location of the bunch center at time $t = 0$.

The rate of energy change per unit length of an elementary charge q at position s is $d\mathcal{E}/ds = q \mathbf{u}(s) \cdot \mathbf{E}(s, t)$. Functions of this type are called wake-fields. Using Eq. (5.1) with the one-dimensional bunch in Eq. (5.2) gives

$$\begin{aligned}\frac{d\mathcal{E}}{ds}(s, t) &= N r_c m c^2 \int_{-\infty}^{\infty} ds' \left[\frac{\mathbf{u}(s) \cdot \mathbf{r}(s, s')}{r(s, s')^3} \lambda(s_r) - \beta \frac{\mathbf{u}(s) \cdot \mathbf{r}(s, s')}{r(s, s')^2} \lambda'(s_r) \right. \\ &\quad \left. + \beta^2 \frac{\mathbf{u}(s) \cdot \mathbf{u}(s')}{r(s, s')} \lambda'(s_r) \right],\end{aligned}\tag{5.3}$$

with the definitions

$$s_r \equiv s' - s_0 + \beta r(s, s'),\tag{5.4}$$

$$s_0 \equiv s_b + \beta ct,\tag{5.5}$$

$$\mathbf{r}(s, s') \equiv \mathbf{X}(s) - \mathbf{X}(s'),\tag{5.6}$$

$$r(s, s') \equiv \|\mathbf{r}(s, s')\|,\tag{5.7}$$

where $N = Q/q$ is the number of elementary particles with mass m and classical radius $r_c = q^2/(4\pi\epsilon_0 m c^2)$, and the prime on λ indicates a derivative of this

function with respect to its argument, *i.e.* $\lambda'(x) = d\lambda/dx$. Additionally, s_0 is the center of the bunch at time t , and this is the only place where the time dependence appears. The integrand is thus the contribution to the wake-field due to particles between the retarded positions s' and $s' + ds'$, with $N\lambda(s_r)$ being the charge density at retarded position s' and retarded time t' .

Unfortunately the integral in Eq. (5.3) diverges as $s - s' \rightarrow 0$, which is a consequence of the one-dimensional line charge model. This problem can be alleviated by using the regularization procedure originating in Saldin *et al.* (1997), where the electric field \mathbf{E} is split into two parts

$$\mathbf{E} = \mathbf{E}_{\text{CSR}} + \mathbf{E}_{\text{SC}}. \quad (5.8)$$

The space charge (SC) part is the electric field of a line charge moving on a straight path,

$$\mathbf{E}_{\text{SC}}(s, t) = \frac{Q}{4\pi\epsilon_0} \mathbf{u}(s) \int_{-\infty}^{\infty} d\tilde{s} \left[\frac{s - \tilde{s}}{|s - \tilde{s}|^3} \lambda(s_l) - \beta \frac{s - \tilde{s}}{|s - \tilde{s}|^2} \lambda'(s_l) + \beta^2 \frac{1}{|s - \tilde{s}|} \lambda'(s_l) \right], \quad (5.9)$$

with $s_l \equiv \tilde{s} - s_0 + \beta|s - \tilde{s}|$, which can be integrated by parts, simplifying to

$$\mathbf{E}_{\text{SC}}(s, t) = -\frac{Q\mathbf{u}(s)}{4\pi\epsilon_0\gamma^2} \int_{-\infty}^{\infty} d\tilde{s} \frac{\lambda'(\tilde{s} - s_0 + \beta|s - \tilde{s}|)}{|s - \tilde{s}|}. \quad (5.10)$$

It will turn out to be useful to change variables in this expression, so that when combined with Eq. (5.3) the function λ' can be factored. This can be done by setting $\tilde{s} - s_0 + \beta|s - \tilde{s}| = s' - s_0 + \beta r(s, s')$, with the convention that $\text{sgn}(s - \tilde{s}) = \text{sgn}(s - s')$. Noting that $\partial r(s, s')/\partial s' = -\mathbf{r}(s, s') \cdot \mathbf{u}(s')/r(s, s')$, this leads to

$$\frac{-1}{|s - \tilde{s}|} = \text{sgn}(s' - s) \frac{1 + \beta \text{sgn}(s' - s)}{s - s' - \beta r(s, s')}, \quad (5.11)$$

$$d\tilde{s} = \frac{1 - \beta \mathbf{r}(s, s') \cdot \mathbf{u}(s')/r(s, s')}{1 + \beta \text{sgn}(s' - s)} ds', \quad (5.12)$$

so that

$$\mathbf{E}_{\text{sc}}(s, t) = \frac{Q}{4\pi\epsilon_0} \frac{\mathbf{u}(s)}{\gamma^2} \int_{-\infty}^{\infty} ds' \lambda'(s_r) \text{sgn}(s' - s) \frac{1 - \beta \mathbf{r}(s, s') \cdot \mathbf{u}(s')/r(s, s')}{s - s' - \beta r(s, s')}. \quad (5.13)$$

The resulting wake-field due to \mathbf{E}_{CSR} , called the CSR-wake, is

$$\left(\frac{d\mathcal{E}_{\text{CSR}}}{ds} \right) = q \mathbf{u}(s) \cdot [\mathbf{E}(s, t) - \mathbf{E}_{\text{sc}}(s, t)]. \quad (5.14)$$

This expression is finite, and shown in Saldin *et al.* (1997) to correctly account for the coherent energy loss due to synchrotron radiation.

The approach here is to be contrasted with the conventional one taken in the literature using Liénard-Wiechert formulas. In terms of the quantities above, the electric field at position s due to a charge q at retarded time $t' = t - r(s, s')/c$ and retarded position s' is

$$\mathbf{E}_{\text{LW}}(s, s') = \frac{q}{4\pi\epsilon_0} \left\{ \frac{\mathbf{r} - \beta r \mathbf{u}(s')}{\gamma^2 [r - \beta \mathbf{r} \cdot \mathbf{u}(s')]^3} + \frac{\mathbf{r} \times \{[\mathbf{r} - \beta r \mathbf{u}(s')] \times \beta^2 \mathbf{u}'(s')\}}{[r - \beta \mathbf{r} \cdot \mathbf{u}(s')]^3} \right\}, \quad (5.15)$$

with \mathbf{r} as in Eq. (5.3) suppressing the arguments. Therefore, the electric field at s due to a charge $\rho(s_t, t) ds_t$ between s_t and $s_t + ds_t$, as in Eq. (5.2), is found by inverting $s_t = s' + \beta r(s, s')$ for s' and using Eq. (5.15). This is often impossible to do analytically, but fortunately for a distribution of charges the inversion can be circumvented by changing variables. Because $\partial r(s, s')/\partial s' = -\mathbf{r} \cdot \mathbf{u}(s')/r$ from before, the charge is

$$\rho(s_t, t) ds_t = Q \lambda(s' - s_b - \beta ct + \beta r) \left[1 - \beta \frac{\mathbf{r} \cdot \mathbf{u}(s')}{r} \right] ds', \quad (5.16)$$

and the total electric field is

$$\mathbf{E}(s, t) = \int_{-\infty}^{\infty} ds_t \mathbf{E}_{\text{LW}}(s, s'(s_t)) \rho(s_t, t) \quad (5.17)$$

$$= Q \int_{-\infty}^{\infty} ds' \left[1 - \beta \frac{\mathbf{r} \cdot \mathbf{u}(s')}{r} \right] \mathbf{E}_{\text{LW}}(s, s') \lambda(s_r). \quad (5.18)$$

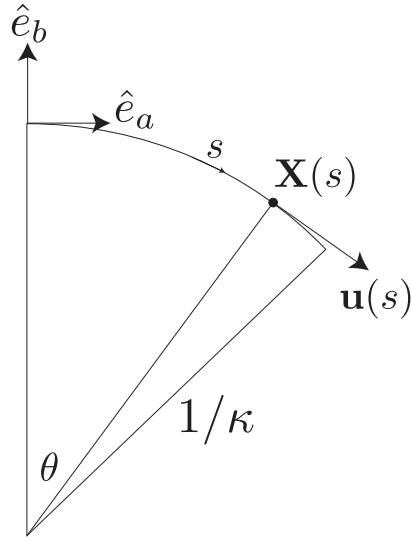


Figure 5.1: Geometry for a single bend. The variable s parameterizes the curve with radius $1/\kappa$. The coordinates are $\mathbf{X}(s)$, and the unit tangent vector is $\mathbf{u}(s)$.

We can use this to verify that \mathbf{E}_{sc} computed this way agrees with the result using the Jefimenko approach. For the SC field one has $\mathbf{r}(s) = (s - s')\mathbf{u}(s)$, $\mathbf{u}(s') = \mathbf{u}(s)$, and $\mathbf{u}'(s) = 0$, giving

$$\mathbf{E}_{\text{sc}}(s, t) = \frac{Q \mathbf{u}(s)}{4\pi\epsilon_0} \int_{-\infty}^{\infty} ds' \frac{\beta + \text{sgn}(s - s')}{(s - s')^2} \lambda(s' - s_0 + \beta |s - s'|). \quad (5.19)$$

Equation (5.19) agrees with Eq. (5.10) when integrated by parts because, for $s_0 = 0$, $\int (\beta + \text{sgn}(s - s'))(s - s')^{-2} ds' = (\beta + \text{sgn}(s - s'))(s - s')^{-1}$, and $-\frac{\partial}{\partial s'} \lambda(s' + \beta(s - s') \text{sgn}(s - s')) = -(1 - \beta \text{sgn}(s - s'))\lambda'(s' + \beta |s - s'|)$, and similarly for all s_0 .

5.2 Single Bending Magnet

Now we apply Eq. (5.3) to the geometry of an arc of a circle of curvature κ and length B , shown in Fig. 5.1. Set $s = 0$ at the entrance of the bend so that $\theta = \kappa s$ is the angle into the bend. In terms of fixed Cartesian unit vectors \hat{e}_a and \hat{e}_b , the

path coordinates and tangent vector are

$$\mathbf{X}(s) = \kappa^{-1} \sin(\kappa s) \hat{e}_a - \kappa^{-1} [1 - \cos(\kappa s)] \hat{e}_b, \quad (5.20)$$

$$\mathbf{u}(s) = \cos(\kappa s) \hat{e}_a - \sin(\kappa s) \hat{e}_b. \quad (5.21)$$

Consider a bunch with its center at angle $\theta_0 = \kappa s_0$, and a test particle at angle θ . The contribution to Eq. (5.3) of this finite arc is

$$\left. \frac{d\mathcal{E}}{ds}(s) \right|_B = Nr_c mc^2 \int_0^{\kappa B} d\theta' \left[\frac{\sin \alpha}{(\kappa r_\alpha)^3} \kappa \lambda(s_\alpha) - \beta \frac{\sin \alpha}{(\kappa r_\alpha)^2} \lambda'(s_\alpha) + \beta^2 \frac{\cos \alpha}{\kappa r_\alpha} \lambda'(s_\alpha) \right], \quad (5.22)$$

with $s = \kappa^{-1}\theta$ and the following definitions:

$$\alpha \equiv \theta - \theta', \quad (5.23)$$

$$s_\alpha \equiv \frac{1}{\kappa} (\theta - \theta_0 - \alpha) + \beta r_\alpha, \quad (5.24)$$

$$r_\alpha \equiv \frac{1}{\kappa} \sqrt{2 - 2 \cos \alpha}. \quad (5.25)$$

Thus α is the angle between the test particle and the retarded source particle, and is positive when the former is ahead of the latter. The first term of Eq. (5.22) can be integrated by parts because $\partial(2 - 2 \cos \alpha)^{-1/2} / \partial \theta' = \sin(\alpha) (2 - 2 \cos \alpha)^{-3/2}$, and the wake greatly simplifies to

$$\left. \frac{d\mathcal{E}}{ds}(s) \right|_B = Nr_c mc^2 \left\{ \frac{-\kappa \lambda(s_\alpha)}{\sqrt{2 - 2 \cos \alpha}} \Big|_{\alpha=-(\kappa B-\theta)}^{\alpha=\theta} + \int_{-(\kappa B-\theta)}^{\theta} d\alpha \frac{\beta^2 \cos(\alpha) - 1}{\sqrt{2 - 2 \cos \alpha}} \lambda'(s_\alpha) \right\}. \quad (5.26)$$

In terms of the variable α , the space charge term in Eq. (5.13) can be split as

$$\frac{d\mathcal{E}_{\text{sc}}}{ds}(s) = -Nr_c mc^2 \left\{ \int_{-\infty}^{-(\kappa B-\theta)} d\alpha I_{\text{sc}}(\alpha) + \int_{-(\kappa B-\theta)}^{\theta} d\alpha I_{\text{sc}}(\alpha) + \int_{\theta}^{\infty} d\alpha I_{\text{sc}}(\alpha) \right\}, \quad (5.27)$$

with the integrand

$$I_{\text{sc}}(\alpha) \equiv -\frac{\text{sgn } \alpha}{\gamma^2} \frac{1 - \frac{\beta \sin(\alpha)}{\sqrt{2 - 2 \cos \alpha}}}{\alpha - \beta \sqrt{2 - 2 \cos \alpha}} \lambda'(s_\alpha), \quad (5.28)$$

so that the contribution of the bend to the CSR-wake is

$$\begin{aligned}
\left. \frac{d\mathcal{E}_{\text{CSR}}(s)}{ds} \right|_B = & Nr_c mc^2 \left\{ \frac{-\kappa \lambda(s_\alpha)}{\sqrt{2-2\cos\alpha}} \Big|_{\alpha=-(\kappa B-\theta)}^{\alpha=\theta} \right. \\
& + \int_{-(\kappa B-\theta)}^{\theta} d\alpha \lambda'(s_\alpha) \left[\frac{\beta^2 \cos(\alpha) - 1}{\sqrt{2-2\cos\alpha}} + \frac{\text{sgn}(\alpha)}{\gamma^2} \frac{1 - \frac{\beta \sin(\alpha)}{\sqrt{2-2\cos\alpha}}}{\alpha - \beta \sqrt{2-2\cos\alpha}} \right] \\
& \left. - \int_{-\infty}^{-(\kappa B-\theta)} d\alpha I_{\text{SC}}(\alpha) - \int_{\theta}^{\infty} d\alpha I_{\text{SC}}(\alpha) \right\}. \quad (5.29)
\end{aligned}$$

5.2.1 Steady State

In the practical environment of a particle accelerator with a bunched beam, one is typically only concerned with electric fields around the bunch center. Due to the rotational symmetry, there will be an angle into a bending magnet beyond which the CSR-wake, relative to the bunch center, does not change. Note that in Eq. (5.24) the quantity $z = \kappa^{-1}(\theta - \theta_0)$ is the distance along the path ahead of the bunch center, and define the extent of the bunch $l_b \equiv z_+ - z_-$, where z_+ is the head particle coordinate, and z_- is the tail particle coordinate. Henceforth the symbol z will refer to the longitudinal coordinate relative to the bunch center: $z = s - s_0$. The particle at z_+ is affected by a particle at z_- at retarded angle α_{max} found by inverting

$$\kappa l_b = \alpha_{\text{max}} - \beta \sqrt{2 - 2 \cos \alpha_{\text{max}}}. \quad (5.30)$$

Similarly, a particle at z_- is affected by a particle at z_+ at retarded angle α_{min} found by inverting

$$-\kappa l_b = \alpha_{\text{min}} - \beta \sqrt{2 - 2 \cos \alpha_{\text{min}}}. \quad (5.31)$$

When the bunch center is at an angle $\theta_0 > \alpha_{\text{max}} - \kappa z_+$, only particles within

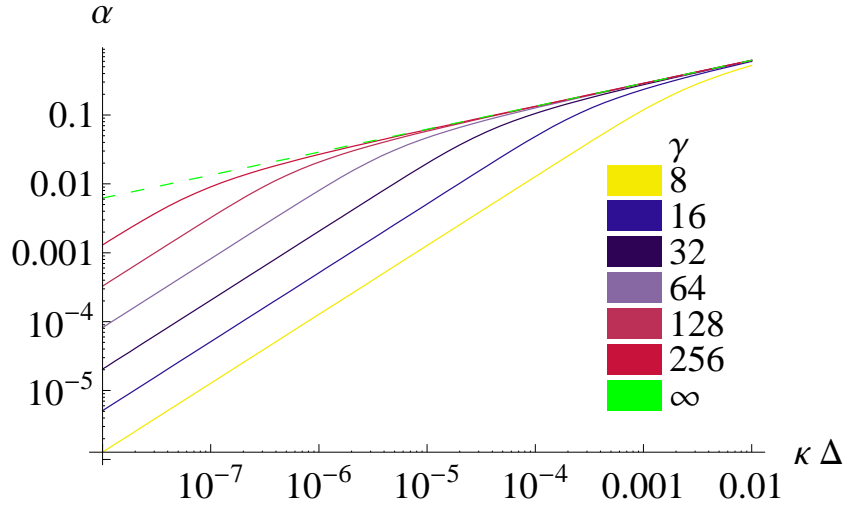


Figure 5.2: The inverse of Eq. (5.33) for positive α at various energies. The dashed green curve ($\gamma \rightarrow \infty$) is $\alpha = (24 \kappa \Delta)^{1/3}$, the inverse of Eq. (5.35).

the bend affect the wake-field. The “steady-state” (s.s.) CSR-wake is then

$$W_{\text{s.s. CSR}}(z) = Nr_c mc^2 \int_{\alpha_{\min}}^{\alpha_{\max}} d\alpha \left[\frac{\beta^2 \cos(\alpha) - 1}{\sqrt{2 - 2 \cos \alpha}} + \frac{\text{sgn}(\alpha)}{\gamma^2} \frac{1 - \frac{\beta \sin(\alpha)}{\sqrt{2 - 2 \cos \alpha}}}{\alpha - \beta \sqrt{2 - 2 \cos \alpha}} \right] \lambda'(z - \Delta(\alpha)), \quad (5.32)$$

where

$$\Delta(\alpha) = \kappa^{-1}(\alpha - \beta \sqrt{2 - 2 \cos \alpha}) \quad (5.33)$$

is the distance behind the test particle at z . The notation

$$W_{\text{CSR}}(z) \equiv \frac{d\mathcal{E}_{\text{CSR}}}{ds}(s_0 + z) \quad (5.34)$$

is used to refer to the CSR-wake immediately surrounding the bunch center at s_0 .

In the ultra-relativistic approximation ($\beta \rightarrow 1$) with a small normalized bunch length $\kappa l_b \ll 1$, and thus $\alpha \ll 1$, the steady-state formula in Eq. (5.32)

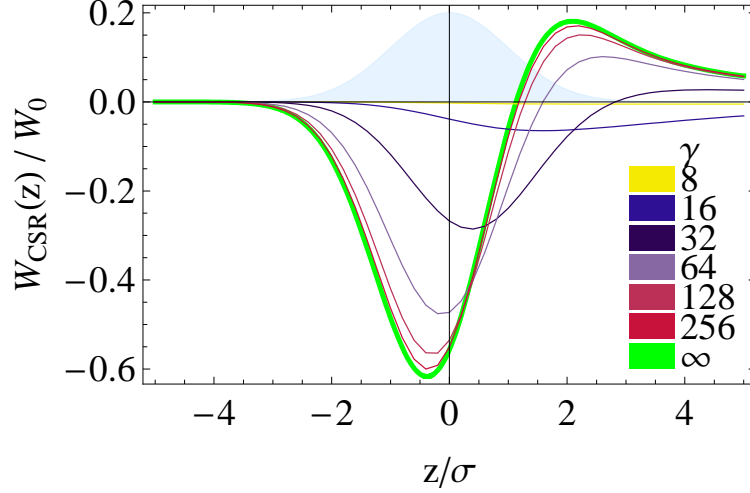


Figure 5.3: The steady-state CSR-wake for various relativistic γ using Eq. (5.32), compared to Eq. (5.36) plotted as green. Here $\kappa\sigma = 3 \times 10^{-5}$ for a Gaussian bunch, represented in light blue.

greatly simplifies. The $1/\gamma^2$ term in Eq. (5.28) puts $I_{sc} \rightarrow 0$, and the term in the integrand $(\beta^2 \cos(\alpha) - 1)/(2|\sin(\alpha/2)|) \approx -|\alpha|/2$. The function $\Delta(\alpha)$ for $\gamma \rightarrow \infty$ is approximately

$$\Delta(\alpha) \approx \begin{cases} \alpha^3/(24\kappa) & \text{for } \alpha > 0 \\ 2\alpha/\kappa & \text{for } \alpha < 0 \end{cases}. \quad (5.35)$$

Figure 5.2 plots the inverse of Eq. (5.33) for positive α and various energies. One sees that the approximation in Eq. (5.35) is increasingly good for higher energies, but greatly overestimates α at the smallest distances. Changing variables using Eq. (5.35), the ultra-relativistic steady-state CSR-wake is

$$W_{\text{CSR}}^{\gamma \rightarrow \infty}(z) = -Nr_c mc^2 \kappa \int_0^{l_b} d\Delta \left[\frac{2\lambda'(z-\Delta)}{(3\kappa\Delta)^{1/3}} + \frac{\kappa\Delta}{8}\lambda'(z+\Delta) \right]. \quad (5.36)$$

The first term in this integral is derived by an alternate method in Saldin *et al.* (1997). The scaling here is apparent by writing the distribution in the normal-

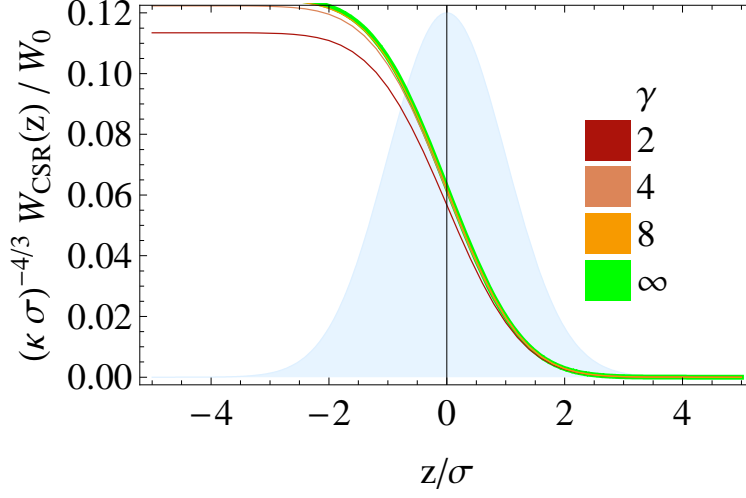


Figure 5.4: The steady-state CSR-wake for various relativistic γ due only to particles ahead of the test particle, *i.e.* negative α in Eq. (5.32), and the second term in the integrand of Eq. (5.36). A Gaussian bunch is used, with $\kappa\sigma = 3 \times 10^{-5}$, and the wake has been scaled by $(\kappa\sigma)^{-4/3}$. Compared with Fig. 5.3 this demonstrates that the contribution to the CSR-wake of particles ahead of the test particle is insignificant compared to those behind.

ized form

$$\lambda(z - \Delta) \equiv \frac{1}{\sigma} \tilde{\lambda} \left(\frac{z - \Delta}{\sigma} \right), \quad (5.37)$$

$$\lambda'(z - \Delta) \equiv \frac{1}{\sigma^2} \tilde{\lambda}' \left(\frac{z - \Delta}{\sigma} \right). \quad (5.38)$$

where σ^2 is the variance of λ , so that $\tilde{\lambda}$ has unit variance. Also using normalized $\tilde{z} \equiv z/\sigma$ and $\tilde{\Delta} \equiv \Delta/\sigma$ gives

$$W_{\text{CSR}}^{\gamma \rightarrow \infty}(\tilde{z}\sigma) = -Nr_c mc^2 \frac{(\kappa\sigma)^{2/3}}{\sigma^2} \int_0^{l_b/\sigma} d\tilde{\Delta} \left[\frac{2\tilde{\lambda}'(\tilde{z} - \tilde{\Delta})}{(3\tilde{\Delta})^{1/3}} + (\kappa\sigma)^{4/3} \frac{\tilde{\Delta}}{8} \tilde{\lambda}'(\tilde{z} + \tilde{\Delta}) \right]. \quad (5.39)$$

Now one can see that the particles in front of the test particle, represented in the last term in the integrand, influence the wake by roughly a factor of $(\kappa\sigma)^{4/3}$ less than particles behind, and that the primary contribution to the CSR-wake scales with the factor in front of the integral in Eq. (5.39). However, it is interesting to note that even as $\gamma \rightarrow \infty$, where a charge radiates infinitely more power in the

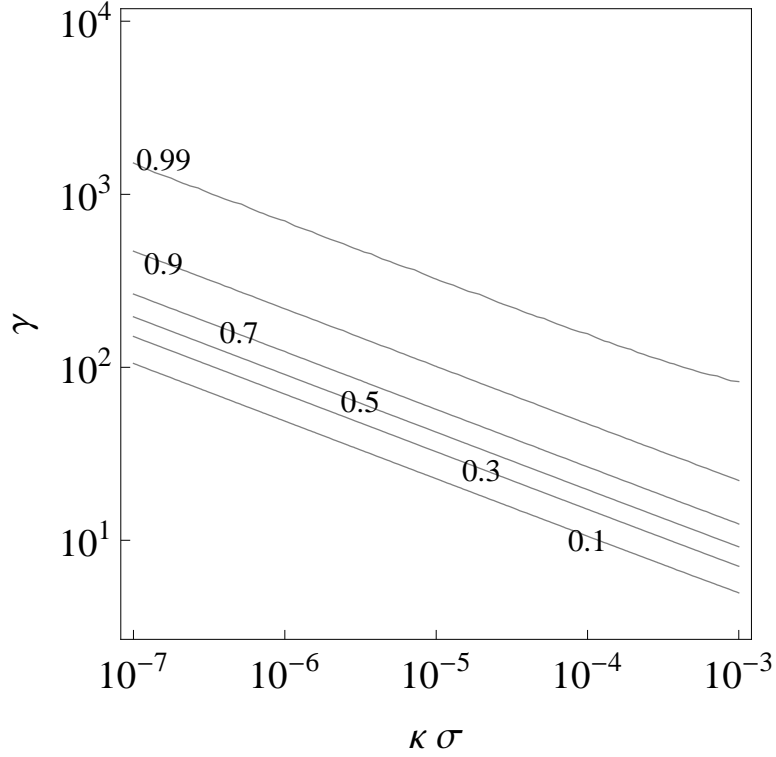


Figure 5.5: The ratio of the average energy of a Gaussian bunch using the exact Eq. (5.32) to that using approximate Eq. (5.36) in a practical range of the parameters γ and $\kappa \sigma$.

forward direction than the backward direction, there is still a finite CSR force from particles ahead of the test particle. In light of the primary scaling, we define a characteristic CSR energy change per unit length as

$$W_0 \equiv Nr_c mc^2 \frac{(\kappa \sigma)^{2/3}}{\sigma^2}. \quad (5.40)$$

The ultra-relativistic approximation in Eq. (5.36) is compared to the exact formula Eq. (5.32) in Fig. 5.3 for various energies and a particular value of $\kappa \sigma$. One sees that Eq. (5.36) represents the largest possible effect. The CSR-wake due only to particles in front of the test particle is shown in Fig. 5.4, emphasizing again that these forward particles contribute only a small amount to the total CSR-wake.

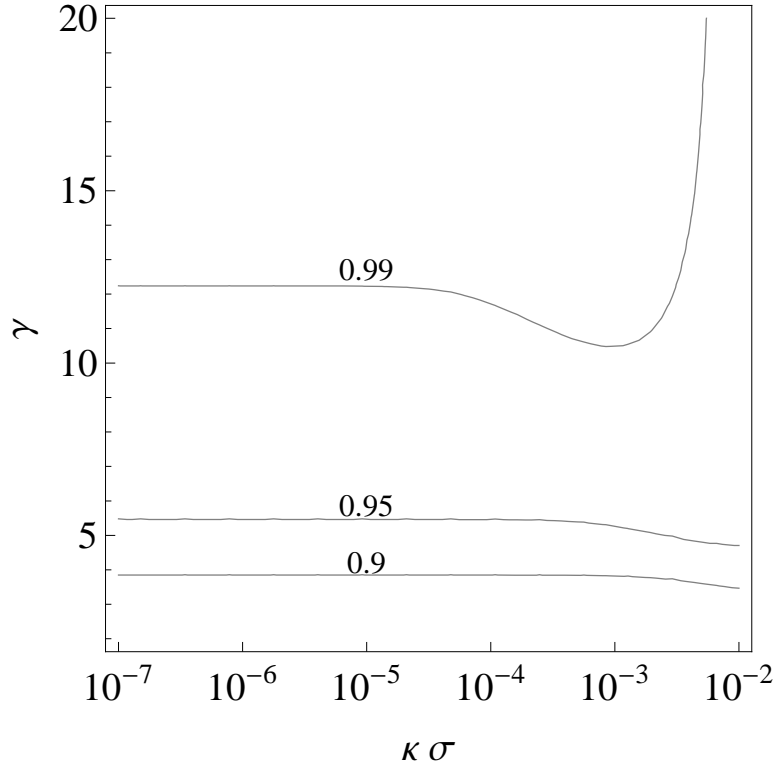


Figure 5.6: Similar to Fig. 5.5, but with the ratio of the average energy of Eq. (5.32) to Eq. (5.41), showing that the latter is an excellent approximation at relatively low energies.

Neglecting the contribution due to forward particles, the ultra-relativistic steady-state CSR-wake in Eq. (5.39) scales with W_0 and depends only on the shape of $\tilde{\lambda}$. Factoring out W_0 from the exact steady-state CSR-wake in Eq. (5.32), the exact result additionally depends on γ and $\kappa\sigma$. Therefore, to quantify the appropriateness of the ultra-relativistic approximation, the ratio of the average energy lost (per unit length) of a Gaussian bunch using the exact Eq. (5.32) to that using approximate Eq. (5.36) is shown in Fig. 5.5 for a practical range of these parameters. At a given energy, one sees that Eq. (5.36) is a good approximation for the relatively long bunches. This can be understood from Fig. 5.2, because the approximation in Eq. (5.35) has a relative error for a finite energy that diverges for small α .

A systematic method for calculating the CSR-wake using Liénard-Wiechert formulas in the small angle, relativistic approximations has been developed in Sagan *et al.* (2008) for arbitrary combinations of drifts and bends. Using the corresponding equation in Sagan *et al.* (2008) for the geometry of a bend, and the appropriate Jacobian factor, the steady-state CSR-wake to second order in α and $1/\gamma$ is

$$W_{\text{SHMS,s.s.}}^{\text{CSR}}(z) = -Nr_c mc^2 \int_0^{\alpha_{\text{max}}} d\alpha \left(\frac{1}{2\gamma^2} + \frac{\alpha^2}{8} \right) \left(\frac{2 + \gamma^2 \alpha^2}{\alpha + \gamma^2 \alpha^3/4} - \frac{1}{\alpha/2 + \gamma^2 \alpha^3/24} \right) \times \lambda' \left(z - \kappa^{-1} \left(\frac{\alpha}{2\gamma^2} + \frac{\alpha^3}{24} \right) \right). \quad (5.41)$$

Compared to Eq. (5.36), this expression is a significantly better approximation of Eq. (5.32) for low γ and a practical range of $\kappa\sigma$, shown in Fig. 5.6.

5.2.2 Shielding by Parallel Plates

The presence of a conducting beam chamber can have a strong effect on the CSR wake-field. For a rectangular cross section, it has been observed that the dominant effect comes from the smaller of the height and width (see, for example, Sagan *et al.* (2008)). If particle trajectories are planar, then a finite chamber height can be represented by infinite parallel plates. In such a geometry, CSR wake-fields can be calculated using the image charge method.

The kick due to a single image bunch at height h is easily adapted from Eq. (5.3) as

$$\frac{d\mathcal{E}}{ds}(s, t, h) = Nr_c mc^2 \int_{-\infty}^{\infty} ds' \left\{ \frac{\mathbf{u}(s) \cdot \mathbf{r}}{(r^2 + h^2)^{3/2}} \lambda(s_h) + \left[\beta^2 \frac{\mathbf{u}(s) \cdot \mathbf{u}(s')}{(r^2 + h^2)^{1/2}} - \beta \frac{\mathbf{u}(s) \cdot \mathbf{r}}{r^2 + h^2} \right] \lambda'(s_h) \right\}, \quad (5.42)$$

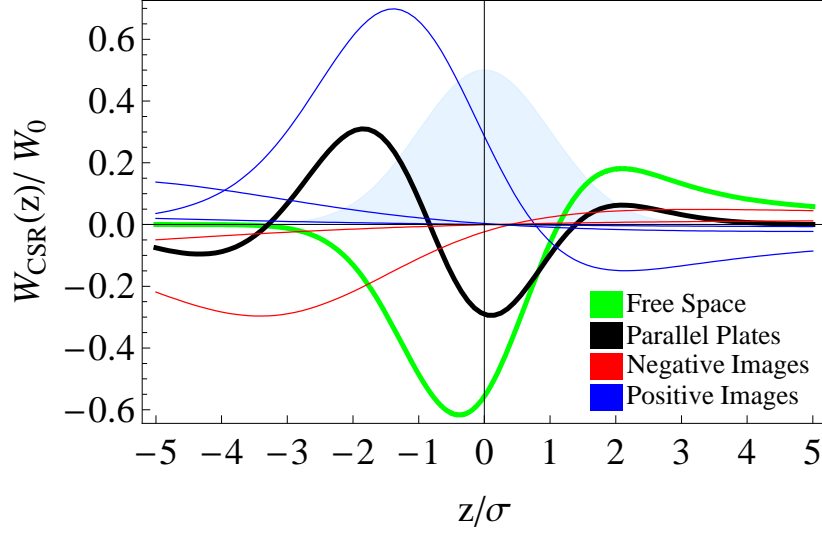


Figure 5.7: The free space and shielded CSR-wakes in a bend. The contributions to the shielded wake of individual image bunches are shown in red and blue. A 1GeV Gaussian bunch with $\sigma = 0.3$ mm is used in a bend of radius $\kappa^{-1} = 10.0$ m. The shielding height $H = 2$ cm.

with the argument

$$s_h \equiv s' - s_b - \beta c t + \beta \sqrt{r^2 + h^2}, \quad (5.43)$$

and with \mathbf{r} and \mathbf{u} retaining their meaning from Eq. (5.3). Parallel plates require an image bunch for each plate, and an image bunch for each of those, *ad infinitum*. For the real bunch with orbit midway between plates separated by a distance H , symmetry gives the total image kick

$$\frac{d\mathcal{E}_{\text{images}}}{ds}(s, t) = \sum_{\substack{n=-\infty \\ n \neq 0}}^{\infty} (-1)^n \frac{d\mathcal{E}}{ds}(s, t, nH) \quad (5.44)$$

$$= 2 \sum_{n=1}^{\infty} (-1)^n \frac{d\mathcal{E}}{ds}(s, t, nH). \quad (5.45)$$

If the real bunch has a vertical offset V , the total image kick is modified to

$$\frac{d\mathcal{E}_{\text{images}}}{ds}(s, t) = \sum_{\substack{n=-\infty \\ \text{even} \\ n \neq 0}}^{\infty} \frac{d\mathcal{E}}{ds}(s, t, nH) - \sum_{\substack{n=-\infty \\ \text{odd}}}^{\infty} \frac{d\mathcal{E}}{ds}(s, t, nH - 2V). \quad (5.46)$$

In a bend, the contribution of the image bunches to the CSR-wake within the

bend, following Eq. (5.26), is

$$\frac{d\mathcal{E}_{\text{images}}}{ds}(s)\Big|_B = Nr_c mc^2 \sum_{n=1}^{\infty} 2(-1)^n \left\{ \frac{-\kappa \lambda(s_{\alpha,n})}{r_{\alpha,n}} \Big|_{\alpha=-(\kappa L_m - \theta)}^{\alpha=\theta} + \int_{-(\kappa L_m - \theta)}^{\theta} d\alpha \frac{\beta^2 \cos(\alpha) - 1}{r_{\alpha,n}} \lambda'(s_{\alpha,n}) \right\}, \quad (5.47)$$

with the definitions

$$r_{\alpha,n} \equiv \sqrt{2 - 2 \cos \alpha + (n \kappa H)^2}, \quad (5.48)$$

$$s_{\alpha,n} \equiv \kappa^{-1} (\theta - \theta_0 - \alpha + \beta r_{\alpha,n}). \quad (5.49)$$

Notice that the integrands do not need to be regularized by the SC term, because they are always finite due to the always positive factor $(n \kappa H)^2$.

Due to the infinite number of image layers needed, a finite bend can never be exactly in the steady-state. However, due to their increased distances and angles, the relevant contribution image number n will be negligible beyond some maximum image number. This point is illustrated in Fig. 5.7, where the contributions to the CSR-wake of five individual images are shown along with their sum with the free space wake, to give the total shielded wake.

Shielded Steady-State CSR

CSR effects in a vacuum chamber have been computed by the Green's function of grounded parallel plates (Schwinger, 1945; Warnock, 1990). These formulas are difficult to compute numerically, due to the presence of high order Bessel functions, so we will use an excellent approximation developed by Agoh & Yokoya (2004). The impedance for the steady-state in a dipole with horizontal

plates separated by a distance h is

$$Z(k) = Z_0 \frac{2\pi}{h} \left(\frac{2}{kR} \right)^{1/3} \sum_{p=0}^{\infty} F_{AY}(\beta_p^2), \quad (5.50)$$

$$\beta_p \equiv (2p+1) \frac{\pi}{h} \left(\frac{R}{2k^2} \right)^{1/3}, \quad (5.51)$$

$$F_{AY}(x) \equiv \text{Ai}'(x) [\text{Ai}'(x) - i \text{Bi}'(x)] + x \text{Ai}(x) [\text{Ai}(x) - i \text{Bi}(x)]. \quad (5.52)$$

where $Z_0 = c\mu_0$ is the free space impedance, k is the wave number, and Ai and Bi are Airy functions. The parallel plate wake-field due to a bunch with longitudinal density $\lambda(z)$ is obtained by Fourier transform:

$$\left(\frac{d\mathcal{E}}{ds} \right)_{\substack{\text{p.p.} \\ \gamma \rightarrow \infty}} = -N_e r_e m c^2 \Re \left[\frac{4}{Z_0} \int_0^{\infty} Z(k) \hat{\lambda}(k) e^{iks} dk \right], \quad (5.53)$$

$$\hat{\lambda}(k) = \int_{-\infty}^{\infty} \lambda(z) e^{-ikz} dz. \quad (5.54)$$

Some manipulation reveals that

$$\beta_p = (2p+1) \pi 2^{-1/3} b_s^{-1} (k\sigma)^{-2/3} \quad (5.55)$$

$$Z(k) = Z_0 2^{4/3} \pi b_s^{-1} (k\sigma)^{-1/3} \kappa^{2/3} \sigma^{-1/3} \sum_{p=0}^{\infty} F_{AY}(\beta_p^2) \quad (5.56)$$

where the bunch length σ has been added and we define a shielding factor

$$b_s \equiv h \left(\frac{\kappa}{\sigma^2} \right)^{1/3}. \quad (5.57)$$

This is useful because the CSR wake shielded by parallel plates (p.p.), in the steady-state and ultra-relativistic approximations, is then

$$W_{\text{p.p.}}(z) = -W_0 \Re \left[\int_0^{\infty} I_b(\bar{k}) \hat{\lambda} \left(\frac{\bar{k}}{\sigma} \right) \exp \left(i \bar{k} \frac{z}{\sigma} \right) d\bar{k} \right], \quad (5.58)$$

$$I_b(\bar{k}) \equiv \frac{2^{10/3} \pi}{b_s \bar{k}^{1/3}} \sum_{p=0}^{\infty} F_{AY} \left(\frac{(2p+1)^2 \pi^2}{2^{2/3} b_s^2 \bar{k}^{4/3}} \right), \quad (5.59)$$

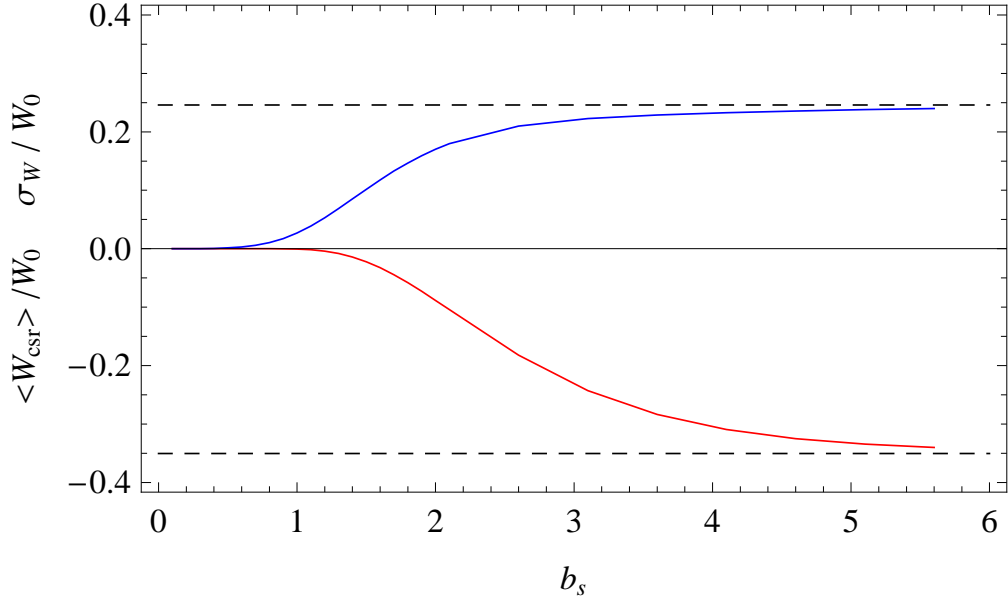


Figure 5.8: Average energy loss and energy spread versus the shielding parameter b_s .

which, besides scaling with W_0 , only depends on z/σ and b_s .

Two principal effects of CSR on the bunch distribution are a loss of energy and an increase in energy spread. These are calculated using the CSR-wake $W_{\text{CSR}}(z)$ and the bunch distribution $\lambda(z)$, where the average energy change per unit length $\langle W_{\text{CSR}} \rangle$ and the standard deviation $\sigma_W(W_{\text{CSR}})$ over the distribution are

$$\langle W_{\text{CSR}} \rangle \equiv \int_{z_-}^{z_+} W_{\text{CSR}}(z) \lambda(z) dz, \quad (5.60)$$

$$\sigma_W \equiv \left[\int_{z_-}^{z_+} W_{\text{CSR}}^2(z) \lambda(z) dz - \langle W_{\text{CSR}} \rangle^2 \right]^{1/2}. \quad (5.61)$$

The term σ_W is important because it contributes to the energy spread in a bunch. These quantities for a Gaussian bunch and the CSR-wake in Eq. (5.58) are calculated versus b_s in Fig. 5.8, indicating that shielding becomes relevant when $b_s \gtrsim 3$.

5.2.3 Retarded Bunch Visualization

For a given particle at time t within the bunch, it is evident that the retarded bunch density can be very distorted relative to the actual bunch density. From Eq. (5.16), the retarded bunch density at position s' as seen by a particle at position s is

$$\lambda_{\text{ret}}(s'; s) = \lambda(s' - s_b - \beta ct + \beta r) \left(1 - \beta \frac{\mathbf{r} \cdot \mathbf{u}(s')}{r} \right). \quad (5.62)$$

In the steady-state, the geometry of a bend can be used in Eq. (5.62). Moving to coordinates relative to the bunch center, the steady-state density seen by a test particle at z_t within the bunch as a function of z' is

$$\lambda_{\text{ret}}^{\text{s.s.}}(z'; z_t) = \left[1 - \beta \frac{\sin(\kappa(z_t - z'))}{\sqrt{2 - 2 \cos(\kappa(z_t - z'))}} \right] \lambda \left(z' + \beta \kappa^{-1} \sqrt{2 - 2 \cos(\kappa(z_t - z'))} \right). \quad (5.63)$$

This retarded density is illustrated in Fig. 5.9 for a Gaussian bunch distribution for various test particles. There one sees that the density in front of the test particle is compressed to roughly $\sigma/(1 + \beta) \approx \sigma/2$, concentrated in an apparent spike at the right of the plot. The density behind the test particle occupies the majority of the plot. While it may seem that the curves shown are Gaussian in form, this is only true for the left sides of the curves; the right sides have been extended and diluted due to the Jacobian factor in Eq. (5.62). Similarly, the retarded density of an image bunch at height h is

$$\lambda_{\text{ret}}(s', h; s) = \left[1 - \beta \frac{\mathbf{r} \cdot \mathbf{u}(s')}{\sqrt{r^2 + h^2}} \right] \lambda \left(s' - s_b - \beta ct + \beta \sqrt{r^2 + h^2} \right). \quad (5.64)$$

Figure 5.10 shows the retarded densities for a Gaussian bunch and several image bunches within a bend. In this example, the first and second image bunches as seen by particles in the rear of the bunch are actually *closer* than the real retarded bunch.

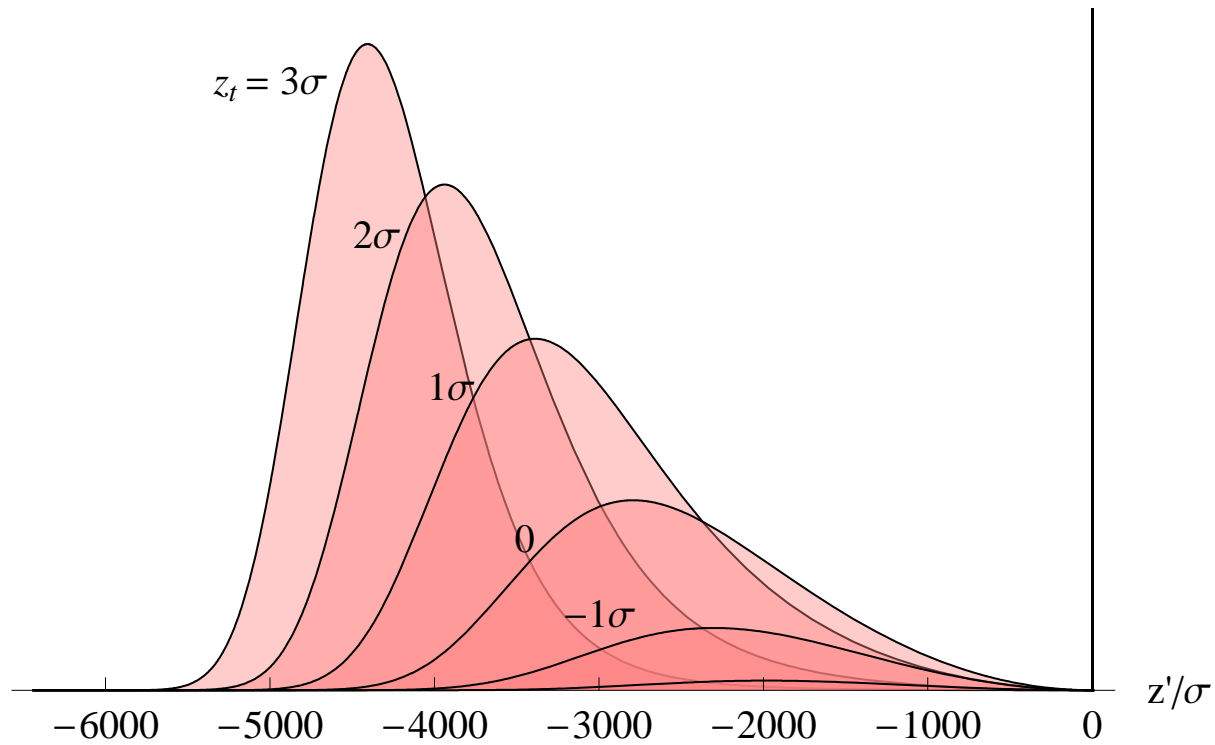


Figure 5.9: The steady-state retarded distribution $\lambda_{\text{ret,s.s.}}(z'; z_t)$ for various test particles z_t in Eq. (5.63) using a Gaussian bunch with standard deviation $\sigma = 0.3$ mm and energy 1 GeV, in a magnet of bending radius $\kappa^{-1} = 10.0$ m.

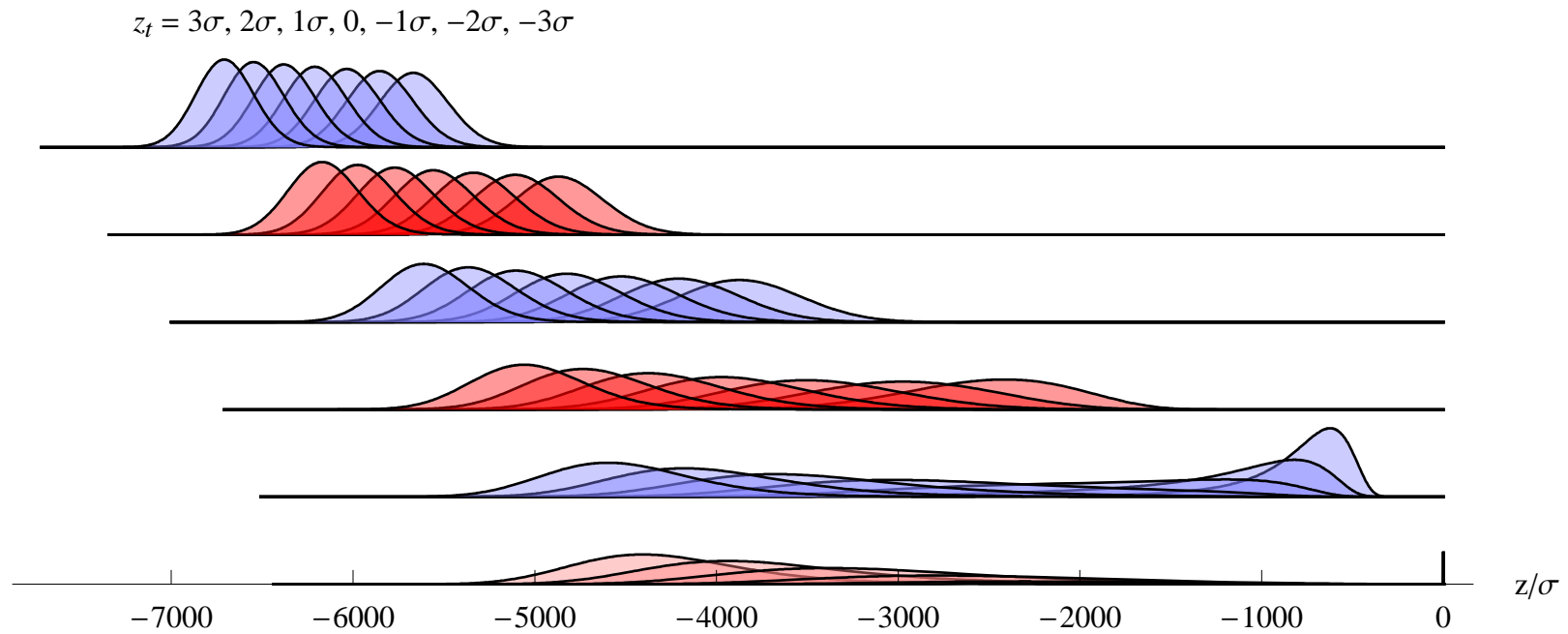


Figure 5.10: The same as Fig. 5.9, along with image charges at heights $nH = n \times 2$ cm (not to scale), which are approximately at heights $n \times 67\sigma$, and calculated using Eq. (5.64).

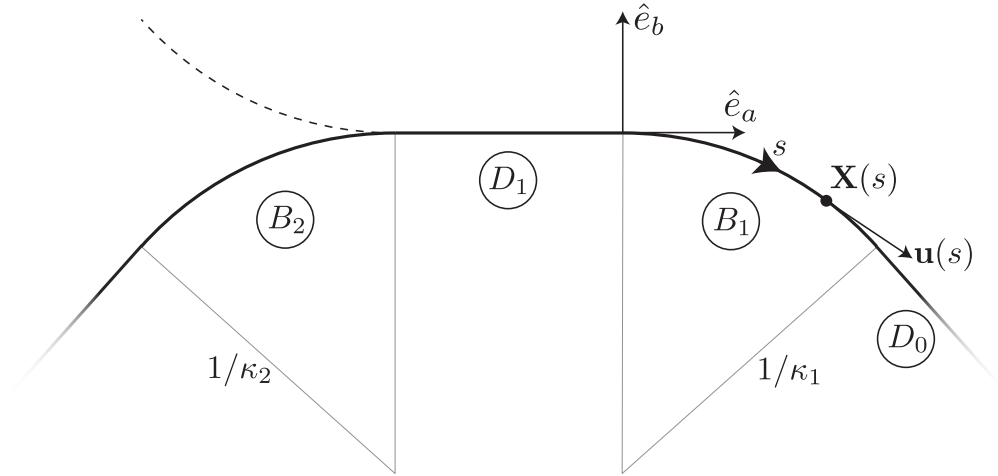


Figure 5.11: Geometry for bends and drifts. The variable s parameterizes the path $\mathbf{X}(s)$, with $s = 0$ at the beginning of element B_1 . The names $B_1, D_1, \text{etc.}$, also serve to indicate the element length. The dashed line is for a prior bend with negative curvature.

5.3 Multiple Bends and Drifts

In this section the general formula Eq. (5.3), regularized by Eq. (5.10), is applied to the geometry of multiply connected bends and drifts. Shielding by conducting parallel plates is added as in Eq. (5.45). It has been seen in Eq. (5.39) that the primary contribution to the CSR-wake in a bend is due to particles behind the test particle, so for brevity the path is given behind the test particle only.

Let the bunch center be at length s_0 inside bend 1 of length B_1 and positive curvature κ_1 , preceded by drift 1 of length D_1 , preceded by bend 2 of length B_2 and curvature $\kappa_2 \neq 0$, as shown in Fig. 5.11. A drift follows bend 1, referred to as D_0 . A negative curvature κ_2 signifies a bend in the opposite direction of bend

1. With $s = 0$ located at the beginning of bend 1, the path coordinates are

$$\mathbf{X}(s) = \begin{cases} \mathbf{X}_{D_0}(s) & \text{for } s > B_1 \\ \mathbf{X}_{B_1}(s) & \text{for } 0 < s \leq B_1 \\ s \hat{e}_a & \text{for } -D_1 < s \leq 0 \\ \mathbf{X}_{B_2}(s) & \text{for } s \leq -D_1 \end{cases} \quad (5.65)$$

where the paths in the individual elements are

$$\begin{aligned} \mathbf{X}_{D_0}(s) \equiv & \left[\frac{\sin(\kappa_1 B_1)}{\kappa_1} + (s - B_1) \cos(\kappa_1 B_1) \right] \hat{e}_a \\ & + \left[\frac{1}{\kappa_1} (\cos(\kappa_1 B_1) - 1) - (s - B_1) \sin(\kappa_1 B_1) \right] \hat{e}_b, \end{aligned} \quad (5.66)$$

$$\mathbf{X}_{B_1}(s) \equiv \frac{\sin(\kappa_1 s)}{\kappa_1} \hat{e}_a - \frac{[1 - \cos(\kappa_1 s)]}{\kappa_1} \hat{e}_b, \quad (5.67)$$

$$\begin{aligned} \mathbf{X}_{B_2}(s) \equiv & \left[\frac{\sin(\kappa_2 D_1 + \kappa_2 s)}{\kappa_2} - D_1 \right] \hat{e}_a \\ & - \frac{1 - \cos(\kappa_2 D_1 + \kappa_2 s)}{\kappa_2} \hat{e}_b. \end{aligned} \quad (5.68)$$

The tangent vector is then

$$\mathbf{u}(s) = \begin{cases} \cos(\kappa_1 B_1) \hat{e}_a - \sin(\kappa_1 B_1) \hat{e}_b & \text{for } s > B_1 \\ \cos(\kappa_1 s) \hat{e}_a - \sin(\kappa_1 s) \hat{e}_b & \text{for } 0 < s \leq B_1 \\ 1 \hat{e}_a & \text{for } -D_1 < s \leq 0 \\ \cos(\kappa_2 D_1 + \kappa_2 s) \hat{e}_a - \sin(\kappa_2 D_1 + \kappa_2 s) \hat{e}_b & \text{for } s \leq -D_1 \end{cases} \quad (5.69)$$

Straightforward calculation gives the total CSR-wake at position s in the bend ($0 < s < B_1$) due to these different sections of the path

$$\left. \frac{d\mathcal{E}_{\text{CSR}}}{ds} \right|_{\text{tot}} (0 < s < B_1) = \left. \frac{d\mathcal{E}_{\text{CSR}}}{ds} \right|_{B_1} + \left. \frac{d\mathcal{E}_{\text{CSR}}}{ds} \right|_{D_1} + \left. \frac{d\mathcal{E}_{\text{CSR}}}{ds} \right|_{B_2} + \dots \quad (5.70)$$

with B_1 , D_1 , and B_2 signifying the contributions from bend 1, drift 1, and bend 2, respectively. Due to their length, these terms are written out in Appendix C.

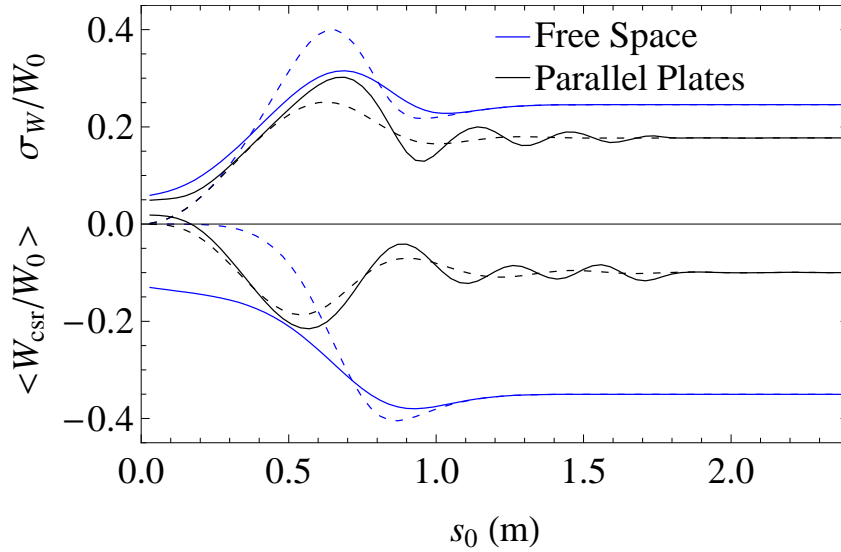


Figure 5.12: The average energy loss and energy spread induced, per unit length, of the CSR-wake for a Gaussian bunch through the length of a bend in free space as well as between parallel plates with $H = 2\text{cm}$. Solid lines have $D_1 = 1\text{m}$, while dashed lines have $D_1 \rightarrow \infty$. Parameters used are $\kappa_1^{-1} = \kappa_2^{-1} = 10\text{ m}$, $\sigma_z = 0.3\text{ mm}$, with an energy of 1 GeV .

A visualization of the retarded bunch and images of this geometry, similar to Fig. 5.10, is shown in Fig. 5.13. Even though the bunch has progressed 50 cm into bend 1, it sees much of the retarded bunch inside bend 2, especially for test particles z_t in the front of the bunch.

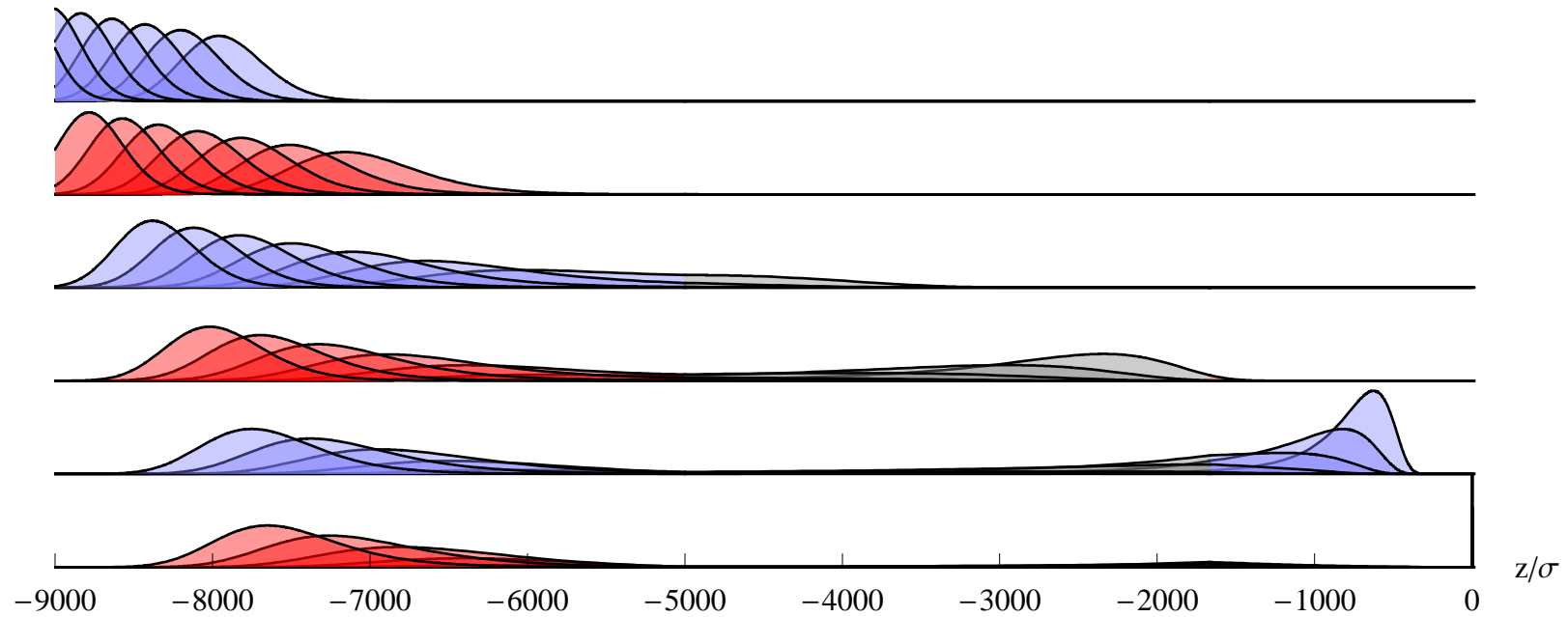


Figure 5.13: Similar to Fig. 5.10, but with a 1m drift (shaded in gray) between two magnets of curvature $\kappa_1 = \kappa_2 = 1/10\text{m}$. The center of the bunch is 50cm into the bend. A Gaussian bunch distribution is used with $\sigma_z = 0.3\text{ mm}$, an energy of 1GeV, and a shielding height $H = 2\text{ cm}$.

To show how the average energy loss (Eq. (5.60)) and energy spread (Eq. (5.61)) change as a bunch progresses through a bend, Fig. 5.12 plots $\langle W_{\text{CSR}} \rangle$ and σ_W , normalized by W_0 , versus different bunch center coordinates s_0 in bend 1 using Eq. (5.70) with $D_1 = 1\text{m}$ and $\kappa_1 = \kappa_2 = 1/10\text{m}$. In the literature, the wake near the beginning of bend 1 is often calculated as if the prior drift length $D_1 \rightarrow \infty$ (Saldin *et al.*, 1997; Agoh & Yokoya, 2004), so such calculations are plotted in dotted lines for comparison. From the difference between the two approaches, one sees the effect of bend 2, where the CSR-wake at $s_0 = 0$ is non-zero. In this example, they coincide after about 1.4 m and 1.8 m for the free space and shielded cases, respectively.

In order for it to be plausible to ignore the vacuum chamber sidewalls, such a chamber must be wide enough to allow a straight path between the retarded bunch and the test particle. In this example, the vector from a source particle at $z = -8000\sigma$ to the center of the bunch ($z = 0$) requires that the vacuum chamber half-width must be greater than approximately 3 cm.

5.4 CSR in a Drift Between Bends

The non-zero CSR-wake at the beginning of bend 1 in Fig. 5.12 is evidence that the wake in a drift region after a bend also needs to be considered. This exit-wake in the region D_0 following bend 1 is calculated using Eq. (5.3) with Eq. (5.65) and Eq. (5.69) around the center of a bunch at $s_0 > B_1$. Because the bunch is moving in a straight line, the regularization procedure simply removes the need to integrate any $s' > B_1$ for the real bunch. Therefore we can use Eq. (5.3) for bend 1, drift 1, and earlier elements, and subtract the space charge terms for $s' < B_1$. Image charges, however, still require terms for $s' > B_1$. The total exit wake is then

$$\left. \frac{d\mathcal{E}_{\text{CSR}}}{ds} \right|_{\text{tot}} (s > B_1) = \left. \frac{d\mathcal{E}_{\text{images}}}{ds} \right|_{D_0} + \left. \frac{d\mathcal{E}_{\text{CSR}}}{ds} \right|_{B_1} + \left. \frac{d\mathcal{E}_{\text{CSR}}}{ds} \right|_{D_1} + \dots, \quad (5.71)$$

where the individual terms due to element elements D_0, B_1, D_1 , are written out in Appendix C.

For a magnet of length $B_1 = 3\text{m}$, the exit wakes in the following drift D_0 are shown in Fig. 5.14 for bunch centers in the following 3 meters between parallel plates and in free space. The average and standard deviation of the wakes through this region are shown in Fig. 5.15. In the shielded situation, one sees that the bunch actually gains some energy in a short length following the bend, and that the total energy loss between parallel plates is negligible compared to the free space losses. Energy spread, however, is qualitatively the same in both cases.

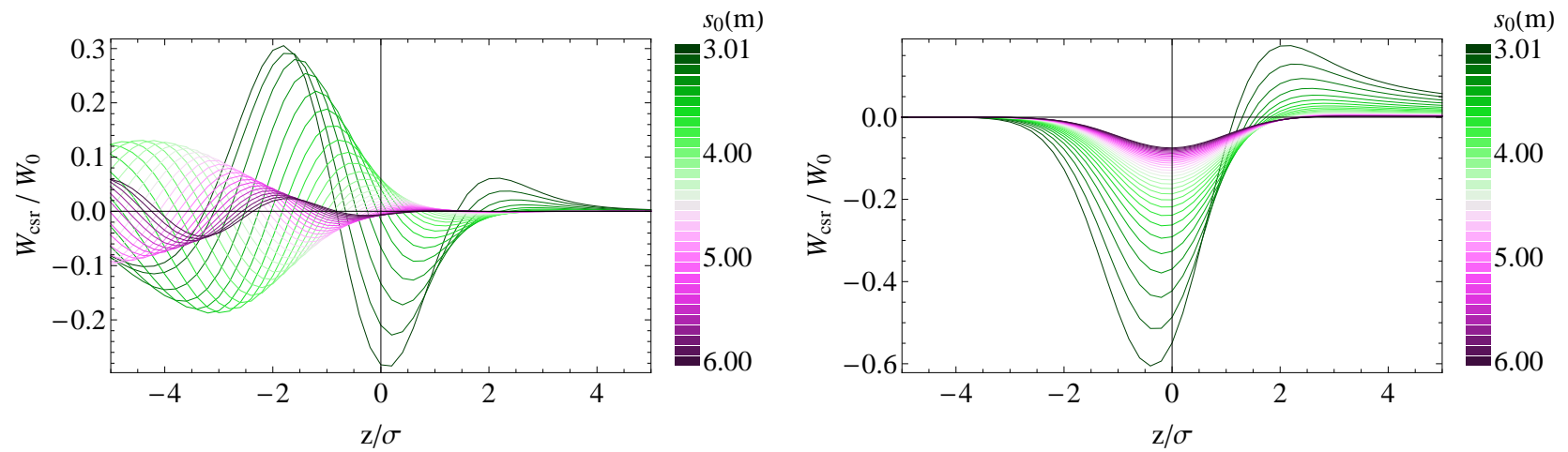


Figure 5.14: CSR-wakes for various bunch centers $s_0 > B_1$ calculated using Eq. (5.71). The left graph uses parallel plates separated by a distance $H = 2\text{cm}$, while the right graph is for free space ($n = 0$ terms only in Eqs. (C.6)-(C.7), and without Eq. (C.5)). The bending radius $\kappa_1^{-1} = 10\text{m}$, and the bunch has a Gaussian profile with $\sigma = 0.3\text{mm}$ and an energy of 1GeV .

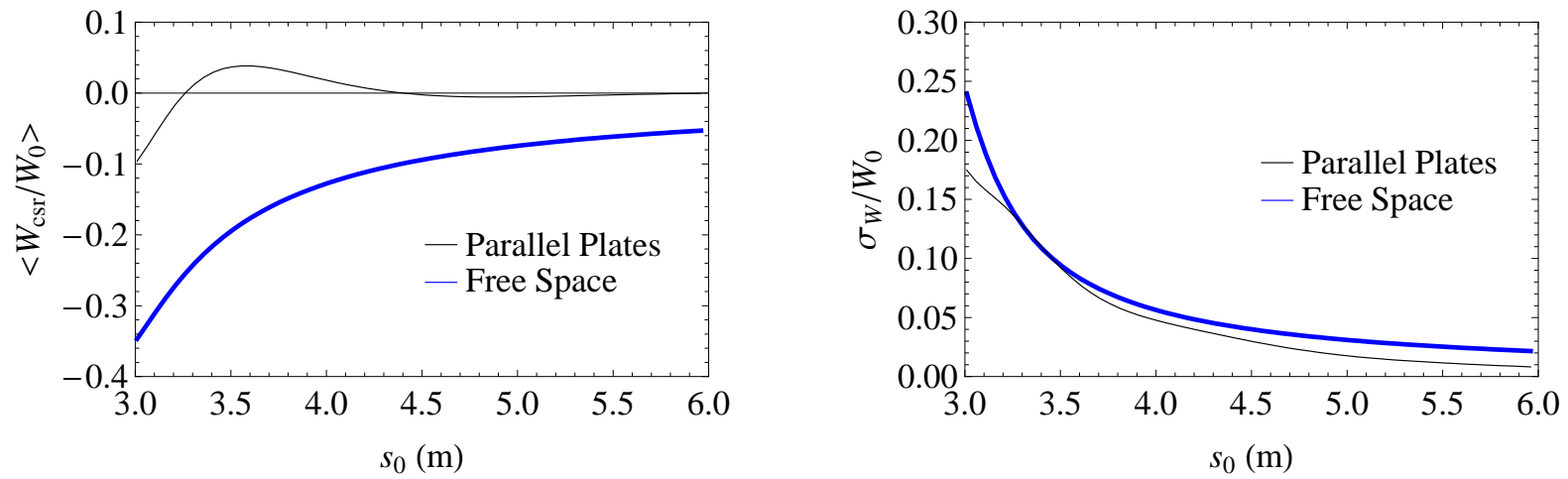


Figure 5.15: The average energy loss and energy spread per unit length of the exit wakes in Fig. 5.14. In this example, shielding by parallel plates drastically reduces the energy loss, but only marginally reduces the energy spread, when compared to free space calculations.

5.5 Bunch Compression

Bunch compression or decompression can be achieved in a bending magnet if there is a correlation between energy and longitudinal position of particles in the bunch. To exactly calculate CSR for this, however, requires at least a 2-dimensional model, because particles of different energies travel on different orbits. In the framework of the 1-dimensional model described by Eq. (5.3), this effect can be approximately modeled by allowing the bunch length to be time dependent, and neglecting variations in the velocity βc . The density and current are then

$$\begin{aligned}\rho(s, t) &= Q \frac{1}{\sigma(t)} \tilde{\lambda} \left(\frac{s - s_b - \beta ct}{\sigma(t)} \right), \\ \mathbf{J}(s, t) &= Q \beta c \frac{1}{\sigma(t)} \tilde{\lambda} \left(\frac{s - s_b - \beta ct}{\sigma(t)} \right),\end{aligned}\tag{5.72}$$

where $\tilde{\lambda}$ has unit norm and variance with respect to s , as in Eq (5.37). The time derivative of $\rho(s, t)$ is

$$\frac{\partial}{\partial t} \rho(s, t) = -\beta c \frac{Q \tilde{\lambda}' \left(\frac{s_t}{\sigma} \right)}{\sigma^2} - \dot{\sigma} \left[\frac{Q \tilde{\lambda} \left(\frac{s_t}{\sigma} \right)}{\sigma^2} + \frac{s_t}{\sigma} \frac{Q \tilde{\lambda}' \left(\frac{s_t}{\sigma} \right)}{\sigma^2} \right].\tag{5.73}$$

with $s_t \equiv s - s_b - \beta ct$. Note that $\dot{\sigma}/(\beta c)$ is on the order of σ/B in a magnet of length B , and $(s - s_b - \beta ct)$ is on the order of σ for all relevant (s, t) , and therefore the term in brackets is on the order of $\sigma/B \ll 1$ relative to the first term, and will be neglected. With such an approximation, the CSR-wake in a bunch compression system can be modeled by simply making the substitutions

$$\lambda(s_r) \rightarrow \frac{1}{\sigma(t_{\text{ret}})} \tilde{\lambda} \left(\frac{s_r}{\sigma(t_{\text{ret}})} \right)\tag{5.74}$$

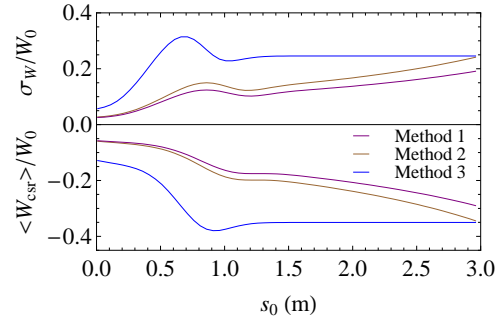
$$\lambda'(s_r) \rightarrow \frac{1}{[\sigma(t_{\text{ret}})]^2} \tilde{\lambda}' \left(\frac{s_r}{\sigma(t_{\text{ret}})} \right)\tag{5.75}$$

$$t_{\text{ret}} = t - \sqrt{r^2 + (nH)^2}/c\tag{5.76}$$

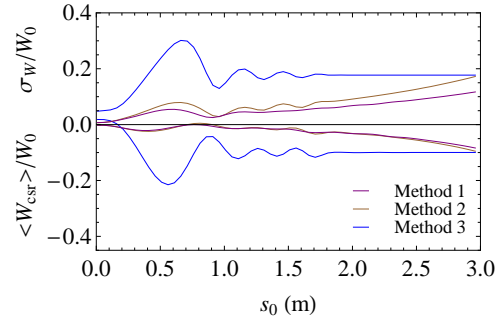
in all of the previous formulas, with $r = \|\mathbf{X}(s) - \mathbf{X}(s')\|$, as in Eq. (5.3). This accounts for the real charges ($n = 0$) and image charges ($n \neq 0$) at the appropriate retarded times.

Calculations for the average and standard deviation of the CSR-wake with a linearly compressing bunch through the length of bend 1 in free space are shown in Fig. 5.16(a). The above approximation is referred to as Method 1. Method 2 calculates the instantaneous CSR-wake of a compressing bunch at each point in the bend *as if* it always had its instantaneous length. Such a scheme is essentially what particle tracking codes use for CSR simulation, *e.g.* `elegant` (Borland, 2000) and `Bmad` (Sagan, 2006). For reference, Method 3 calculates the CSR-wake for a non-compressing bunch that maintains the same length as the final compressed length in Methods 1 and 2. In this example, Method 2 overestimates the CSR effect compared to the more realistic Method 1, and both exhibit a much smaller effect than Method 3. At the end of the magnet ($s_0 = 3$ m), the CSR-wake, according to Method 1, has yet to reach its corresponding steady-state strength.

Figure 5.16(b) shows these same calculations but between parallel plates with $H = 2$ cm. One sees that the energy loss in method 2 is similar to that in method 1, but the energy spread induced is overestimated. Free space and shielded calculations are repeated with $D_1 \rightarrow \infty$ in Figs. 5.16(c)–5.16(d), which when compared with Figs. 5.16(a)–5.16(b) one can see the effect of the previous bend B_2 .



(a) Free Space Bunch Compression



(b) Parallel Plates Bunch Compression

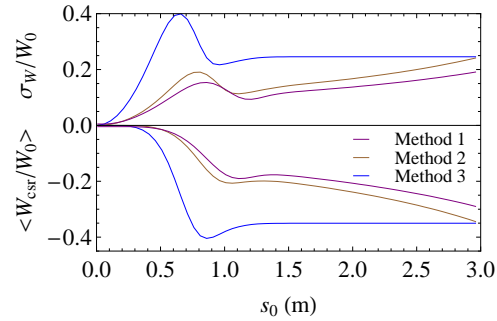
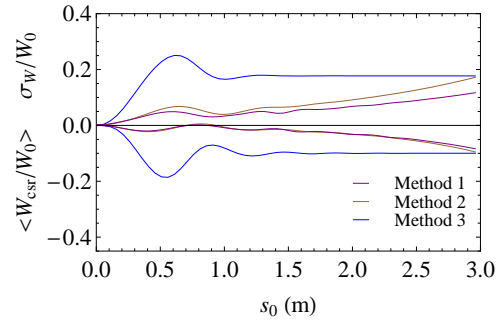
(c) Free Space Bunch Compression, $D_1 \rightarrow \infty$ (d) Parallel Plates Bunch Compression, $D_1 \rightarrow \infty$

Figure 5.16: The average and standard deviation of the CSR-wake in free space (Fig. 5.16(a)) and between parallel plates with $H = 2\text{cm}$ (Fig. 5.16(b)) over a Gaussian bunch, compressing from $\sigma = 0.9\text{mm}$ to $\sigma = 0.6\text{mm}$ linearly through bend 2, and from $\sigma = 0.6\text{mm}$ to $\sigma = 0.3\text{mm}$ linearly through bend 1, using methods described in the text. Figures 5.16(a)–5.16(b) have $D_1 = 1\text{m}$, while Figs. 5.16(c)–5.16(d) have $D_1 \rightarrow \infty$. The lengths $B_1 = B_2 = 3\text{m}$, the bending radii are $\kappa_1^{-1} = \kappa_2^{-1} = 10\text{m}$, and the energy is 1GeV .

5.6 Coherent Power Spectrum

Some of the first CSR calculations are found in an originally unpublished report by Schwinger (1945). Here we use one of his methods to derive an exact expression for the coherent energy loss by a Gaussian beam, which is then used to verify our earlier calculations. Consider the power spectrum due to a *single* particle moving on a circle with velocity βc , which is proportional to the absolute square of the Fourier transform electric field $\mathbf{E}^{(1)}(\Omega, t)$, integrated over solid angle Ω , as in

$$\frac{dP^{(1)}}{d\omega} \propto \int d\Omega \left| \int_{-\infty}^{\infty} dt e^{i\omega t} \mathbf{E}^{(1)}(\Omega, t) \right|^2. \quad (5.77)$$

For N particles moving on this circle with positions $s = s_n + \beta ct$, the total electric field can be written in terms of the single particle's electric field ($s_n = 0$), as in

$$\mathbf{E}^{(N)}(\Omega, t) = \sum_{n=1}^N \mathbf{E}^{(1)}(\Omega, t - t_n), \quad (5.78)$$

where the time deviations $t_n = s_n/(\beta c)$. By changing variables, this means that the N particle power spectrum is simply

$$\frac{dP^{(N)}}{d\omega} = \left| \sum_{n=1}^N e^{i\omega t_n} \right|^2 \frac{dP^{(1)}}{d\omega}. \quad (5.79)$$

These phase factors can be separated into terms with $m = n$ and $m \neq n$,

$$\begin{aligned} \frac{dP^{(N)}}{d\omega} &= \left(\sum_{m=1}^N e^{i\omega t_m} \sum_{n=1}^N e^{-i\omega t_n} \right) \frac{dP^{(1)}}{d\omega} \\ &= N \frac{dP^{(1)}}{d\omega} + \frac{dP^{(1)}}{d\omega} \sum_{m=1}^N \exp\left(i\omega \frac{s_m}{\beta c}\right) \sum_{\substack{n=1 \\ n \neq m}}^N \exp\left(-i\omega \frac{s_n}{\beta c}\right), \end{aligned} \quad (5.80)$$

so that the second term can be written as a correlation between different particles

$$\sum_{m \neq n} \exp\left(i\omega \frac{s_m - s_n}{\beta c}\right) \simeq N(N-1) \int ds \lambda(s) \exp\left(i\omega \frac{s}{\beta c}\right) \int ds' \lambda(s') \exp\left(-i\omega \frac{s'}{\beta c}\right) \quad (5.81)$$

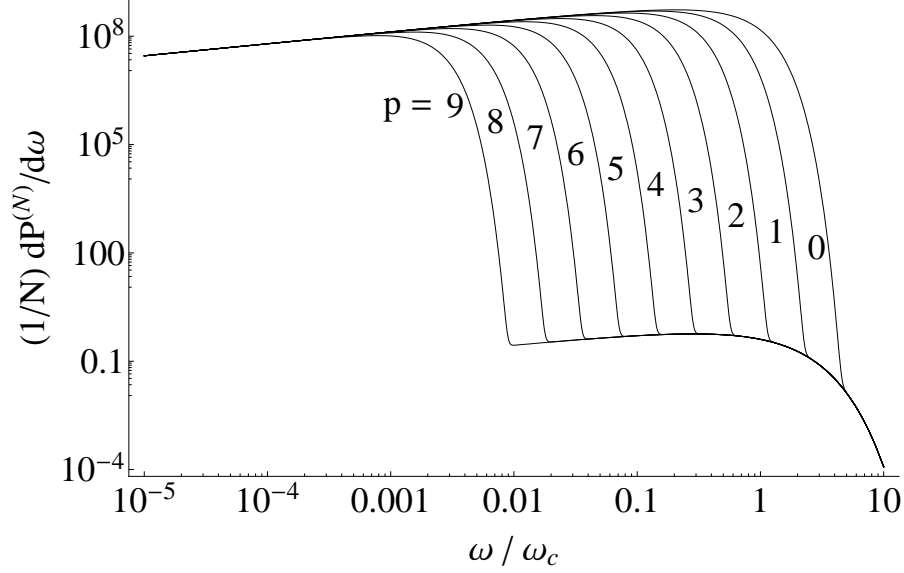


Figure 5.17: The power spectrum in Eq. (5.82), per particle, using a Gaussian form factor with various values of the coherence parameter $a_c = 2^p$, defined in Eq. (5.87). The lower frequencies are enhanced by a factor of N , and in this example $N = 10^9$.

using the normalized particle distribution $\lambda(s)$ along the circle. The N particle power spectrum is then

$$\frac{dP^{(N)}}{d\omega}(\omega) \simeq \underbrace{N \frac{dP^{(1)}}{d\omega}}_{\text{incoherent}} + \underbrace{N(N-1) \left| \int ds \lambda(s) \exp\left(i \frac{\omega s}{\beta c}\right) \right|^2}_{\text{coherent}} \frac{dP^{(1)}}{d\omega}. \quad (5.82)$$

The first term in Eq. (5.82) is the incoherent power spectrum, while the second is the coherent power spectrum. The squared integral is called the form-factor.

In free space, the well-known single particle power spectrum is

$$\frac{dP^{(1)}}{d\omega}(\omega) = \frac{P^{(1)}}{\omega_c} S\left(\frac{\omega}{\omega_c}\right), \quad (5.83)$$

where $\omega_c \equiv \frac{3}{2}\gamma^3 c \kappa$ is the critical frequency (Jackson, 1999; Chao & Tigner, 2006).

The function S is defined as

$$S(\xi) \equiv \frac{9\sqrt{3}}{8\pi} \xi \int_{\xi}^{\infty} dx K_{5/3}(x), \quad (5.84)$$

in which K is a modified Bessel function. The integral $\int_0^\infty S(x) dx = 1$, and the total power lost by a single particle is

$$P^{(1)} \equiv \frac{2}{3} r_c m c^3 \beta^4 \gamma^4 \kappa^2. \quad (5.85)$$

For a Gaussian distribution with variance σ^2 and $\kappa \sigma \ll 1$, the form-factor is, extending the integration limits to infinity,

$$\begin{aligned} \left| \int_{-\infty}^{\infty} ds \frac{\exp\left(i \frac{\omega s}{\beta c} - \frac{s^2}{2\sigma^2}\right)}{\sqrt{2\pi} \sigma} \right|^2 &= \exp\left(-\frac{\sigma^2 \omega^2}{\beta^2 c^2}\right) \\ &= \exp\left\{-\left(a_c \frac{\omega}{\omega_c}\right)^2\right\}, \end{aligned} \quad (5.86)$$

defining the coherence factor

$$\begin{aligned} a_c &\equiv \frac{3}{2\beta} \gamma^3 \kappa \sigma \\ &= \frac{\sigma}{\beta c} \omega_c. \end{aligned} \quad (5.87)$$

The total power spectrum per particle for an N -particle Gaussian distribution with various values of a_c is shown in Fig. 5.17. One sees from the exponential that the lower frequencies, up to a cutoff frequency around $\omega = \beta c/\sigma$, are enhanced by a factor of N by the coherent part of Eq. (5.82). The spectrum at higher frequencies agrees with the familiar single particle spectrum in Eq. (5.83).

It turns out that Eq. (5.82) can be integrated exactly for a Gaussian distribution. Explicitly, the total power radiated by N particles is

$$\begin{aligned} P^{(N)} &= NP^{(1)} \int_0^\infty S(x) dx + N(N-1)P^{(1)} \frac{9\sqrt{3}}{8\pi} \int_0^\infty x e^{-a_c^2 x^2} \left[\int_x^\infty K_{5/3}(y) dy \right] dx \\ &= NP^{(1)} + N(N-1)P^{(1)} \frac{9\sqrt{3}}{8\pi} \int_0^\infty K_{5/3}(y) \left[\int_0^y x e^{-a_c^2 x^2} dx \right] dy \\ &= NP^{(1)} + N(N-1)P^{(1)} T_c \left(\frac{3}{2\beta} \gamma^3 \kappa \sigma \right), \end{aligned} \quad (5.88)$$

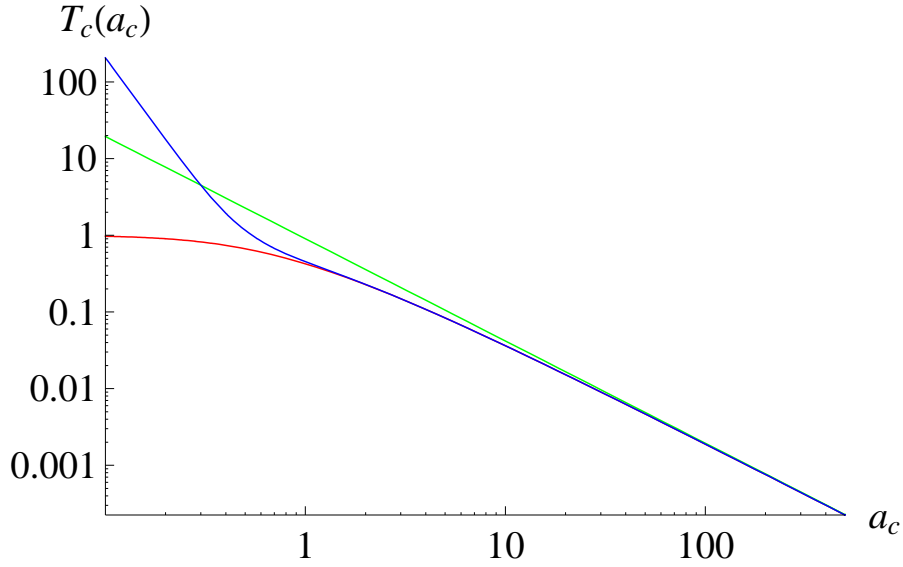


Figure 5.18: The coherence function $T_c(a_c)$ of Eq. (5.89) is plotted in red. The green curve is the first term in the asymptotic expansion in Eq. (5.90) (Nodvick & Saxon, 1954), and the blue curve uses all three terms in Eq. (5.90).

in which the final integral yields the coherence function defined as

$$T_c(a_c) \equiv \frac{9}{32 \sqrt{\pi} a_c^3} \exp\left(\frac{1}{8a_c^2}\right) K_{5/6}\left(\frac{1}{8a_c^2}\right) - \frac{9}{16a_c^2}. \quad (5.89)$$

The limit $\lim_{a \rightarrow 0^+} T_c(a) = 1$, which is to say that an infinitely narrow bunch radiates as one charge. In practical situations $a_c \gg 1$, so an asymptotic expansion of T_c gives the useful approximation

$$T_c(a_c) \sim \frac{9 \Gamma\left(\frac{5}{6}\right)}{16^{2/3} \sqrt{\pi}} \left(\frac{1}{a_c}\right)^{4/3} - \frac{9}{16} \left(\frac{1}{a_c}\right)^2 + \frac{9 \Gamma\left(\frac{5}{6}\right)}{32 \cdot 2^{2/3} \sqrt{\pi}} \left(\frac{1}{a_c}\right)^{10/3} + \dots \quad (5.90)$$

The first term in Eq. (5.90) is given in Nodvick & Saxon (1954). Figure 5.18 compares this first term to the exact expression in Eq. (5.89) and to all three terms in Eq. (5.90). One sees an excellent approximation for $a_c \gtrsim 50$ using the first term and for $a_c \gtrsim 1$ using all three terms in Eq. (5.90). Also, the average

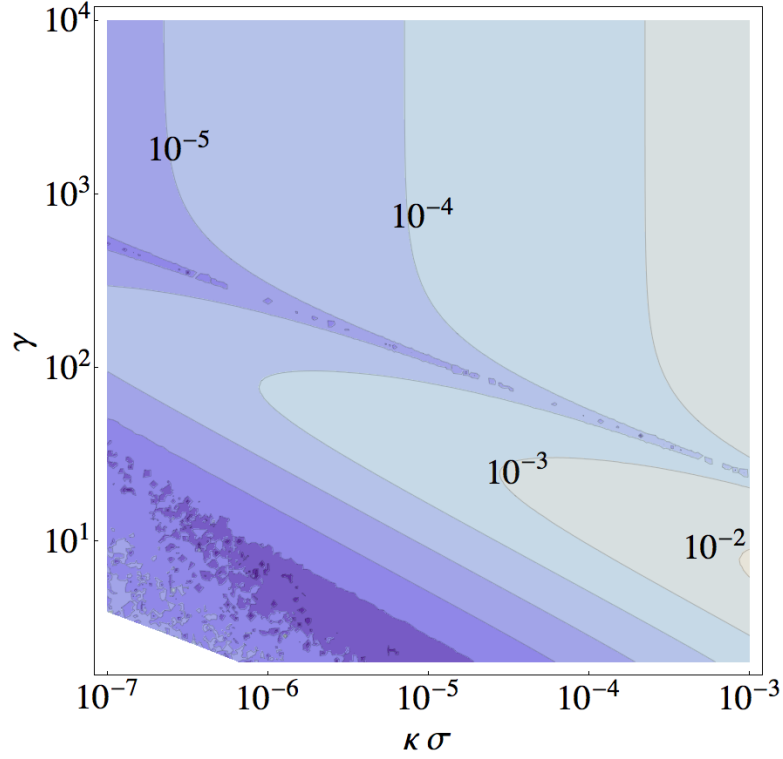


Figure 5.19: The relative difference $|(b - a)|/b$ for a the average energy lost using Eq. (5.32), and b being the result in Eq. (5.91).

coherent energy lost per particle per unit length is

$$\left\langle \frac{P^{(N)}}{N\beta c} \right\rangle_{\text{coh.}} = -\frac{2}{3}(N-1)r_c m c^2 \gamma^4 \beta^3 \kappa^2 T_c \left(\frac{2}{3} \gamma^3 \kappa \sigma \right) \quad (5.91)$$

$$\sim -\frac{\Gamma\left(\frac{5}{6}\right)}{6^{1/3} \sqrt{\pi}} W_0 + \dots, \quad (5.92)$$

using W_0 defined in Eq. (5.40). The numerical coefficient $\Gamma(5/6) 6^{-1/3} \pi^{-1/2} \simeq 0.350$. The same procedure in Eq. (5.88) and Eq. (5.90) can be carried out for a uniform distribution of length ΔL with the same variance σ^2 , implying that $\Delta L = 2\sqrt{3}\sigma$. The result yields the same form as Eq. (5.92), except with the numerical coefficient $2^{-4/3} \simeq 0.397$. This term was originally derived in Schwinger (1945).

To verify that the CSR-wake does indeed represent the coherent energy lost,

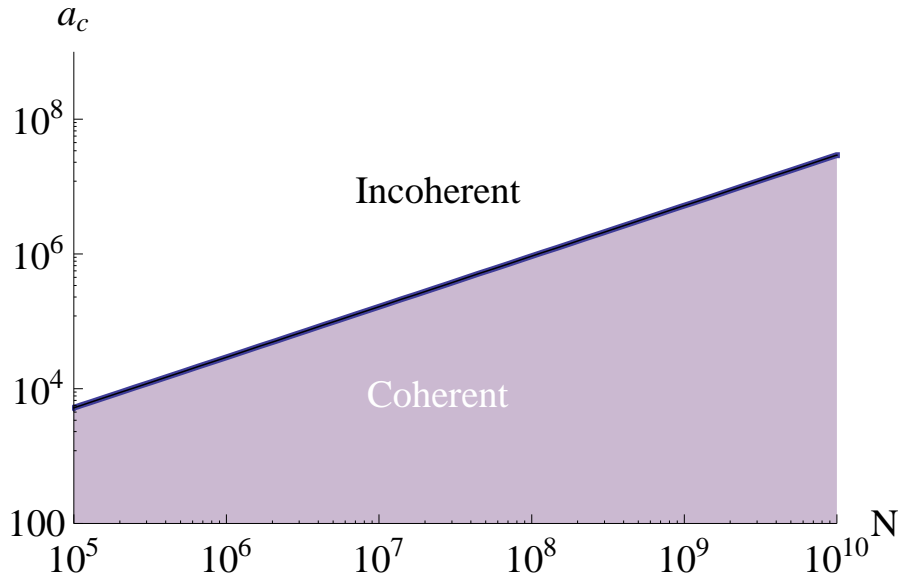


Figure 5.20: The dividing line where the coherent power equals the incoherent power, *i.e.* the total power is twice the incoherent power. Below this line, the coherent power dominates the total power.

the relative difference of the average energy loss using the steady-state wake of a Gaussian bunch in Eq. (5.32) to the result in Eq. (5.91) is plotted in Fig. 5.19. One sees that the relative difference is at most 1% in this practical parameter range, and that occurs with relatively long bunches. We speculate that this error is caused by the regularization procedure that subtracts the space charge term from the longitudinal electric field.

The relevance of the coherence function depends on the number of particles $N - 1 \simeq N$. The coherent power radiated equals the incoherent power radiated when $N \cdot T_c(a_c) = 1$, illustrated in Fig. 5.20. Using Eq. (5.90), the coherent power dominates the total power when

$$\kappa \sigma \lesssim \frac{N^{3/4}}{\gamma^3}. \quad (5.93)$$

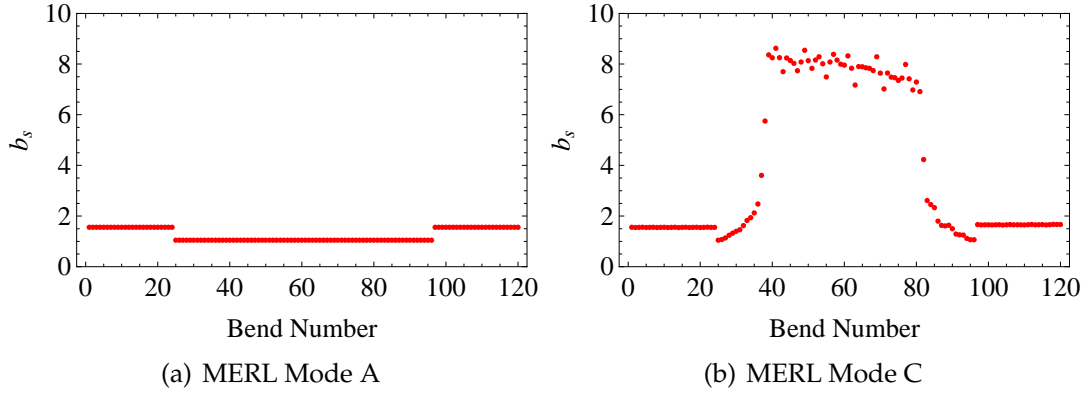


Figure 5.21: The shielding parameter b_s described in Section 5.2.2 for all of the bending magnets in the MERL, including the second TA pass.

5.7 CSR in the MERL

As we have seen, the exact 1D CSR calculations can be quite involved even for simple series elements. In order to simulate CSR in a realistic accelerator lattice, we use the *Bmad* libraries to track particles through elements and apply the CSR-wake calculated from the longitudinal bunch density. The *Bmad* method is described in Sagan *et al.* (2008), and is thoroughly tested against other CSR codes, including the exact 1D method described in this chapter.

These simulations can be relatively time consuming, as the details of the bunch distribution constantly change as the bunch evolves. Nevertheless, we can give estimates of the importance of CSR in the MERL using lattice information such as chamber height, dipole bending radius, *etc.*, along with bunch lengths through particle tracking without CSR. For example, to see if shielding is a factor, we plot the parameter b_s described in Section 5.2.2 for each of the bending magnets, including the second TA pass, in Fig. 5.21. According to Fig. 5.8, shielding will be effective when $b_s \lesssim 3$, and we see in Fig. 5.21(a) that this is the case for Mode A. However, in Mode C the bunch becomes sufficiently

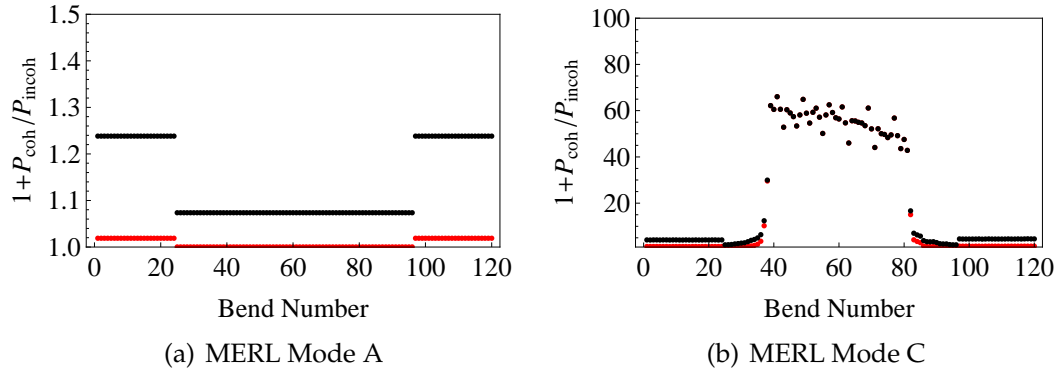


Figure 5.22: The ratio of the steady-state incoherent radiation power P_{incoh} to the coherent power P_{coh} , plus one, for all of the bends in the MERL, including the second TA pass.

short in the middle of the RA that shielding is no longer effective, as shown in Fig. 5.21(b).

Even in free space, CSR is only important relative to incoherent radiation when Eq. (5.93) is satisfied. To estimate this, the ratio of the incoherent radiation power to the coherent radiation power, plus one, is shown in Fig. 5.22 for free space and with shielding for each bend in the MERL. These quantities are calculated for the steady-state, which typically gives the worst case effect. This number is therefore the multiplicative factor of the incoherent power to give the total radiation power. In Fig. 5.22(a) we see that the shielding practically eliminates the coherent radiation power in Mode A, whereas the short bunches in Mode C produce coherent radiation which dominate the total radiation power, as shown in Fig. 5.22(b).

These estimates imply that CSR is not very important for Mode A, and this is confirmed through particle tracking with *Bmad* (not shown). However, we can expect that CSR in Mode C, due to the large number of particles and short bunches, will play a dominant role. This is illustrated in Fig. 5.23, which shows the bunch length through the MERL RA with and without shielding, and compared with the bunch length when the CSR effect is turned off in the code. As expected, the shielding plays a negligible role. Also shown in the figure are results from tracking a bunch with a lower charge of 77 pC, the same charge as Mode A, and there we see that CSR becomes unimportant.

In all cases we see that the bunches can be compressed to 100 fs, but the lengths of the 1 nC bunches degrade through the following cells. To explain this, the longitudinal phase space slices at the first and last short pulse undulators in the RA, for non-shielded, shielded, and lower charge bunches, are shown in Fig. 5.24. There we can see, for the 1 nC bunches, that particles in the center and the tail of the bunch lose energy due to CSR and are sheared to the left in the plot due to high order time of flight terms.

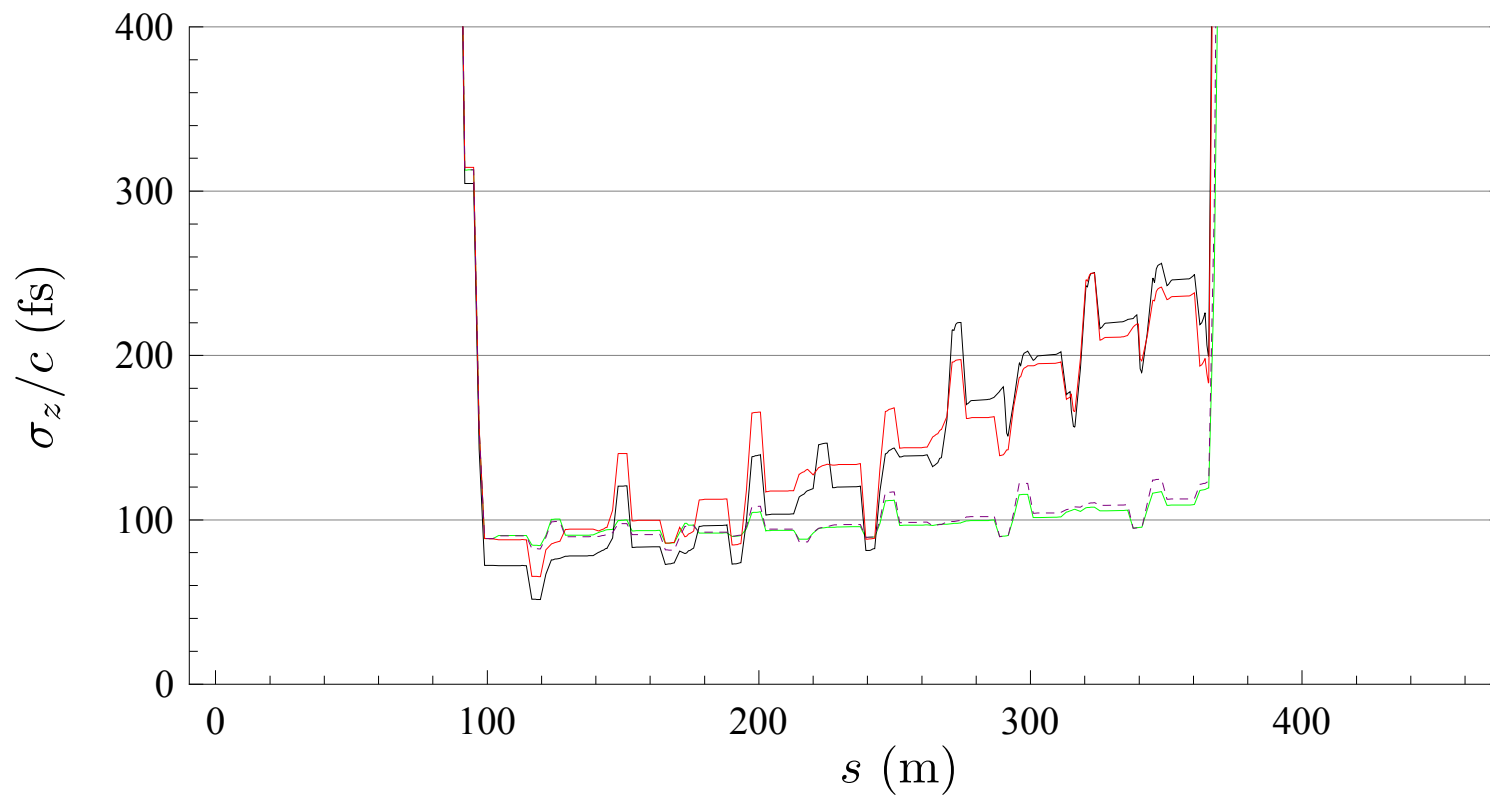


Figure 5.23: The bunch length σ_z for Mode C through the MERL RA using *Bmad* for particle tracking with CSR. The black curve is for 1 nC of charge without shielding, and the red curve is for 1 nC of charge with shielding. The dashed purple curve is for 77 pC of charge with shielding, and the green curve is with the CSR effects turned off.

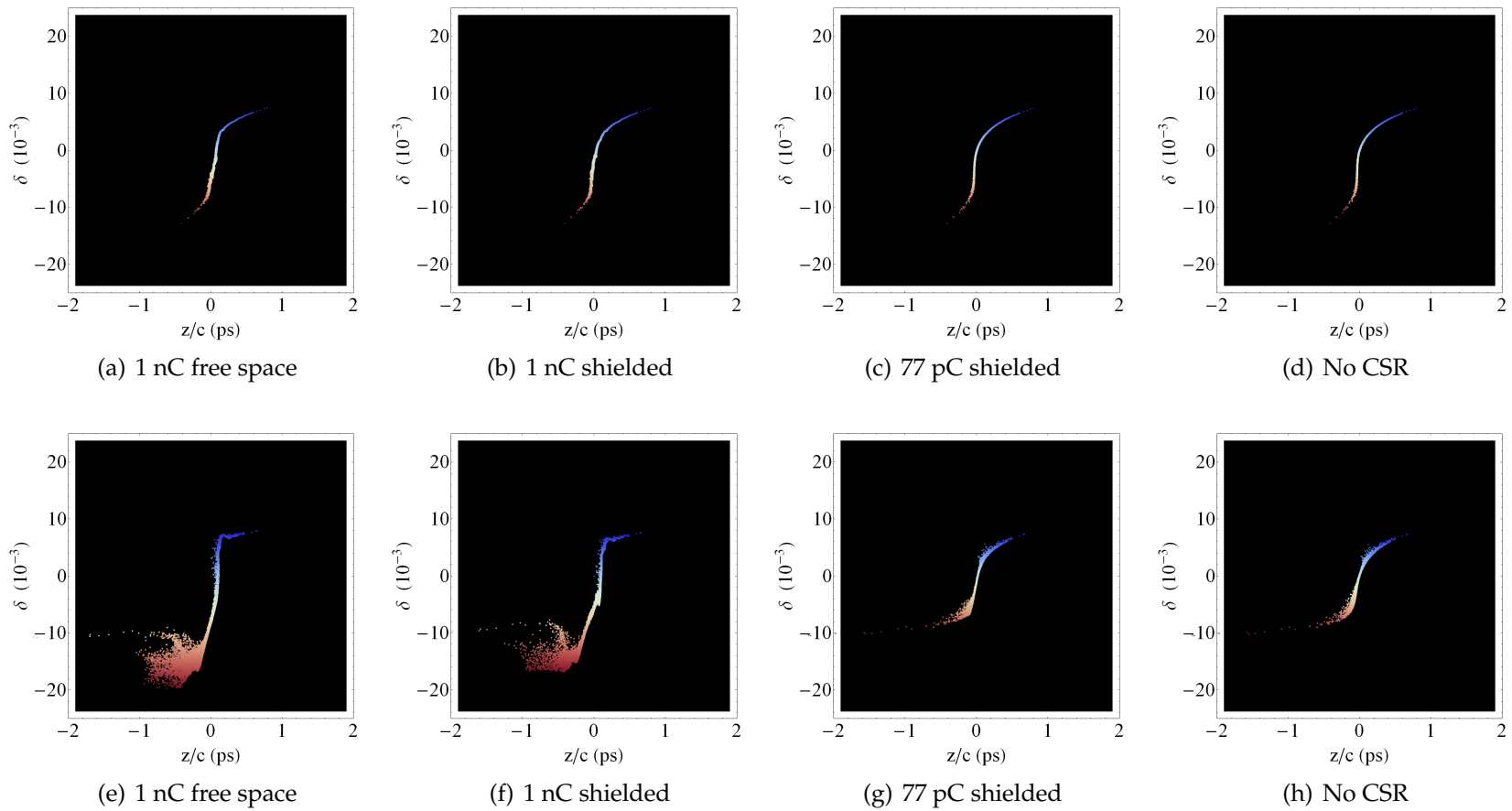


Figure 5.24: Longitudinal phase space slices in the first short pulse undulator (top row) and the last short pulse undulator (bottom row) in the MERL RA. Particles are tracked with CSR effects using *Bmad*.

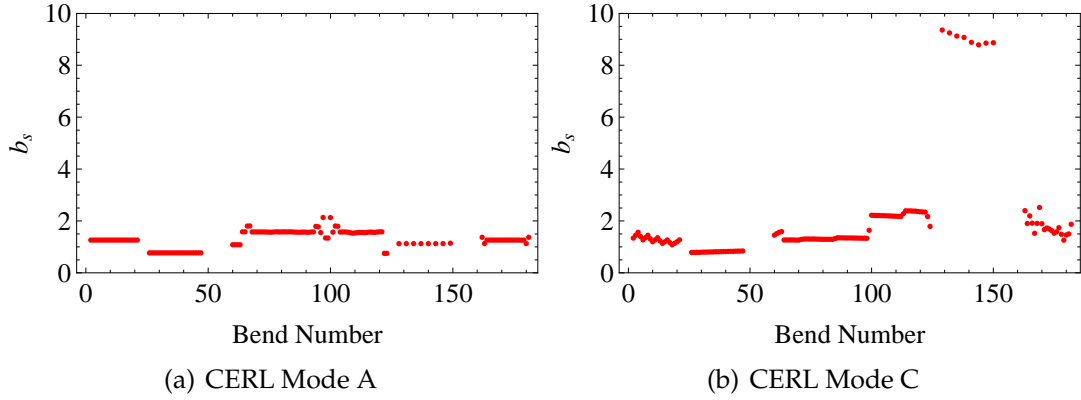


Figure 5.25: The shielding parameter b_s described in Section 5.2.2 for all of the bending magnets in the CERL. Note that Mode C uses the upgraded CE section.

5.8 CSR in the CERL

The same analysis in Section 5.7 can be done for the CERL lattice. For Mode C, we will use the upgraded CE section. The shielding parameter b_s for all of the bends in the CERL is shown in Fig. 5.25. There we see that shielding plays a role in both Mode A and Mode C for all sections other than the compressed bunch section in the NA. The ratio of the incoherent power to the coherent power, plus one, is shown in Fig. 5.26.

The bunch lengths from particle tracking with CSR effects using $Bmad$ for Mode C through the SA-CE-NA sections are shown in Fig. 5.27. Unlike the MERL results, the compressed bunch lengths using shielded and non-shielded tracking for 1 nC of charge are very different.

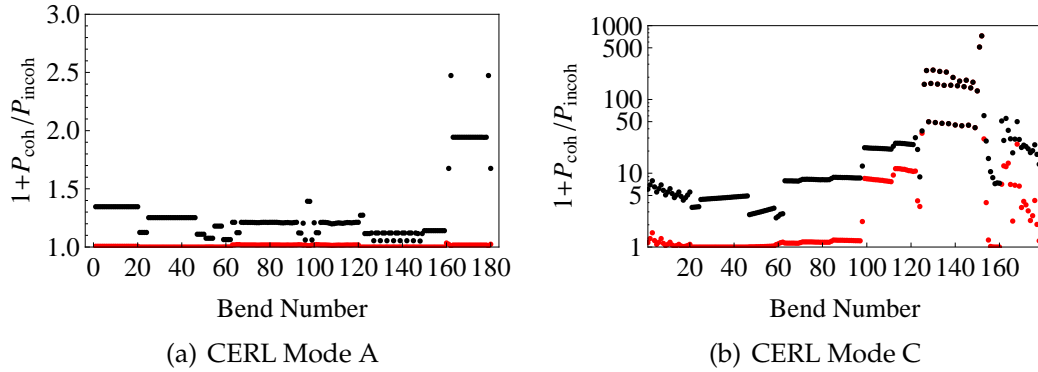


Figure 5.26: The ratio of the steady-state incoherent radiation power P_{incoh} to the coherent power P_{coh} , plus one, for all of the bends in the CERL, including the second TA pass. Note that Mode C uses the upgraded CE section.

The longitudinal phase space slices in the first and last short pulse undulators for these cases are shown in Fig. 5.28. There we can see that the CSR-wake in the free space CSR case changes the energy distribution so much through the partially compressed section from approximately $s = 800$ m to $s = 1100$ m, that the time of flight terms for the final section before the first NA undulator shear the bulk of the lower energy particles to the right of the plot, resulting in a relatively long bunch length. When the shielding is taken into account, these energy changes are less drastic, resulting in a moderately well compressed bunch. Like the MERL, when 77 pC bunches are used the CSR effect is less apparent.

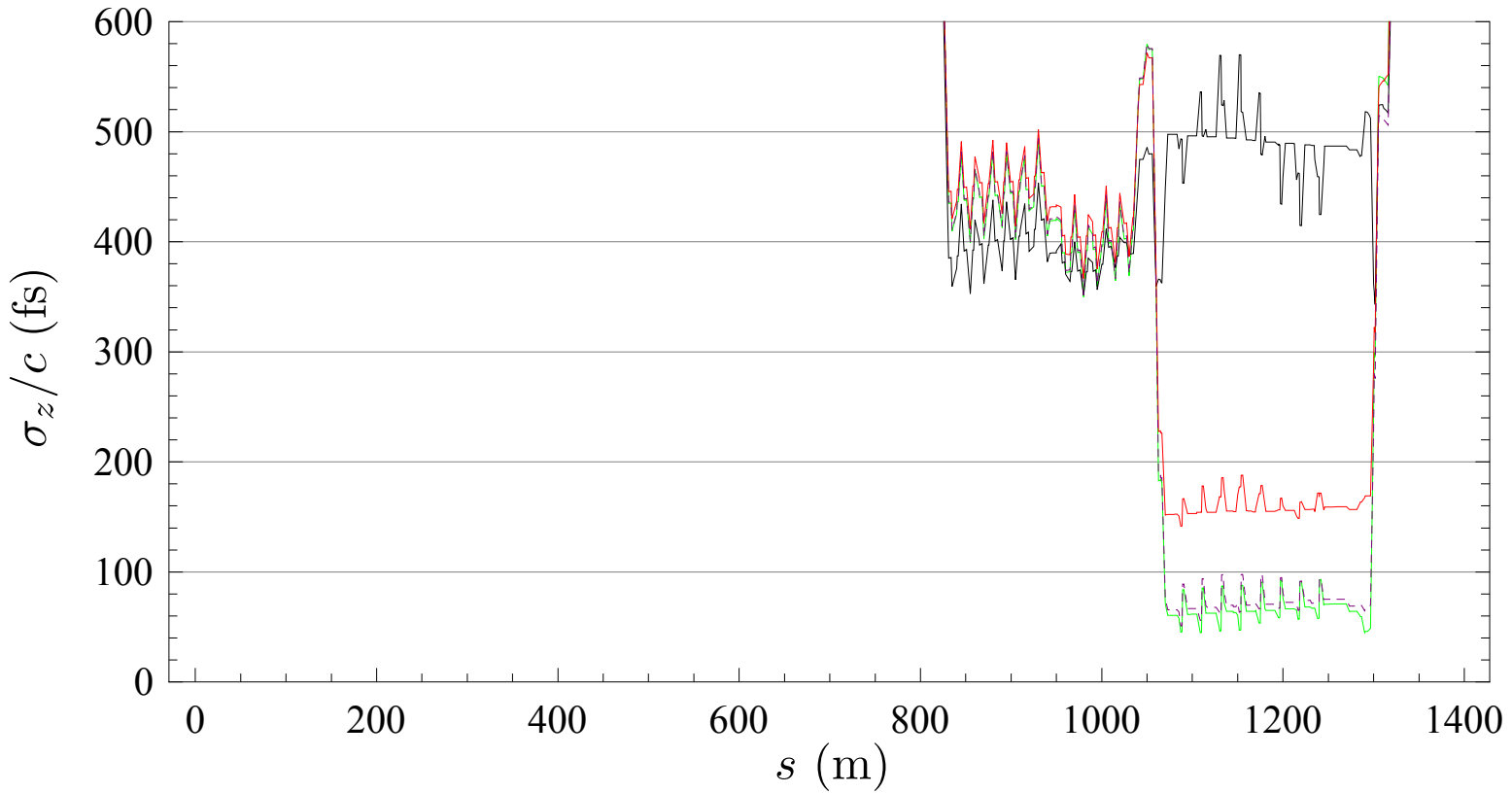


Figure 5.27: The bunch length σ_z for Mode C through the CERL SA-CE-NA sections (with upgraded CE) using *Bmad* for particle tracking with CSR. The black curve is for 1 nC of charge without shielding, and the red curve is for 1 nC of charge with shielding. The dashed purple curve is for 77 pC of charge with shielding, and the green curve is with the CSR effects turned off.

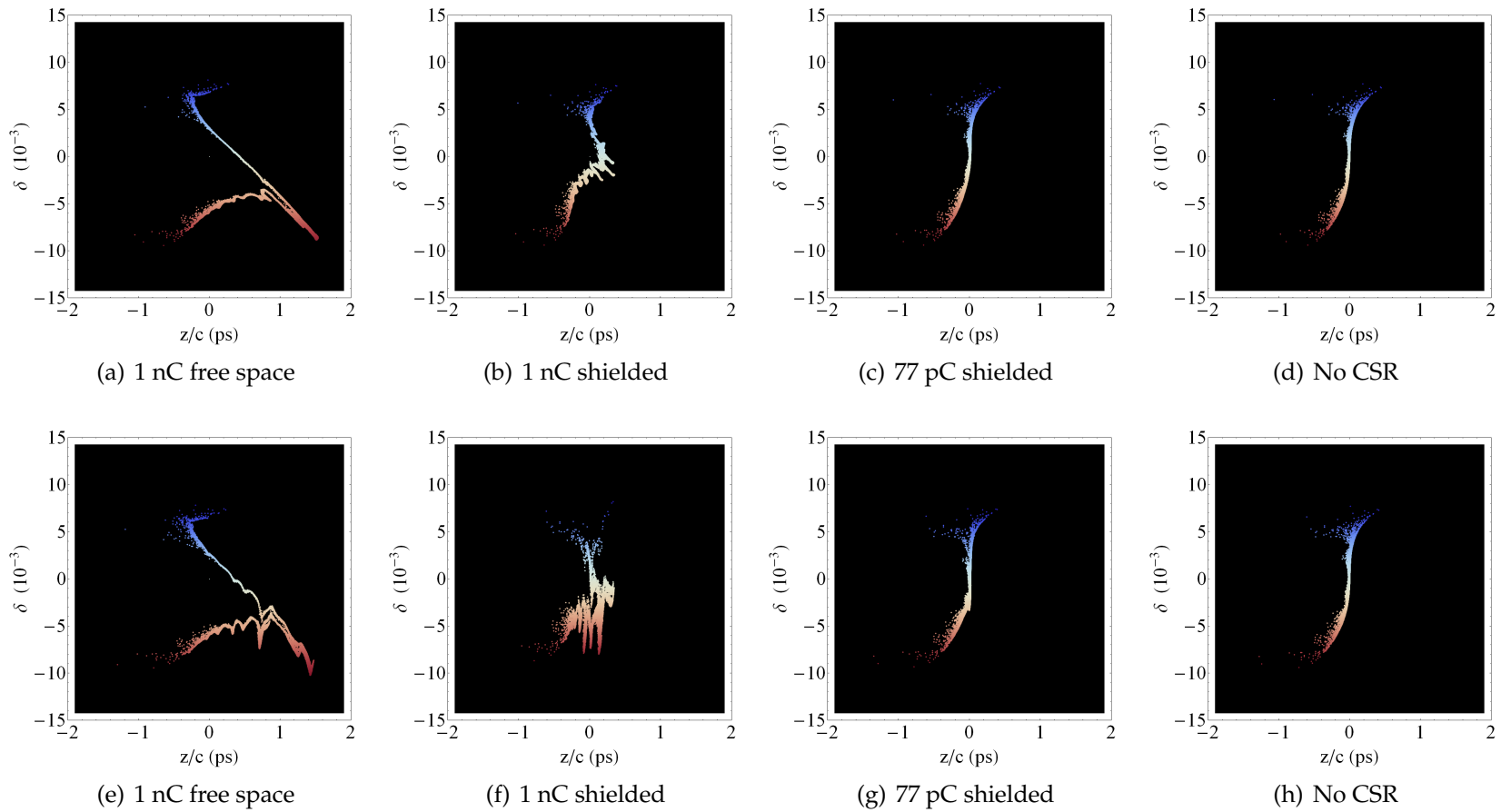


Figure 5.28: Longitudinal phase space slices in the first short pulse undulator (top row) and the last short pulse undulator (bottom row) in the CERL NA. Particles are tracked with CSR effects using *Bmad*.

5.9 Conclusion

The wake-field due to CSR of a 1-dimensional bunch traveling on a curve without small angle or high energy approximations has been derived using Jefimenko's forms of Maxwell's equations. This exact solution allowed us to quantify the accuracy of the approximations of the steady-state CSR-wake in a bend given in Saldin *et al.* (1997) and Sagan *et al.* (2008) showing that the former is inaccurate at low energies and long bunch lengths, and that the latter is much more accurate down to low energies. All approximations tend to overestimate the CSR-wake. For planar orbits the equations are extended to include shielding by perfectly conducting parallel plates using the image charge method.

The formulas have been applied to the geometry of a bend preceded by a drift, preceded by another bend, and show that the CSR-wake well inside the downstream bend is influenced by the upstream bend for the parameters used. In fact, a bunch near the entrance of a bend is influenced by the CSR-wake due to the previous bend much more than by that due to the previous drift. Shielding by parallel plates reduces the energy loss rate significantly, but the effect on reducing energy spread increase is far less dramatic, in both the drift and bend regions.

Bunch compression has been added to this model by allowing the bunch length to be time dependent, so that the retarded charge density seen by a test particle is appropriately taken into account. This method has been compared to simple methods used by particle simulation codes *Bmad* and *elegant*, and it is shown that these tend to overestimate the effect.

Additionally, an exact expression for the coherent power lost by a 1-dimensional Gaussian bunch moving in a circle has been derived by integrating the power spectrum, following the method of Schwinger (1945). When compared to the energy loss rate by the CSR-wake, the two show slight deviations. This could be due to the regularization procedure for the 1-dimensional CSR-wake that subtracts off the space charge term.

Finally, the effect of shielded CSR in the MERL and the CERL has been calculated by tracking particles through the respective lattices using *Bmad*. There we see that CSR in Mode A is well shielded, whereas the high charge in Mode C can disturb the bunch compression process.

APPENDIX A
EQUATIONS OF MOTION

Here an alternative derivation of the equations of motion in curvilinear coordinates is given by directly using the geodesic equations. Background material can be found in books by Carroll (2004) and Misner, Thorne, and Wheeler (1973). For this section only, the speed of light $c = 1$.

In curvilinear coordinates (t, x, y, s) , the infinitesimal line element is

$$-d\tau^2 = -dt^2 + dx^2 + dy^2 + h^2 ds^2, \quad (\text{A.1})$$

where $h = h(x, y, s)$ is a function of the space coordinates only. The time is t , and τ is the proper time. The spacetime metric and its inverse are then

$$g_{\mu\nu} = \text{diag}(-1, 1, 1, h^2), \quad (\text{A.2})$$

$$g^{\mu\nu} = \text{diag}(-1, 1, 1, h^{-2}). \quad (\text{A.3})$$

Now let a particle with mass m and charge q travel on a curve parameterized by τ with coordinates $X^\mu(\tau)$. Written in the natural coordinate system $\mathbf{e}_\mu = \partial_\mu$, the components of the four-velocity $V = V^\mu \mathbf{e}_\mu$ are

$$V^\mu = \frac{dX^\mu}{d\tau}, \quad (\text{A.4})$$

or explicitly

$$(V^t, V^x, V^y, V^s) = \left(\frac{dt}{d\tau}, \frac{dx}{d\tau}, \frac{dy}{d\tau}, \frac{ds}{d\tau} \right). \quad (\text{A.5})$$

The middle two terms can be written in terms of derivatives with respect to s , since

$$\begin{aligned} \frac{dx}{d\tau} &= \frac{ds}{d\tau} \frac{dx}{ds} \\ &= V^s \frac{dx}{ds}. \end{aligned} \quad (\text{A.6})$$

Also defining the relativistic factor $\gamma \equiv dt/d\tau$, the four-velocity components are

$$(V^t, V^x, V^y, V^s) = (\gamma, \gamma \dot{x}', \gamma \dot{y}', \gamma \dot{s}), \quad (\text{A.7})$$

with primes denoting s derivatives and dots denoting t derivatives.

In general, the motion of this particle in the presence of external electromagnetic fields is governed by the equations of motion

$$\frac{dV^\mu}{d\tau} + \Gamma_{\alpha\beta}^\mu V^\alpha V^\beta = \frac{q}{m} F^{\mu\nu} V_\nu. \quad (\text{A.8})$$

The Christoffel symbols are given in terms of the metric as

$$\Gamma_{\alpha\beta}^\mu = \frac{1}{2} g^{\mu\nu} (\partial_\alpha g_{\beta\nu} + \partial_\beta g_{\alpha\nu} - \partial_\nu g_{\alpha\beta}), \quad (\text{A.9})$$

and the Faraday tensor components are

$$F^{\alpha\beta} = \begin{bmatrix} 0 & -E^x & -E^y & -E^s \\ E^x & 0 & -B^s & B^y \\ E^y & B^s & 0 & -B^x \\ E^s & -B^y & B^x & 0 \end{bmatrix}. \quad (\text{A.10})$$

Individual components are to be read from this with α being the column and β being the row. For example, $F^{tx} = E^x$.

Using the metric in Eq. (A.2), the only nonzero Christoffel symbols are

$$\Gamma_{ss}^x = -h \partial_x h, \quad (\text{A.11})$$

$$\Gamma_{ss}^y = -h \partial_y h, \quad (\text{A.12})$$

$$\Gamma_{sx}^s = \Gamma_{xs}^s = h^{-1} \partial_x h, \quad (\text{A.13})$$

$$\Gamma_{sy}^s = \Gamma_{ys}^s = h^{-1} \partial_y h, \quad (\text{A.14})$$

$$\Gamma_{ss}^s = h^{-1} \partial_s h. \quad (\text{A.15})$$

The equations of motion for this system are then

$$\frac{dV^t}{d\tau} = \frac{q}{m} (V^x E^x + V^y E^y + h^2 V^s E^s), \quad (\text{A.16})$$

$$\frac{dV^x}{d\tau} - (V^s)^2 h \partial_x h = \frac{q}{m} (V^t E^x + V^y B^s - h^2 V^s B^y), \quad (\text{A.17})$$

$$\frac{dV^y}{d\tau} - (V^s)^2 h \partial_y h = \frac{q}{m} (V^t E^y - V^x B^s + h^2 V^s B^x), \quad (\text{A.18})$$

$$\frac{dV^s}{d\tau} + \frac{V^s}{h} (2V^x \partial_x h + 2V^y \partial_y h + V^s \partial_s h) = \frac{q}{m} (V^t E^s + V^x B^y - V^y B^x). \quad (\text{A.19})$$

To bring these in line with Eqs. (2.20-2.23), we have to address a subtlety regarding vectors in the moving frame. The basis vectors used here are in the natural frame $\mathbf{e}_{\mu'}$ and are related to basis vectors in the moving frame $\mathbf{e}_{\hat{\mu}}$ by

$$\mathbf{e}_{\hat{t}} = \mathbf{e}_t, \quad (\text{A.20})$$

$$\mathbf{e}_{\hat{x}} = \mathbf{e}_x, \quad (\text{A.21})$$

$$\mathbf{e}_{\hat{y}} = \mathbf{e}_y, \quad (\text{A.22})$$

$$\mathbf{e}_{\hat{s}} = \frac{1}{h} \mathbf{e}_s. \quad (\text{A.23})$$

This means that the usual three-velocity \mathbf{v} can be written as

$$\mathbf{v} = \frac{V^x}{V^t} \mathbf{e}_x + \frac{V^y}{V^t} \mathbf{e}_y + \frac{V^s}{V^t} \mathbf{e}_s \quad (\text{A.24})$$

$$= \frac{V^x}{V^t} \mathbf{e}_{\hat{x}} + \frac{V^y}{V^t} \mathbf{e}_{\hat{y}} + h \frac{V^s}{V^t} \mathbf{e}_{\hat{s}} \quad (\text{A.25})$$

$$= \dot{s} x' \mathbf{e}_{\hat{x}} + \dot{s} y' \mathbf{e}_{\hat{y}} + \dot{s} h \mathbf{e}_{\hat{s}}, \quad (\text{A.26})$$

which is exactly Eq. (2.9). Slightly more complicated is the Faraday tensor \mathbf{F} written in the two bases,

$$\mathbf{F} = F^{\alpha\beta} \mathbf{e}_\alpha \otimes \mathbf{e}_\beta \quad (\text{A.27})$$

$$= F^{\hat{\alpha}\hat{\beta}} \mathbf{e}_{\hat{\alpha}} \otimes \mathbf{e}_{\hat{\beta}}, \quad (\text{A.28})$$

$$(\text{A.29})$$

with the components of $F^{\hat{\alpha}\hat{\beta}}$ labeled similarly to Eq. (A.10), e.g. $F^{\hat{t}\hat{x}} = E^{\hat{x}}$ and $F^{\hat{x}\hat{y}} = B^{\hat{s}}$. The bases are related by $\mathbf{e}_{\hat{t}} \otimes \mathbf{e}_{\hat{x}} = \mathbf{e}_t \otimes \mathbf{e}_x$, $\mathbf{e}_{\hat{t}} \otimes \mathbf{e}_{\hat{s}} = h^{-1} \mathbf{e}_t \otimes \mathbf{e}_s$, etc., so equating components gives the following identifications

$$E^x = E^{\hat{x}}, \quad (\text{A.30})$$

$$E^y = E^{\hat{y}}, \quad (\text{A.31})$$

$$E^s = E^{\hat{s}}/h, \quad (\text{A.32})$$

$$B^x = B^{\hat{x}}/h, \quad (\text{A.33})$$

$$B^y = B^{\hat{y}}/h, \quad (\text{A.34})$$

$$B^s = B^{\hat{s}}. \quad (\text{A.35})$$

Putting all this together, and converting τ derivatives to s derivatives, Eqs. (A.16-A.19) give

$$\dot{\gamma} = \frac{q}{m} \dot{s} (x' E^{\hat{x}} + y' E^{\hat{y}} + h E^{\hat{s}}), \quad (\text{A.36})$$

$$x'' + x' \frac{1}{(\gamma \dot{s})^2} \frac{dV^s}{d\tau} - h \partial_x h = \frac{q}{m \gamma \dot{s}^2} E^{\hat{x}} + \frac{q}{m \gamma \dot{s}} (y' B^{\hat{s}} - h B^{\hat{y}}), \quad (\text{A.37})$$

$$y'' + y' \frac{1}{(\gamma \dot{s})^2} \frac{dV^s}{d\tau} - h \partial_y h = \frac{q}{m \gamma \dot{s}^2} E^{\hat{y}} + \frac{q}{m \gamma \dot{s}} (h B^{\hat{x}} - x' B^{\hat{s}}), \quad (\text{A.38})$$

$$h \frac{1}{(\gamma \dot{s})^2} \frac{dV^s}{d\tau} + 2x' \partial_x h + 2y' \partial_y h + \partial_s h = \frac{q}{m \gamma \dot{s}^2} E^{\hat{s}} + \frac{q}{m \gamma \dot{s}} (x' B^{\hat{y}} - y' B^{\hat{x}}). \quad (\text{A.39})$$

Noting that

$$\frac{1}{(\gamma \dot{s})^2} \frac{dV^s}{d\tau} = \frac{\ddot{s}}{\dot{s}^2} + \frac{\dot{\gamma}}{\gamma \dot{s}}, \quad (\text{A.40})$$

and with $h = 1 + \kappa_0(s) x$, the results in Eqs. (2.20-2.23) are recovered. Also note that $\partial_s x \neq x'$.

APPENDIX B
LINEAR TRANSFER MATRICES

The six-dimensional transfer matrix for a drift with length L is

$$\begin{bmatrix} 1 & L & 0 & 0 & 0 & 0 \\ 0 & 1 & 0 & 0 & 0 & 0 \\ 0 & 0 & 1 & L & 0 & 0 \\ 0 & 0 & 0 & 1 & 0 & 0 \\ 0 & 0 & 0 & 0 & 1 & 0 \\ 0 & 0 & 0 & 0 & 0 & 1 \end{bmatrix}, \quad (\text{B.1})$$

and for a dipole magnet with length L and radius $1/\kappa_0$ is

$$\begin{bmatrix} \cos(\kappa_0 L) & \frac{1}{\kappa_0} \sin(\kappa_0 L) & 0 & 0 & 0 & \frac{1}{\kappa_0} [1 - \cos(\kappa_0 L)] \\ -\kappa_0 \sin(\kappa_0 L) & \cos(\kappa_0 L) & 0 & 0 & 0 & \sin(\kappa_0 L) \\ 0 & 0 & 1 & L & 0 & 0 \\ 0 & 0 & 0 & 1 & 0 & 0 \\ -\sin(\kappa_0 L) & \frac{1}{\kappa_0} [\cos(\kappa_0 L) - 1] & 0 & 0 & 1 & \frac{1}{\kappa_0} \sin(\kappa_0 L) - L \\ 0 & 0 & 0 & 0 & 0 & 1 \end{bmatrix}. \quad (\text{B.2})$$

The transfer matrix for a quadrupole magnet focusing in the horizontal plane with length L and quadrupole strength k_1 is

$$\begin{bmatrix} \cos(\sqrt{k_1} L) & \frac{1}{\sqrt{k_1}} \sin(\sqrt{k_1} L) & 0 & 0 & 0 & 0 \\ -\sqrt{k_1} \sin(\sqrt{k_1} L) & \cos(\sqrt{k_1} L) & 0 & 0 & 0 & 0 \\ 0 & 0 & \cosh(\sqrt{k_1} L) & \frac{1}{\sqrt{k_1}} \sinh(\sqrt{k_1} L) & 0 & 0 \\ 0 & 0 & \sqrt{k_1} \sinh(\sqrt{k_1} L) & \cosh(\sqrt{k_1} L) & 0 & 0 \\ 0 & 0 & 0 & 0 & 1 & 0 \\ 0 & 0 & 0 & 0 & 0 & 1 \end{bmatrix}, \quad (\text{B.3})$$

and for a quadrupole magnet focusing in the vertical plane with length L and quadrupole strength k_1 is

$$\begin{bmatrix} \cosh(\sqrt{k_1} L) & \frac{1}{\sqrt{k_1}} \sinh(\sqrt{k_1} L) & 0 & 0 & 0 & 0 \\ \sqrt{k_1} \sinh(\sqrt{k_1} L) & \cosh(\sqrt{k_1} L) & 0 & 0 & 0 & 0 \\ 0 & 0 & \cos(\sqrt{k_1} L) & \frac{1}{\sqrt{k_1}} \sin(\sqrt{k_1} L) & 0 & 0 \\ 0 & 0 & -\sqrt{k_1} \sin(\sqrt{k_1} L) & \cos(\sqrt{k_1} L) & 0 & 0 \\ 0 & 0 & 0 & 0 & 1 & 0 \\ 0 & 0 & 0 & 0 & 0 & 1 \end{bmatrix}. \quad (\text{B.4})$$

APPENDIX C

CSR FORMULAS FOR MULTIPLE BENDS AND DRIFTS

For ease of reading, the individual terms terms in Eq. (5.70) and Eq. (5.71) have been deferred to here. They are calculated by applying Eq. (5.3), regularized by Eq. (5.10), including image charges as in Eq. (5.45), to the geometry in Eq. (5.65).

In Eq. (5.70), the first term $d\mathcal{E}_{\text{csr}}/ds|_{B_1}$ is the sum of Eq. (5.29) and Eq. (5.47) with $\kappa \rightarrow \kappa_1$ and $\theta \rightarrow \kappa_1 s$, explicitly

$$\begin{aligned}
 \frac{d\mathcal{E}_{\text{CSR}}(s)}{ds}\Big|_{B_1} = & N r_c m c^2 \left\{ \int_{\alpha_a}^{\alpha_b} d\alpha \left(\frac{\beta^2 \cos(\alpha) - 1}{2|\sin(\alpha/2)|} + \frac{1}{\gamma^2} \frac{\text{sgn}(\alpha) - \beta \cos(\alpha/2)}{\alpha - 2\beta|\sin(\alpha/2)|} \right) \lambda'(s_\alpha) \right. \\
 & - \frac{\kappa_1 \lambda(s_\alpha)}{2|\sin(\alpha/2)|} \Big|_{\alpha_a}^{\alpha_b} + \int_{\Delta_a}^{\infty} d\Delta \frac{1}{\gamma^2} \frac{\lambda'(z - \Delta)}{\Delta} + \int_{\Delta_b}^{\infty} d\Delta \frac{1}{\gamma^2} \frac{\lambda'(z + \Delta)}{\Delta} \\
 & \left. + \sum_{n=1}^{\infty} 2(-1)^n \left[\frac{-\kappa_1 \lambda(s_{\alpha,n})}{r_{\alpha,n}} \Big|_{\alpha_a}^{\alpha_b} + \int_{\alpha_a}^{\alpha_b} d\alpha \frac{\beta^2 \cos(\alpha) - 1}{r_{\alpha,n}} \lambda'(s_{\alpha,n}) \right] \right\}
 \end{aligned} \tag{C.1}$$

with the definitions

$$\begin{aligned}
\alpha_a &\equiv \kappa_1(s - B_1), \\
\alpha_b &\equiv \kappa_1 s, \\
\Delta_a &\equiv s - 2\beta \frac{1}{\kappa_1} \sin\left(\frac{\kappa_1 s}{2}\right), \\
\Delta_b &\equiv B_1 - s + 2\beta \frac{1}{\kappa_1} \sin\left(\frac{\kappa_1(B_1 - s)}{2}\right), \\
r_{\alpha,n} &\equiv \sqrt{2 - 2 \cos \alpha + (n \kappa_1 H)^2}, \\
s_\alpha &\equiv s - s_0 - \frac{1}{\kappa_1} \left(\alpha - \beta \sqrt{2 - 2 \cos \alpha}\right), \\
s_{\alpha,n} &\equiv s - s_0 - \frac{1}{\kappa_1} (\alpha - \beta r_{\alpha,n}).
\end{aligned} \tag{C.2}$$

Some trigonometric functions have been simplified, and the space charge integrals have changed variables to $\Delta = (\alpha - \beta \sqrt{2 - 2 \cos \alpha})/\kappa_1$. These terms account for the regularized CSR-wake and image charges in bend 1. The next terms are

$$\begin{aligned}
\left. \frac{d\mathcal{E}_{\text{CSR}}}{ds} \right|_{D_1} &= Nr_c mc^2 \int_0^{D_1} dL \sum_{n=0}^{\infty} (2 - \delta_{n,0}) (-1)^n \\
&\quad \times \left\{ \frac{T_L}{R_{L,n}^3} \lambda(s_{L,n}) + \left[\beta^2 \frac{\cos(\kappa_1 s)}{R_{L,n}} - \beta \frac{T_L}{R_{L,n}^2} \right] \lambda'(s_{L,n}) \right\} \\
R_{L,n} &\equiv \frac{1}{\kappa_1} \sqrt{2 - 2 \cos(\kappa_1 s) + 2\kappa_1 L \sin(\kappa_1 s) + (\kappa_1 L)^2 + (\kappa_1 n H)^2} \\
T_L &\equiv L \cos(\kappa_1 s) + \frac{1}{\kappa_1} \sin(\kappa_1 s) \\
s_{L,n} &\equiv -L - s_0 + \beta R_{L,n}
\end{aligned} \tag{C.3}$$

$$\begin{aligned}
\left. \frac{d\mathcal{E}_{\text{CSR}}}{ds} \right|_{B_2} &= Nr_c mc^2 \int_0^{B_2} dL \sum_{n=0}^{\infty} (2 - \delta_{n,0}) (-1)^n \\
&\quad \times \left\{ \frac{T_L}{R_{L,n}^3} \lambda(s_{L,n}) + \left[\beta^2 \frac{\cos(\kappa_1 s + \kappa_2 L)}{R_{L,n}} - \beta \frac{T_L}{R_{L,n}^2} \right] \lambda'(s_{L,n}) \right\} \\
R_{L,n} &\equiv \sqrt{\left(\frac{\cos(\kappa_1 s) - 1}{\kappa_1} + \frac{1 - \cos(\kappa_2 L)}{\kappa_2} \right)^2 + \left(D_1 + \frac{\sin(\kappa_1 s)}{\kappa_1} + \frac{\sin(\kappa_2 L)}{\kappa_2} \right)^2 + (nH)^2} \\
T_L &\equiv D_1 \cos(\kappa_1 s) + \frac{\kappa_2 - \kappa_1}{\kappa_1 \kappa_2} \sin(\kappa_1 s) + \frac{1}{\kappa_2} \sin(\kappa_1 s + \kappa_2 L) \\
s_{L,n} &\equiv -L - D_1 - s_0 + \beta R_{L,n}.
\end{aligned} \tag{C.4}$$

Note that the lower limit of the sums have been set to $n = 0$ to account for the real charges as well as image charges, necessitating the use of Kronecker's delta. Alternatively, if only free space terms are desired, the above formulas can be used with the $n = 0$ term only. The dummy variable s' has been rescaled to L which integrates backwards over the length of the appropriate element. The terms $R_{L,n}$, T_L , and $s_{L,n}$ are redefined after each equation in order to keep the naming sane.

Similarly, the wake at $s > B_1$ after bend, as in Eq. (5.71), contains the terms

$$\begin{aligned}
\left. \frac{d\mathcal{E}_{\text{CSR}}}{ds} \right|_{D_0} &= -Nr_c mc^2 \left\{ \int_{-\infty}^{B_1} ds' \left[\frac{1}{(s-s')^2} \lambda(s' - s_0 + \beta(s-s')) \right. \right. \\
&\quad \left. \left. + \beta \frac{\beta - 1}{s-s'} \lambda'(s' - s_0 + \beta(s-s')) \right] \right. \\
&\quad + \sum_{n=1}^{\infty} 2(-1)^n \frac{\lambda(B_1 - s_0 + \beta \sqrt{(s-B_1)^2 + (nH)^2})}{\sqrt{(s-B_1)^2 + (nH)^2}} \\
&\quad \left. + \sum_{n=1}^{\infty} 2(-1)^n \int_0^{\infty} dL \frac{\lambda'(L + B_1 - s_0 + \beta \sqrt{(s-B_1-L)^2 + (nH)^2})}{\gamma^2 \sqrt{(s-B_1-L)^2 + (nH)^2}} \right\},
\end{aligned} \tag{C.5}$$

$$\begin{aligned}
\left. \frac{d\mathcal{E}_{\text{CSR}}}{ds} \right|_{B_1} &= Nr_c mc^2 \sum_{n=0}^{\infty} (2 - \delta_{n,0}) (-1)^n \int_0^{B_1} dL \left\{ \frac{T_L}{R_{L,n}^3} \lambda(s_{L,n}) \right. \\
&\quad \left. + \left[\beta^2 \frac{\cos(\kappa_1 L)}{R_{L,n}} - \beta \frac{T_L}{R_{L,n}^2} \right] \lambda'(s_{L,n}) \right\} \\
R_{L,n} &\equiv \sqrt{\frac{2 - 2 \cos(\kappa_1 L)}{\kappa_1^2} + 2 \frac{(s - B_1) \sin(\kappa_1 L)}{\kappa_1} + (s - B_1)^2 + (nH)^2} \\
T_L &\equiv s - B_1 + \frac{1}{\kappa_1} \sin(\kappa_1 L) \\
s_{L,n} &\equiv -L + B_1 - s_0 + \beta R_{L,n},
\end{aligned} \tag{C.6}$$

$$\begin{aligned}
\left. \frac{d\mathcal{E}_{\text{CSR}}}{ds} \right|_{D_1} &= Nr_c mc^2 \sum_{n=0}^{\infty} (2 - \delta_{n,0}) (-1)^n \int_0^{D_1} dL \left\{ \frac{T_L}{R_{L,n}^3} \lambda(s_{L,n}) + \right. \\
&\quad \left. \left[\beta^2 \frac{\cos(\kappa_1 B_1)}{R_{L,n}} - \beta \frac{T_L}{R_{L,n}^2} \right] \lambda'(s_{L,n}) \right\} \\
(R_{L,n})^2 &\equiv \left(L + (s - B_1) \cos(\kappa_1 B_1) + \frac{\sin(\kappa_1 B_1)}{\kappa_1} \right)^2 \\
&\quad + \left(\frac{\cos(\kappa_1 B_1) - 1}{\kappa_1} - (s - B_1) \sin(\kappa_1 B_1) \right)^2 + (nH)^2 \\
T_L &\equiv s - B_1 + L \cos(\kappa_1 B_1) + \frac{1}{\kappa_1} \sin(\kappa_1 B_1) \\
s_{L,n} &\equiv -L - s_0 + \beta \sqrt{R_L^2 + (nH)^2}.
\end{aligned} \tag{C.7}$$

BIBLIOGRAPHY

- Agoh, T. and K. Yokoya, "Calculation of coherent synchrotron radiation using mesh," *Physical Review Special Topics - Accelerators and Beams* **7**, 054403 (2004)
- Antokhin, E. A., *et al.*, "First Lasing at the high-power free electron laser at Siberian center for photochemistry research," *Nuclear Instruments & Methods in Physics Research A* **528** (2004) 15–18
- Arthur, J. *et al.*, "Linac Coherent Light Source (LCLS) Conceptual Design Report," Report SLAC-R-593 (2002)
- Bazarov, I. V. and G. .H. Hoffstaetter, "Lattice Options for a 5 GeV Light Source at Cornell," *Proceedings of the 2003 Particle Accelerator Conference*, IEEE 0-7803-7739-9 (2003) 842–844
- Bazarov, I. V., G. A. Krafft, and L. Merminga, "Linac Optics for Energy Recovery Linacs," *Proceedings of the 2001 Particle Accelerator Conference*, IEEE Cat. No. 01CH37268 **5** (2001) 3347–3349
- Berz, M., *Modern Map Methods in Particle Beam Physics* (Academic Press, San Diego, 1999)
- Bilderback, D. H., P. Elleaume, and E. Weckert, "Review of Third and Next Generation Synchrotron Light Sources," *Journal of Physics B: Atomic, Molecular, and Optical Physics* **38** (2005) S773–S797
- Blewett, J. P., "Radiation Losses in the Induction Accelerator," *Physical Review* **69** (1946) 87–95

- Borland, M., "elegant: A Flexible SDDS-Compliant Code for Accelerator Simulation," Argonne National Laboratory Advanced Photon Source Report No. LS-287 (2000)
- Borland, M., "Simple method for particle tracking with coherent synchrotron radiation," *Physical Review Special Topics - Accelerators and Beams* **4** 070701 (2001)
- Borland, M., G. Decker, A. Nassiri, and M. White, "Configuration, Optics, and Performance of a 7 GeV Energy Recovery Linac Upgrade for the Advanced Photon Source," *Proceedings of PAC07, Albuquerque, New Mexico* (2007)
- Carroll, S. M., *Spacetime and Geometry—An Introduction to General Relativity* (Addison Wesley, San Francisco, 2004)
- Chao, A. W. and M. Tigner, *Handbook of Accelerator Physics and Engineering* (World Scientific, Singapore, 2006)
- Corson, D. R., "Radiation by Electrons in Large Orbits," *Physical Review* **90** (1953) 748–753
- Courant, E.D. and H.S. Snyder, "Theory of the Alternating-Gradient Synchrotron," *Annals of Physics* **3** (1958) 1–48, reprinted in *Annals of Physics* **281** (2000) 360-408
- Derbenev, Y. S., J. Rossback, and E. L. Saldin, "Microbunch Radiative Tail-Head Interaction," Report TESLA-FEL 1995-05 (1995)
- Douglas, D., "Design Considerations for Recirculating and Energy Recovering Linacs", Report JLAB-TN-00-027 (2000)

- Forest, E., *Beam Dynamics—A New Attitude and Framework* (Harwood Academic Publishers, Amsterdam, 1998)
- Goldstein, H., *Classical Mechanics* (Addison-Wesley, Reading Massachusetts, 1965)
- Gradshteyn, I. S. and I. M. Ryzhik, *Table of Integrals, Series, and Products—Sixth Edition*, (Academic Press, San Diego, 2000)
- Grote, H. and F. C. Iselin, “The MAD Program—Version 8.1,” Report CERN/SL/90-13(AP) (1991)
- Gruner, S. M. and D. H. Bilderback, “Energy Recovery Linacs as Synchrotron Light Sources,” *Nuclear Instruments & Methods in Physics Research A* **500** (2003) 25–32
- Gruner, S. M. and M. Tigner, editors, “Study for a proposed Phase I Energy Recovery Linac (ERL) Synchrotron Light Source at Cornell University,” Reports CHESS 01-003 and JLAB-ACT-01-04 (2001)
- Hoffstaetter, G. H., I. V. Bazarov, D. Sagan, and R. Talman, “A Lattice for a 5 GeV ERL in the CESR Tunnel,” *Proceedings of the 2003 Particle Accelerator Conference*, IEEE 0-7803-7739-9 (2003) 848–850
- Hoffstaetter, G., M. P. Ehrlichman, and A. B. Temnykh, “Intra beam scattering in linear accelerators, especially ERLs,” *Proceedings of the 11th European Particle Accelerator Conference*, Genoa, Italy (2008) 1631–1633
- Hoffstaetter, G. H. and Y. H. Lau, “Compensation of Wake-field-Driven Energy Spread in Energy Recovery Linacs,” *Physical Review Special Topics - Accelerators and Beams* **11** 070701 (2008)

- Hoffstaetter, G. and C. Spethmann, "Equilibrium ion distribution in the presence of clearing electrodes and its influence on electron dynamics," *Physical Review Special Topics - Accelerators and Beams* **11**, 013001 (2008)
- Iwanenko, D. and I. Pomeranchuk, "On the Maximal Energy Attainable in a Betatron," *Physical Review* **65** (1944) 343–343
- Jackson, J. D., *Classical Electrodynamics—Third Edition* (Wiley, New York, 1999)
- Landau, L. D. and E. M. Lifshitz, *Mechanics—Third Edition* (Butterworth-Heinemann, Oxford, 2001)
- Landau, L. D. and E. M. Lifshitz, *The Classical Theory of Fields—Fourth Revised English Edition* (Butterworth-Heinemann, Oxford, 2002)
- Landau, L. D. and E. M. Lifshitz, *Quantum Mechanics—Third Edition* (Butterworth-Heinemann, Oxford, 2002)
- Larmor, J., "On the Theory of the Magnetic Influence on Spectra, and on the Radiation from Moving Ions," *Philosophical Magazine* **44** (1897) 503–512
- Liénard, A., "Champ électrique et magnétique produit par une charge électrique concentrée en un point et animée d'un mouvement quelconque," *L'Éclairage Électrique* **16** (1898)
- Liepe, M., S. A. Belomestnykh, E. P. Chojnacki, Z. A. Conway, R. Ehrlich, R. P. K. Kaplan, V. Medjidzade, H. Padamsee, P. Quigley, J. J. Reilly, D. M. Sabol, J. Sears, V. D. Shemelin, E. N. Smith, V. Veshcherevich, and D. Widger, "First Test Results from the Cornell ERL Injector Cryomodule," *Proceedings of the 11th European Particle Accelerator Conference, Genoa, Italy* (2008) 883–885

- Madden, R. P. and K. Codling, "New Autoionizing Atomic Energy Levels in He, Ne, and Ar," *Physical Review Letters* **10** (1963) 516–518
- Mayes, C. and G. Hoffstaetter, "Exact 1D model for coherent synchrotron radiation with shielding and bunch compression," *Physical Review Special Topics – Accelerators and Beams* **12**, 024401 (2009)
- McIntosh P. A. *et al.*, "Development of a prototype superconducting CW cavity and cryomodule for energy recovery," *Proceeding of EPAC, MOPCH161*, (2006)
- Misner, C. W., K. S. Thorne, and J. A. Wheeler, *Gravitation* (W. H. Freeman and Company, New York, 1973)
- Motz, H., "Applications of the Radiation from Fast Electron Beams," *Journal of Applied Physics* **22** (1951) 527–535
- Murphy, J. B., "An Introduction to Coherent Synchrotron Radiation in Storage Rings," *ICFA Beam Dynamics Newsletter No. 35* (2004)
- Murphy, J. B., S. Krinsky, and R. L. Gluckstern, "Longitudinal Wakefield for Synchrotron Radiation," *Proceedings of the 1995 Particle Accelerator Conference Volume 5* (1995) 2980–2982
- Neil, G. R. *et al.*, "Sustained Kilowatt Lasing in a Free-Electron Laser with Same-Cell Energy Recovery," *Physical Review Letters* Volume **84** (2000) 662–665
- Nodvick, J. S. and D. S. Saxon, "Suppression of Coherent Radiation by Electrons in a Synchrotron," *Physical Review* **96** (1954) 180–184
- Parzen, G., "The Radiation from an Electron Moving in a Uniform Magnetic Field," *Physical Review* **84** (1951) 235–239

- Pollock, H. C., "The Discovery of Synchrotron Radiation," *American Journal of Physics* **51** (1983) 278–280
- Press, W. H., S. A. Teukolsky, W. T. Vetterling, and B. P. Flannery, *Numerical Recipes—The Art of Scientific Computing, Third Edition* (Cambridge University Press, Cambridge, 2007)
- Price, K. V., R. M. Storn, and J. A. Lampien, *Differential Evolution—A Practical Approach to Global Optimization* (Springer, Berlin, 2005)
- Robinson, A. L., "History of Synchrotron Radiation" in *X-ray Data Booklet* edited by A. C. Thompson and D. Vaughan (Lawrence Berkeley National Laboratory, Berkeley, 2001)
- Rosenzweig, J. and L. Serafini, "Transverse particle motion in radio-frequency linear accelerators," *Physical Review E* **49** (1994) 1599–1602
- Sagan, D., "Bmad: A relativistic charged particle simulation library," *Nuclear Instruments & Methods in Physics Research A* **558** (2006) 356–359
- Sagan, D. C., G. H. Hoffstaetter, C. E. Mayes, and U. Sae-Ueng, "Extended one-dimensional method for coherent synchrotron radiation including shielding," *Physical Review Special Topics – Accelerators and Beams* **12**, 040703 (2009)
- Saldin, E. L., E. A. Schneidmiller, and M. V. Yurkov, "On the coherent radiation of an electron bunch moving in an arc of a circle," *Nuclear Instruments and Methods in Physics Research A* **398** (1997) 373–394
- Sands, M., "The Physics of Electron Storage Rings—An Introduction," Report SLAC-121 (1970)

- Sawamura, M., R. Hajima, N. Kikuzawa, E. J. Minehara, R. Nagai, and N. Nishimori, "Performance and Upgrade of the JAERI ERL-FEL," Proceedings of the 2003 Particle Accelerator Conference, IEEE 0-7803-7739-9 (2003) 3446-3448
- Schott, G. A., *Electromagnetic Radiation* (Cambridge University Press, Cambridge, 1912)
- Schwinger, J., "On Radiation by Electrons in a Betatron," in Report LBNL-39088 and *A Quantum Legacy: Seminal Papers of Julian Schwinger* edited by K. A. Milton, (World Scientific, Singapore, 2000) 307-331
- Schwinger, J., "Electron Radiation in High Energy Accelerators," *Physical Review* **70** (1946) 798-799
- Schwinger, J., "On the Classical Radiation of Accelerated Electrons," *Physical Review* **75** (1949) 1912-1929
- Smith, S., B. D. Muratori, H. I. Owen, G. H. Hoffstaetter, *et al.*, "Optics Issues in Ongoing ERL Projects," *Nuclear Instruments and Methods in Physics Research A* **557** (2006) 145-164
- Stupakov, G. and P. Emma, "CSR Wake for a Short Magnet in Ultrarelativistic Limit," *Proceeding of the European Particle Accelerator Conference, Paris* (2002) 1479-1481
- Tigner, M., "A Possible Apparatus for Electron Clashing-Beam Experiments," *Nuovo Cimento* **37** (1965) 1228-1231
- Tomboulia, D. H. and P. L. Hartman, "Spectral and Angular Distribution of Ultraviolet Radiation from the 300-MeV Cornell Synchrotron," *Physical Review* **102** (1956) 1423-1447

Warnock, R., "Shielded coherent synchrotron radiation and its effect on very short bunches," Report SLAC-PUB-5375 (1990)

Warnock, R., G. Bassi, and J. A. Ellison, "Vlasov treatment of coherent synchrotron radiation from arbitrary planar orbits," *Nuclear Instruments and Methods in Physics Research A* **558** (2006) 85–89

Wiedemann, H., *Particle Accelerator Physics I* (Springer-Verlag, Berlin, 1999)

Wiedemann, H., *Particle Accelerator Physics II* (Springer-Verlag, Berlin, 1999)

Wille, K., *The Physics of Particle Accelerators* (Oxford University Press, Oxford, 2000)